FAULT MAPPING WITH THE REFRACTION MICROTREMOR AND SEISMIC REFRACTION METHODS ALONG THE LOS OSOS FAULT ZONE

A Thesis

Presented to the Faculty of

California Polytechnic State University

San Luis Obispo

In Partial Satisfaction

Of the Requirements for the Degree of

Master of Science in Civil and Environmental Engineering

By

Justin Riley Martos

November 2012

COMMITTEE MEMBERSHIP

TITLE:	Fault Mapping with the Refraction Microtremor and Seismic Refraction Methods along the Los Osos Fault Zone
AUTHOR:	Justin Riley Martos
DATE SUBMITTED:	November 2012
Committee Chair:	Robb Moss, Associate Professor
Committee Member:	Gregg Fiegel, Professor
Committee Member:	John Jasbinsek, Assistant Professor

ABSTRACT

Fault Mapping with the Refraction Microtremor and Seismic Refraction Methods along the Los Osos Fault Zone

By Justin Riley Martos

The presence of active fault traces in proximity to any new infrastructure project is a major concern for the design process. The relative displacements that can be experienced in surface fault rupture during a seismic event must be either entirely avoided or mitigated in some way. Blind faults present a significant challenge to engineers attempting to identify these hazards. Current standards of practice employed to locate these features are time consuming and costly. This work investigates the geophysical methods of refraction microtremor (ReMi) and seismic refraction with regard to their applicability in this task. By imaging a distinct lateral variation in the shear wave velocity (V_s) profile across a short horizontal distance, these methods may provide a means of constraining traditional investigation techniques to a more focused area. The ReMi method is still very new, but holds key advantages over other geophysical methods in its ease of application and ability to achieve good results in highly urban settings. It is one of the few geophysical techniques that does not suffer in the presence of high amplitude ambient vibrations. The seismic refraction method is here applied in an attempt to corroborate data obtained through the ReMi analysis procedure. Sensitivity, precision parametric studies are carried out in order to learn how to best apply the ReMi method. Both tests are then applied at a previously trenched fault trace to determine whether the data can be matched to the subsurface information. Finally, the methods are deployed at a location with an inferred fault trace where little to nothing is known about the subsurface. The precision study indicates a coefficient of variation

for the ReMi method on the order of 7%. At the known fault trace both methods generally agree qualitatively with available subsurface data and each other. Using the ReMi method, a marked shift is observed in the V_s profile laterally across the fault trace. In the case of the inferred fault trace, the same type of lateral variation in the V_s profile is observed using the ReMi method. The seismic refraction at this site does not agree with the ReMi data, but seems reasonable given the visible geomorphology. Receiver arrays placed in close proximity to the inferred fault trace recorded erratic signals during seismic refraction testing, and displayed abnormal response modes after transforming the ReMi data to frequency-slowness space. These anomalies may possibly be attributed to the presence of abnormal subsurface structural geometry indicative of faulting.

ACKNOWLEDGEMENTS

This work would not have been possible without the help I received from the many people involved with this project. First and foremost among them is my advisor, Prof. Robb Moss. His guidance throughout this endeavor was essential to its success from start to finish. I greatly appreciate the patience and encouragement he provided during my struggles. The help and direction provided me a framework that aided the steady progress toward my goal, while also allowing me the space to draw my own conclusions along the way.

I would like to express my deep gratitude to Professors Gregg Fiegel and John Jasbinsek for taking the time to review my work and provide insightful suggestions of ways to improve upon it. I only provided them with one week to read this entire paper because of my rush to complete the degree requirement, but they both adjusted their schedules to accommodate my needs. I consider this a personal favor and am in their debt.

Jason Auyeung and Dr. Moss both contributed a significant amount of their own time to help me with the data collection process in the field. I cannot thank them enough for the many hours we spent together in the hot sun placing arrays and swinging sledge hammers. Without their help my job would have been beyond exhausting.

This work involved learning the use of a lot of software I had no previous experience using. Satish Pullammanappallil of Optim Software provided me with continual support in using the Optim programs for data processing and analysis. Throughout this project he supplied invaluable help with troubleshooting, general procedural guidelines, and

interpretive insight. I am very thankful for his patient aid with many questions I'm sure seemed very novice to someone with his experience.

Thomas Blake of Fugro Consultants, Inc. also deserves a sincere thank you for his suggestions on how to better collect and analyze seismic refraction data. Tom had no obligation to help me, but he immediately dedicated time to answer my many questions, and even processed some of the data himself with software unavailable to me.

During my research it was at times necessary to turn to more experienced geophysicists for explanations of subtle theory and terminology usage. It was very helpful to be able to turn to Prof. Brady Cox and his doctoral student Clinton Wood in these instances. They always took the time to fully answer any questions and to ensure that I understood the explanations. I enjoyed the time I was able to spend with them collecting geophysical data for a National Science Foundation project at the San Francisco Trans-bay Transit Center construction site.

I extend a special thanks to John Madonna and Diane Sawyer of San Luis Obispo County for their contributions to my work. Without their help this project would have been impossible. I greatly appreciate their patience and cooperation throughout this work.

Finally I must thank my family and friends, especially my mother and father, who have been there for me through good times and bad. Their emotional support was essential to get me through to the end. It was the laughter and relaxation their company provided during my small breaks from this work that enabled me to keep returning to it. I would have never reached the finish line without some occasional time to unwind.

Table of Contents

LIST OF TABLES

LIST OF FIGURES

Chapter 1: Statement of Research

1.1: Introduction

In recent decades the advances in the field of applied geophysics have provided engineers with a new tool to aid in shallow subsurface investigations. Theory originally developed to help determine the Earth's deep layer structure is now employed widely in the near surface for a variety of purposes. These methods have been successfully used for a number of engineering applications, a few among them include locating petroleum reserves, determining water table depths for well water drilling, and developing soil stiffness profiles to aid in characterizing site response during seismic events.

There are a number of different methods available that involve the measurement of either body or surface waves. These methods are discussed in detail in chapter 2. The field of applied geophysics is expanding rapidly as more and more scientists and engineers have begun to explore its potential. Within just the last 20 years a number of new techniques have surfaced that provide different means of applying the same underlying principals of wave propagation. As is always the case, new methods warrant significant amounts of research into their applicability. Many questions remain unanswered with regards to the circumstances where these methods provide accurate and/or precise results.

Some of the geophysical techniques available to engineers have significant advantage over other investigation methods in the areas of cost, and time. It is for this reason that many private companies in addition to academic institutions now apply these techniques to corroborate traditional investigation results. In many cases, a field team as small as two persons can collect all the necessary data at a small site in a full day's

work. With some methods, such as the refraction microtremor (ReMi) and seismic refraction techniques, achieving adequate results requires no more equipment than what will fit in a small gardening wagon.

This body of work investigates the potential of the two methods mentioned in the previous paragraph as fault mapping tools. Should these techniques prove efficient and effective, engineers would have available a much cheaper and faster means of locating fault traces.

1.2: Fault Rupture and Blind Fault Mapping

During seismic events it is not uncommon for the relative displacement between structural blocks to propagate to the ground surface. This can result in offsetting horizontally, vertically, or a combination of the two depending upon the fault regime. Any structures that rest atop a fault trace that suddenly displaces in this nature could sustain significant damage depending on the degree of offsetting. No man-made structure can resist such forces, but some have been designed with enough ductility to allow for some degree of displacement. Where possible, building on sites with active faults should always be avoided.

After the 1971 San Fernando earthquake in California, the state legislature passed the Alquist-Priolo Act in an attempt to reduce future damages from surface fault rupture. This act prohibits building new structures for human occupancy within mapped zones containing known active fault traces (R. Moss, personal communication, April 13, 2011). Although this law helps reduce the risk of damage from surface fault rupture, many active faults exist that remain unmapped.

Many known active fault traces exhibit some surface expression and are easily identifiable to trained geologists. Unfortunately, it is not uncommon for them to be blind in nature (show no surface expression). Blind faults exist where the feature has been covered by newer material that has not yet experienced rupture. Under small displacements this material may behave in a ductile manner rather than exhibiting a brittle rupture, and the trace will remain masked.

Locating these blind fault traces can be very expensive and time consuming with traditional drilling or trenching techniques. These methods provide highly localized information when the area being searched is often quite expansive. The application of geophysical methods could potentially become a much more cost and time effective tool to aid in narrowing down the possible trace location.

1.3: Project Scope

The primary goal of this thesis project is to investigate the possible application of the refraction microtremor and seismic refraction methods as tools for fault mapping. In order to reach this goal it was necessary to carry out a number of studies within the refraction microtremor method to learn how to best apply the technique. These included parametric studies to determine the effects of array geometry, relative source location, and signal type, as well as a precision study to characterize the uncertainty involved in the measurement process.

After determining best practices for each technique, this work attempts to identify a significant lateral variation in the soil stiffness profile across a reverse fault trace at locations with trench and borehole data, and where little to no subsurface information is available.

1.4: Organization of Thesis

This work presented herein is organized so that the reader is presented with some background understanding of the testing methods and analysis processes prior to examining the collected data. Chapter 2 provides an overview of available methods for characterizing the subsurface shear wave velocity profile. Presented are a number of methods that allow for direct or indirect measurement of the soil stiffness profile through recordings of surface and body waves. Chapter 3 includes a detailed summary of the testing and analysis methods applied in this work. Step by step instructions for field setup, data processing and modeling are presented. The chosen testing sites are discussed in chapter 4, along with the reasoning behind their selection for this work. Chapters 5-7 contain the quantitative and qualitative findings of the collected data, paired with in-depth discussions and interpretations of these findings. Conclusions and recommendations for further research reside in chapter 8.

Chapter 2: Review of Methods to Obtain a Site Shear Wave Velocity Profile

2.1: Introduction to Vs logging

In today's ground motion site response analyses the primary parameter of interest is the in situ shear wave velocity in the upper 30m of soil strata (V_{s30}). The Universal Building code assigns a site class ranging from A-E depending upon this parameter and applies varying requirements to the analysis accordingly. V_{s30} is also a useful parameter in liquefaction or cyclic failure analyses and numerous other seismic applications. When modeling a soil column, V_{s30} is useful in determining shear modulus values from the following equation:

$$G = \rho V_s^2 \qquad \text{EQ 2.1}$$

where G is the small strain shear modulus, ρ is the material density, and V_s the shear wave velocity in that layer.

Although current methods of measuring V_{s30} are only capable of measuring small strain shear wave velocities (less than 0.001), the parameter is considered the simplest approximation available for the behavior that will be exhibited during a seismic event. There are a number of methods currently employed to determine V_{s30}, including direct measurement methods, analysis of body wave movement through the stratified medium, and analysis of surface wave propagation. The waves of interest for these techniques are primary (P) or compressional waves, secondary (S) or shear waves and Rayleigh (R) waves, which are the vertical component of surface waves. The horizontal component of surface waves, called Love waves, are also being investigated as a

possible means of characterizing the V_s profile at a site (R. Moss, Personal Communication, August 8, 2012). The more notable methods will be discussed briefly to give the reader an understanding of the techniques available.

2.2: Direct Measurement Methods

Direct measurement methods are more readily accepted due to the limited analysis required to develop the S-wave velocity profile. It is unsurprising that direct measurement would be considered to be more reliable; however, these methods require significant labor, time and equipment. The more common techniques of direct measurement include suspension, downhole, crosshole, and Seismic Cone Penetration Test (SCPT) logging. All of these methods require placing a sensor in the soil strata within a borehole or CPT probe at varying depths to receive an induced wave signal.

2.2.1: Downhole Logging

The Downhole and crosshole methods require that a borehole be drilled, cased and grouted to house the receiver(s). The American Society for Testing and Materials (ASTM) provides standards for down and crosshole testing, D7400 and D4428 respectively, that outline the important aspects of the tests, and indicate proper procedures to ensure repeatability. The casing must be properly coupled and grouted at least to the desired depth of logging to insure a good contact with the surrounding strata and adequate signal reception.

This method allows for measurement of both P and S-wave velocities, which can be useful in determining elastic constants of the material by solving a simple system of equations. The following equations define the relationships between body wave velocities and elastic constants:

$$V_p = \sqrt{E(1 - \nu) / [\rho (1 - 2\nu) (1 + \nu)]} \qquad \text{EQ 2.2}$$

$$V_s = \sqrt{G/\rho} = \sqrt{E/[2\rho (1 + \nu)]} \qquad \text{EQ 2.3}$$

E = Young's Modulus

G = Shear Modulus

ρ = Density

v = Poisson's Ratio

These elastic properties are useful in many engineering applications and thus the ability of the method to directly measure both P and S-wave velocities can be advantageous.

In order to induce the wave signals at the surface, a shear beam is placed on the ground, restrained by some heavy weight, and then impacted transversely. A shear beam can be metal or wood, with the ends typically encased in steel. Cleats along the bottom of the shear beam can help prevent sliding and insure that the energy is transferred to the soil in the form of an S-wave. These S-waves travel down to the receiver suspended in the borehole. In order to induce a P-wave a metal plate can be struck normal to the ground surface. These wave signals can be recorded to significant depths and are only limited by the signal to noise ratio.

It is preferable to have multiple receivers in the hole spaced at the desired interval of measurement to pick up the difference in arrival times at each receiver. Such a setup is depicted in Figure 2.1. This allows the velocity of that interval to be more directly measured, however, through a more complex analysis a single receiver can be used. The receiver is lowered down into the hole in intervals of depth dependent upon

the resolution desired. With only one receiver, each point of measure will give the average velocity from source to receiver; however, by discretizing the upper intervals that have already been imaged, the true velocity in the new interval can be determined.

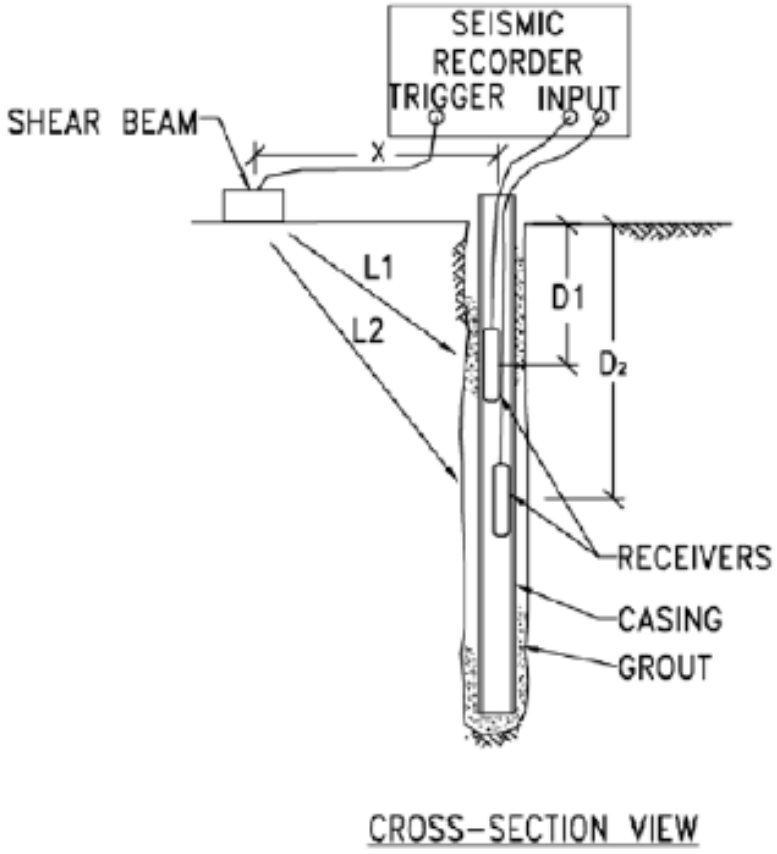

Figure 2.1: Schematic of Downhole V_s Logging Setup (from ASTM D7400-08)

It is standard practice to strike the shear beam in both transverse directions in order to receive reversely polarized signals and insure that the first break of the desired wave signal is consistent. An example of records obtained through downhole logging is shown in Figure 2.2.

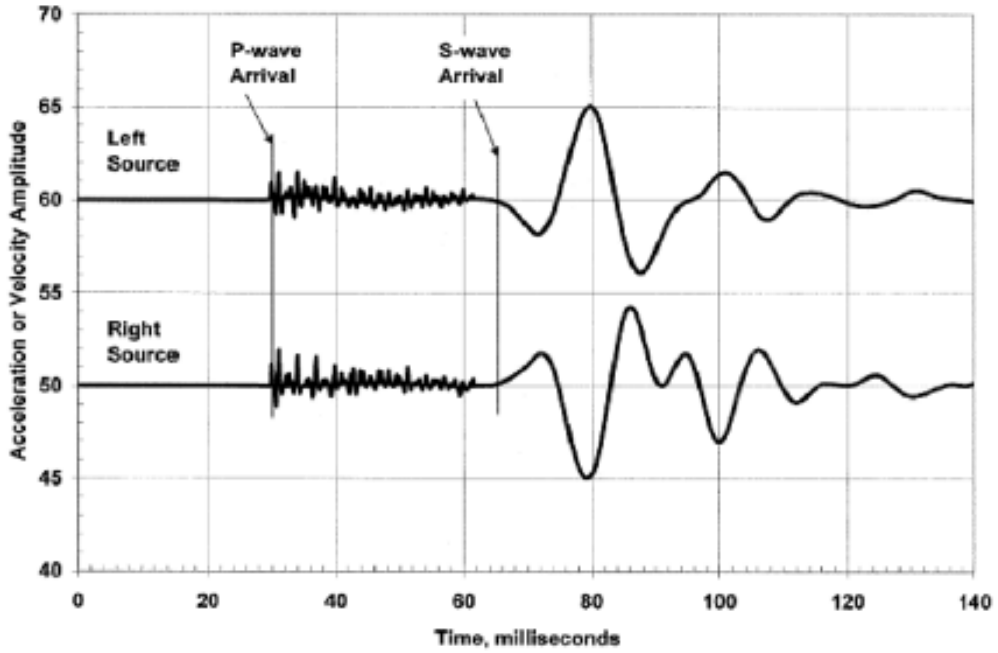

Figure 2.2: Example of Downhole Seismogram Showing First Arrivals of P and S-Waves (from ASTM D7400-08)

2.2.2: Crosshole Logging

The crosshole method is outlined in the aforementioned ASTM D4428 specification. Discussion in this section is summarized and paraphrased from the ASTM code. This method requires the drilling and casing of an additional hole or holes to house the source and redundant receivers. For this reason the cross-hole method often requires much time and cost to prepare the holes. However, it does offer advantages over the downhole and suspension logging methods. As depicted in Figure 2.3, the source and receivers are placed on the same horizontal plane. Assuming minimal lateral variation, this means that the velocity at that depth is being directly measured rather than an average over a depth interval. In this manner, small seams of higher or lower velocity will not affect the signals path to the receiver. Again, only one receiver is required to obtain the shear wave velocity profile; however, redundant receivers can help

in the analysis procedure to determine coherence of the signal and produce more robust results.

The crosshole method can be used to determine both P and S-wave velocities, but the energy source must be appropriate depending upon which attribute is being measured. A typical source for P-wave generation is the use of a small explosive within the borehole casing. In order to generate S-waves the source must create distortion transverse to the direction of wave travel. Vibratory equipment is available that can generate the necessary signals within the borehole casing. Some amount of P-wave generation will be present regardless of the source type. The ASTM code specifies that when measuring S-wave arrivals, the amplitude must be at least twice that of the earlier P-wave arrivals. It is also helpful to reverse polarization of the generated waves and then overlay the records to more precisely and confidently locate the arrival. Another method to increase confidence in the arrival data involves measuring both the vertical and horizontal components of the S-wave arrivals. The two data sets can then be compared for agreement.

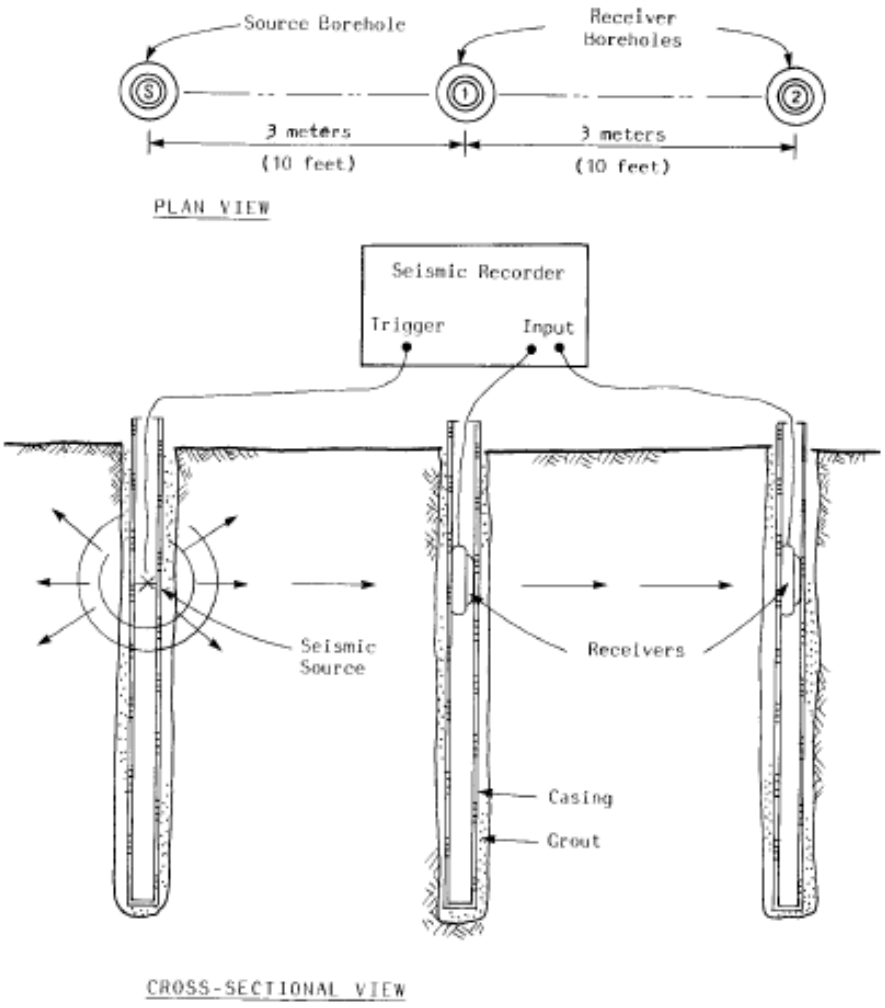

Figure 2.3: Schematic of Crosshole V_s Logging (from ASTM D4428M-07)

2.2.3: Suspension PS-Logging

Some shortcomings in the down and crosshole methods prompted Kitsunezaki (1975) to suggest an idea for placing both source and receivers in the same hole. First presented as a standard method by Ohya et al. (1984) in the offshore technology conference, the Suspension PS-logging method is very similar to the downhole and crosshole methods with some significant and important differences. As shown in Figure 2.4, the signal source is placed in the same hole as the receivers all as part of one apparatus. The receivers are separated from the source and each other by flexible

tubing. The method requires that the logging occur below the water table as the source creates a pressure wave in the borehole fluid that is then converted to seismic P and S-waves at the borehole wall. The signals travel along the borehole walls until they are converted back to a pressure wave at the receiver(s).

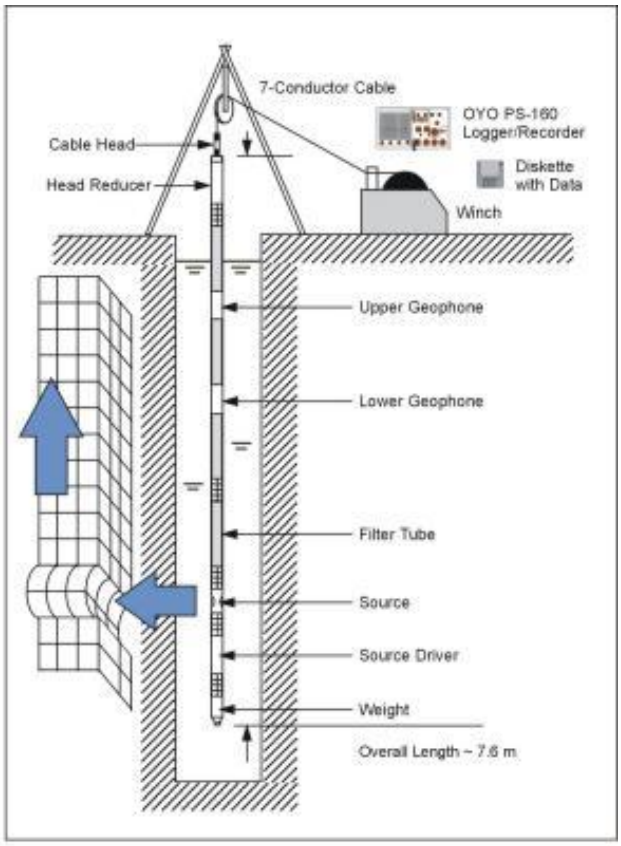

Figure 2.4: Schematic of Up-hole Suspension Logging Setup

(from GEOVision Geophysical Systems)

It is important to note that this is the only method that can image depths beyond about 100m (limited only by borehole depth) with only one hole. In downhole logging, the source is at the ground surface, meaning that the signal will attenuate at excessive depths. While theoretically crosshole testing seems to be capable of also profiling extremely deep, it is difficult to keep verticality of boreholes to such depths, and thus the distance from source to receivers may change with depth (Ohya et al. 1984). Crosshole

testing also requires multiple borings, which quickly drive up cost. Casing installation is optional, and it is often that better results are achieved with an uncased hole. This can translate to significant saving in both time and cost. The suspension PS-logging method can attain high resolution of up to 1m.

2.2.4: Seismic Cone Penetration Test (SCPT)

The SCPT method is almost identical to the downhole logging method. The difference is that, rather than drilling and casing a hole for the receiver to be suspended in, a geophone is placed inside a CPT probe as depicted in Figure 2.5, and measurements can be made between intervals of a typical investigation. CPT trucks are often outfitted with a shear beam, which is restrained by the weight of the truck itself. Logging in this manner is limited by the inability to push the cone through overly stiff material. For example, in cases where a cone is stopped due to a seam of dense sand or gravel, it may be necessary to drill and use traditional downhole or suspension logging to image strata below the problematic location.

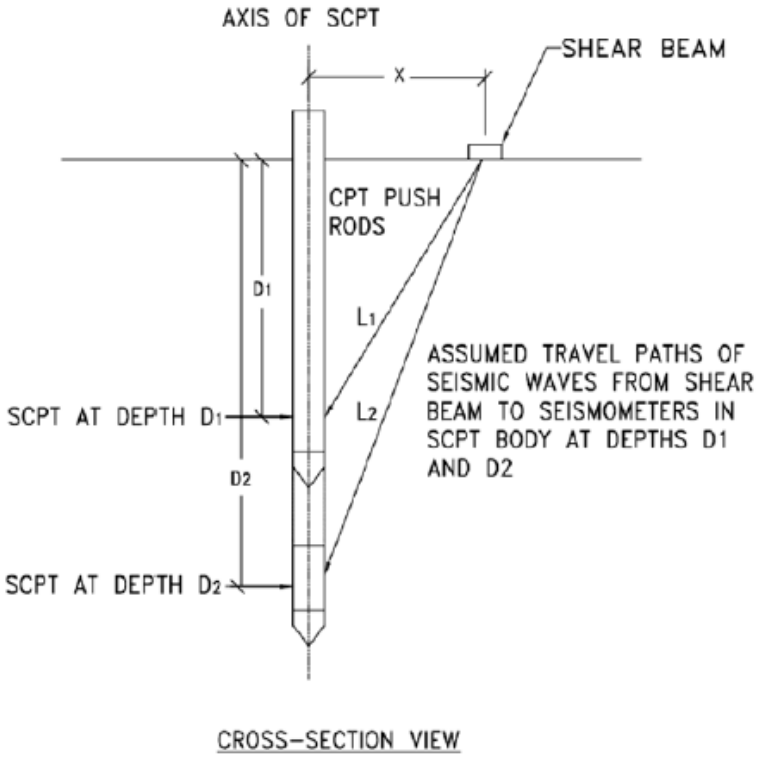

Figure 2.5: Schematic of SCPT V_s Logging (from ASTM D7400-08)

2.3: Body Wave Methods

Body wave analysis methods such as Seismic Refraction and Reflection rely upon the properties of P-waves traveling through strata of varying stiffness. Both methods can be accomplished using standard geophones like the 4.5 Hz phones employed by this study. This paper will focus primarily upon seismic refraction since it is the body wave method implemented in this investigation and the concepts of reflection are fairly similar.

2.3.1: Seismic Refraction

Accepted methods for data collection and analysis of Seismic Refraction are provided in ASTM specification D5777 and Redpath's overview in his 1973 paper (Redpath, 1973). Simply put, the analysis compares the arrival times of refracted body

waves to that of the direct P-wave arrival along the ground surface along a linear array of geophones. A typical array setup is shown in Figure 2.6.

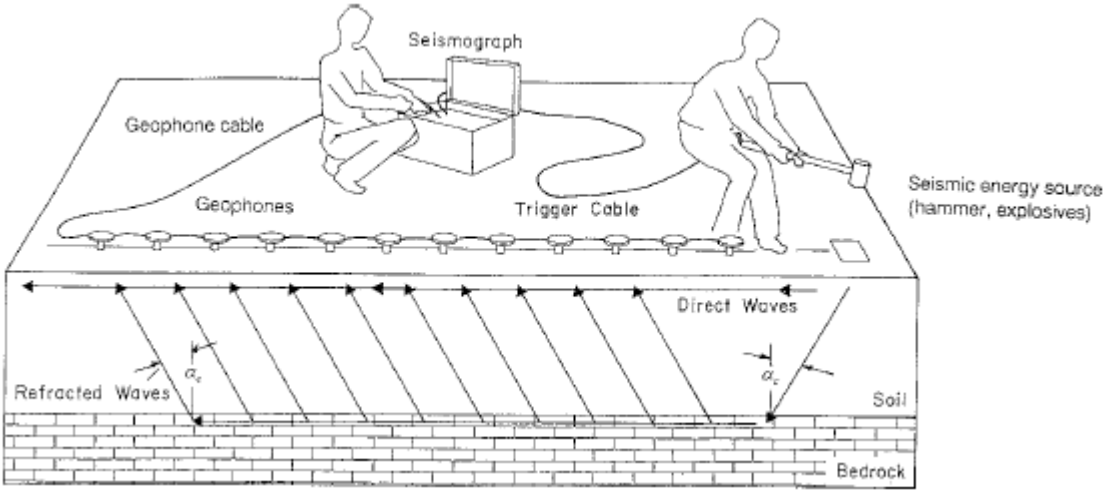

Figure 2.6: Schematic of Seismic Refraction Array Setup (from ASTM D5777)

P-waves moving through a layered soil profile will refract at interfaces of differing stiffness in accordance with Snell's law. At the critical angle of incidence the wave will be converted to a headwave, which moves along the interface between two strata of different stiffness. This headwave then acts like a new signal source moving along the interface at the rate of the higher stiffness material sending P-waves back up to the receivers at the critical angle. Figure 2.7 depicts wave refraction at an interface and the conditions for headwave generation.

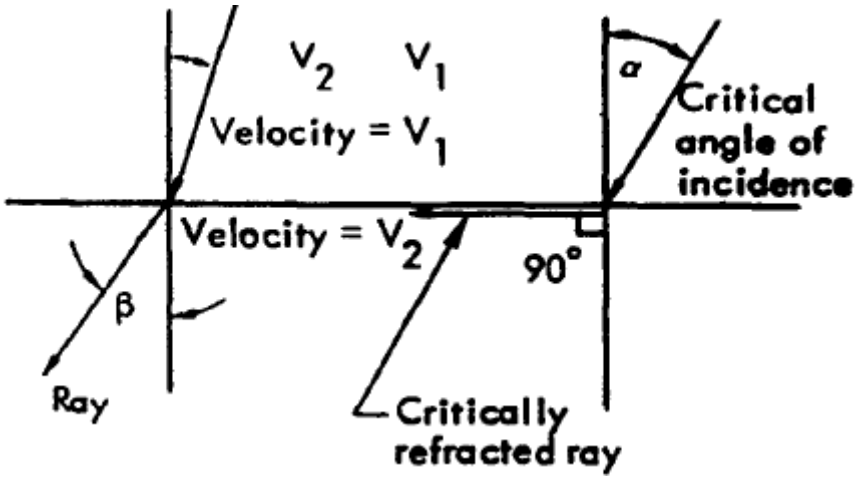

Figure 2.7: Wave Refraction and the Critical Angle of Incidence (from Redpath 1973)

Snell's Law is the relationship between wave speed in each medium and refraction angle given by:

$$\sin\alpha/\sin\beta = V_1/V_2 \qquad \text{EQ 2.4}$$

α = Angle of Incidence

β = Refracted Angle

V_1 = Wave Velocity in Incident Medium

V_2 = Wave Velocity in Refracting Medium

and critical angle of incidence α_c given at β = 90°:

$$\sin\alpha_c = V_1/V_2 \qquad \text{EQ 2.5}$$

Due to the ability for the signal to move faster as a headwave in the stiffer material, at some critical distance the refracted waves will reach the geophones at the surface before the direct wave arrivals as shown in Figure 2.8. The figure depicts a simple two-layer case with a bilinear distance-time curve whose slopes are equal to the inverses of the wave velocity in each respective medium.

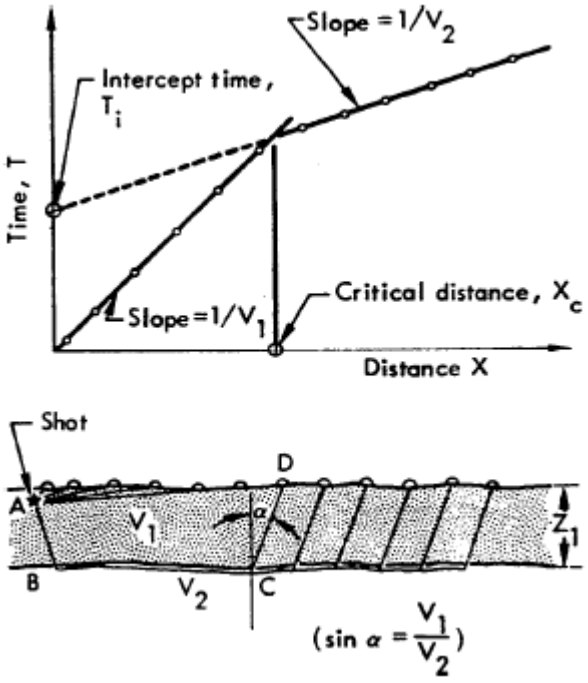

Figure 2.8: Schematic Showing First Arrivals from Direct and Refracted Waves with a Corresponding Distance-Time Plot (from Redpath 1973)

If we consider the travel path ABCD shown in Figure 2.8, by simple mathematics we can find the travel time to be given by the following expression:

$$T = {[AB + CD]}/{V_1} + {BC}/{V_2} \qquad \text{EQ 2.6}$$

Then, with simple geometry and Snell's Law, we can find the depth to the refracting surface Z_1 from the following relationship:

$$Z_1 = {T_i V_1}\Big/{\left[2\cos\left(\sin^{-1}\left({V_1}/{V_2}\right)\right)\right]} \qquad \text{EQ 2.7}$$

T_i = Intercept Time as Shown in Figure 2.8

The full derivation of this equation can be found in many resources, including Redpath (1973). It is possible to apply this same logic to profiles with more than two

layers, but the derivations are redundant and will not be addressed here. Another method often used is the critical distance method; however, it follows the same general logic as the previously described method and provides the same results. For this reason the critical distance method will not be discussed here, however, a good discussion is provided in Redpath (1973).

The examples to this point have explored horizontally layered profiles with source points off one end of the array. If, however, the profile contains dipping layers, it becomes necessary to analyze the distance-time curves from sources off of each end of the array. As Redpath points out, the previously shown theory yields true velocities only if the layering is horizontal. If this is not the case, this simplistic analysis will only yield apparent velocities, and thus, erroneous depths. Figure 2.9 shows how the distance-time curves are affected by the dipping beds.

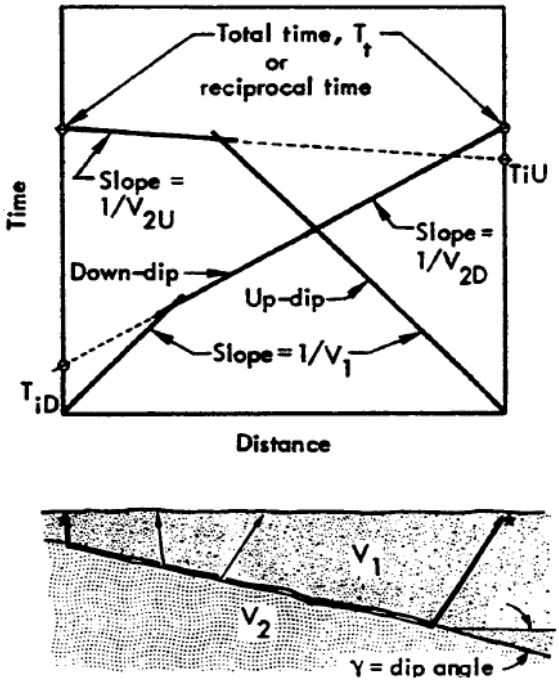

Figure 2.9: Waves Refracting along Dipping Beds and the Corresponding Distance Time Plot (from Redpath 1973)

If we take γ to be the dip angle of the interface, and α as the critical angle of incidence for the refracting wave, the following relationships derived from Snell's law define the apparent refractor velocities up and down the array:

$$V_{2U} = {V_1}/{\sin(\alpha - \gamma)} \qquad \text{EQ 2.8}$$

$$V_{2D} = {V_1}/{\sin(\alpha + \gamma)} \qquad \text{EQ 2.9}$$

and solving the system of equations the dip angle is found to be:

$$\gamma = 0.5\left[\sin^{-1}\left({V_1}/{V_{2D}}\right) - \sin^{-1}\left({V_1}/{V_{2U}}\right)\right] \qquad \text{EQ 2.10}$$

Redpath goes on to explain that the true refractor velocity V_2 is the harmonic mean of the up and down array velocities multiplied by the cosine of the dip angle as follows:

$$V_2 = \left[{2V_{2U}V_{2D}}/{(V_{2U} + V_{2D})}\right]\cos\gamma \qquad \text{EQ 2.11}$$

While this process adequately determines the true refractor velocity, the depth of the refracting surface found by the intercept-time method is the depth of the projected inclined plane below the shot point. The delay time method allows a depth calculation to be made at each receiver and thus a much more detailed profile can be obtained.

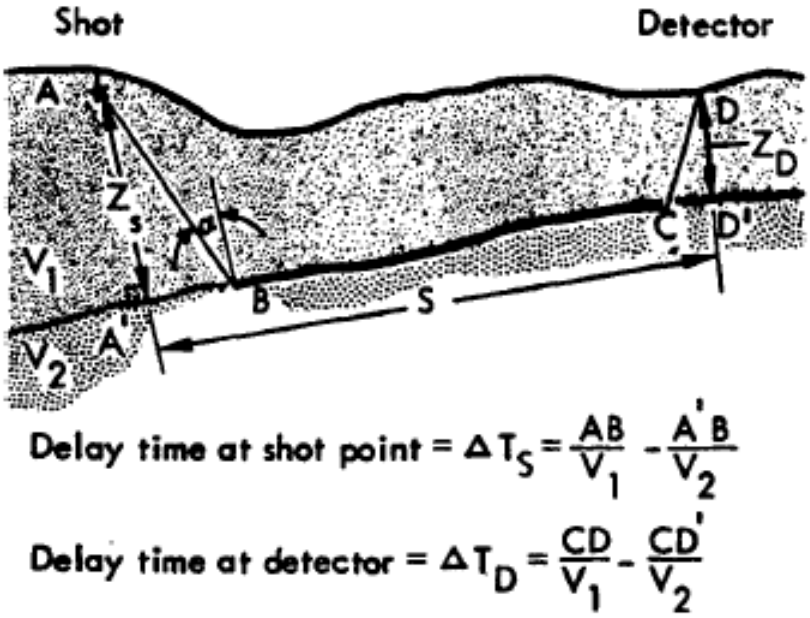

Figure 2.10: Definition of Delay Times (from Redpath 1973)

A delay time can be thought of in simple terms as the time it takes from the wave to propagate vertically from the source to the refractor interface, or the interface to receiver. The exact definition is displayed in Figure 2.10 to provide a more complete explanation. Employing Snell's law, algebra and several trigonometric identities to the ray path depicted above, the depth to the refracting interface beneath each receiver can be defined as:

$$Z_D = {}^{\Delta T_D V_1}\Big/_{\cos\left[\sin^{-1}\left({}^{V_1}/_{V_2}\right)\right]} \qquad \text{EQ 2.12}$$

This equation is very similar to the intercept-time method's equation for refractor depth. In order to determine the refractor depths, it is necessary to determine the delay time at each receiver. If the delay time at the shot is known, it is possible to determine the receiver delay times with a single off-end shot. However, if the delay time at the source is unknown, it is necessary to use shots off of both ends to determine material

velocities and dip angles as previously described. The total delay time at shot and receiver can be described by either of the following two equations:

$$\Delta T_{SD} = \Delta T_S + \Delta T_D \qquad \text{EQ 2.13}$$

$$\Delta T_{SD} = T_t - {}^{S}/_{V_2} \qquad \text{EQ 2.14}$$

T_t = Total Travel Time

ΔT_s and ΔT_D Defined in Figure 2.10

The equations combine to define the detector delay time as:

$$\Delta T_D = T_t - {}^{S}/_{V_2} - \Delta T_S \qquad \text{EQ 2.15}$$

After determining true velocities and the dipping geometry of the strata through the intercept-time method previously discussed, the delay time at each receiver can be calculated using EQ 2.15. Inputting these values into EQ 2.12 then yields the refractor depth beneath each receiver. For more layers and more complicated geometries the analysis rapidly becomes nontrivial, however, the same concepts apply. Redpath provides multiple examples of these principals at work in realistic applications in his 1973 paper.

2.3.2: Seismic Reflection

The seismic reflection method was developed in the US some decades after the seismic refraction method to better resolve deep imaging for the petroleum and mining industries (Parasnis 1986). The array setup is very similar to that of the seismic refraction method and is depicted below in Figure 2.11. While the array setup for a refraction investigation needs to be thought out carefully prior to implementation to

insure correct resolution and depth of imaging, reflection surveys are much more standardized and can be employed in numerous situations. Refraction surveys are still primarily used by engineers for very near surface imaging; however, for deeper imaging reflection is preferable due to the reduced array length requirements. And while a refraction survey is only capable of imaging to depths of approximately a fourth or fifth of the array length, reflection surveys can image much deeper.

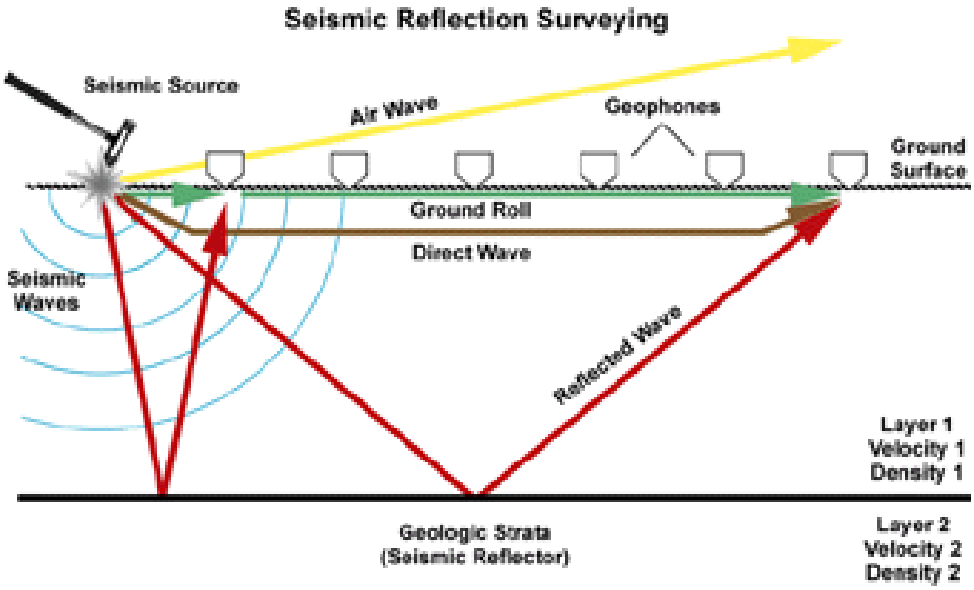

Figure 2.11: Schematic of Seismic Reflection Survey (Illinois State Geologic Survey)

This method relies upon wave propagation principals and boundary interfaces as described in Lay and Wallace's book "Modern Global Seismology" (1995). At any given boundary, depending upon the acoustic impedances of the media, the energy will be partitioned into refracted and reflected waves accordingly. Should the angle of incidence exceed the critical angle of refraction, all of the energy will be reflected at the interface. Again, the seismograms are analyzed for break points of reflected and direct arrivals. At times it can be very difficult to differentiate reflected from refracted arrivals. The

refracted arrival often appears as an elongated arrival in front of the reflected wave when the waves have not had sufficient travel time to fully separate.

For near surface surveys, a refraction analysis does a better job of resolving the weathered layer(s) since more of the energy is partitioned to refracted waves until a large change in impedance ratio is encountered. However, for complicated subsurface geometries where impedance ratios are highly variable in the near surface, it is possible that reflection will provide better results and an easier analysis.

2.4: Surface Wave Methods

Surface wave methods utilize unique properties of Rayleigh wave propagation to develop the shear wave velocity profile. Rayleigh waves, or the vertical component of the ground roll phenomenon, are the resultant wave produced by P and S-wave interaction at the edge of a halfspace (Lay & Wallace 1995). The wave propagation mechanism is depicted in Figure 2.12. An important characteristic of Rayleigh wave propagation is that they move at a phase velocity that is independent of frequency in a uniform halfspace. This trait allows inferences to be made about the medium through which the wave is moving based upon the dispersion of different frequencies. This is the basis for all surface wave analysis techniques. It should also be noted that Rayleigh waves move at a slower rate than body waves, allowing them to be parsed out on a seismogram, and do not attenuate as quickly.

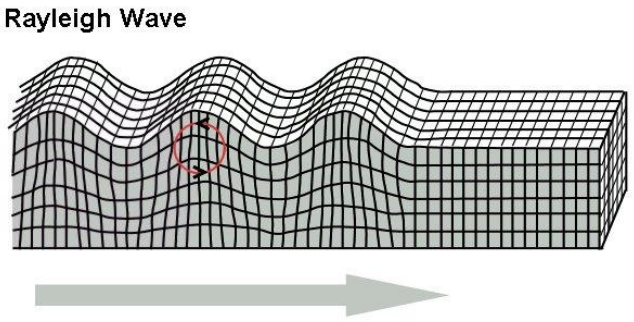

Figure 2.12: Schematic of Rayleigh wave Propagation and Particle Motion

Rayleigh wave techniques can employ both active and passive source signals. Surface waves attenuate slower than body waves, and the longer the wave length, the slower the attenuation (Park et al. 1999). Large wavelength waves created by earthquakes can travel tremendous distances before attenuating and provide good long wavelength passive sources of energy; however, the uncertainty in source location can cause significant complexity in data reduction (Yuan 2011).

2.4.1: Steady-State Method

The steady-state method was the original basis for the Spectral-Analysis-of-Surface-Waves (SASW) method. An electromagnetic shaker is used as a source, and oscillates at the frequency (f) of interest. The array setup usually employs either two or three receivers with equal source-receiver and receiver-receiver spacings (Jones 1958). These spacing are manipulated until a steady-state wave form is achieved as shown in Figure 2.13. Once this is achieved, the geophone spacing is equivalent to the wavelength (λ), and the Rayleigh wave phase velocity can be calculated using the following formula:

$$V_R = f\lambda \qquad \text{EQ 2.16}$$

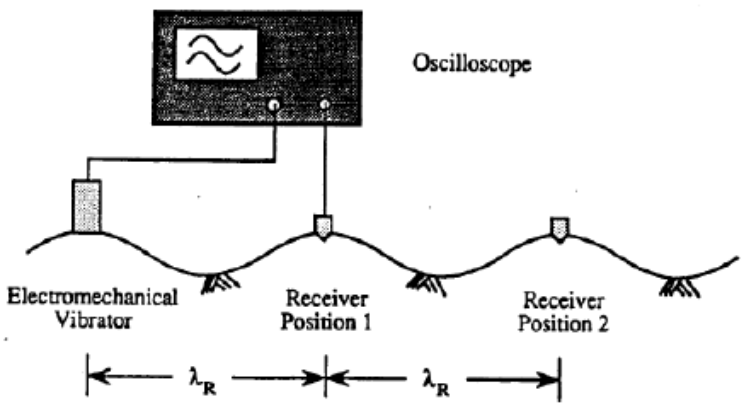

Figure 2.13: Schematic of Steady State Method Array and Wave Field (from Yuan 2011)

This process is repeated for a variety of frequencies in order to determine the Rayleigh wave dispersion. Once a good spread of data has been collected, the dispersion curve is constructed by plotting wavelength versus phase velocity. Figure 2.14 illustrates the influence depths of Rayleigh waves with varying wave lengths. The influence depth is approximately one wavelength, with the primary motion contained within half a wavelength in depth. The V_s profile can then be graphed by taking the depth of imaging as half the wavelength at a given point, and the S-wave velocity equal to 110% of the Rayleigh wave phase velocity. This transformation from Rayleigh to S-wave velocity is a rough approximate since the relationship depends upon density and elastic constants of the material.

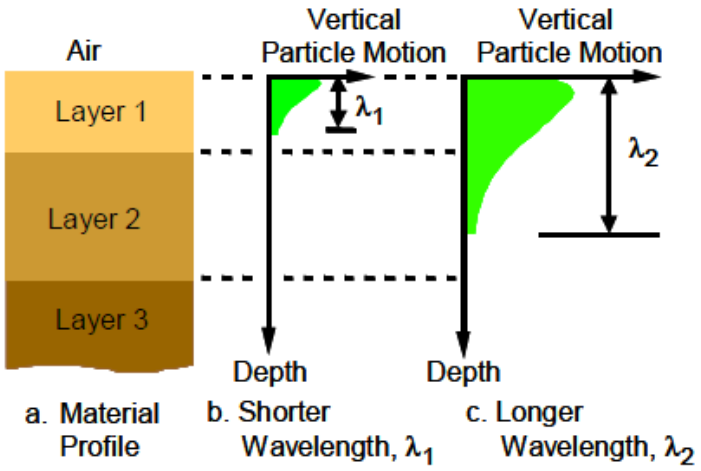

Figure 2.14: Rayleigh wave Particle Motion at Varying Depths as a Function of Wavelength (from Yuan 2011)

2.4.2: Spectral Analysis of Surface Waves (SASW)

Nazarian and Stokoe (1984) presented a more rapid and cost effective means of developing an S-wave velocity profile by analysis of surface waves. The data collection method is extremely similar to the steady state method, but simplified to reduce the labor intensive procedure. The authors suggest that through a spectral analysis of Rayleigh wave propagation it is possible to determine the S-wave velocity profile, and thus also the shear modulus profile of a site. A typical array is displayed in Figure 2.15. By inducing Rayleigh waves at a given source point, and then measuring the phase shift of those waves between two receiver points, it is possible to find the wavelengths, and thus the phase velocities. This is typically done with various receiver and source spacings in order to capture the entire range of wavelengths. Longer wavelengths allow for deeper imaging; however, receiver spacing must be between half and three times the wavelengths being tracked in order to avoid spacial aliasing. Spacial aliasing occurs when the receiver spacing is such that it does not adequately sample the wave being

measured. It is necessary to sample a given wave at multiple points in order to fully characterize it. A given spacing may characterize one range of wavelengths well, but poorly define waves lie outside of the previously stated guidelines. Source spacing from the first receive is usually taken as equal to the spacing between the receivers themselves. After the range of desired spacings has been recorded, the data can all be compiled.

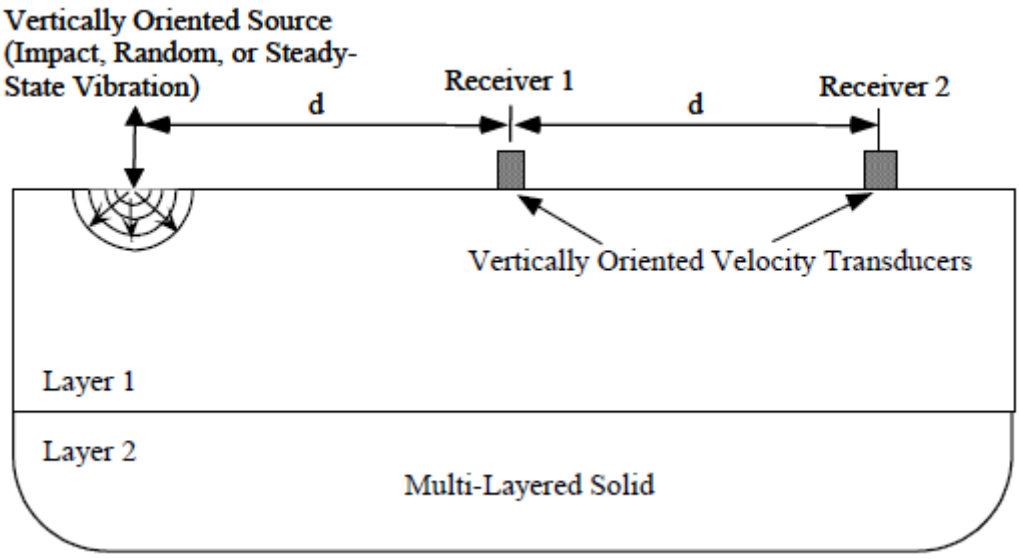

Figure 2.15: Schematic of SASW Array (from Yuan 2011)

From here, one can construct a composite dispersion curve from the different spacing ranges. Figure 2.16 provides an example of such a composite experimental dispersion curve with a theoretical fit. In this method the fundamental mode is of primary interest. The fundamental mode is found as the lowest response velocity at a given wavelength. The method discussed in section 4.4.2 can be employed at this point under simple normally dispersive conditions. There are many inversion processes that involve more complicated iterative procedures and algorithms that are more accurate, however, for sites where the soil properties do not vary greatly, this crude method can yield

reliable results. The authors present several case studies where the method is shown to be very comparable to results obtained by cross or downhole testing to within 10% (Nazarian and Stokoe 1984).

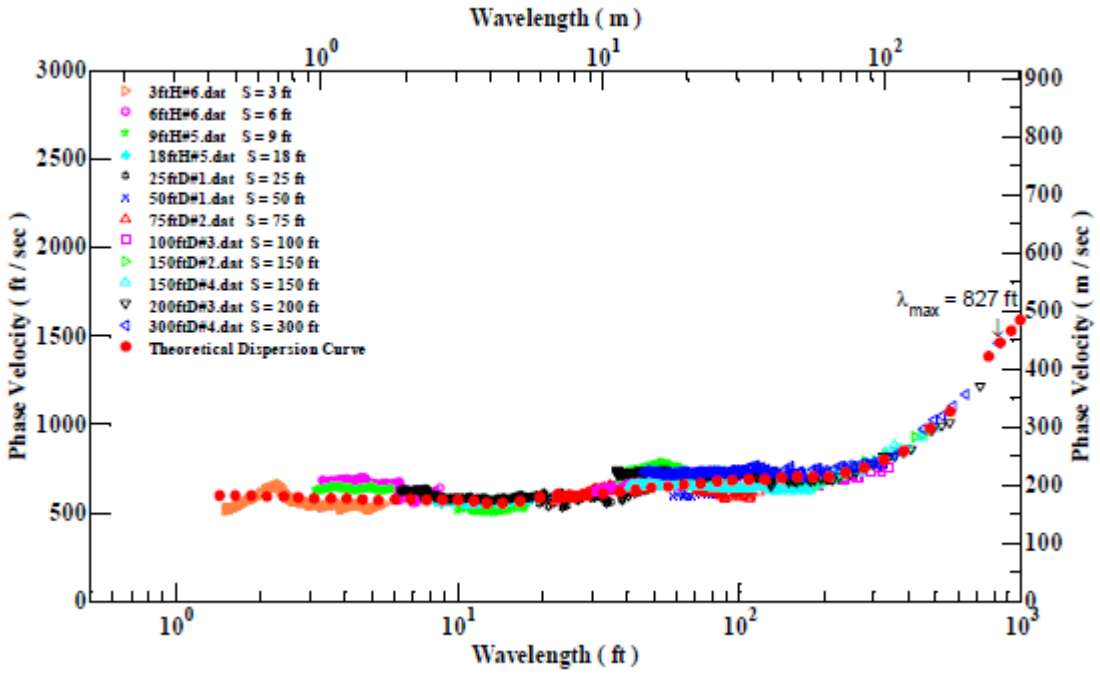

Figure 2.16: Example of Composite Experimental Dispersion Curve with Theoretical Dispersion Curve Fit (from Yuan 2011)

2.4.3: Microtremor Analysis

The concept of using a microtremor analysis was originally explored by Aki (1957) when he introduced the theory for the spacial autocorrelation method (SPAC). He suggested that through combining knowledge of the wave spectrum in both time and space one can obtain both the azimuth distribution of wave propagation and the dispersion curve. The method employs autocorrelation between receiver signals at

different spacial coordinates. Combining this with a phase analysis yields a dispersion curve and thus an indication of the medium through which the waves are propagating.

Tokimatsu et al. (1992) presented a new method of combining the use of ambient microtremors and active sources to expand the frequency range of analysis. Tests like steady-state or SASW rely completely on active sources, and it can be very difficult to actively create surface waves of wavelengths significant enough to image below 10-20m. On the other hand, while the use of microtremors had been previously employed as a method for imaging very deep structure, ambient Rayleigh waves at high frequencies have typically attenuated before reaching the array. A combination of active and passive sources can take advantage of the utility of both methods. Table 2.1 lists the methods available and applicable depth ranges.

Table 2.1: Applicability of Analysis Methods (from Tokimatsu et al. 1992)

Method (1)	Source (2)	Sensor array (3)	Analysis (4)	Applicable depth (5)
Active	Steady-state point loading	Linear	Spectrum analysis	Shallow
Active	Random point loading	Linear	Multiple filter analysis	Shallow to Intermediate
Passive	Short-period microtremors	Two-dimensional	*F-K* Spectrum Analysis	Shallow to Intermediate
Passive	Long-period microtremors	Two-dimensional	Spatial Autocorrelation analysis	Deep

In order to resolve the azimuth of the microtremor arrivals in a passive analysis, it is necessary to setup a two-dimensional array. Tokimatsu et al. (1992) suggest the circular array presented in Figure 2.17 with varying diameters. As with receiver spacing in a linear array, the diameter must be adjusted to record certain desired frequency ranges and avoid spacial aliasing. The authors recommend starting at a 5m diameter and doubling it repeatedly until all wavelengths desired have been correctly recorded.

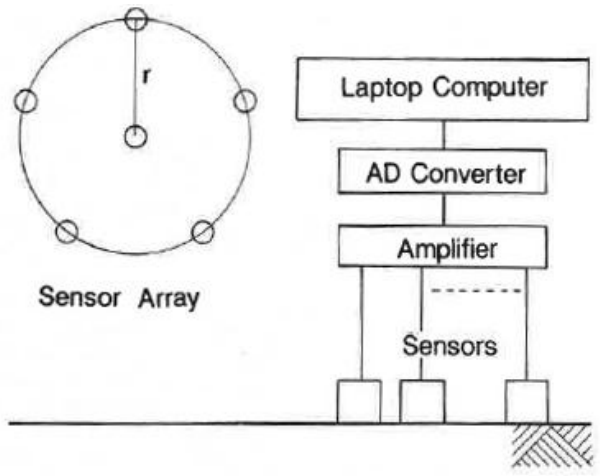

Figure 2.17: Suggested Sensor Array for Microtremor Analysis

(from Tokimatsu et al. 1992)

The method presented by Tokimatsu et al. (1992) uses a “high-resolution frequency-wave number space transformation”. Figure 2.18 includes the frequency-wave number (f-k) spectra at selected frequencies and illustrates an example where the primary azimuth of the propagating waves is towards the northeast. Again, the phase differences are recorded of coherent arrivals passing through the array, and a composite dispersion curve can be constructed once the desired range of data has been collected.

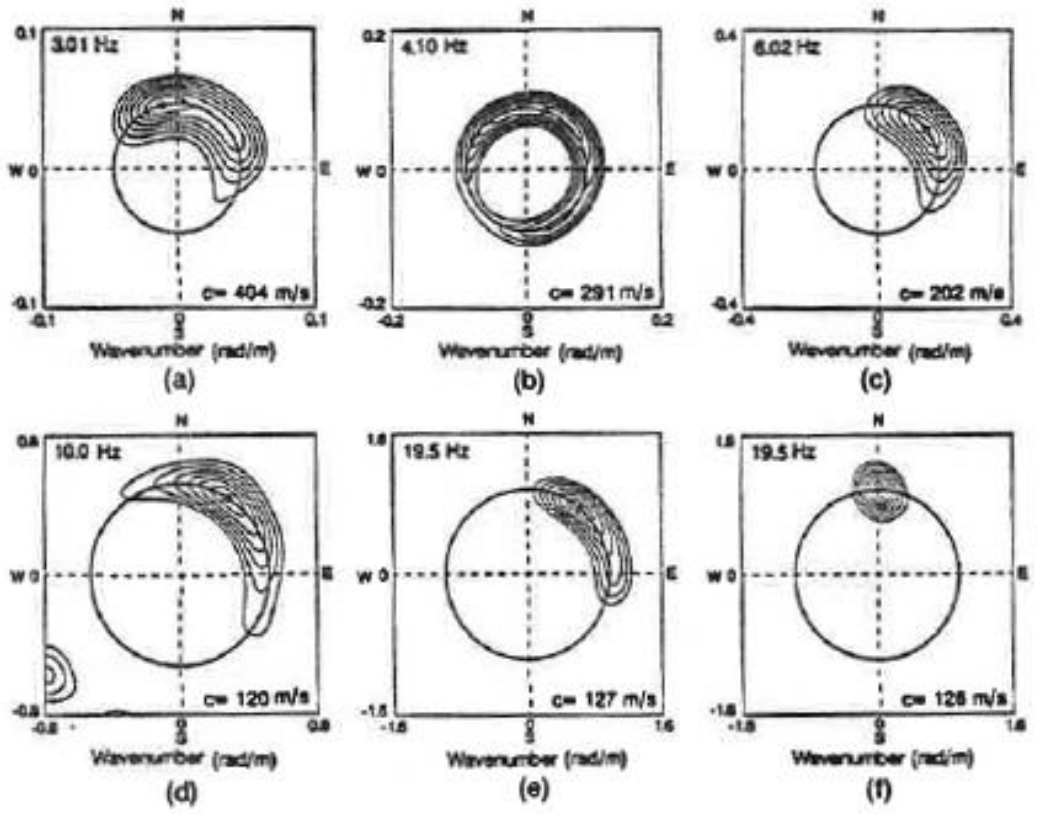

Figure 2.18: Example of F-K Spectra at Selected Frequencies

(from Tokimatsu et al. 1992)

2.4.4: Multichannel Analysis of Surface Waves (MASW)

Park et al. (1998) began experimenting with the construction of dispersion curves from a multichannel record, and in 1999 presented the full method. MASW varies from SASW in the data collection process in that there are a number of redundant channels as shown in Figure 2.19. This method provides advantages in speed of data collection, as well as redundant records. In addition, the records can be quickly analyzed in the field for noise contamination at each Rayleigh wave frequency by examining the coherence from geophone to geophone of amplitude and arrival. With the SASW method, it can be difficult to determine signal from noise with only two to three receivers. This signal coherence anlaysis allows adjustments to be made in the field during the

data collection process to insure better signal to noise ratios. It is important to note that due to the increased length in the array, lateral variations are more likely to be encountered, and for this reason Park recommends keeping arrays as short as possible.

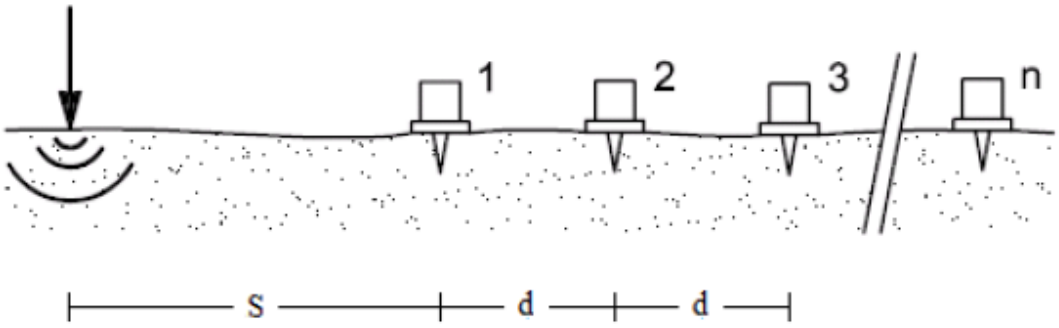

Figure 2.19: Schematic of MASW Array (from Yuan 2011)

With the MASW method, Park also attempts to mitigate issues that arrive due to near and far offset effects. Near offset effects are expressed as errors in phase velocity recorded for a wavelength and are due to cylindrical surface wave propagation in the near field rather than the plane wave assumption the analysis requires (a “plane wave” is considered to be a wave front arriving as a propagating plane of rays parallel to one another). To mitigate this issue, the near offset must be set to at least half the maximum desired wavelength. This would require significant source offsets to record longer wavelength Rayleigh waves accurately.

Far offset effects arise due to the rapid attenuation of short period Rayleigh waves. The shorter the wavelength the faster the wave will attenuate, thus, when the source is significantly offset from the receivers, the high frequency signals can become contaminated by ambient body waves. To correct for this, Park recommends carefully choosing a correct medium offset, or to create a composite dispersion curve from a set of near and far offset data.

Park et al. (2005) presented a method of utilizing ambient surface waves as an MASW source, and a way to mitigate near offset affects. Passive sources can be assumed to be in the far field, thus even very long wavelength Rayleigh waves should be propagating as plane waves. However, by itself, an ambient record would have significant far offset effects present. The use of L-shaped arrays can allow the user to resolve the azimuth of the passive signal arrivals. Figure 2.20 illustrates a combination of passive and active records to develop a composite experimental dispersion curve. Again, numerous forward modeling or inversion methods are available to fit a theoretical dispersion curve to the experimental data.

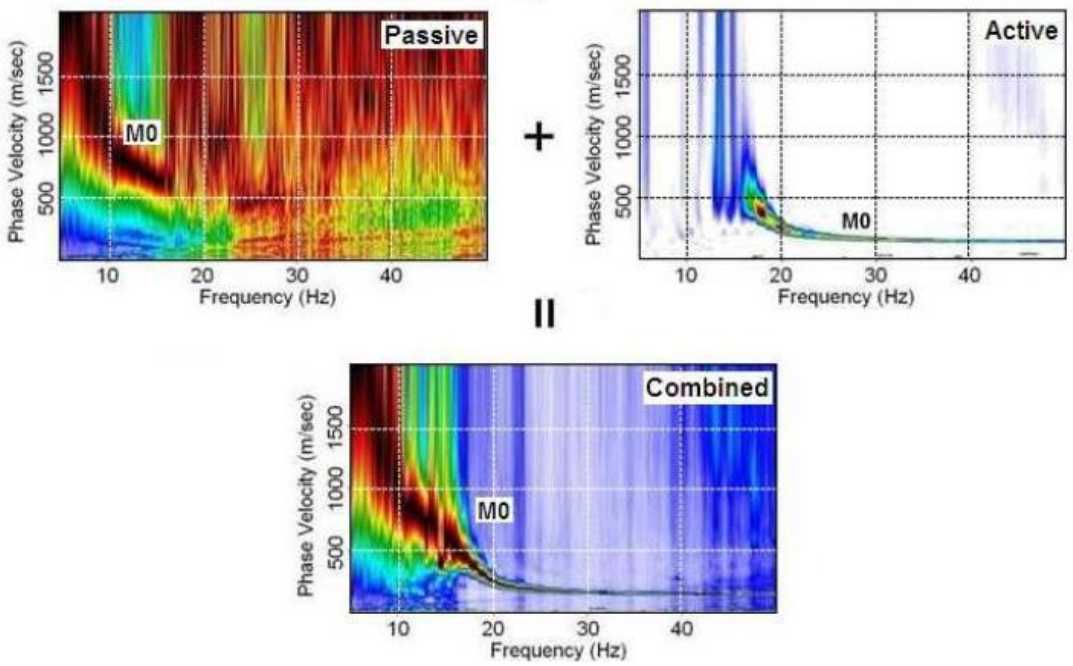

Figure 2.20: Example of Expanded Frequency Range of Data from Combined Passive and Active Records (from Yuan 2011)

2.4.5: Refraction Microtremor (ReMi)

Louie (2001) first presented the ReMi method of developing an S-wave velocity profile. The intent was to develop a cheaper, faster and easier tool than those currently available. While the method has received significant scrutiny, it has proven capable of estimating average S-wave velocities to depths of up to 100m and within 20% accuracy of more widely accepted measurement methods. Louie (2001) attempted to combine the most effective aspects of the microtremor, SASW and MASW methods. The ReMi method has gained acceptance today in many applications of shallow shear wave velocity profiling. Despite relying upon passive signal sources, Louie (2001) indicates that good results can be obtained with a simple linear array and typical seismic refraction geophones (i.e. 4.5 Hz) and data acquisition systems. Another important characteristic is that its primary reliance on passive source signals allows it to be utilized in an urban setting where noise or body waves would drown out an active source signal.

2.4.5.1: Theory

Some important adjustments in data processing allow accurate results to be obtained through the use of a linear array and passive signals. ReMi employs a slantstack as described by Thorson and Claerbout (1985), also known as beam forming. It is similar to a 2D Fourier-spectrum or f-k analysis, but with some differences that make analysis simpler and more complete. Louie's (2001) method is to take longer recordings of as much as 50s and apply the slantstack to combine seismograms. The data is analyzed through the p-f, or frequency-slowness, method originally suggested by McMechan and Yedlin (1981). This method allows all phases to be included where an f-k analysis would potentially alias data as shown in Figure 2.21. The dispersion curve takes a unique slope in this space and thus is easily parsed out from body and air waves

(Louie 2001). Air waves are sound waves traveling, as their name suggests, through the air and are generally caused by some nearby noise source. The spectral power is calculated for each point and then normalized into a spectral power ratio to allow peaks in spectral power to be more easily identified.

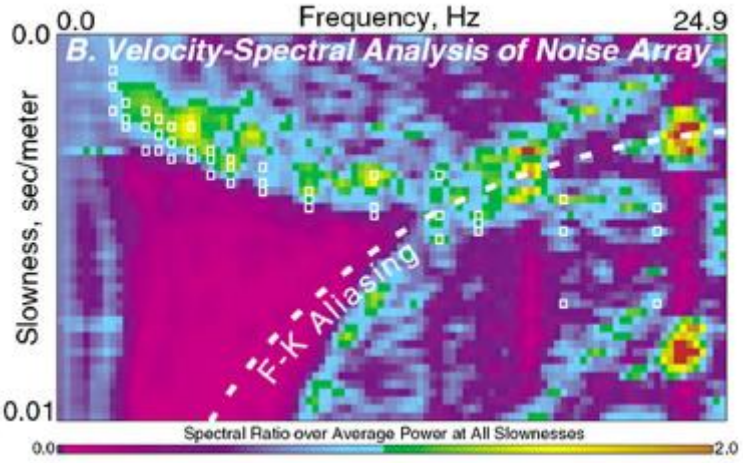

Figure 2.21: Example Slowness-Frequency Plot Depicting Dispersion Picks and Zone of F-K Aliasing (from Louie 2001)

One hurdle that had to be overcome was the issue of observing high apparent phase velocities due to obliquity of arrivals in the planar wave fronts. The method assumes, as in previously described tests, that the Rayleigh waves are propagating as a plane front, and that the signals should be arriving equally from all azimuths (Louie 2001). This is an important assumption because arrivals that are not in line with the azimuth of the array will give apparent phase velocities higher than that of the true velocity at a given frequency. The lower bound of apparent velocity at a given frequency must be the arrivals traveling parallel to the array, and thus represents the true velocity. Table 2.2 shows that 40.9% of the energy will appear at a phase velocity that is approximately 125% of the true velocity. The rest is “smeared” around the edges, and the lower bound can be easily picked in this zone in frequency-slowness space where

the spectral power ratio drops off. In this way, a linear array can achieve accurate results without actually resolving the azimuth of individual arrivals. Another advantage to this method of lower bound picking is that the higher mode Rayleigh waves will have higher phase velocities than the fundamental mode, and thus, the technique yields the fundamental mode velocities.

Table 2.2: Angular Coverage of Slowness Intervals (from Louie 2001)

Proportion of Inverse Velocity *vp*	Propagation Angle *a*	Coverage of 360° Energy
0–10%	90.0°–84.2°	6.3%
10–20%	84.2°–78.4°	6.4%
20–30%	78.4°–72.5°	6.6%
30–40%	72.5°–66.4°	6.8%
40–50%	66.4°–60.0°	7.1%
50–60%	60.0°–53.1°	7.6%
60–70%	53.1°–45.5°	8.4%
70–80%	45.5°–36.8°	9.7%
80–90%	36.8°–25.8°	12.2%
90–100%	25.8°–0°	28.7%
	Total:	100.0%

While automatic algorithms for inversion have since been suggested, the original method of fitting a theoretical dispersion curve to the picks made in p-f space involves an interactive forward modeling process. The graphical forward modeling process relies heavily upon the experience of the user, but can yield more appropriate profiles based on the interpreter's knowledge and available information. It should be noted that the profiles determined from this process are highly non-unique, leading Louie (2001) to recommend finding at least two different models that adequately fit the experimental curve and determining the true model through prior understanding of the site.

2.4.5.2: Comparisons with other methods

As stated previously, the variability of the results both within the test method and compared to other methods has caused some scrutiny. Louie (2001) compared his newly developed method with others in 10 different sites and found that the shear wave velocities could be found to within 20% accuracy to up to 100m depths of strata, and suggest structure below that. Figure 2.22 depicts an example of inter-method variability at a site in New Zealand. While Louie (2001) notes that ReMi cannot duplicate the detail that downhole, crosshole or suspension ps-logging can provide; it does approximate average velocities of 10-20m depth intervals very accurately.

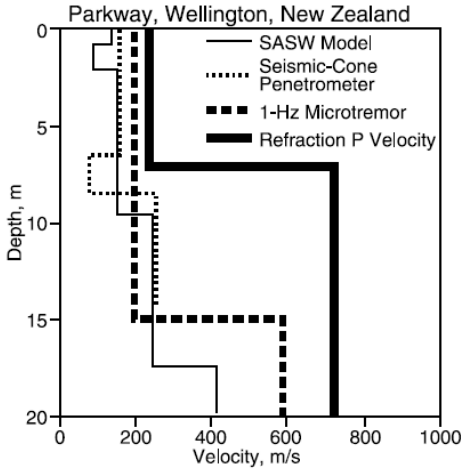

Figure 2.22: Plot of Inter-method at Parkway, Wellington, New Zealand (from Louie 2001)

In Spain, a group of geophysicists (Pérez-Santisteban et al., 2011) compared ReMi, suspension PS-logging and SASW constructions of the shear wave velocity profile under the railway embankment shown in Figure 2.23. This study had the advantage that the profile was artificially constructed, and thus, highly controlled. The averaged results from each method, plotted in Figure 2.24, showed that PS-logging provided the most accurate profile followed by ReMi, and finally SASW. It is important to note that the ReMi

and SASW data required a fixed embankment depth in the inversion process in order to yield the correct results. When the depth was unconstrained the methods produced variable results. Unfortunately, the study was inconclusive as to the coefficients of variation within each method for the same site.

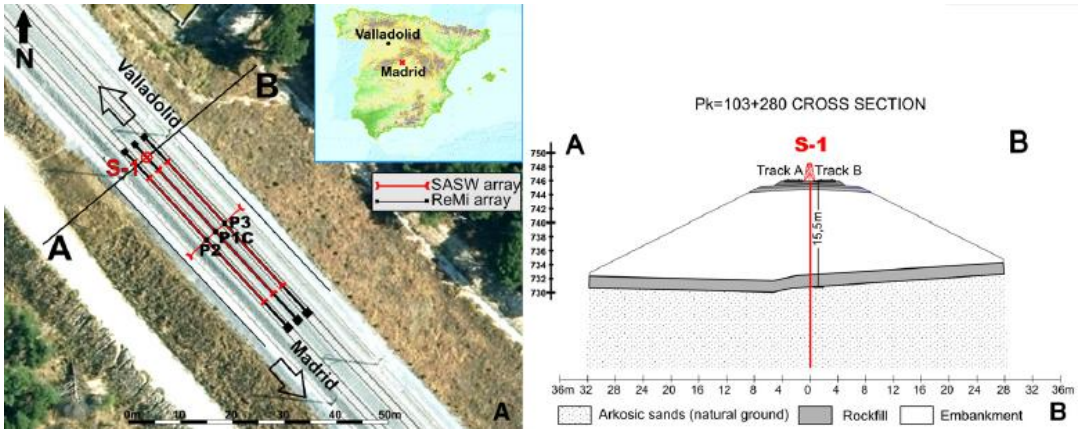

Figure 2.23: (A) Placement on a Railway Embankment of SASW and ReMi Arrays with Suspension PS-Logged Hole Shown at S-1 and (B) Cross Section of Embankment Soil Profile (from Pérez-Santisteban et al. 2011)

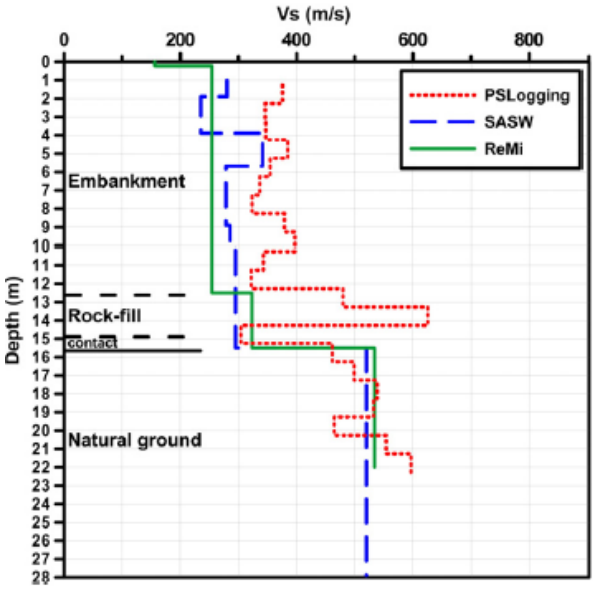

Figure 2.24: Plot Illustrating Comparison between Methods on a Railway Embankment (from Pérez-Santisteban et al. 2011)

2.5: Intra-method Variability

2.5.1: Variability within the ReMi Method

Due to the complicated assumptions and mathematics involved in ReMi paired with wide variability of test results within the method, many are skeptical of the results obtained. Cox and Beekman (2011) explore this variability within the test method itself (not compared with true values). Much is assumed and unknown about the wavefield analyzed in ReMi, thus, by comparing data obtained through different array orientations and active versus passive signal sources, the authors attempted to determine the degree of variability one could expect at a given site. The results shown in Table 2.3 indicate that the phase velocities at a given frequency could vary by as much as 85-100% between passive and active sources. Orientation of the line of sensors showed less impact on the results, as the active-active/passive-passive data groups tended to agree with each other regardless of orientation. Figure 2.25 helps to emphasize the degree of variation each variable can produce in the results. The variation that was observed between orientations could be as much due to lateral change in soil strata as to abnormalities in the wavefield.

Table 2.3: Intra-method Variability Analyzing Array Orientation and Signal Source Influences (from Cox & Beekman 2011)

University of Arkansas site name	Array orientation	Noise conditions	Optim, Inc., designation	V_{s30} (m/s)	IBC site classification
Site B	N-S	Passive	2	745	C
36° 5′ 44.9″ N	N-S	Active[a]	5	634	C
94° 11′ 15.5″ W	E-W	Passive	3	768	B
	E-W	Active[a]	6	634	C
Site C	N-S	Passive	7A	1,010	B
36° 7′ 7.7″ N	N-S	Active[a]	9	730	C
94° 20′ 38.5″ W	E-W	Passive	8	844	B
	E-W	Active[a]	10	796	B
Site D	N-S	Passive	12	1,090	B
36° 5′ 25.0″ N	N-S	Passive	11	1,100	B
94° 11′ 22.0″ W					

[a]Active noise generated by driving a truck back and forth along the array as suggested by Louie (2001b).

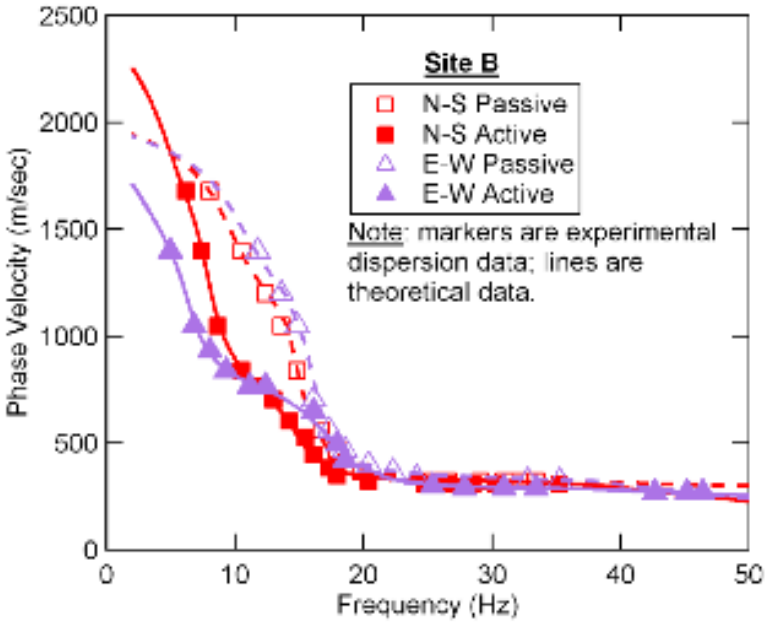

Figure 2.25: Plot Illustrating Comparisons of Array Orientation and Signal Source Type (from Cox & Beekman 2011)

2.5.2: Intra-method Variability of Other Tests

This section is based upon Moss (2008), which investigates the intra-method epistemic measurement uncertainty associated with a number of the methods discussed in this chapter. This is a topic not widely explored. As the author points out, "There has been little research to date evaluating the measurement uncertainty of individual tests because of the amount of time and money required to run the tests…" This is an important topic for engineers because the uncertainties involved in the analysis process will compound upon the original inherent measurement uncertainty. Allowable stress design and the use of factors of safety may at times be insufficient if the overall uncertainty is large enough to allow a significant probability of failure (R. Moss, personal communication, October 13, 2011). Despite the limited amount of data available to help

quantify these measurement uncertainties, Moss (2008) provides a basis upon which future work can build a more robust dataset.

Moss (2008) segregates V_s profiling methods into two categories and suggests preliminary coefficients of variation that can serve as tools to estimate the measurement uncertainty associated with each. Those described as “invasive” methods correspond to the tests described previously in this work as “direct measurement” methods. Conversely, “noninvasive” methods refer to tests that do not involve placing source or receivers at depth. In this case, the entire investigation occurs at the ground surface such as those methods outlined in sections 2.3 and 2.4 of this chapter. The coefficients of variation (standard deviation / mean) for these categories of measurement were found to be on the order of 1-3% and 5-6% respectively. It should be noted, however, that the noninvasive coefficient of variation refers specifically to the SASW method since the others lacked the data to make any reliable conclusions. The paper presents coefficients of variation for ReMi that are slightly lower than the range found for SASW, but Moss (2008) points out that this may be an artifact of the small sample size.

Chapter 3: Testing Methods

The procedures and guidelines presented in this chapter are summarized from the software manuals for SeisOpt ReMi v4.0, SeisOpt @2D v5.0 and Seismic Source VibraScope.

3.1: Refraction Microtremor

The ReMi method consists of four primary steps. These include the array setup in the field, data collection and exportation, data processing and, finally, forward modeling.

3.1.1: Field Setup

In order to reduce complications in the analysis and in compliance with recommendations by SeisOpt, the ReMi arrays employed by this study are all as near to linear as possible. According to Optim, a 5% deviation in linearity will not affect the accuracy of the method. It was occasionally necessary to record elevation data of the receiver locations in order to adjust for the vertical deviation from linear; however, horizontally speaking, all arrays in this study were within tolerable limits.

When using linear arrays, the ReMi method provides a 1D V_s profile at the midpoint of the line by essentially averaging the profile along the array. For this reason, when placing the array for a ReMi analysis, it is important to attempt to achieve a placement approximately parallel to the feature of interest. Any change in the V_s profile from one end of the array to the other will go unnoticed when looking at the condensed 1D profile yielded by the analysis. In this study, multiple arrays were situated on both the hanging and footwalls approximately parallel to the anticipated locations of the fault

traces, and with varying offsets. Some judgment is necessary in determining the approximate location of the fault trace. Given the known fault regime in the region, along with a quick analysis of the geomorphic expression at the ground surface, it is possible to develop a rough idea as to the likely location of the trace and place arrays accordingly.

Once the array azimuth and starting point location has been determined, the setup process can begin. Depth of accurate modeling is a function of the length of the sensor array, and resolution is a function of the sensor spacing. As discussed in section 2.4.2, theoretically reliable data can only be collected for wavelengths between one third the minimum geophone spacing, and twice the maximum receiver-receiver offset (overall length of the array). The type of geophone is often the true limiting factor in maximum imaging depth since low frequencies are necessary to image at depth and sampling is very unreliable below the resonant frequency of the receiver. Sensors can be purchased at varying resonant frequencies depending upon the needs of the project. Guidelines provided by SeisOpt indicate that the maximum reliable imaging depth is approximately 1/2 to 1/3 the array length, and the resolution 1/2 to 1/3 the geophones spacing.

The equipment employed in this study includes the following:

1. 4.5 Hz single channel vertical motion geophones
2. Refraction cable allowing for 8m spaced connections to geophone split leads
3. DaqLink II Data acquisition hardware (Seismic Source)
4. Laptop with VScope software (Seismic Source) installed
5. Power source (12V Battery)
6. 10 and 16 lb sledge hammers
7. Piezoelectric trigger and cable extension
8. Metal striking plate
9. 100m measuring tape

When using 8m spacings, the cable itself can act as the measurement tool. For other spacings, the measuring tape is used to set the line. The cable is then laid out as close to linear as possible, with the connection points at the desired spacings. The geophones are then placed at each connection point by planting the spike in the soil so that it has a firm contact with the ground, especially in the vertical direction. If the ground at the surface is loose or covered with plant matter, excavate to firmer material if possible. The SeisOpt ReMi v4.0 User's Manual states: "the geophones can be as much as 15 degrees off vertical without compromising ReMi data quality."

Once all geophones are situated, the cable can be connected to the DaqLink II along with the power source and laptop. The array is now ready for data collection in VScope.

3.1.2: Data Collection and Exportation with VScope

In order to correctly link with the data acquisition hardware, the laptop needs to be disconnected on all network connections excepting the local port, which is linked to the DaqLink II. It is also important to disable the firewall on the local network connection which links to the data acquisition hardware. These steps can be completed in Windows XP under Network Connections in the control panel. At this point, the DaqLink II is ready to communicate with VScope.

It is best to begin a separate project for each array in order to maintain organization. Select “New Project” from the “File” pull-down menu. Once a new project has been created in VScope, the recording parameters can be verified and adjusted by selecting “Device” from the “Options” pull-down menu. The window shown in Figure 3.1 should pop up and show the DaqLink. To adjust the settings, select the DAQ and click the “DAQ Settings” button.

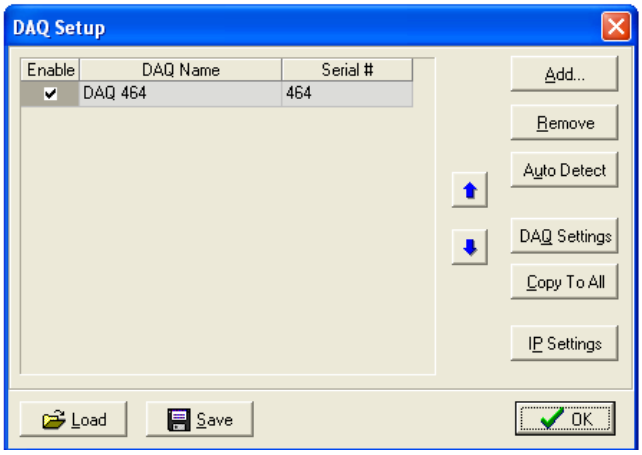

Figure 3.1: DAQ Setup Menu

The window shown in Figure 3.2 should appear, allowing configuration of the data acquisition system. Under the “Acquisition” tab, insure that only the desired channels are turned on. The channel settings shown in Figure 3.2 are adequate for this

type of testing. An acquisition time of 30s at 2ms intervals is adequate to provide good resolution and capture a full spectrum of microtremors. Under the “Trigger” tab, “Auto Trigger” should be selected in order to start recordings automatically when the “Start” button is clicked on the main window. The “Order” tab allows adjustment of the order of the traces in the records plot should multiple spreads be used. The normal setting is typically correct, however, this can be checked by taking a recording with a signal moving down the line to insure that the traces receive the signal in correct order. Once these parameters have been set, select “OK”.

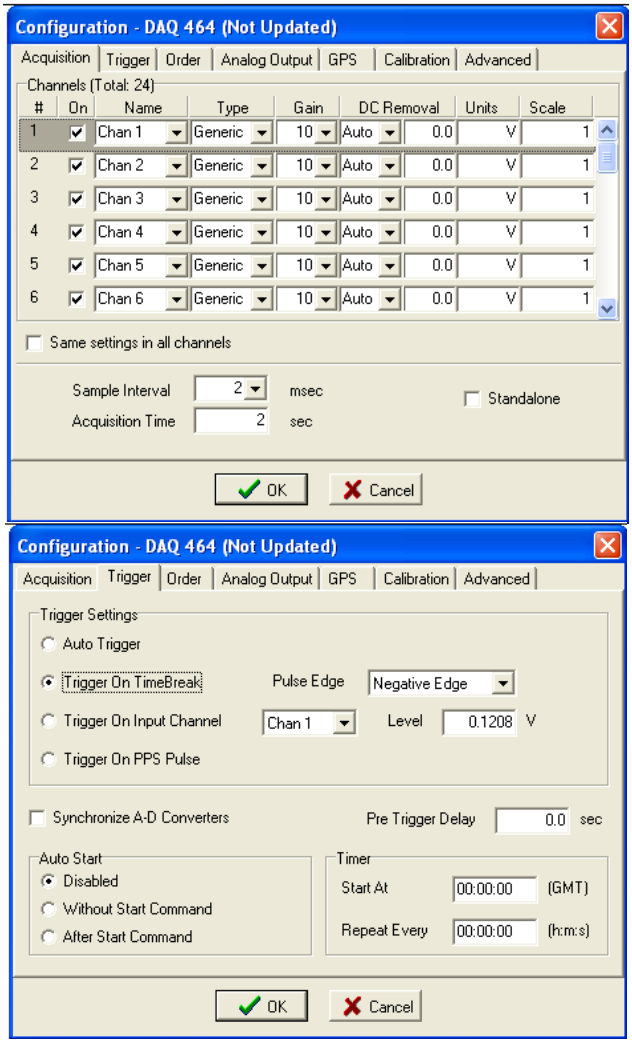

Figure 3.2: Data Acquisition Configuration Settings Window

On the main window recording is started by pressing the start button depicted in Figure 3.3. The program should start recording and display that it is receiving in the bottom left hand corner as shown in Figure 3.3. A good practice is to take a test recording to insure that all channels are recording at approximately the same levels and look reasonable. It is important not to induce any vibrations during this recording so that the scale is not affected by the near channels receiving higher energy. Should any traces appear abnormal, a quick inspection of the split lead connections to the cable, and the seating of the geophone will typically solve the problem.

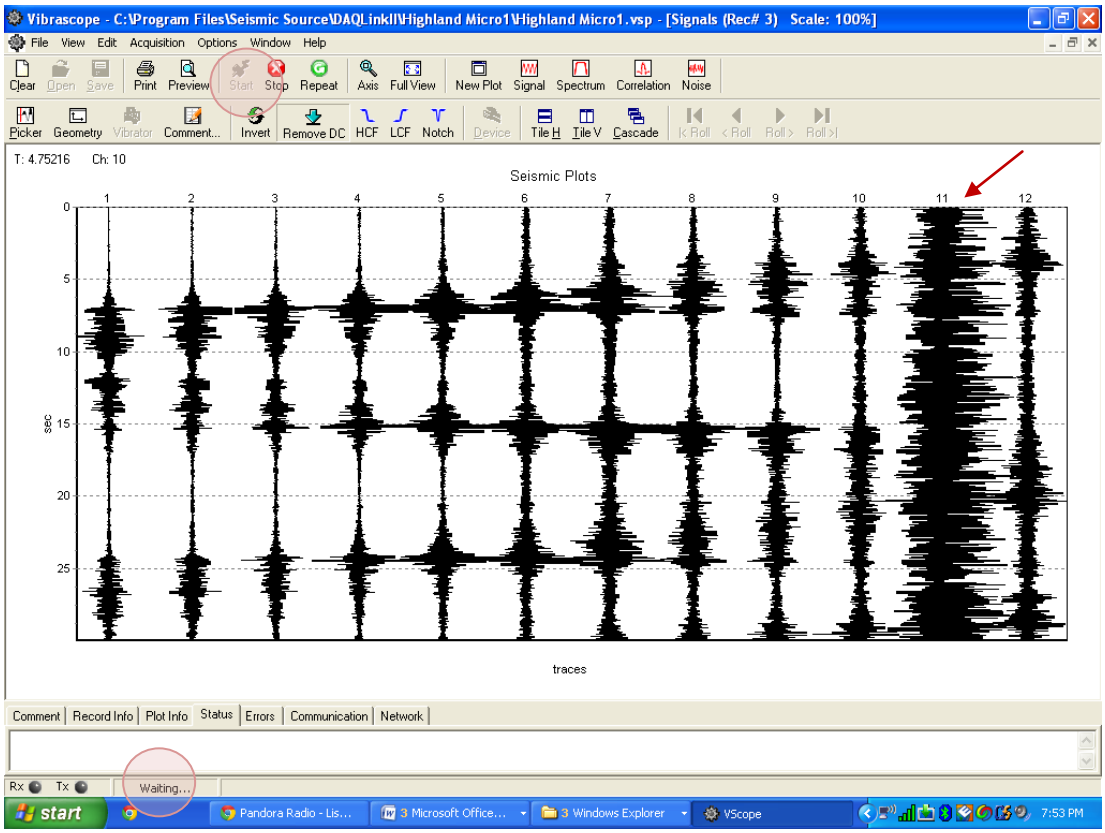

Figure 3.3: VScope Home Window Showing “Start” Button, Recording Status Bar, and an Example Abnormal Trace Record

Upon verification that all traces are properly recording testing can begin. Typically ten 30s recordings are sufficient to characterize a site. It is helpful at

particularly quiet sites to drive a vehicle back and forth off-end the array or walk along the line (Louie, 2001). Striking a steel plate with a sledge hammer off-end of the array provides another useful tool to enhance the higher frequency range of data. Higher frequency waves attenuate more quickly, so this is typically the range where a more remote site will be deficient of energy. If nearby traffic vibrations are available as a source, the frequency range of the data can be improved by waiting for a particularly large vehicle to approach to begin recording.

Once all desired recordings are made, the files need to be exported to a format readable by the SeisOpt ReMi v4.0 software. To do this, select the “Open” button on the home window near the top left corner. This will bring up the database of records as shown in Figure 3.4. Each record needs to be exported individually in order to be correctly read into ReMi Vspect v4.0. To do this, the desired record must be selected, and then the second small icon in the top left corner will begin the exportation process.

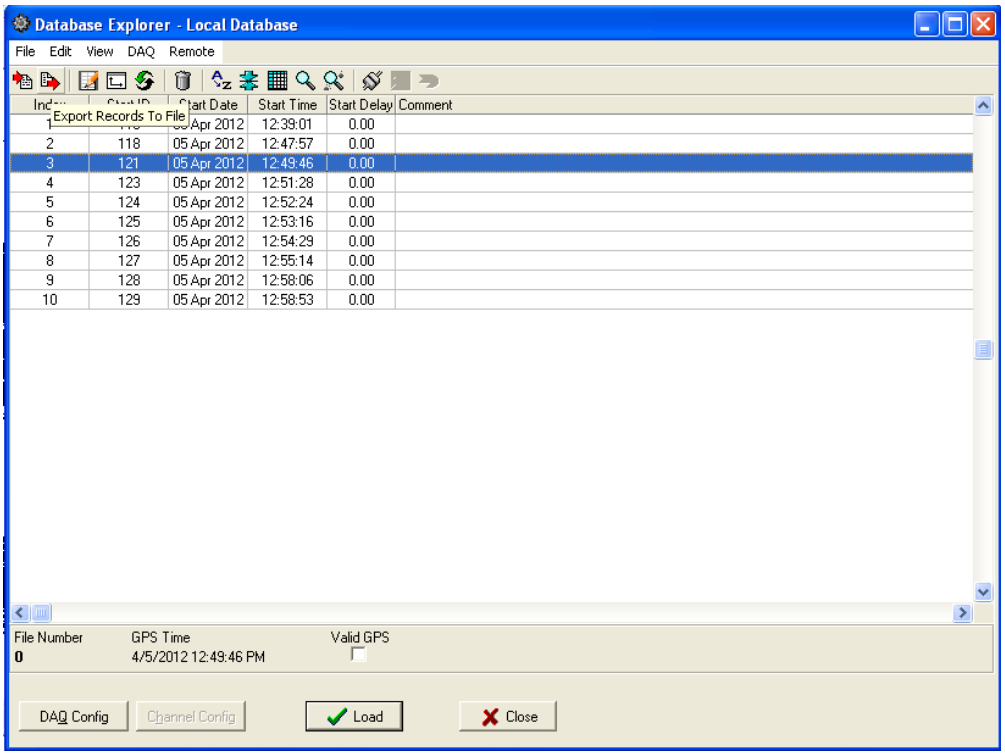

Figure 3.4: Local Database of Recordings from the Current Project

The program prompts the user to select a file type for exportation. While multiple file types can be read by ReMi Vspect, SEG-Y is the easiest to import. The file is then saved in the desired location with some simple name, such as X01 to keep organization.

3.1.3: Data Processing and Analysis

Optim provides two separate programs for analyzing ReMi data. ReMi Vspect v4.0 reads in the data and transforms it into spectral power displayed in slowness-frequency space. The user can view and combine records to make dispersion curve picks that are then exported to ReMi Disper v4.0 for forward modeling. ReMi Disper v4.0 also includes a tool for assembling a 2D cross section from multiple 1D profiles. For software installation procedures, please see the SeisOpt ReMi v4.0 User's Manual.

3.1.3.1: Processing Data and Making Dispersion Curve Picks in ReMi Vspect v4.0

All data processing steps are located under the drop-down menu “Vspect Process” of each window. It is important to select the next step from the most recent window opened to insure that all previous steps are included. SEG-Y data is read into ReMi Vspect v4.0 by selecting “Step 1b: Open SEG-Y Seismic Records…” on the opening window. Once all desired files are selected and loaded, the window shown in Figure 3.5 should appear, prompting the user for the data parameters.

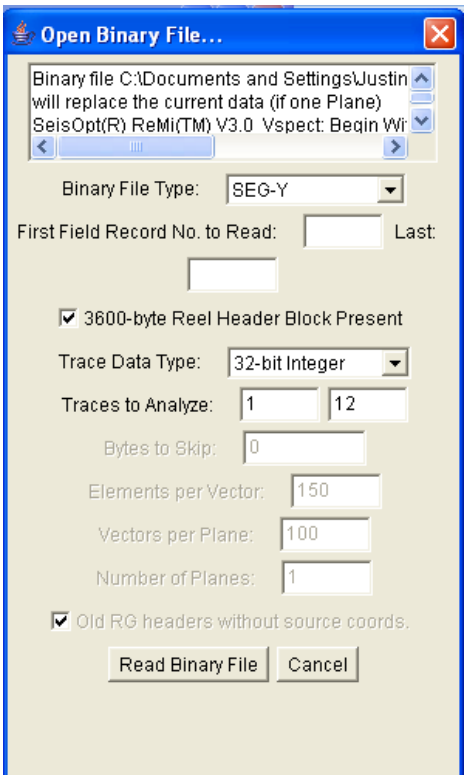

Figure 3.5: ReMi Vspect v4.0 Data Reading Parameters

The easiest way to insure all data is read into the program from each record, the values for first and last field record numbers to read are left blank. “Traces to Analyze” should be from one to the number of recorded channels, typically either twelve or twenty-four. The window in Figure 3.6 should appear after clicking “Read Binary File”,

showing the recorded data graphically. To verify that the data was correctly read in, the number of data points shown is compared to the number that should be present. Each trace should have 15000 points (the acquisition time divided by the recording interval), so this number should appear at the bottom of the column as shown in Figure 3.6.

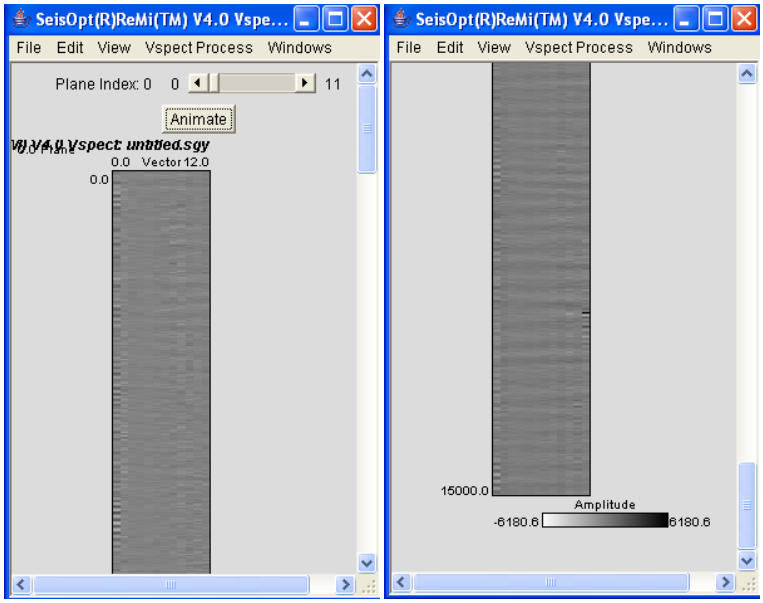

Figure 3.6: Graphically Represented Data with Correct Number of Points

If the data is correctly read, “Step 2: Pre-Processing” should now be chosen from the process drop-down menu. This step will change the appearance of the data somewhat. Next, “Step 3: Erase or Apply Geometry…” is selected to adjust the input geometry of the array. Unless the geometry varies from linear beyond the allowance discussed in section 3.1.1, no geometry needs to be inputted. Instead, click the “Erase All” button and then click OK on the popup window. If the geometry is not within tolerable limits, it must be inputted during this step. The “Show Format” button provides instructions on how to apply geometry. Optim customer support can also help with this process. Once finished, the geometry window can be closed.

"Step 4: Compute p-f of Each Record…" transforms the data into spectral power in slowness-frequency space (p-f). The window in Figure 3.7 allows the user to adjust the parameters of this transformation. "dt" is the sampling interval and "dx" the geophone spacing. The maximum frequency of interest (Fmax) and the minimum velocity of interest (Vmin) adjust the axes of the p-f plots.

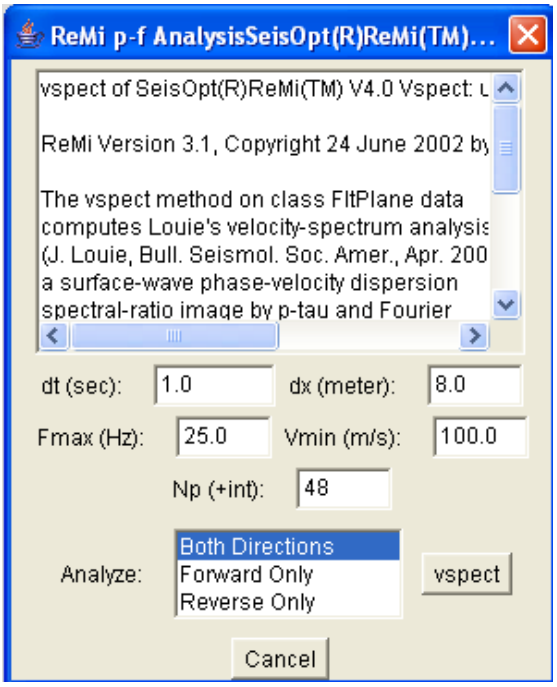

Figure 3.7: p-f Transformation Input Parameters

It is important to note that the Fmax and Vmin parameters can also drastically affect the appearance of the plotted data. The reason for this is that the program actually plots the spectral ratio, or the normalized spectral power. This is done by dividing the spectral power at each data point by the average spectral power in the analysis space. By changing the size of the space that the program is analyzing, it is also possible to significantly change the spectral ratios displayed. Because the p-f plots depict anything above a spectral ratio of 2.5 as the same color (red), when the average spectral power in the space is too low the plot will appear saturated in the response

regions. Conversely, if the analysis space contains a high average spectral power, the ratios throughout the plots may not be high enough to clearly define the dispersion curve. One must iterate through trial and error to find an ideal analysis space.

The process of iterating to find an ideal p-f space is highly dependent upon the particular dataset, but the following guidelines work adequately in most cases. The Fmax value should be determined first by varying the parameter up and down until the user can fix it at approximately 0-5 Hz above the top frequency where the dispersion trend is still apparent. In order to determine the Vmin value, the maximum slowness (reciprocal Vmin) should first be set such that the bottom of the dispersion trend is just captured in the analysis space. The interpreter should then decrease the Vmin value in intervals of about 20Hz to determine if a better defined dispersion trend is attainable. A higher Vmin allows better resolution, so the final space should be the highest value that captures the entire dispersion trend and provides adequate spectral ratio peaks to make reliable picks.

After finding an appropriate analysis space, the user must subjectively identify a common trend between records of higher spectral ratios sloping generally down from left to right (indicating increasing stiffness with depth). Sites that are not normally dispersive (stiff over soft layers) may show an inversion in the dispersion curve slope, but typically this downward slope can be expected throughout the plot. “Step 5: Combine Record p-fs…” will stack the plots to help exaggerate this trend and help to reduce the prevalence of random scatter. The resulting final plot can be greatly improved by excluding those records that do not fit the trend the others show, or do not make sense given the known local geology.

Making dispersion curve picks from the final combined p-f plot is made easier by increasing the plot zoom size under the “View” drop-down menu. Picks are made by left-clicking a pixel, and removed by right-clicking. As discussed in section 2.4.5.1, the lower bound of the apparent phase velocities represents the true value, and can be picked along the bottom edge of the trend of peak spectral ratios as shown in Figure 3.8. Choosing points along the boundary between green and light blue shades is a good rule of thumb. Multiple picks can be made at a given frequency to provide a bracket within which the true value likely lies. The final picks are saved by selecting “Step 6: Pick and Save Dispersion…” and choosing the file destination. The picks are now ready for forward modeling in ReMi Disper v4.0. To save a JPEG of the p-f plot and picks, select “Write JPEG File…” from the “File” drop-down menu and choose the file destination. Adding the file extension .jpg after the file name will allow the file to be more readily opened by picture viewing software.

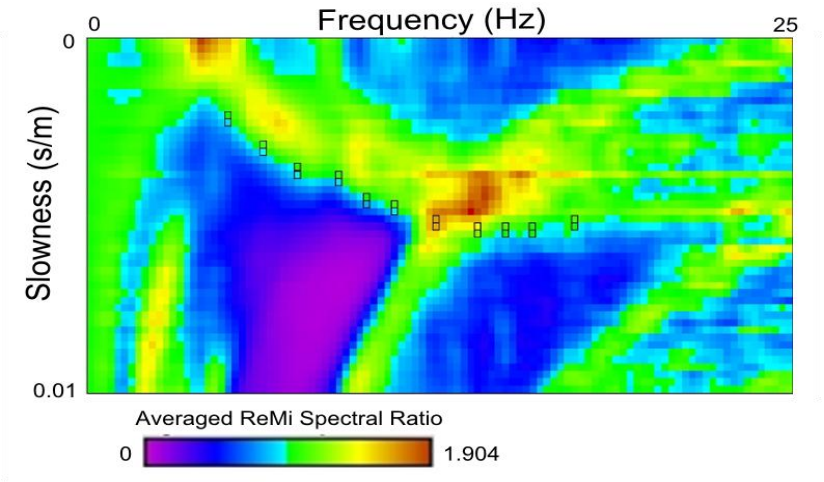

Figure 3.8: SeisOpt JPEG Output File after Making Picks on a Combined p-f Plot

3.1.3.2: Forward Modeling of a 1D Profile in ReMi Disper v4.0

After opening ReMi Disper v4.0, the saved picks are read into the program by selecting “Load Picks…” from the “File” drop-down menu. To process data from ReMi Vspect v4.0 the picks should be specified to be loaded from a dispersion file on the following prompt. The program allows the user to then browse the hard-drive for the file and loads the picks. The file path should appear at the top of the main window, and the picks should appear as red dots on the velocity-period space at the bottom as shown in Figure 3.9.

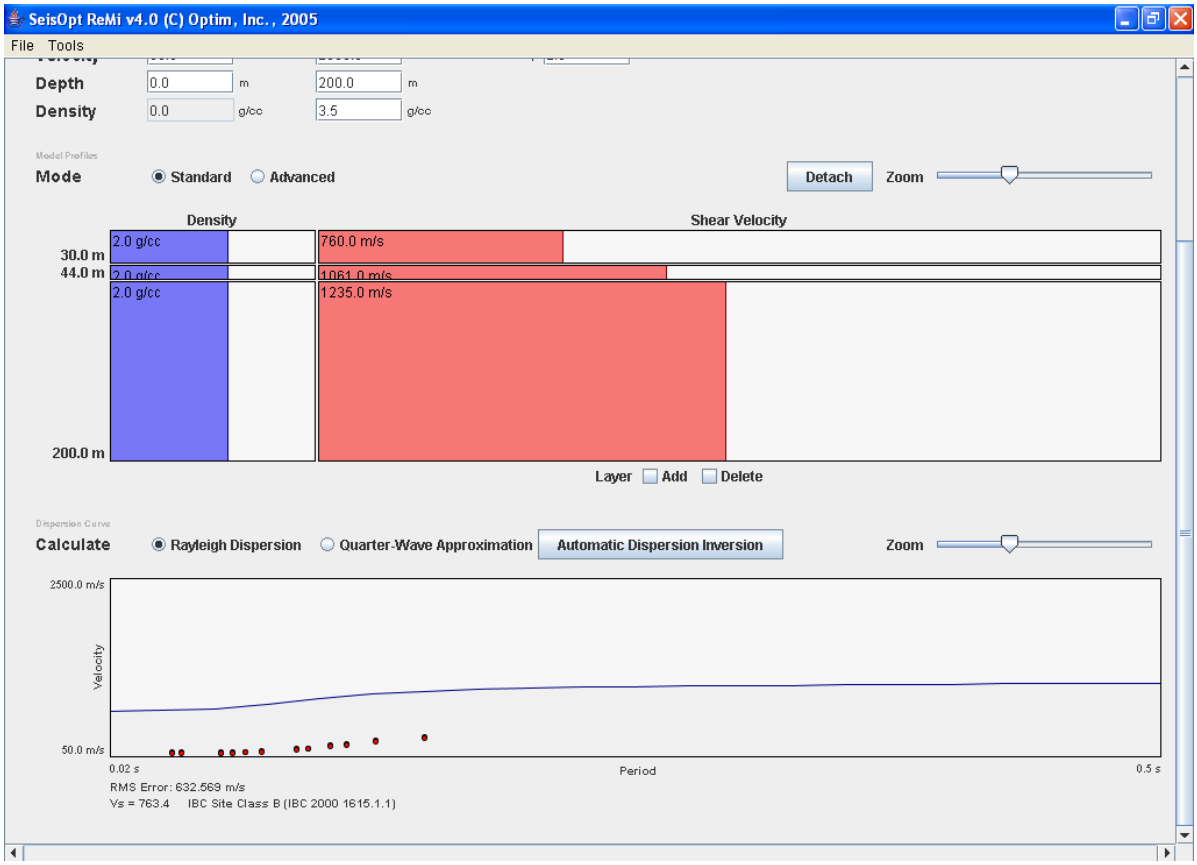

Figure 3.9: Model Profile Prior to Dispersion Curve Fitting Showing Experimental Picks vs. Theoretical Dispersion Curve

From here, the model can be fit to the picks either manually or using the built-in "Automatic Dispersion Inversion" tool located just above the dispersion plot. The most rapid means of obtaining a reasonable fit is to employ the automatic inversion, then refine the optimized model manually to reflect a reasonable approximation of the known local geology. When the automatic inversion tool is selected, the window shown in Figure 3.10 will appear with a number of modeling parameters. All of the parameters affecting the profile space can be adjusted manually at the top of the home window. Units should be consistent with those in the loaded picks. Most parameters can be simply left as default; however it is often good to specify the number of layers desired in the model and a maximum depth. A two or three layer model is sufficient for most data sets. It is unreasonable to expect much more detail out of the ReMi method due to the uncertainty in the picking process. The maximum model depth should be approximately in accordance with the guidelines provided in section 3.1.1. A velocity inversion should only be allowed in sites where stiff over soft layers are known to be present or the dispersion picks clearly show existence of such structure. Once the parameters are set the optimizer is run by pressing the button at the top of the window.

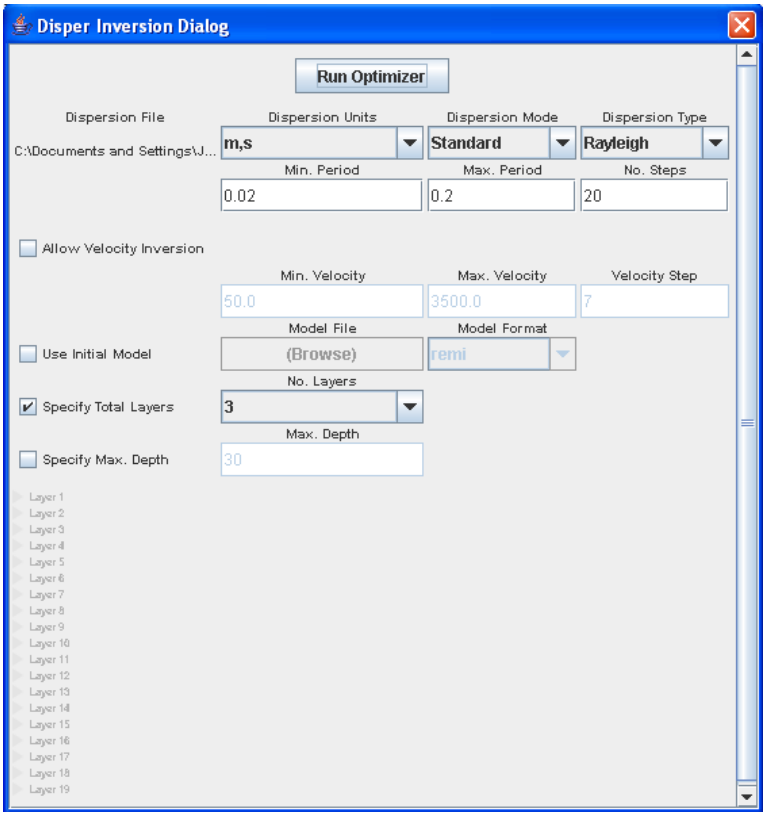

Figure 3.10: Automatic Dispersion Inversion Tool Parameters Window

Often the automated tool will give adequate results immediately. The operator can try different maximum model depths and adjust the number of layers to try to find the best model fit for the experimental data. If, after the optimizer has run, the curve still does not fit the picks closely enough, the model can be manually adjusted by simply dragging the pink velocity bars in each layer or the layer boundaries to more closely match the data. The model fit is affected far more by V_s than density, so the default density values are sufficient in most cases. This is a subjective and iterative process that relies heavily upon user experience. The model fit is also highly non-unique, leaving it up to the user to determine which profile makes the most sense. The displayed RMS error beneath the dispersion curve plot can aid in the fitting process. When satisfied with the model profile, JPEGs of the profile and dispersion curve can be exported from the "File" drop-down menu. Again, appending .jpg to the end of the file name will make it

more readily accessed by picture viewing software. If the user desires to assemble a 2D cross-section, a model file should also be exported from this same menu.

3.1.3.3: Assembling a 2D Cross-Section in ReMi Disper v4.0

When assembling a 2D Cross-section, ReMi Disper v4.0 will interpolate between 1D models to create a smooth 2D profile. If more than two models are included in the 2D assembly it is important that they all lay in approximately the same 2D plane. The model file exported from each 1D profile must be edited to reflect the horizontal offset relative to the others. To do this, the model file is opened in WordPad or some other text editing program, and the first line of text reading “m,s” or “ft,s” is replaced by the coordinates of horizontal offset and top elevation respectively. These values only need to be separated by a single space. The first profile in the section should be set at a horizontal value of zero, and all bottom-of-profile elevations should be modified to be equal. Each model’s floor elevation is located in the last line of text in the first column. The final model is clearer if the same number of layers is used in each model, and velocities do not vary drastically from model to model within a given layer.

To assemble the sections, simply select “Create 2D Profile” from the “Tools” pull-down menu on the main window of ReMi Disper v4.0. The program will ask the user to choose the files of all models to be included. All files must be selected and loaded at once, so all included models need to be in the same folder and selected simultaneously by holding the control key. The “Next” button will bring up the profile parameters window, allowing for selection of minimum and maximum elevation and velocity, as well the pixel resolution on each axis. The “Smoothing” bar allows the degree of smoothing between layers to be adjusted, representing gradually changing boundary velocities. Once the desired parameters are set, the “Finish” button will assemble the model as

shown in Figure 3.11. The window may need to be expanded in order to properly view the plot.

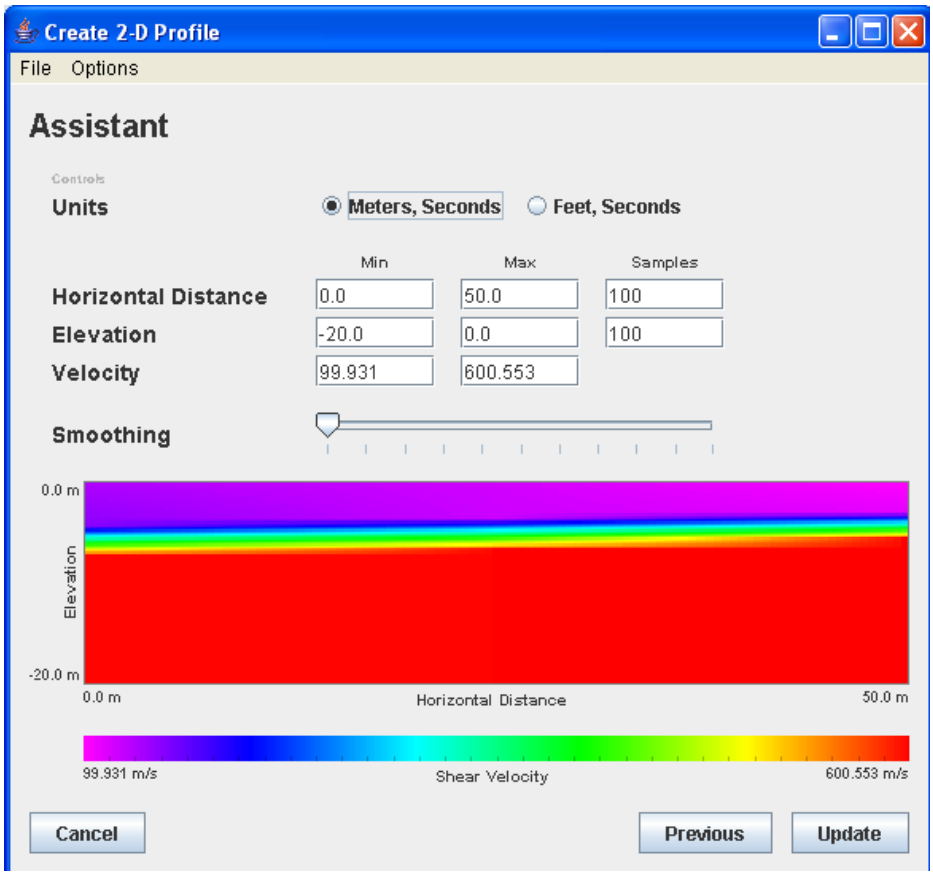

Figure 3.11: Example of a 2D Cross Section Assembled from Multiple 1D ReMi Profiles

The data from this file can be exported as an ASCII text file for importation into Excel or other programs by choosing this option from the “File” drop-down menu. A JPEG of the plot can also be exported from the “File” menu.

3.2: Seismic Refraction

The seismic refraction method is made up of the same general steps of the ReMi method. After array setup in the field the data must be analyzed to determine first break points at each receiver and for each shot point record. These first break points and

survey geometry information are then exported to the modeling software to fit a profile to the data.

3.2.1: Field Setup

The field setup for Seismic Refraction arrays is identical to the setup discussed in section 3.1.1 with a few exceptions. It is important to note that array length needs to be approximately three to five times the depth of desired imaging (Redpath, 1973). Due to this restraint, without a large signal source, such as an explosive, it is difficult to image depths more than 20-30m. The hammer and plate method used in this research does not produce sufficient amplitudes to reach further than approximately 100m in ideal conditions. In terms of resolution, Optim representatives recommend: “For 2-D refraction horizontal resolution is about half geophone spacing, while vertical resolution is about 0.375 times geophone spacing.”

One additional step in setup is to prepare the 10 or 16lb sledge hammer with the piezoelectric trigger. The trigger should be taped securely to the top side of the handle approximately 5cm above the head. The trigger cable can then be attached to an extension cable and ultimately the DaqLink II. This trigger will queue the laptop to begin recording.

3.2.2: Data Collection with VibraScope

The setup process for the acquisition software is very similar to that discussed in section 3.1.2 with a few modifications and additional steps. Referring back to Figure 3.2, the acquisition time should be set to 2 seconds, which is generally more than adequate to capture full wave propagation down the entire array. 2ms sample intervals provide decent continuous data sampling as well as reasonable record file sizes. The sample interval can be set lower if desired for higher resolution of first break point definition. Having a higher resolution can help immensely during the picking process. On the "Trigger" tab, the option "Trigger on TimeBreak" should be selected with the default settings.

With seismic refraction data, it is important to be able to track the first arrival of P-waves at each receiver. The first arrival is often very difficult to separate from random noise with only a single recording. It's helpful to stack multiple records In order to increase the amplitude of these arrivals and cancel some of the random noise. 5 records per shot point are typically sufficient, and more than 10 will not significantly improve the data. To set the software to automatically stack records, select "Preferences" from the "Options" pull-down menu at the top of the main window. The window shown in Figure 3.12 should appear after choosing the "Auto Operation" tab.

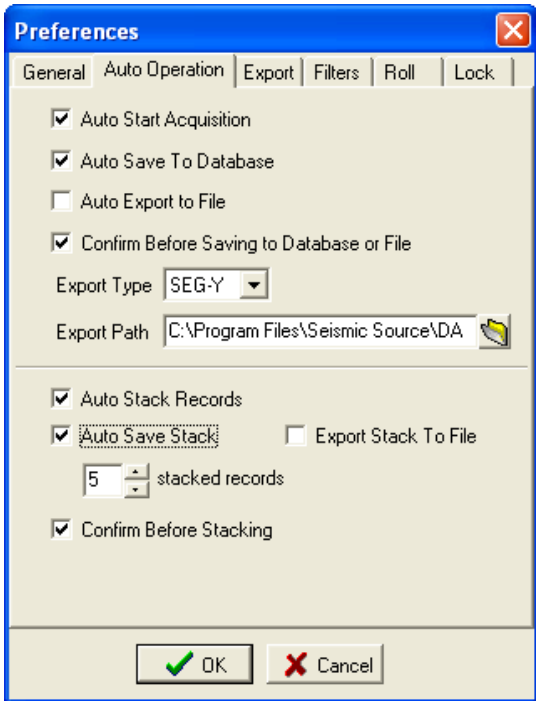

Figure 3.12: Auto Operation Settings for Automated Seismic Refraction Data Collection

Recording is made easiest if the settings shown in Figure 3.12 are selected. The number of records can be adjusted depending upon the needs of the project. It is important to set the program to confirm before stacking and saving records to insure that poor records are not included in the stack. When the setting “Auto Start Acquisition” is turned on, the program will immediately wait for the next trigger signal to begin recording after saving the previous record.

Optim recommends collecting records at a minimum of 7 shot points for 12 geophone arrays, or 14 points for 24 arrays. The locations of these shots for a 12 receiver setup are in plane with the array at twice the geophone spacing off of each end of the array, and then at the midpoints between receivers 2-3, 4-5, 6-7, 8-9 and 10-11. This same pattern is extrapolated for 24 receiver arrays. More source points will yield better results during analysis; however, computation time will also be significantly increased with more data to process.

It is important to be relatively precise with the shot point locations since travel times are used to directly calculate velocities in each layer. It does not take a great deal of difference in travel times to drastically change apparent velocities and cause conflicting data between sources. After clicking the “Start” button on the home window, the metal plate should be placed on the ground and firmly seated at the desired shot location, then struck with the hammer. Given the settings described previously, the program should record a shot with each strike of the hammer until the number of recordings specified per stack have been recorded and accepted by the user. Once the stack is complete, the user will be prompted to save the stack and input comments. This is a good place to specify the location of the shot in order to maintain organization. This procedure is repeated for each desired source point.

3.2.3: Data Processing and Analysis

Although Optim offers a program called SeisOptPicker that exports array geometry and first break point picks in a data format compatible with SeisOpt@2D v5.0, there are many disadvantages to its user interface. For this reason VScope is a preferable choice for making picks. The data can be manually inputted into the text file formats required by the modeling software without much extra effort, and there are a number of functions that are far easier to access and use with Seismic Source’s software.

Once the data has been exported to SeisOpt@2D v5.0, the program can fit 2D models of varying resolution to the data. The user can adjust experimental picks within the program and iterate to develop the most reasonable and accurate solution.

3.2.3.1: Interpretation of Seismograms and Making First Brake Point (FBP) Picks in VScope

VScope provides the user with a wide array of tools to help in analysis of the seismograms. To open a stacked record to make picks, select the “Open” button in the top left corner of the main window. The database will open, and the desired record is opened by double-clicking it or selecting it and clicking “Load”. The first step is to activate the picker module by clicking the icon for “Picker” to the top left of the plots. A red line will appear at the top of each trace indicating that the program is ready to begin picking. At this point it is helpful to right click in the plot space and select both “Scale” and “Picks Table” so that the window appears as shown in Figure 3.13. These windows help track the picks that are being made and allow the user to apply a variety of scale options. The “Axis” window allows the maximum time values displayed to be adjusted so that picks can be made more precisely and extraneous data excluded from the plot. This window is accessed from either the icon near the top of the screen or by right clicking the plot space and selecting “Axis”.

The best scaling option for this analysis is to apply Automatic Gain Control (AGC). Depending upon the data, AGC may be adjusted to a wide range of values until the FBPs are visible enough to be accurately picked. With good data and a relatively quiet site this is often the only necessary adjustment in order to make precise FBP picks. As the theory directs, the first arrivals at each trace should be chosen rather than tracking a single wave signal across each trace. Picking the same wave through all channels is essentially tracking only the direct arrivals and yields information only about the velocity at the surface. Example picks are displayed at the red lines in Figure 3.13.

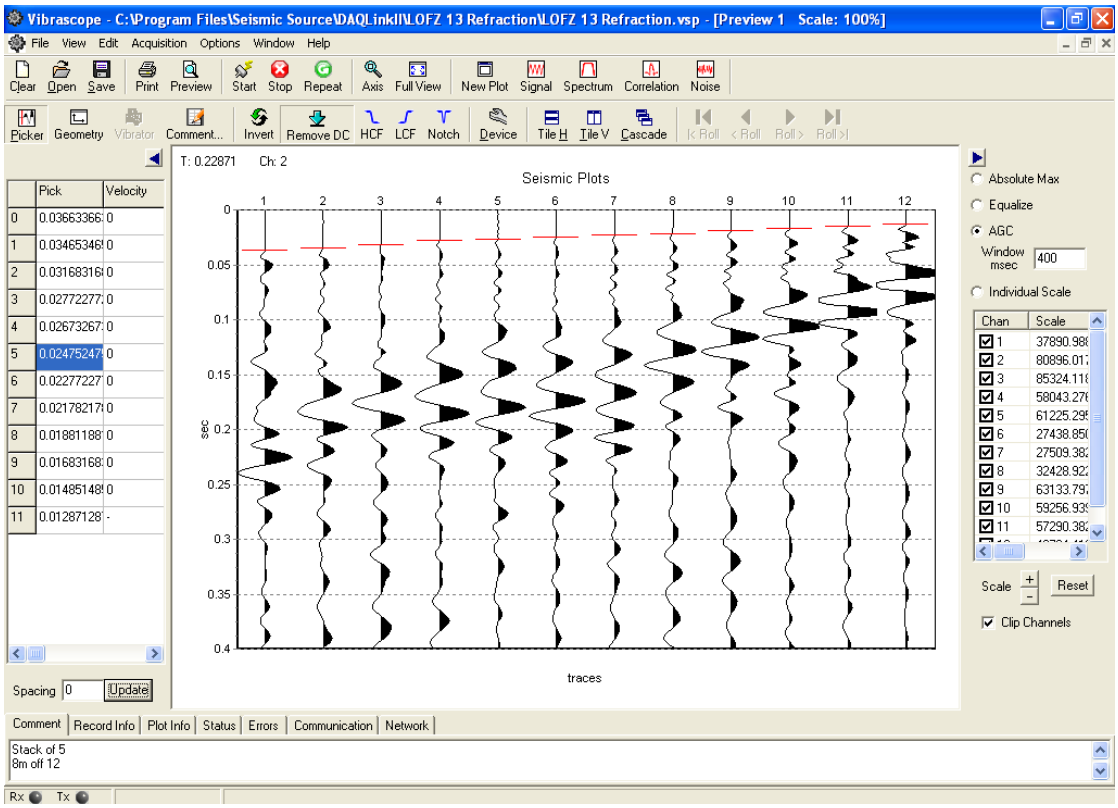

Figure 3.13: View of VScope Picker Module showing Scale Options, Picks Table and Example First Break Point Picks

VScope also offers low cut, high cut and notch filters that are easily applied to the data by simply toggling the icons just above the seismic plots. The frequency ranges for these filters can be adjusted on the “Filters” tab of the “Preferences” window previously accessed in section 3.2.2. It is preferable not to apply any filter to the data since doing so can potentially cause the apparent FBP to move slightly. However, if the site is particularly noisy, a high cut filter set to 80 Hz can help clean up those traces furthest from the signal source and aid in making approximate FBP picks. Best practice would be to make as many picks as possible without the filter, then turn it on only for the traces that are difficult to analyze.

Once all picks are made for a record, they can be saved by selecting “Save Picks…” from the “File” pull-down menu. Three files will be saved with extensions

_src.txt, _rec.txt and _obs.txt. Only the _obs.txt files need to be saved. This entire picking process is then repeated for each source point.

3.2.3.2: Exporting for Processing through SeisOpt@2D v5.0

SeisOpt@2D v5.0 requires three separate text files as inputs. These files contain the source location information, receiver location information, and the FBP picks found in section 3.2.3.1. If the SeisOpt software

The source file is made up of three columns separated only by spaces or tabs. The first column contains the horizontal distance along the survey line where each source is located, the second describes the elevation, and the third indicates the number of picks associated with each source (usually the number of receivers unless some channels are neglected due to poor data). The units for both the source and receiver files can be either in feet or meters.

The receiver file contains only two columns separated again by spaces or tabs. The first column consists of the horizontal distance along the survey where each receiver is located, and the second contains the elevation of each receiver. There must be a receiver coordinate corresponding to each FBP pick, so the total number of rows should equal the sum of the third column in the source file.

The file containing the pick times consists of a single column containing the FBP for each receiver. The row number for a pick must be the same as the row number of its corresponding geophone in the receiver file. The units can be either in seconds or milliseconds.

Once the described text files have been created the data is ready to be processed into a cross-section using SeisOpt@2D v5.0.

3.2.3.3: Creating a 2D P-Wave Velocity Profile Using SeisOpt@2D v5.0

Modeling in SeisOpt@2D v5.0 is a subjective process where many models of varying resolution must be run to find the best optimization. Even after the best resolution is found in the default uniform grid mesh, results can be further fine tuned through several very involved methods that require significant user experience to successfully yield improved results. For the sake of brevity, the procedure outlined here is limited to the necessary steps in modeling a profile roughly (without any fine tuning). Should the user wish to further refine a model, the SeisOpt@2D v5.0 User's Manual provides detailed guidelines to do so.

In order to import and process the data in SeisOpt@2D v5.0, open the program and click "Cancel" when asked to browse for a file to open. An alert will inform the user that the "pickfile" cannot be modified. The main window shown in Figure 3.14 will appear. This is where the model profile will be viewed after being fit to the data. In order to set up the modeling parameters, click the "RIOTS Settings" button to the bottom left of the plot space. The window in Figure 3.15 should appear, asking the user for a number of parameters for the input file.

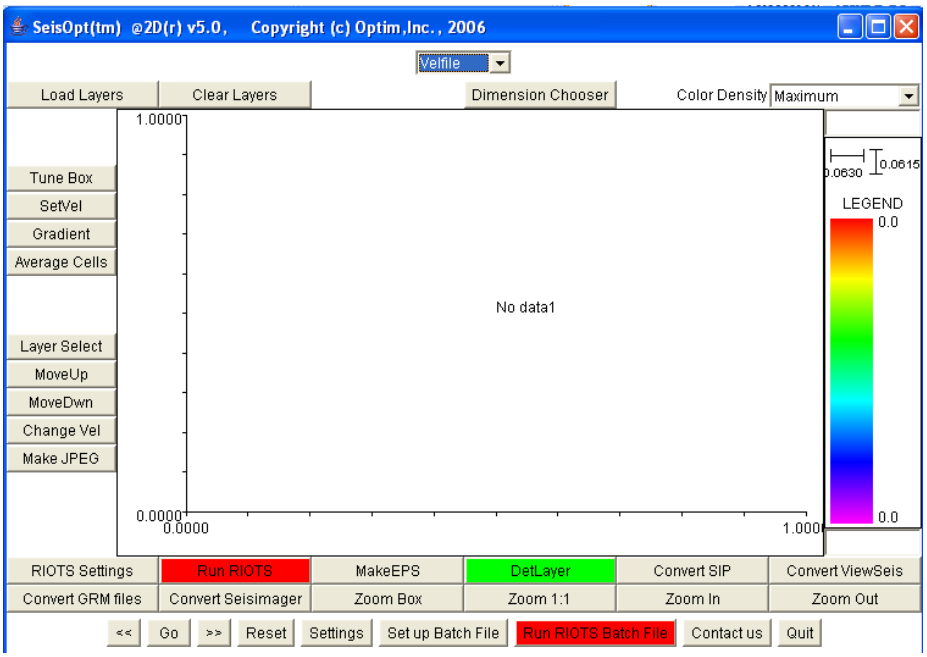

Figure 3.14: Velocity Model Viewing Window

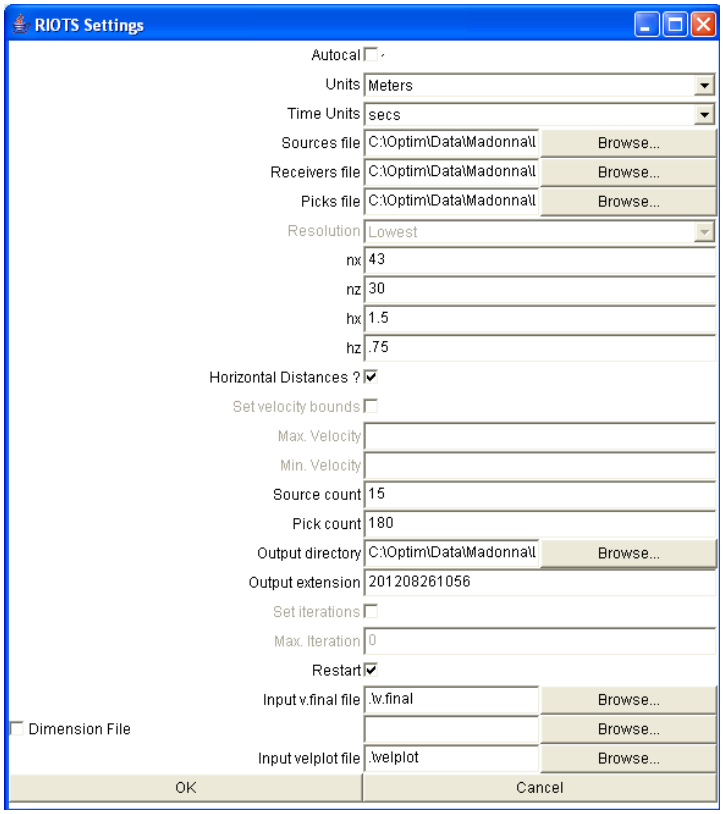

Figure 3.15: RIOTS Settings Window

For the first pass on a new data set, it is best to set the program to “Autocal” at medium, high or highest resolution. Higher resolutions will typically yield better results, however, the higher the setting the longer the analysis will take. It is also possible in some cases that a “High” resolution setting will yield a better fit model than “Highest”. The models obtained from these three settings should be compared, and the most accurate fit should be the baseline resolution/grid mesh for subsequent runs. The unit settings should be set to be consistent with those in the input files described in section 3.2.3.2. The “Browse” buttons allow the user to select the three input files, but it should be noted that the program has difficulties with any path or filename that has a space in it. This is a common issue with some tools in Optim programs in general, so spaces should be avoided in file and folder names as a matter of course.

The “Horizontal Distances” box should be checked, the “Source Count” box reflects the number of source points, and the “Pick Count” field specifies to the total number of picks in the data set. For organizational purposes, a folder should be created for the output directory so that the many output files do not clutter the @2D folder and can be easily located. A file extension such as _autocal should be used to denote this first run as the default resolution settings. It’s best to leave the “Set Iterations” box unchecked so that the program will apply as many as necessary. The “Restart” and “Set Velocity” buttons only need to be checked for fine tuning.

When the “OK” box is clicked, a “riotsinput” file with the specified extension will be saved to the chosen output directory. The “riotsinput” file without extension in the 2Dv50 folder will also be overwritten with these settings. It is this file without extension that will be used as the input for the optimization. On the velocity plot window the red “Run RIOTS” button begins the optimization process.

Should the process need to be terminated before complete, the task manager is the preferable method of doing so due to a bug in the program that can cause the computer to freeze if the “End/Terminate Process” button is pushed. The run time length is dependent upon the resolution and size of the data set, as well as the processing power of the machine. When complete, a number of files will be saved to the output directory with the specified extension.

Once the best “Autocal” resolution model has been selected, subsequent runs are still necessary. According to the Optim User’s Manual, “The default nz values that are used when RIOTS is run using the default resolution settings (that is, when run at ‘High’, ‘Highest’ etc), is approximated one-third the maximum offsets in the survey. This is not necessarily the one that will give you the best result.” To account for this, it is recommended to run the optimization with the same values of hx, nx, and hz that were used in the “Autocal” model, but with varying values of nz. Optim suggests reducing or increasing the value by increments or decrements of 1 for each run with a minimum total of 10 additional runs (5 decrements and 5 increments). This process can be automated by creating a batch file using the tool provided in the “Set up Batch File” button.

The default values of hx, nx, hz and nz are found in the “riotsmsg” file with extension corresponding to the model and can be opened in text editing software. These values are then manually inputted in the “RIOTS Settings” window with the nz value edited. A new extension must be applied to each settings file in order to keep track of which is which and avoid overwriting. This process should be repeated for each desired value of nz until all input files have been created. At this point the batch file is created using the built-in tool.

When the “Set up Batch File” button is selected, a window will pop up asking the user to specify the number of files to be included, and to browse for those files. After specifying the number of files, pressing the “OK” button will refresh the window to reflect the new number. The blank process window that appears can be closed. Each field is then filled with a “riotsinput” file and the “OK” button will now set up the batch file named “riotsbat.BAT” located in the 2Dv50 folder. To begin the batch processing, simply double click this file.

Once the batch is completed, the RMS error associated with each can be found in the “riotsmsg” files. Typically the lowest error corresponds to the best model; however, the velocity plots should also be examined to insure that they make sense. To view the velocity plots, click on the “Settings” button and choose the plots to be viewed. The velocity plots are located in the files named “velfile_extension”. It is also helpful to look at the files named “hitfile_extension” and “pickfile_extension”. The “hitfiles” shows how many times each pixel was sampled by the data, and the “pickfile” displays the experimental and modeled time-distance plots simultaneously. “velfile” and “hitfiles” are both viewed using the “Interactive Velocity Graph” option, while “pickfile” requires the selection “Model Graph”. After clicking “OK”, user is prompted for the source, receiver and observations files. Without selecting these, the user will not be able to modify the experimental picks interactively on the “pickfile” plot. The plot to be viewed is selected from the drop-down menu at the top of the window, and the “Go” button will bring up the plot. When editing picks on the “pickfile” plot, changes are automatically saved to the observations file after pressing the “Enter” or “Return” key.

Review of these plots will help the user determine which model is the best fit for the data and known local geology. The “hitfiles” can be especially useful because they display the ray coverage of the model space. Large gaps in ray coverage are modeled with high uncertainty, so any resolution setting that outputs models exhibiting this coverage deficiency can be eliminated.

Reducing the “Color Density” value on the drop-down menu in the top right corner of the velocity plot viewing window to the number of expected layers will help to illustrate the approximate interface locations. To more accurately locate these interfaces, the green “DetLayer” button will open a module to aid in this process. Details on the use of this module can be located in the user’s manual. This module was not used in this body of work because it requires some knowledge about the layer velocities to determine the layer depths.

A JPEG of any of the plots can be readily obtained by using the “Make JPEG” button to the left of the plot area. The user will be asked for the desired number of pixels in the horizontal and vertical dimensions of the image. The

Chapter 4: Site Locations and Array Placement

Three sites local to San Luis Obispo were chosen for the testing in this project. The suitability of each site will be discussed in the following sections as each was chosen for different reasons. These include Crops Field C-31 of Cal Poly campus, the Ingley site, originally named and trenched by Lettis and Hall (1994), and a third parcel dubbed the Frontera site. The general locations of Crops Field C-31 and the Ingley site are displayed in Figure 4.1. The Frontera site is not shown per the wishes of the land owner.

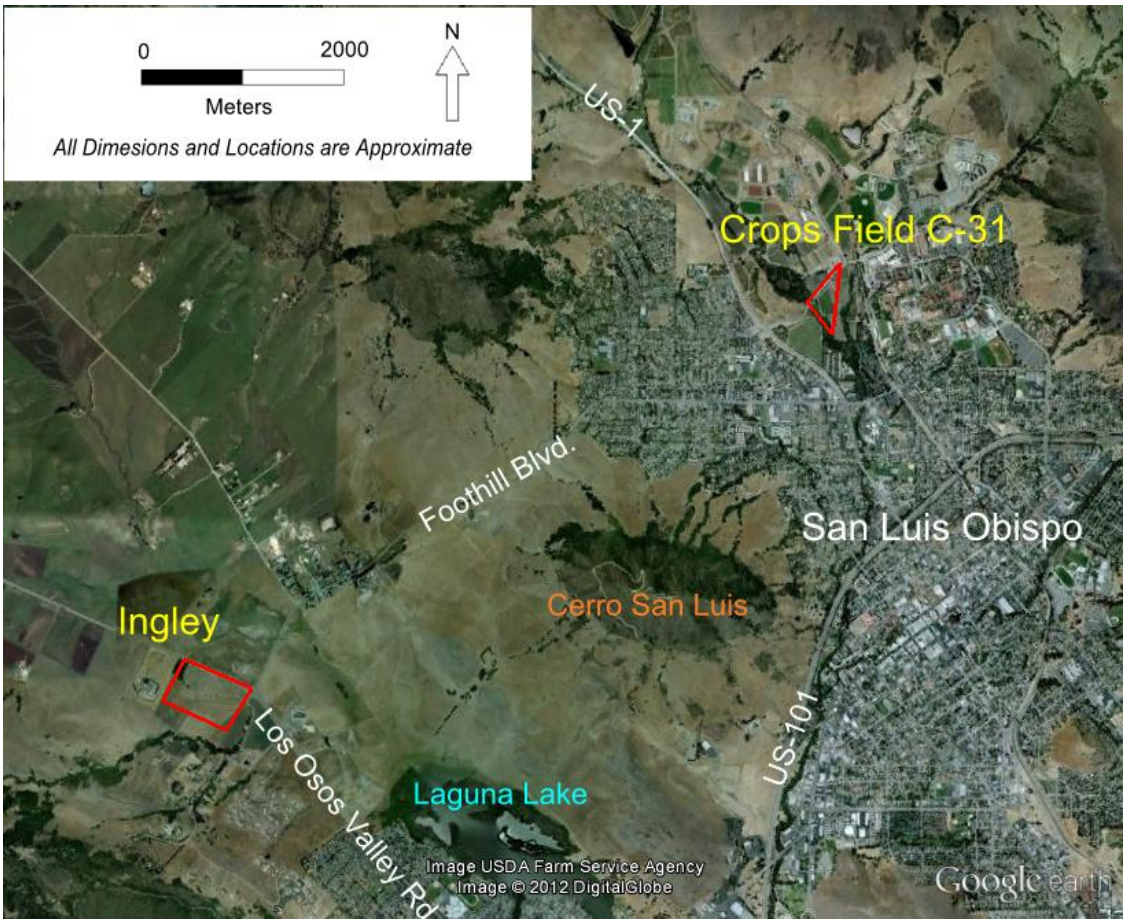

Figure 4.1: Vicinity Map Depicting Ingley, and Crops Field C-31 Sites

4.1: Crops Field C-31

Crops Field C-31 was an ideal location to calibrate the data collection and analysis process due to the locality and availability of subsurface data. Although no known faulting is present at this site, it was a convenient location to run parametric studies and learn the ReMi and Seismic Refraction methods in terms of the real world application.

Subsurface information was readily available for Crops Field C-31 due to prior geotechnical investigations. This work included SCPT soundings and borehole logs at two locations as shown in Figure 4.2. The data from these investigations can be found in Appendix A. This information proved helpful in comparing models obtained through the ReMi and Seismic Refraction methods to the more accepted V_s profiles obtained through SCPT soundings. The arrays were set near the prior investigations to minimize lateral variation in the profile. Placement was limited by existing pavement and extremely loose topsoil tilled for agricultural purposes. Loose topsoil would dampen any signal significantly, and the equipment used in this research was not suitable for testing on paved surfaces. The chosen locations of the arrays are shown in Figure 4.2 denoted as CF-#. For a list of tests run at each array location, refer to Table 4.1.

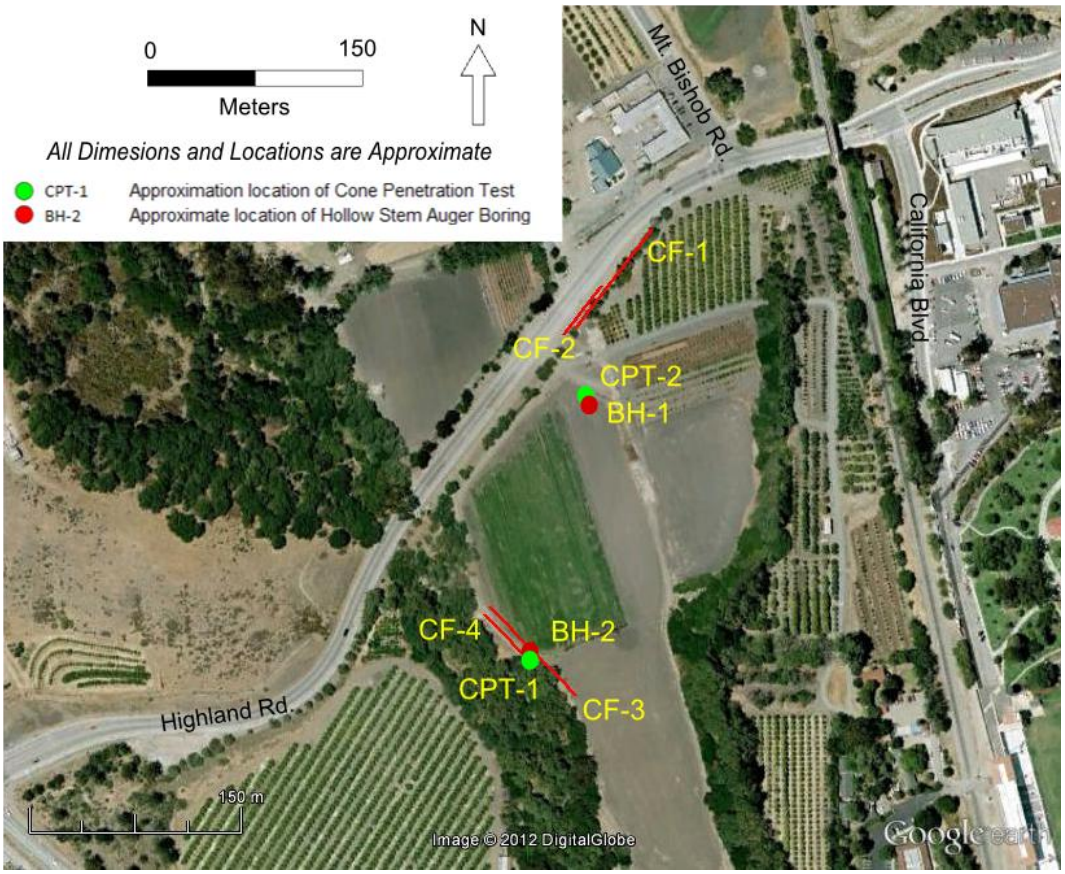

Figure 4.2: Site Plan of Crops Field C-31 Depicting Array Locations as Line Segments

Table 4.1: Testing Schedule for Crops Field C-31 Arrays

Array	# of Receivers	Receiver Spacing	Tests Run
CF-1	12	8m	3 Suites ReMi Seismic Refraction
CF-2	12	4m	1 Suite ReMi Seismic Refraction
CF-3	12	8m	1 Suite ReMi
CF-4	12	4m	1 Suite ReMi Seismic Refraction

*Multiple suites of ReMi imply that records were taken over multiple array deployments in the same location. Each suite consists of a number of 30 second records at a time step of 0.002s.

4.2: Ingley Site

The Ingley site was chosen for a number of reasons. The thrust faulting regime of the Los Osos fault zone is coincides with our aim to identify lateral variation in the V_s profile. This site was previously trenched as part of a fault investigation by Lettis and Hall (1994). Our intention was to attempt to image the fault at a location with a known geologic profile. The Irish Hills segment of the Los Osos fault zone shows particularly good geomorphic expression allowing it to be thoroughly investigated in such locations by trenching (Lettis and Hall, 1994). The information from this earlier study combined with evident geomorphic expression served as guides for array placement.

4.2.1: Existing Information

Figure 4.3 depicts the site locations from the work of Lettis and Hall (1994) on the Irish Hills segment of the Los Osos fault zone. The investigation involved trenching at three separate sites near the intersection (not shown) of Los Osos Valley Road and W Foothill Blvd. Unfortunately, many of the locations originally trenched in 1994 have since been encroached upon by urban sprawl, leaving only the Ingley site as an accessible testing area. Additionally, although trench T-1 of the Ingley site clearly identified lateral variation in geologic structure, it sits adjacent to Sycamore Canyon Creek in a small thicket of trees. The creek and trees surrounding T-1 make placement of arrays problematic, leading to the decision to focus this study on trench T-2 of the Ingley site.

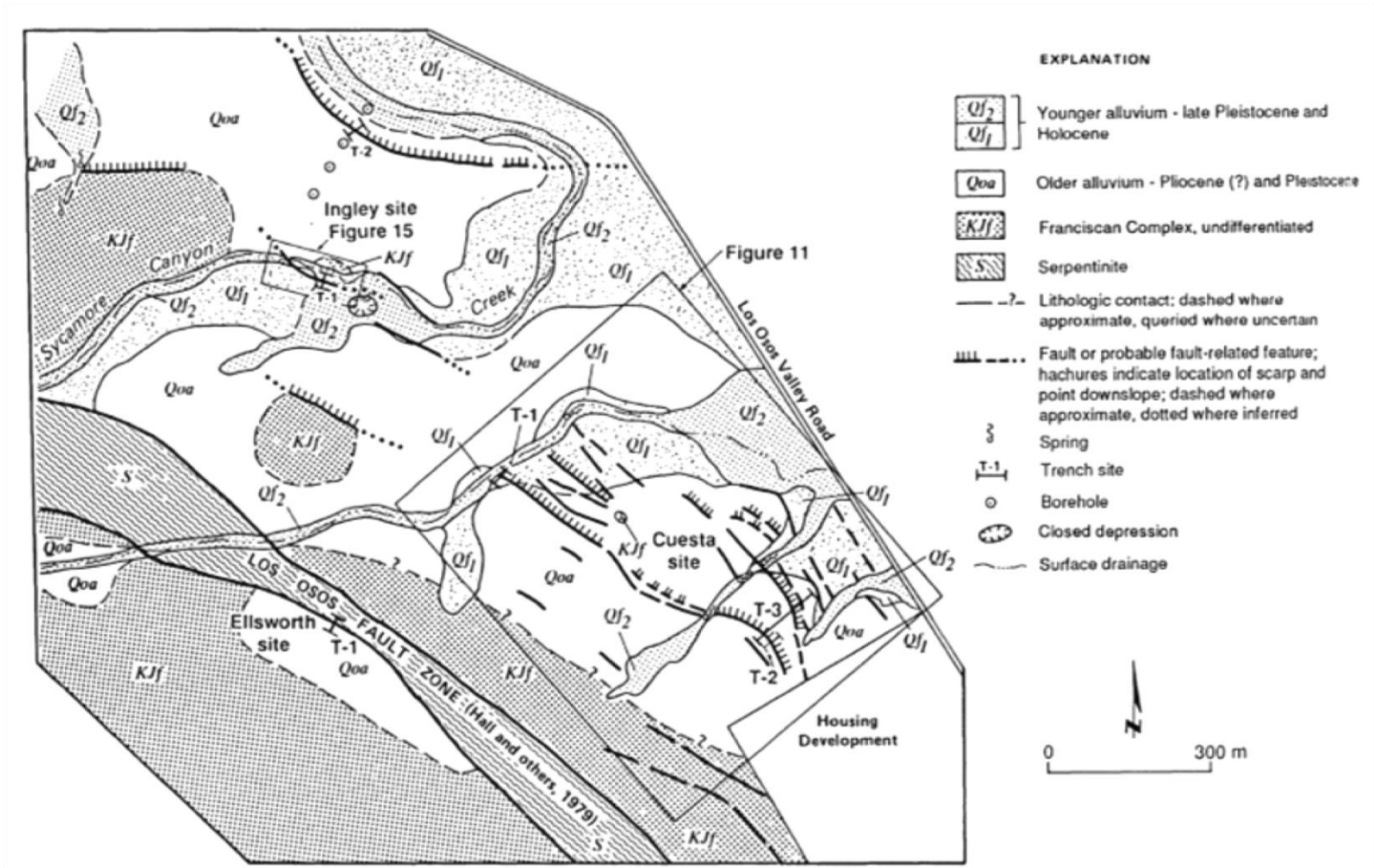

Figure 4.3: Detailed Geologic Map Showing Investigation Locations as well as Observed and Inferred Fault Traces (from Lettis and Hall, 1994)

4.2.1.1: Trenching at Ingley Site T-2

Although T-2 does not expose the Franciscan Complex bedrock, it does capture the primary fault trace, as well as evidence of older alluvium overlying younger as shown in Figure 4.4. The trench is located on what Lettis and Hall (1994) identify as “a prominent northeast-facing, 6-m-high topographic scarp”. The authors go on to offer possible interpretations of the geomorphic and stratigraphic features in Figure 4.5. These interpretations show a significant, though uncertain, offset in depth to bedrock across this primary fault trace. Ideally, this offset would show up in geophysical data as a noticeable difference in depth to bedrock or lateral stiffness across the fault.

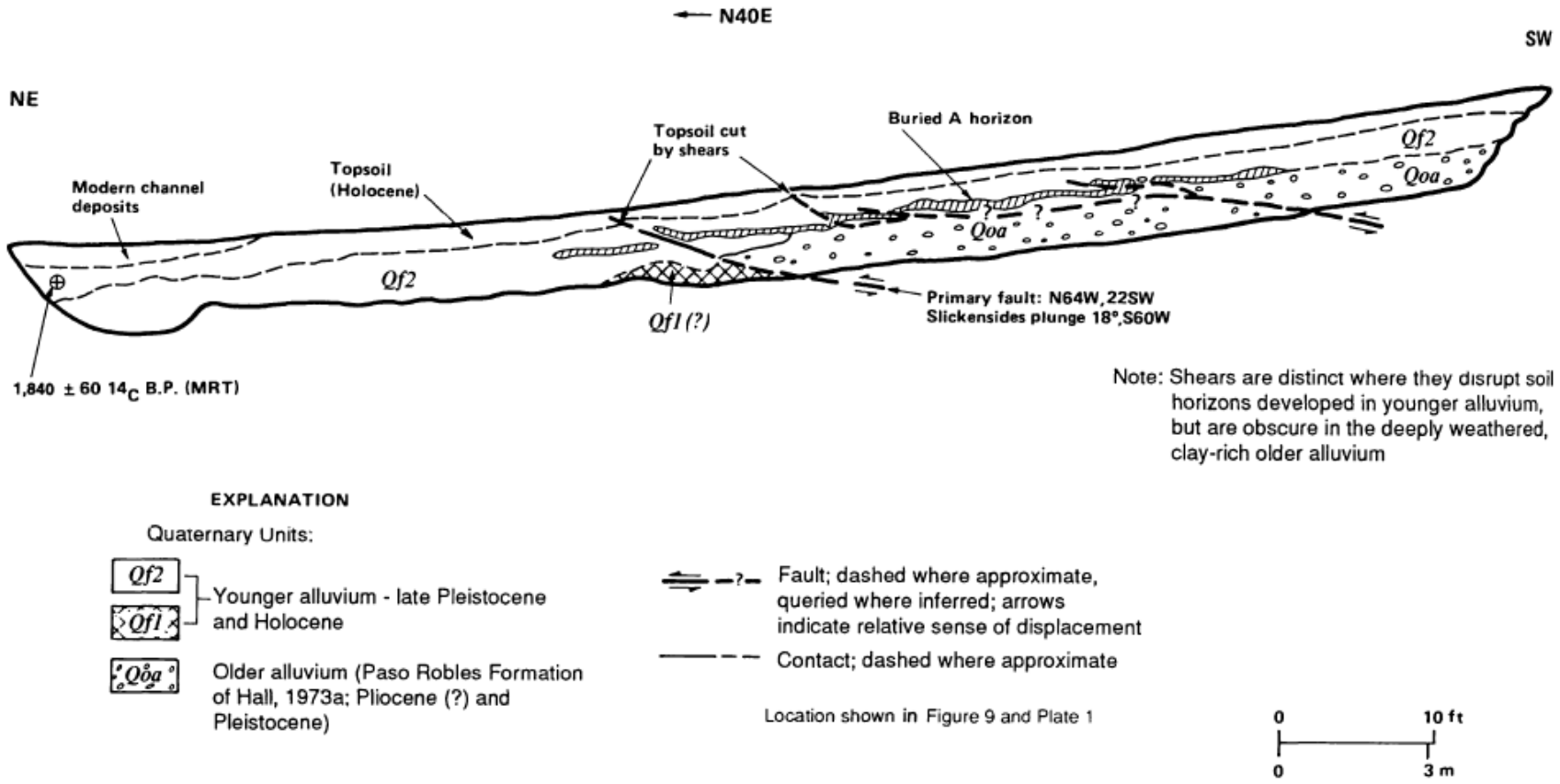

Figure 4.4: Diagrammatic Log of Ingley Trench T-2 Showing Older Alluvium Thrust over Younger (from Lettis and Hall, 1994)

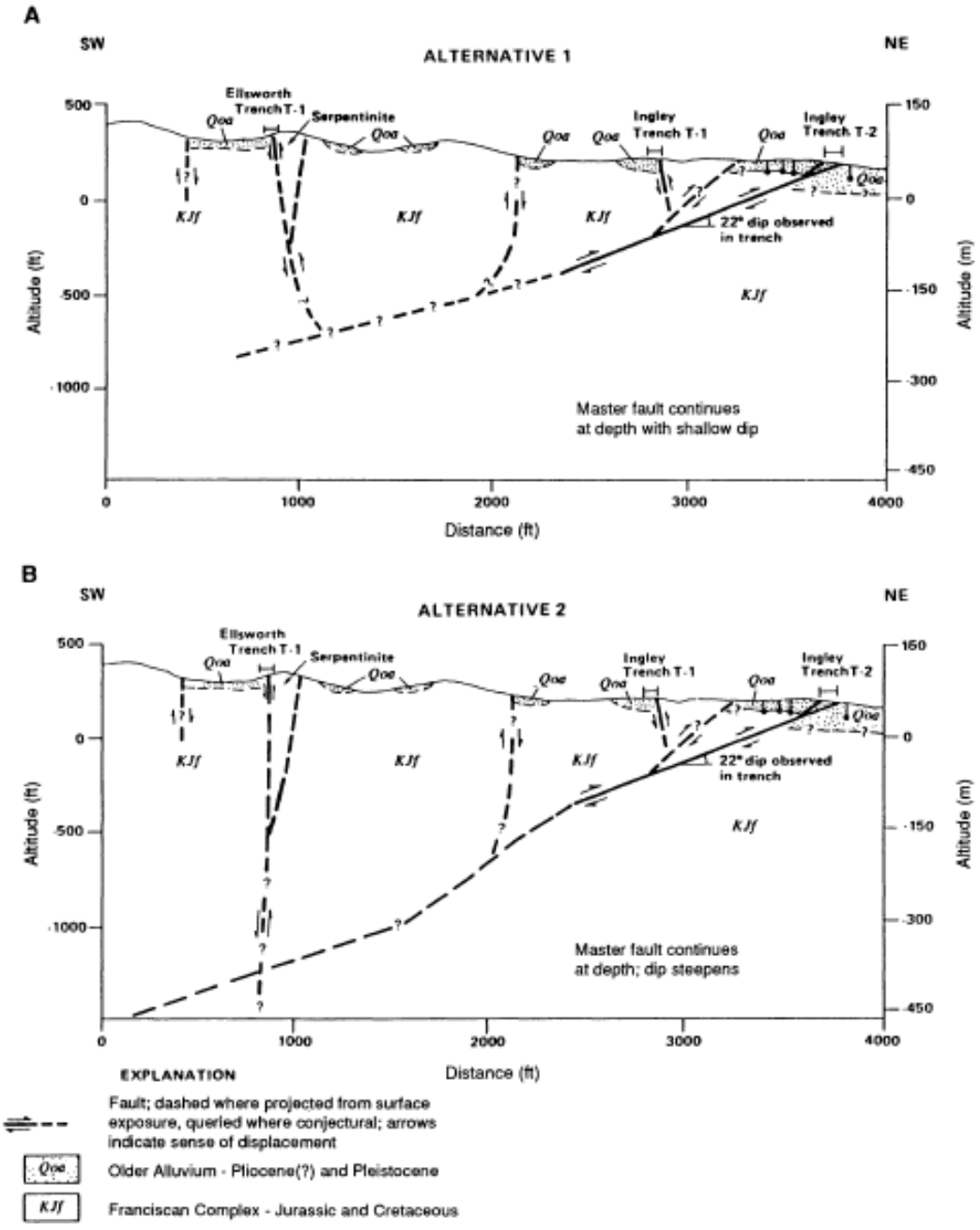

Figure 4.5: Possible Interpretations of the Overall Fault Behavior Based Upon Trench Logs and Geomorphic Expression (from Lettis and Hall, 1994)

4.2.1.2: Geomorphology

Upon a preliminary site walk of the Ingley site, the scarp referred to by Lettis and Hall (1994) was easily identified. Despite the present agricultural use of the land, the scarp remains essentially intact with a small creek bed running along the length of the toe. The topography to the northeast of the scarp is extremely flat, indicating that all major faulting lies southwest of the feature. The level ground also made array placement easier with no need for surveying elevation differences in receiver coordinates. The site is generally located in close proximity to wetlands, which leads to the conclusion (supported by Trench T-2) that soft recent channel deposits overlie the young alluvium from late Pleistocene or Holocene eras.

4.2.2: Array Placement

Given the information from Lettis and Hall (1994) and preliminary site walks investigating geomorphology and accessibility, the arrays were placed as depicted in Figure 4.6. The creek running east to west is visible in the figure along the toe of the scarp. Arrays I-1 through I-3 are located on the floodplain below the toe of the scarp, I-4 through I-6 are located on the scarp itself, and I-7 crosses the floodplain and climbs the face of the scarp. Refer to Table 4.2 for array details.

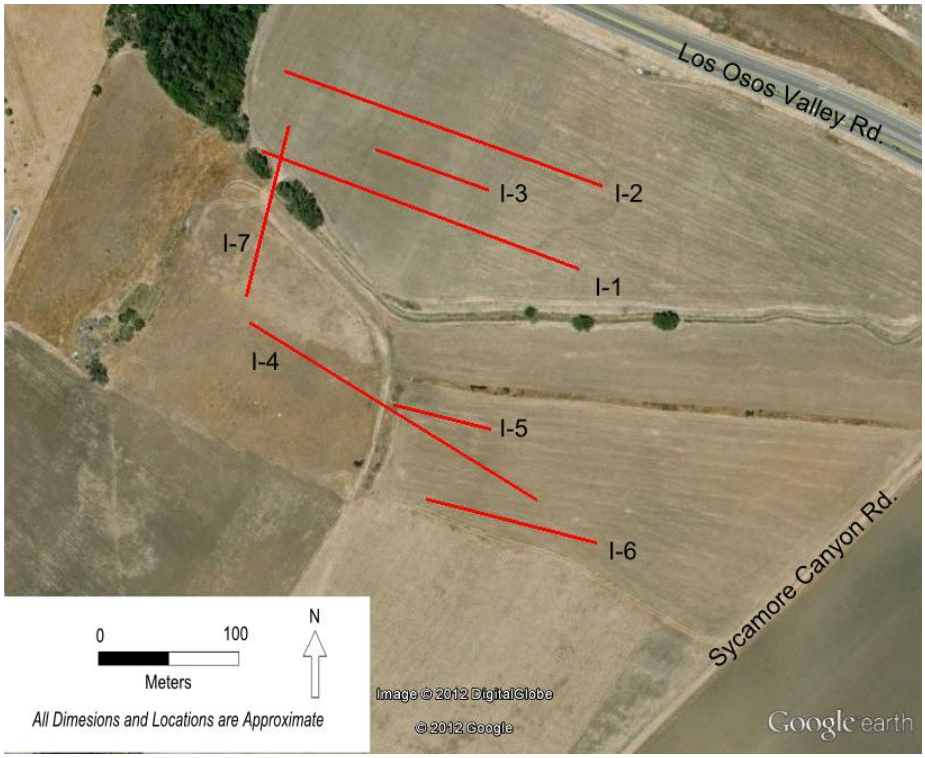

Figure 4.6: Plan of the Ingley Site Showing Sensor Array Placement in proximity to the 6m Scarp and Trench T-2 Discussed in Lettis and Hall (1994)

Table 4.2: Sensor Array Details and Testing Schedule for the Ingley Site

Array	# of Receivers	Receiver Spacing	Tests Run
I-1	24	8m	1 Suite ReMi
I-2	24	8m	1 Suite ReMi
I-3	12	6m	1 Suite ReMi
I-4	24	8m	1 Suite ReMi
I-5	12	5m	1 Suite ReMi
I-6	12	8m	1 Suite ReMi
I-7	24	4m	Seismic Refraction

4.3: Frontera Site

The Frontera site was chosen as a location for attempting the ReMi and Seismic Refraction methods to help find an unmapped fault trace with poor geomorphic expression. This location has experienced little direct investigation, but Lettis and Hall (1994) infer thrust fault traces in the detailed geologic map (figure not shown) printed with their publication. The site lies where the Irish Hills structural sub-block appears to begin to uplift on its eastern end.

4.3.1: Geomorphology

The site lies where the Irish Hills meet the floodplain of Los Osos Valley. Here there is an immediate change in the topography that likely results from the uplift seen throughout the Irish Hills section of the Los Osos fault zone. In preliminary site walks, the geomorphic expression shown in Figure 4.7 was identified as the ideal place to focus the attention of this work. The topography at this expression is not so extreme as to hinder the ReMi or Seismic Refraction methods, and the surface material consists of sufficient topsoil to develop good contact with the geophones.

4.3.2: Array Placement

During field work it was determined that the typical 8m spacing was yielding poor results, so all arrays were spaced at 4m. This spacing seemed to improve the prominence of the dispersion curve in the p-f plots processed in the field. 4m spacing also proved necessary around the inferred scarp expression due to geometric constraints. Possible reasons for the effect receiver spacing showed in the data will be discussed in Chapter 7. Figure 4.7 illustrates the array locations, and Table 4.3 provides array details and the testing schedule.

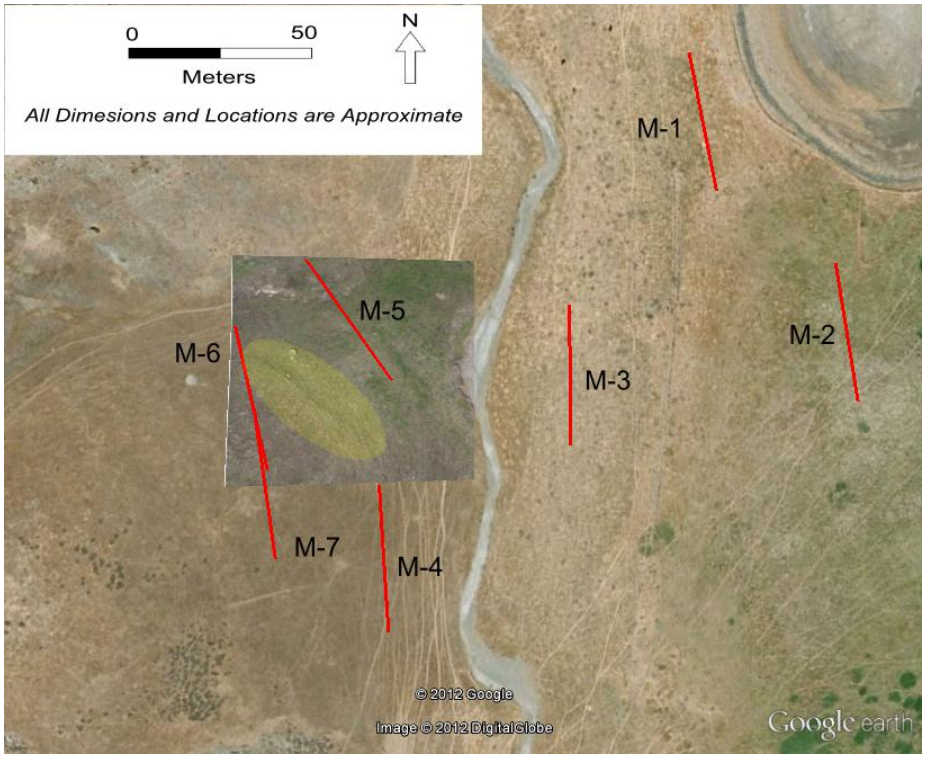

Figure 4.7: Plan of the Frontera Site Arrays with a Recent Satellite Overlay Depicting the Geomorphic Expression Identified in the Field in the Shaded Area

Table 4.3: Table 4.2: Sensor Array Details and Testing Schedule for the Frontera Site

Array	# of Receivers	Receiver Spacing	Tests Run
M-1	12	4m	1 Suite ReMi
M-2a	12	8m	1 Suite ReMi
M-2b	12	4m	1 Suite ReMi
M-3	12	4m	1 Suite ReMi
M-4	12	4m	1 Suite ReMi
M-5	12	4m	1 Suite ReMi Seismic Refraction
M-6	12	4m	1 Suite ReMi Seismic Refraction
M-7	12	4m	1 Suite ReMi Seismic Refraction

Chapter 5: Crops Field C-31 Data Analysis

Crops Field C-31 was investigated through the deployment of four arrays as shown on Figure 5.1 and described in Table 4.1. Array CF-1 was deployed in the same location three separate times to assess the precision of the ReMi method. Array CF-2 is also in approximately the same location and allows for a comparison with the records of CF-1 to determine how much of an impact spacing of receivers may have upon results. CF-2 also proved to be an ideal location to run a simple parametric study. The data from array CF-3 yielded no clear dispersion trend, and CF-4 showed only slightly better definition. Seismic refraction data was collected for all arrays except CF-3.

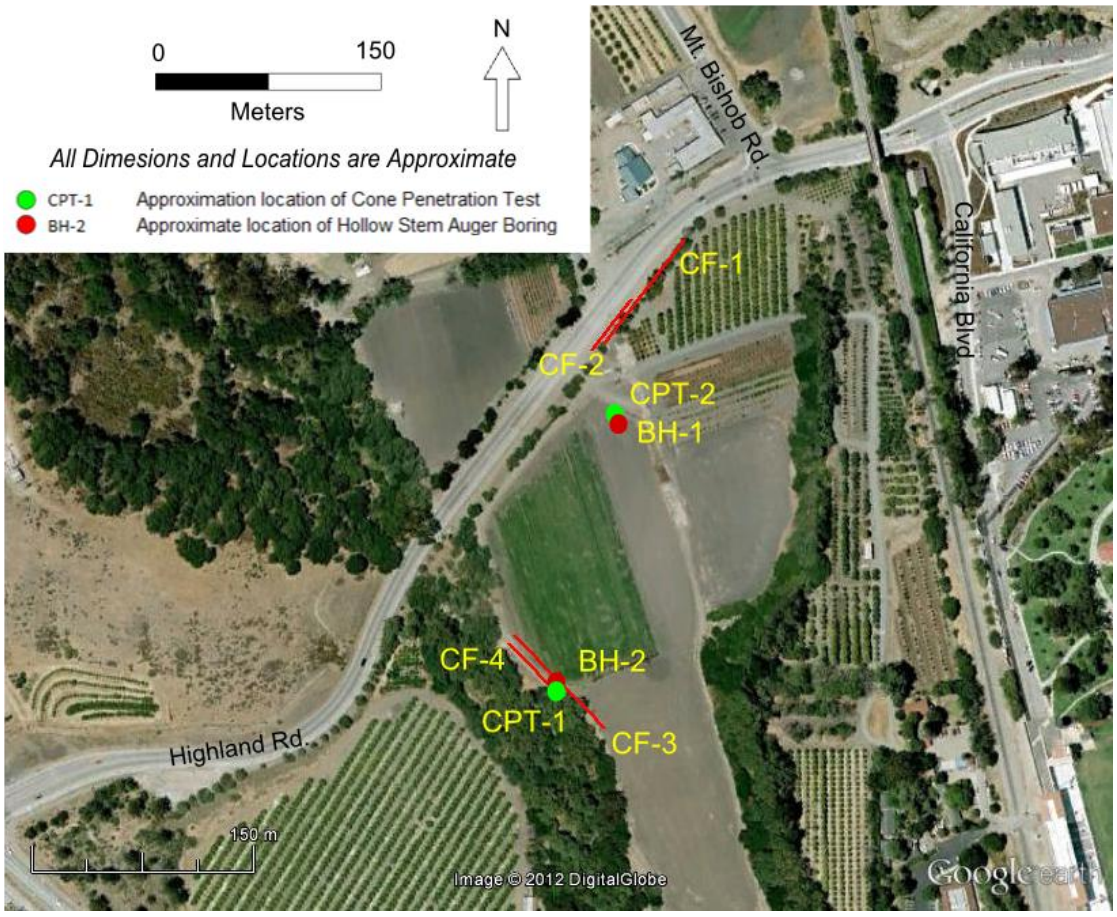

Figure 5.1: Site Plan of Crops Field C-31 Depicting Array Locations as Line Segments

5.1: Refraction Microtremor

All of the ReMi arrays deployed throughout this work collect data in 30s records at a 2ms time-step. The data at Crops Field C-31 was expected to be fairly good due to the presence of a multitude of ambient signal sources in the area. With the proximity of Highland road, activities on Cal Poly campus and any agricultural work going on in the neighboring fields, Crops Field C-31 seems an ideal location for passive data collection.

5.1.1: Highland Road Arrays

Despite the presence of plenty of ambient signal sources in the area, the p-f plots obtained through multiple suites of testing along Highland road lacked good definition of the dispersion trend. The spectral ratios along the typical slope of a dispersion curve seemed "washed out" by the low-frequency artifact produced by the Fourier transform that expresses the data in p-f space. The plots also seem to be highly saturated with incoherent noise in the upper frequencies, possibly due to the presence of body waves. Figures 5.2a-c show the p-f plots obtained through the three suites of data obtained through array CF-1 and corresponding dispersion picks made along the lower bound of the trend.

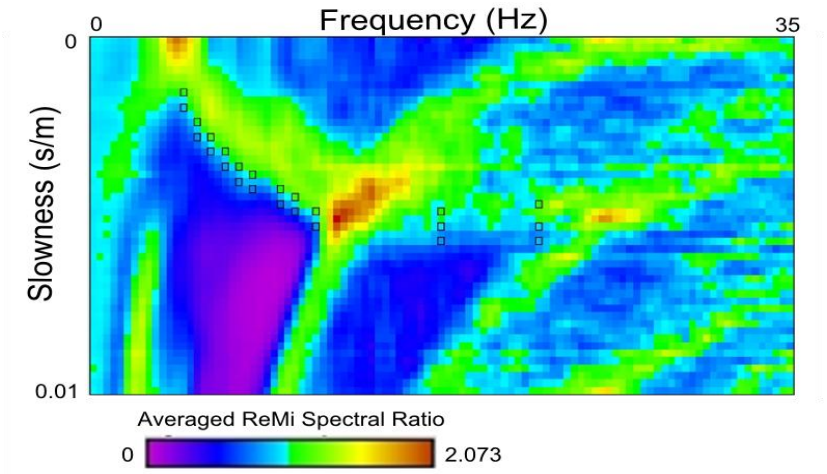

a)

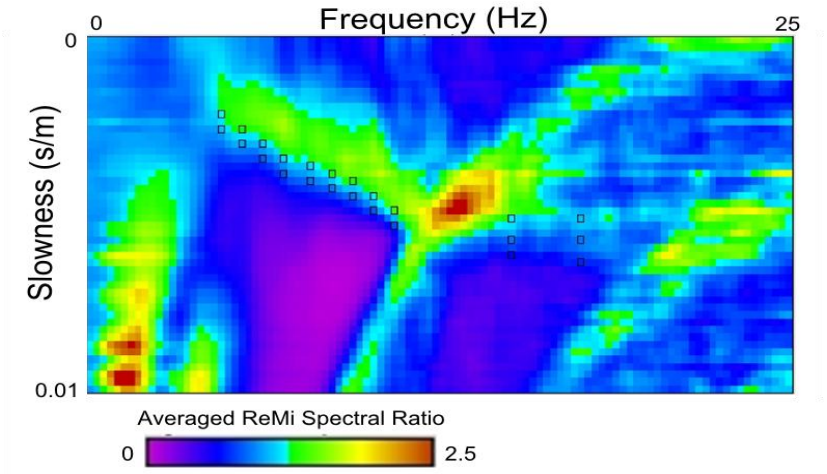

b)

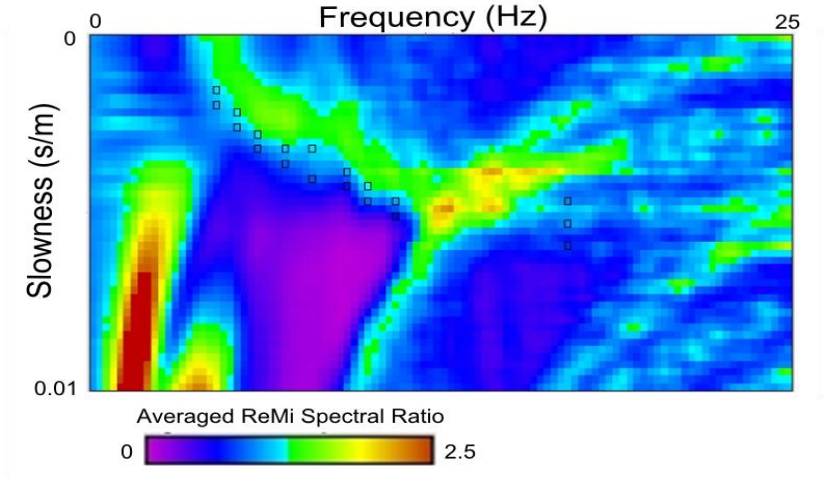

c)

Figure 5.2: SiesOpt p-f Spectral Ratio Plots for CF-1 Showing (a) Suite 1, (b) Suite 2 and (c) Suite 3

The plots obtained from CF-2 will be discussed in section 5.1.1.2 as they illustrate the results of a parametric study. They may be compared generally with the p-f plots obtained from CF-1 in terms of the quality and definition of the dispersion trend, but due to the offset in array midpoints and shorter array length lateral variation is an uncontrolled variable. For this reason the results should not be directly compared with CF-1 in the precision analysis discussed in section 5.1.1.1.

5.1.1.1: Highland Road Precision Study

The accuracy of the ReMi method has been tested by Louie (2001) and others in relation to other more accepted methods such as suspension or downhole logging. Literature on measurement uncertainty and repeatability within the method is less prevalent, although Cox and Beekman (2011) investigate some aspects of the test. This precision study here attempts to determine the repeatability of the ReMi method given that the array location and orientation are held constant.

The data from the first trial was taken several months prior to the other two trials. Trials two and three were taken on the same day with the third trial offset from the second trial array by approximately 1/3 of a meter perpendicular to the line. Lateral variation affects in this case should be negligible. While it is impossible to remove human judgment entirely due to the need for dispersion picks from the p-f plots, the profiles were modeled entirely by using the same automatic inversion algorithm for all three trials. Each trial is specified to include three layers to a bottom depth of 30m. While the profiles generated using solely the automatic algorithm may not be as well fit to the data as it is possible to achieve manually, this was the best possible method to develop a pseudo-blind comparison.

The results of the study are plotted in Figure 5.3 and summarized in Tables 5.1 and 5.2. Although trials two and three were taken on the same day and better controlled in terms of receiver placement, the results differ as much between these trials as with the first data set. The maximum percent difference in V_{s30} between the three trials was found to be 12.7% and the coefficient of variation (COV) is 7%. Statistical analyses for each layer and interface appear summarized in Table 5.2 and suggest that at larger depths and higher phase velocities the ReMi method is more stable. The coefficient of variation in the bottom layer is less than half that of the top layer. Interface depths in this study showed coefficients of variation on the order of 10-15%.

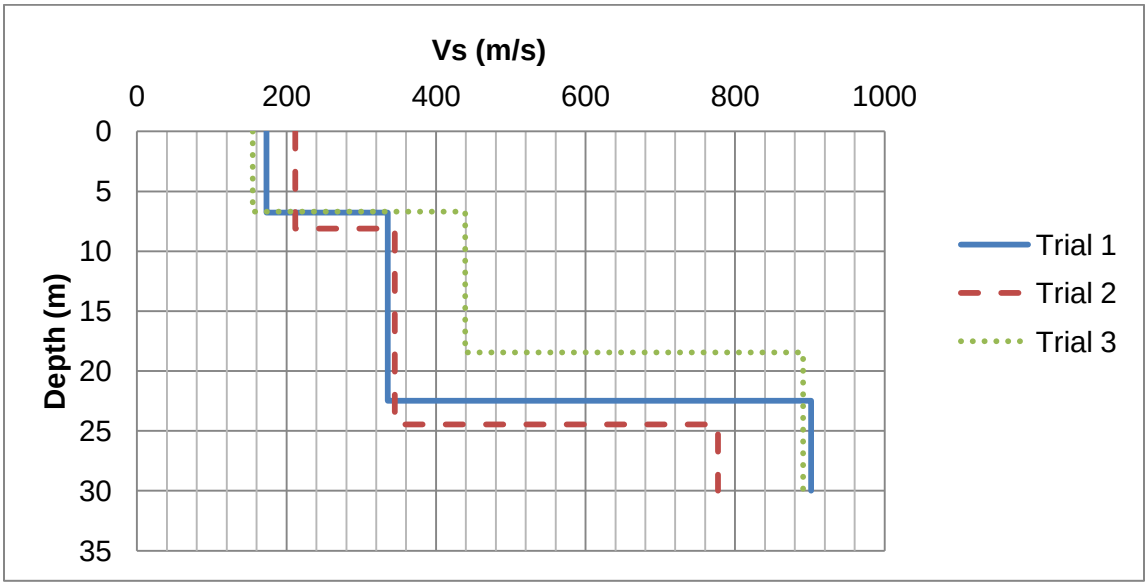

Figure 5.3: V_{s30} Profile Illustrating Variance within the ReMi Method While Holding Array Location and Orientation Constant

Table 5.1: V_{s30} Statistics for Precision Study on Highland Road

Trial	$V_{s(30)}$ (m/s)
1	321.7
2	326.0
3	364.5
Average	337.4
Coef. Of Var. (%)	7.0
Max % Diff.	12.7

Table 5.2: Layer Depth and Velocity Statistics for Precision Study on Highland Road

	Min	Max	Average	StDev	COV (%)
Depth to Interface					
1st Interface (m)	6.7	8.1	7.2	0.79	11.0
2nd Interface (m)	18.4	24.5	21.8	3.07	14.1
Velocity of Layer					
1st Layer V_s (m/s)	155	212	179.9	29.08	16.2
2nd Layer V_s (m/s)	336	439	373.1	57.35	15.4
3rd Layer V_s (m/s)	777	902	856.6	68.90	8.0

The theoretical dispersion curve fits to the data are shown in Figure 5.6 and indicate that the automatic inversion may produce a poorly fit model. In fact, Figures 5.4 and 5.5 reveal that the picks from all p-f plots conform to a fairly tight trend. All three sets of data fit considerably well to a single manually optimized model. Due to the reciprocal transformation from slowness to velocity, the lower the slowness of a given pick the higher the uncertainty is at that point. Figures 5.3, 5.4 and 5.5 demonstrate that the pick spread for a given frequency, even within trials, becomes much more uncertain at higher phase velocities.

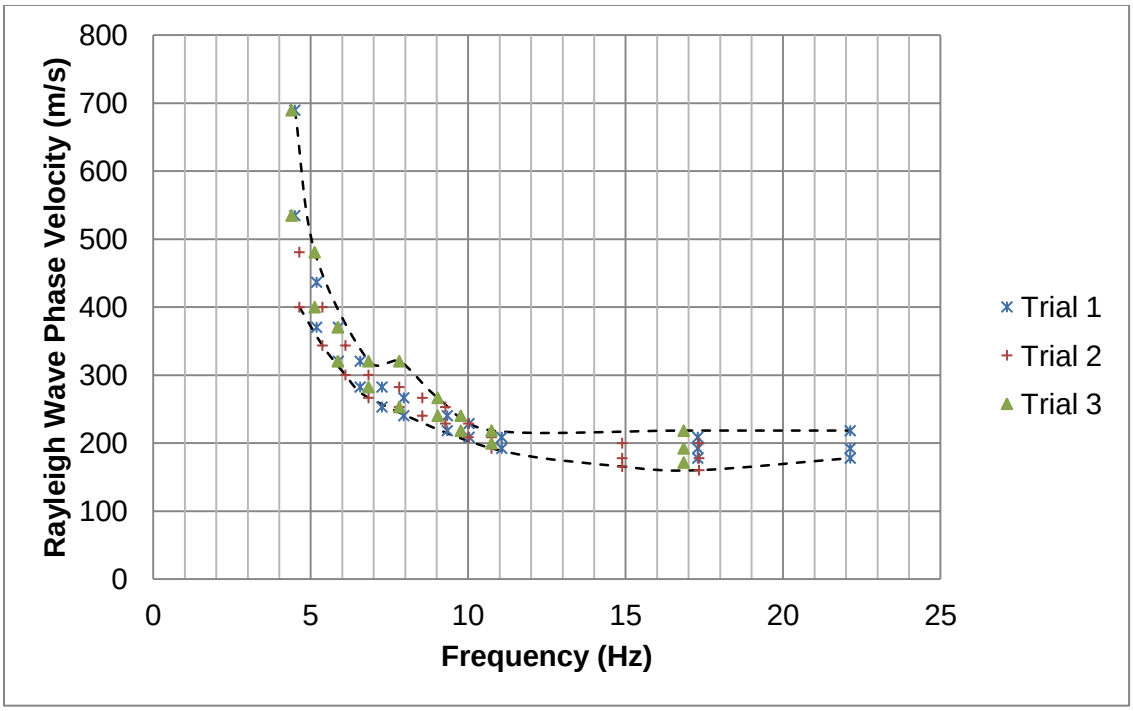

Figure 5.4: Picks from All Precision Study Trials Plotted Simultaneously in Frequency-Phase Velocity Space

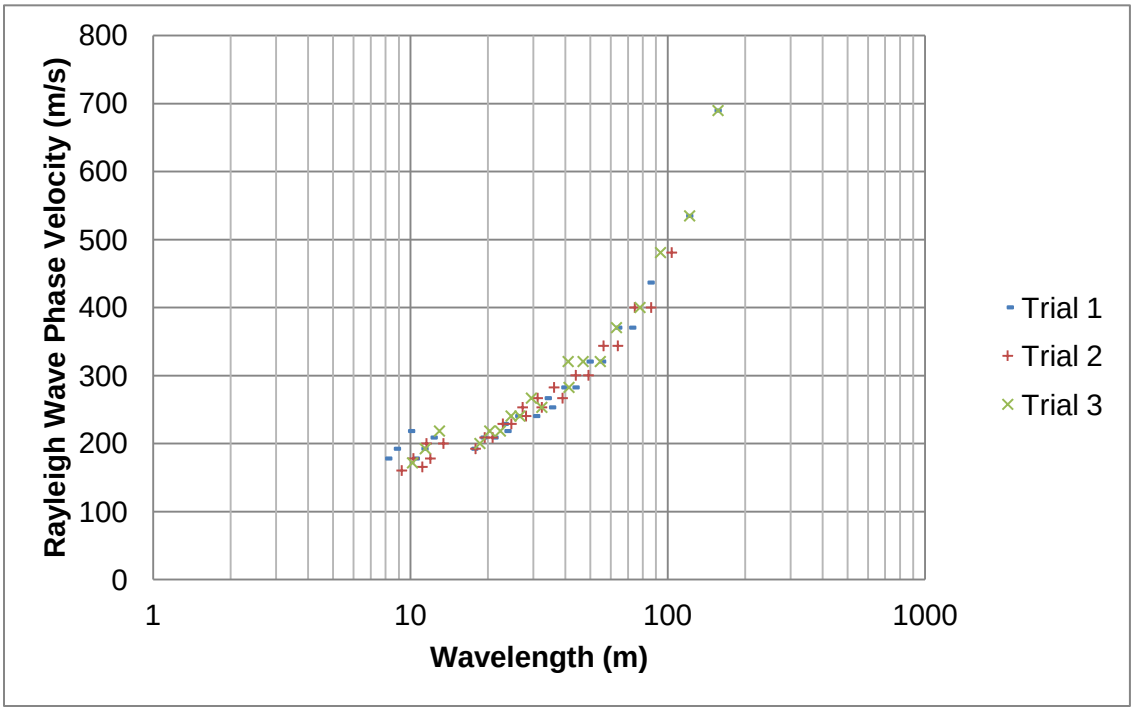

Figure 5.5: Picks from All Precision Study Trials Plotted Simultaneously in Wavelength-Phase Velocity Space

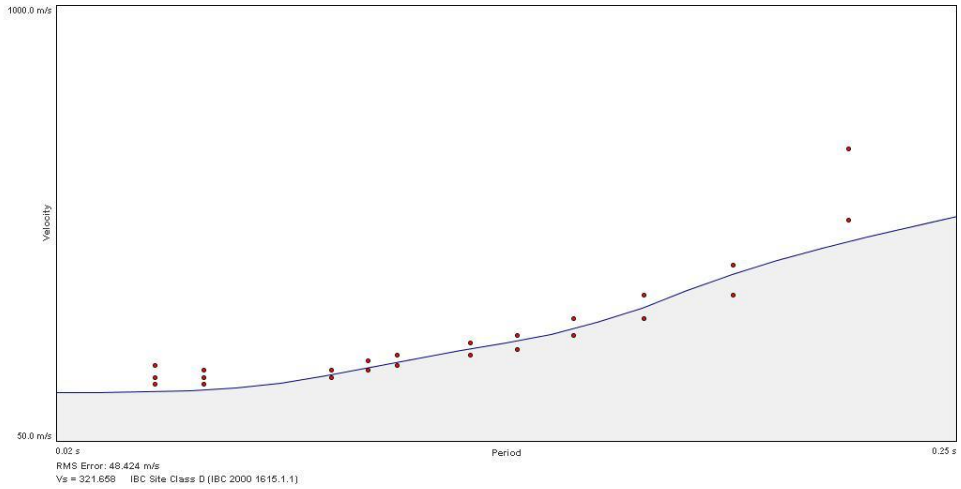

a)

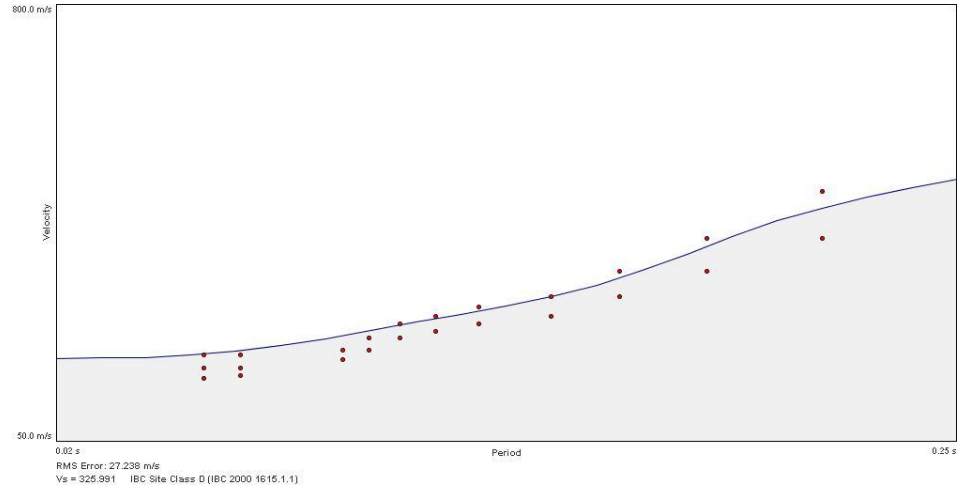

b)

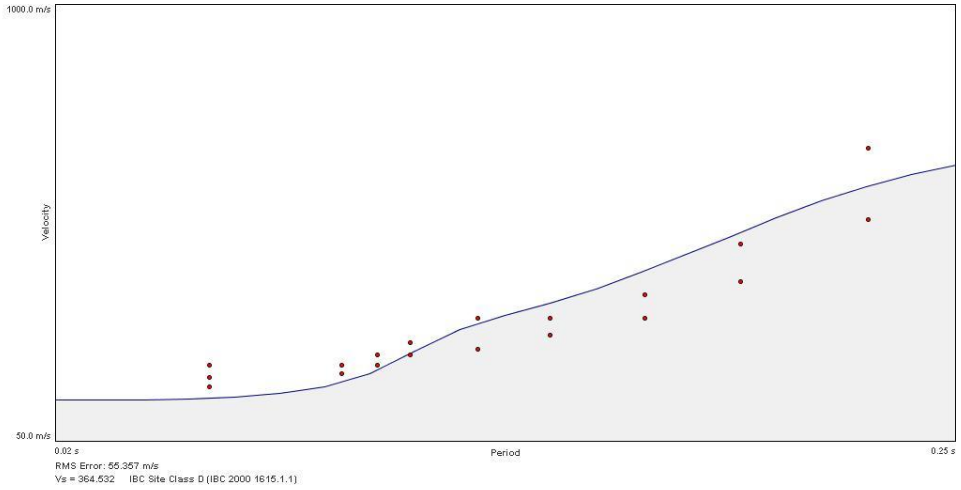

c)

Figure 5.6: Theoretical Dispersion Curve Fits from Automatic Inversion for (a) Trial One, (b) Trial Two and (c) Trial Three in Period-Velocity Space

The point here is that, as Louie (2001) warns, the forward modeling process can produce multiple models that fit the data equally well. Any lack of precision in the data collection process in this study is far outweighed by the interpreter's choices during the forward modeling process. Poor choice of picks made on the p-f plots can lead the interpreter incorrectly during the modeling process. This is why it is important to choose multiple picks at a given frequency, attempting to bracket the possible range of values within which the true slowness or phase velocity should lie. It is ultimately up to the interpreter to make the call on what profile makes the most sense and to optimize the model with this in mind.

5.1.1.2: Highland Road Parametric Study

ReMi array CF-2 was primarily used to run a parametric study. This tests the affect that active signals coming from different azimuths and offsets have on the transformed p-f plot. Figure 5.7 displays the results obtained through combined spectral ratios from four ambient signal recordings. The dispersion trend is poorly defined with very weak response in the lower frequency range and shows a wide distribution of energy response along the mid and high frequencies. The wide distribution of energy and poorly defined lower bound make the picking process uncertain at best.

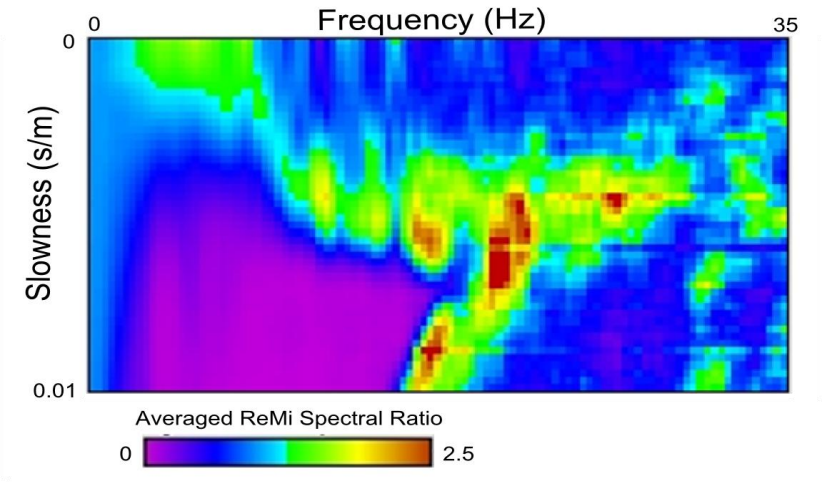

Figure 5.7: CF-2 p-f Plot of Combined Passive Signal Records

By contrast, when introducing an active source, in this case sledge hammer blows, the quality of the data can be much improved. Figure 5.8 helps to testify to the difference that can be achieved. In this case, the signal source (10lb sledge on a steel plate) was located off-end of the array approximately 10m. The range of frequencies from approximately 25-35Hz shows a constant slowness across frequencies. This is either indicative of a constant or near constant stiffness in the upper layers of the strata, or is a product of some other response than that of a Rayleigh wave. Air waves can look similar, but the phase velocity is considerably lower than the speed of sound.

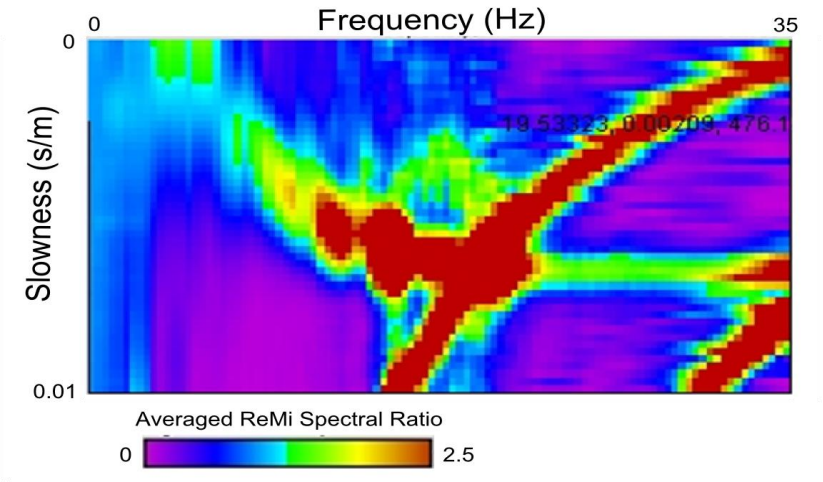

Figure 5.8: CF-2 Recording with Hammer Blows on a Steel Plate Off-End of the Array

The hammer was then employed without the striking plate to evaluate the difference in frequency range response. Figure 5.9 displays the results of the two combined spectral ratio plots obtained during this activity. While it seems intuitive that the steel plate would generate more high frequency content, the plots appear to show the opposite. The steel plate response is much stronger in the mid-range frequencies, where the direct strike to the ground surface showed much higher response in the upper-range. Due to the nature of the spectral ratio display, the poorly defined low-mid range frequencies may be a result of "wash out" caused by the strong response in the upper range. When the term "wash out" is used in this work it is referring to the poor definition of lower amplitude responses resulting from the spectral power normalization that transforms the data to spectral ratios.

It is also possible that the upper frequency range is better lit in Figure 5.9 because of poor coupling and energy transfer between the plate and the soil surface. The higher frequency waves will attenuate rapidly, thus the more energy that can be transferred to the strata the better. The direct strike removes any contact issues,

however the reduced strike area can also reduce energy transfer to wave signals as a result of plastic deformation in the soil (B. Cox, personal communication, July 4, 2012).

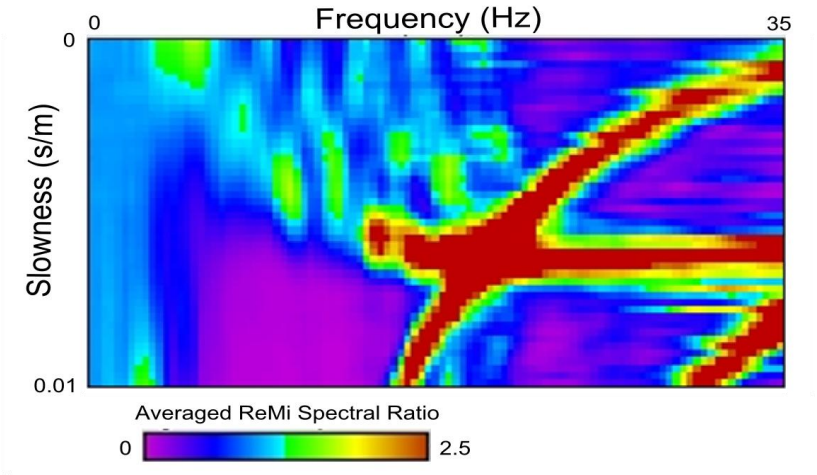

Figure 5.9: CF-2 Recording with Hammer Blows and no Plate Off-End of the Array

The records shown in Figure 5.10 attest to the effects of the plane wave arrival assumption when the source is close to the array. When the receiver array is far enough from the source, the radius is large and the difference in ray approach angles small. With a source placed closely to the array the radius of the wave field is still small enough that these approach angles will vary across the array such that the results are clearly affected. As depicted in Figure 5.11, the closer the source, the more extreme the difference in arrival times between the end geophones and those near the midpoint. The further the array lies from the signal source the more closely together the receivers will observe the signal.

The effect of a small radius source-array offset manifests itself in the p-f plots as a marked shift in the steepness of the dispersion trend. When the source is further from the array the angles of the arrivals with the line approach perpendicular, and the spectral peaks indicate higher apparent velocities. A closer source will indicate lower velocity spectral peaks, since the wave front arrives more obliquely, especially at the geophones

near the end of the array. Introducing an active source in this manner will also “wash out” any passive signal that was arriving from azimuths more in line with the sensor array (the arrivals that would indicate true phase velocity).

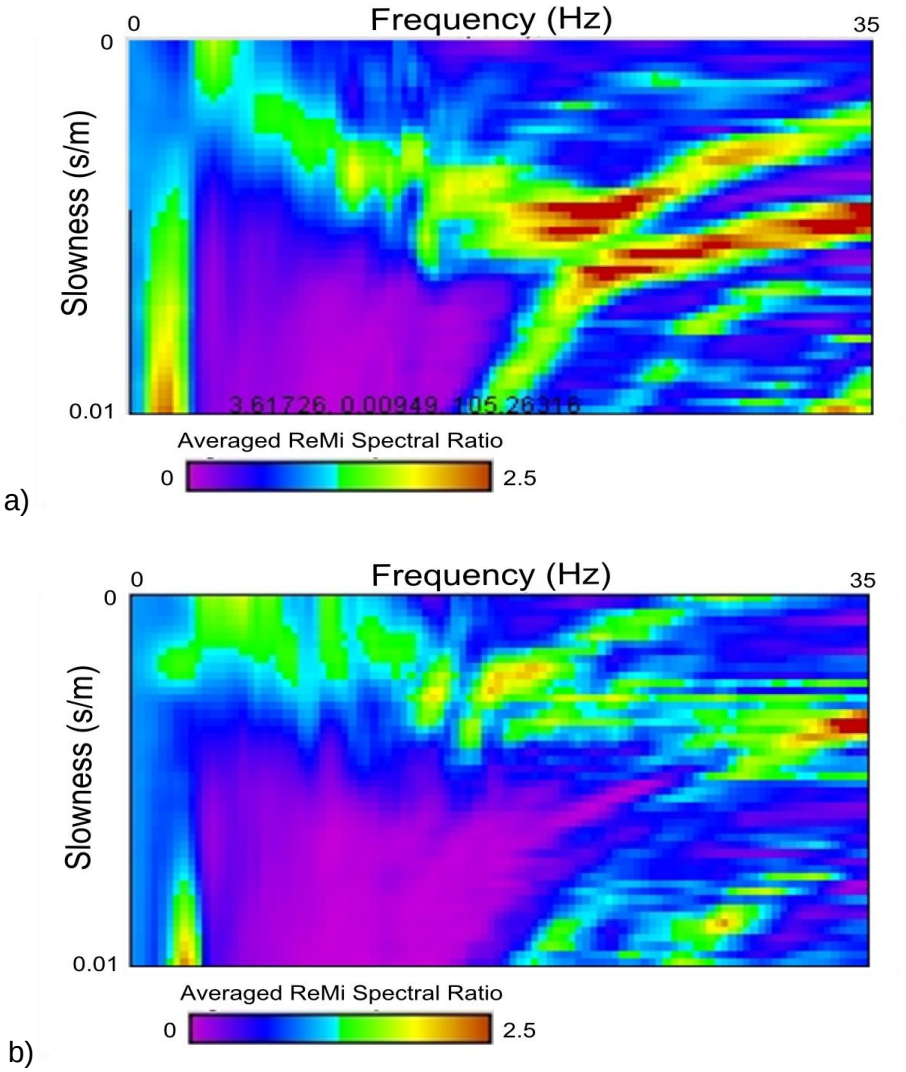

Figure 5.10: CF-2 Recordings with Hammer Blows at (a) 5m and (b) 15m Offsets from the Array Line Perpendicular to the Midpoint

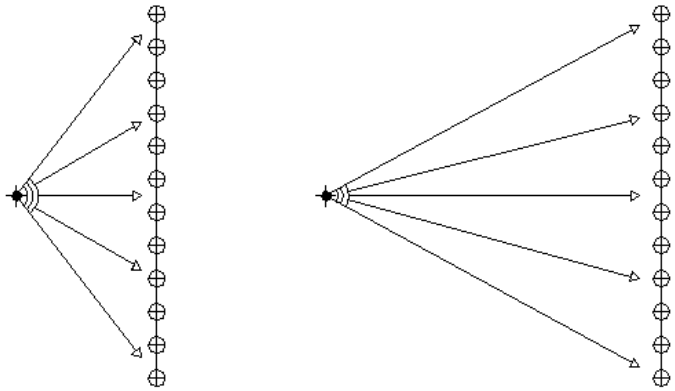

Figure 5.11: Diagram of Wave-Front Propagation from Sources Offset Perpendicular to the Receiver Array

5.1.2: Stenner Creek Arrays

The ReMi data recorded along Stenner creek appears very poor in all records, but combining some passive and active records on array CF-4 generates the plot shown in Figure 5.12. The results from array CF-3 are unusable, and there are a number of issues why this may be the case. The possible causes are discussed in section 5.1.3, but it should be noted that arrays CF-3 and CF-4 were expected to provide better dispersion trends given the perpendicular orientation of the lines to Highland Road. The road should be providing the most energy of any local sources, and is off-end of the array, which is ideal for defining the lower bound of the dispersion trend. The picks from CF-4 were fit to a stiffness profile, and the results are discussed in comparison with other available data in section 5.3.1.

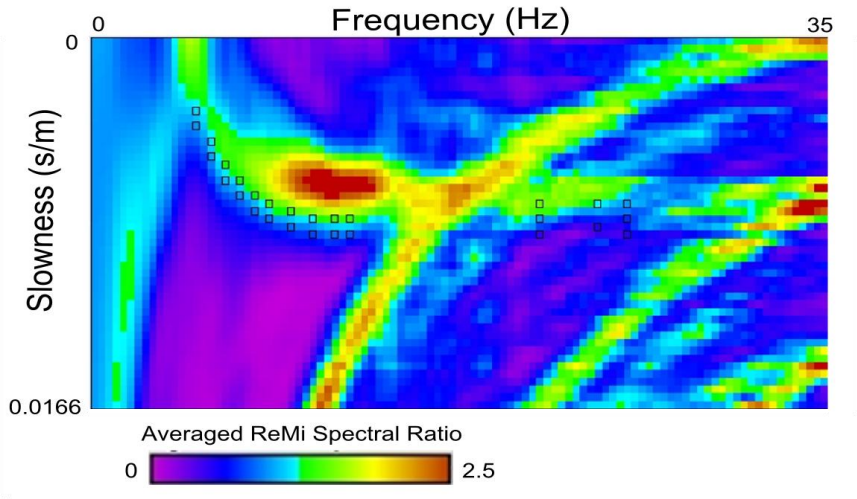

Figure 5.12: CF-4 p-f Spectral Plot with Picks

5.1.3: Quality and Uncertainty of Measurements

The p-f plots resulting from any ambient recordings showed very poorly lit spectral power ratios in all of the Crops Field C-31 arrays. CF-3 in particular was uninterpretable. One of the primary advantages to the ReMi method as presented by Louie (2001) is in its ability to use only ambient signal to develop good results. With that said, adding an active source off end of the array does not require much additional work. However, with the shortage of active records available in this study it is difficult to evaluate the bulk uncertainty of the active method.

One point observable with the available data was that at times even active off-end hammer blows produced little to no improvement. Figure 5.13 illustrates the data obtained by employing the hammer and steel plate source off the opposite end of the array from that shown in Figure 5.8. The results obtained are dramatically different, and in this case provide only a minor improvement in the upper range frequencies over the ambient data shown in Figure 5.7. The lower frequency range appears worse due to the

"wash out" caused by the extreme peaks found in the 25-35Hz range. This observation brings about questions as to the reliability from trial to trial of active source records.

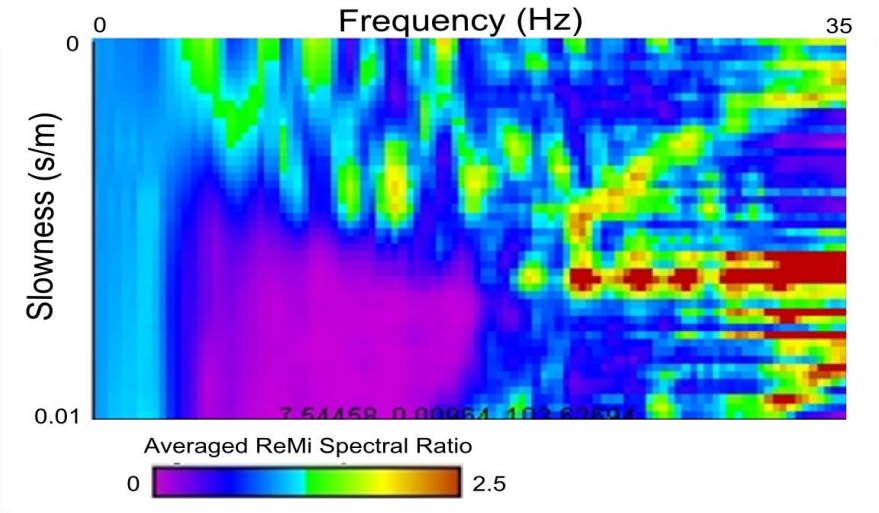

Figure 5.13: CF-2 Recording with Hammer Blows on a Steel Plate Off-End of the Array Symmetrically Opposite to the Data Shown in Figure 5.7

With geophysical testing, and especially the ReMi method, there are such a multitude of uncontrolled variables that it is impossible to make definite conclusions regarding the cause of the data anomalies. The remainder of this section will attempt to highlight some possibilities.

The problems encountered with arrays CF-1 and CF-2 may possibly be attributed to the presence of some man-made subsurface structure, or more likely, the presence of buried utility lines. The amplitude plot of the twelve traces of CF-2 depicted in Figure 5.14 indicates that some type of interference is especially affecting traces 11 and 12. The seismographs and frequency spectrum plot shown in figures 5.15 and 5.16 seem to support this hypothesis. They clearly show traces 11 and 12 to be much more saturated than the others, although the amplitudes are comparable. This is also the side of the

array the off-end source was located when data in the p-f plot shown in Figure 5.13 was recorded.

The frequency spectrum plot shows a clear difference between channels at the near end of the line and those near this interference. The frequencies above 80Hz show a clearly stronger response with the interfering signal. While this is far higher than is included on the p-f plots, there may also be significant lower frequency wave signals that are not obvious on the frequency spectrum plot, but cause confusion during the data transformation and in the wave signal coherence function. The high frequencies can be filtered out, but the difference in the p-f plots appears negligible. There is evidence in all four of the arrays at this site of some type of subsurface structure or utility interference. Because electrical frequencies would show up around 60Hz and the site is located on an agricultural field, the most likely culprit is the irrigation network.

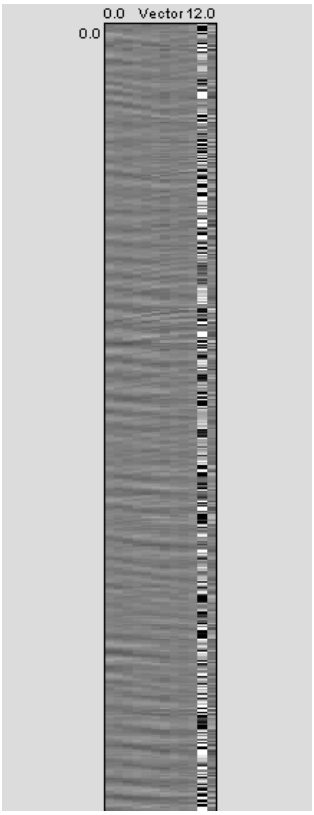

Figure 5.14: Plot of Amplitude Recordings for Array CF-2 Indicating Interference in Channels 11 and 12

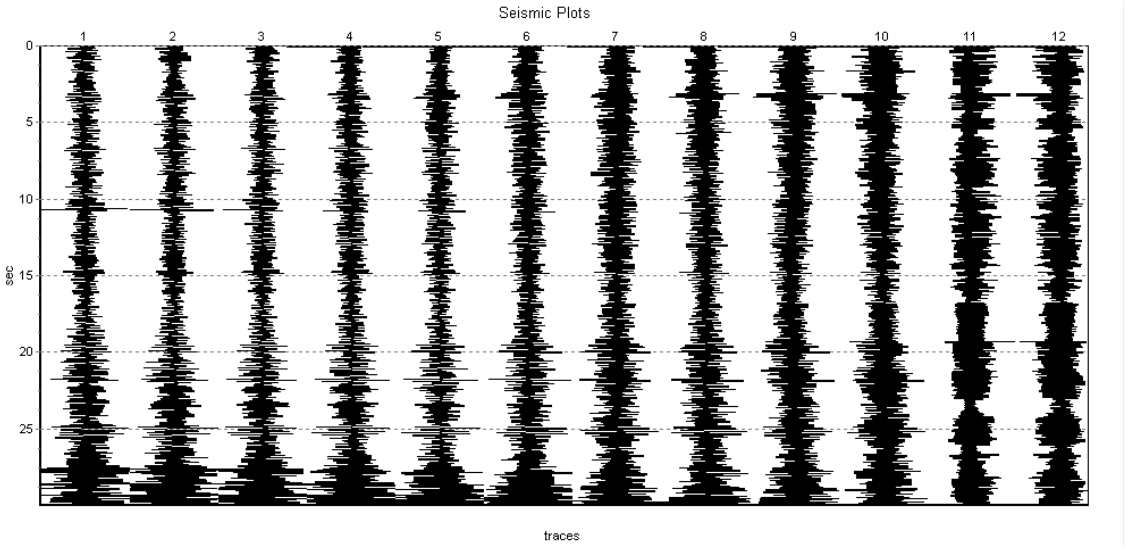

Figure 5.15: Seismograms of Array CF-2 showing Interference Noise of a Possible Utility Line along Highland Road

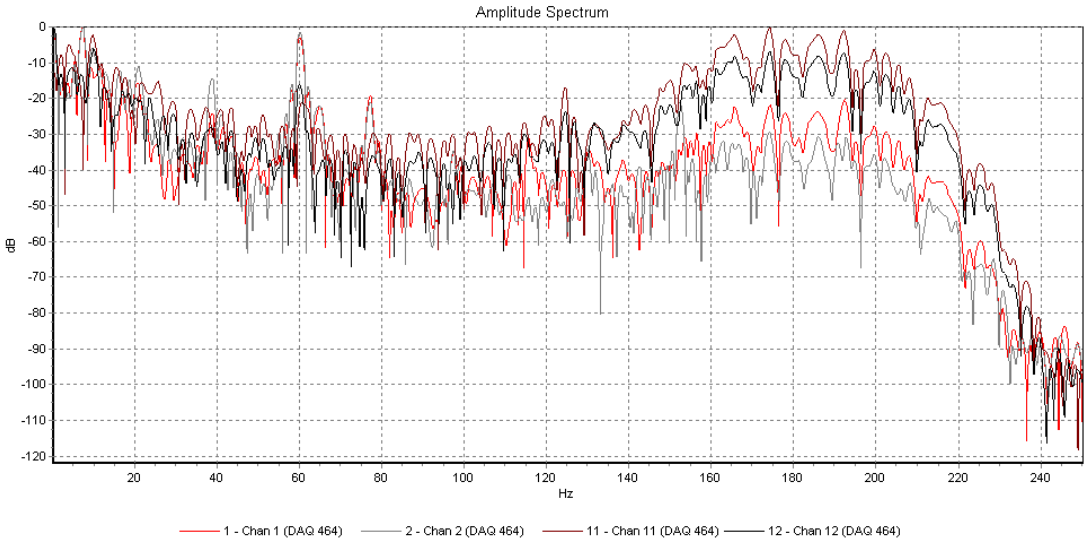

Figure 5.16: Frequency Spectrum Plot of Channels 1,2,11 and 12 for Array CF-2 Showing Differences in High Frequency Amplitudes

In the case of arrays CF-3 and CF-4, the data looked worse than that obtained along Highland Road. This could have also been due to the utility line issue, the proximity of the nearby slope down to Stenner Creek, or a combination of the two. An array placed too closely to a steep slope may experience anomalies in the wave field, especially in the lower frequencies. The break in the traveling medium can cause changes in the way the waves propagate. The longer wavelengths require more space laterally to insure that these effects will not be an issue.

5.2: Seismic Refraction

The seismic refraction data was collected on arrays CF-1, CF-2 and CF-4. The receiver and source diagrams are depicted in Figure 5.17. The hope was to learn the seismic refraction method and also obtain some data that could be compared to the historical SCPT and new ReMi data. Due to a number of reasons discussed in subsequent sections, all goals were not met, but the process did provide a valuable learning experience

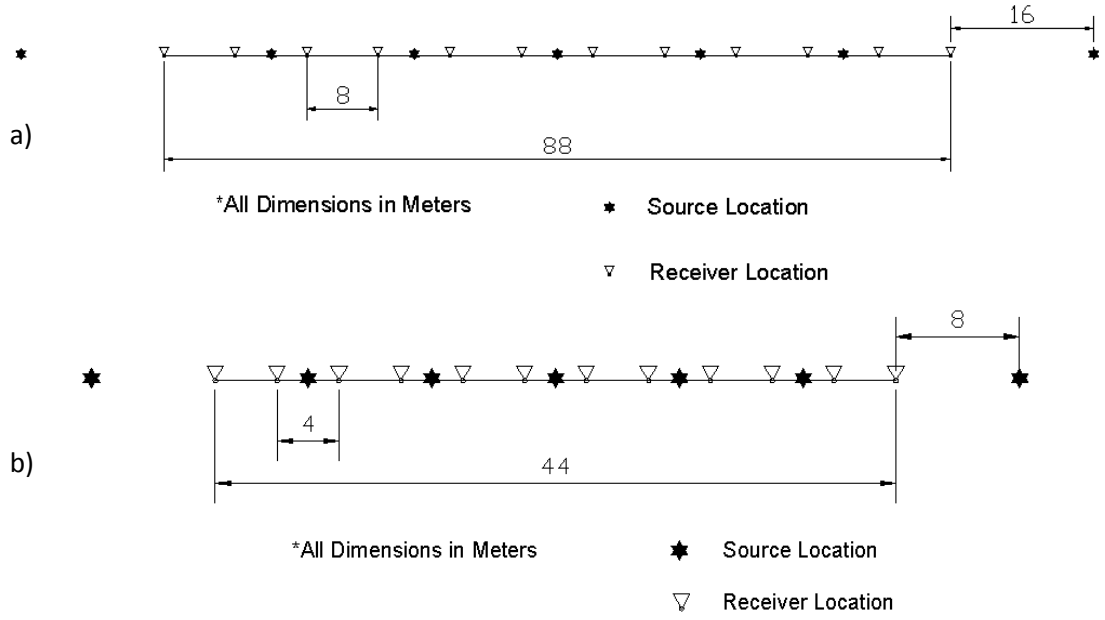

Figure 5.17: Receiver and Source Coordinate Diagrams for (a) CF-1, (b) CF-2 and CF-4

5.2.1: Quality and Uncertainty of Measurements

The seismograms obtained during data collection on all of the Crops Field C-31 arrays turned out to be insufficient to make even approximate first break point picks. The obvious proximity of Highland Road and the same utility interference experienced in the ReMi data caused a very poor signal to noise ratio. The presence of this noise coupled with large signal-receiver offsets did not allow good measurements to be made of first break arrivals. Even using 4m receiver spacing, the larger offsets were enough to attenuate the signal to the point that is appears untraceable on the seismograms. With a larger hammer or an explosive as the signal source the quality of measurements could be greatly improved. Stacking 5-10 records using the 10 lb sledge and the array setups depicted in Figure 5.17 did help improve the data but was not adequate in this case.

5.2.2: Theoretical Travel Times

The modeling module of a software called Geogiga (www.geogiga.com) is capable of providing theoretical travel time curves and seismograms for a given array geometry and soil stiffness profile. This function seemed a useful way to constrain first break picking in the data collected at Crops Field C-31. The input data was obtained through density and shear wave velocity measurements taken during the prior CPT and borehole investigations shown in Figure 5.1. This theoretical data was meant to only be an approximation due to all the uncertainty involved in measurement, interpretation and random error as well as spacial variability. Whether due to these uncertainties or other causes, the theoretical and experimental data are so far from agreement that the initial hope of constraining picks using theoretical data proved impossible. Figures 5.18 and 5.19 illustrate the poor quality of experimental data and the disconnect between the theoretical and experimental first break points.

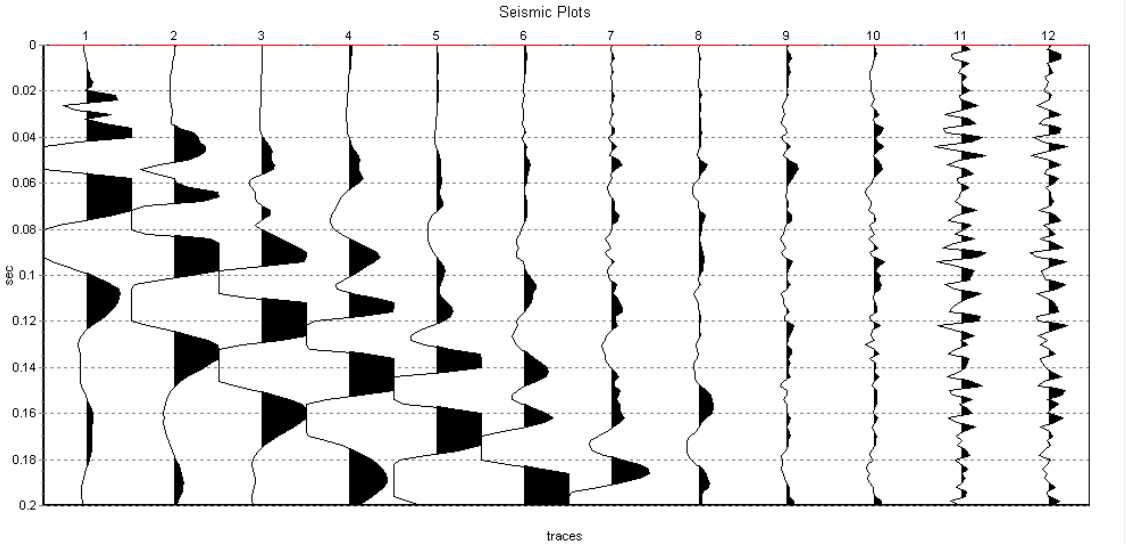

Figure 5.18: Experimental Seismic Refraction Seismograms Obtained with Source 8m Off-End of CF-2

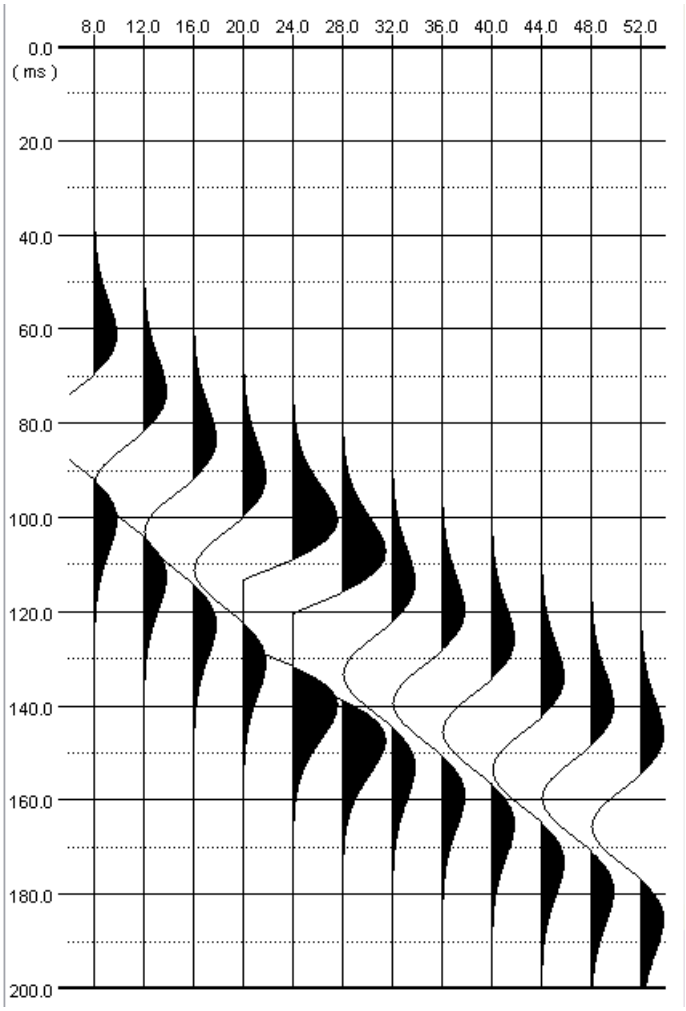

Figure 5.19: Theoretical Seismic Refraction Seismograms for the Area Adjacent to CF-2

It is plain at first glance that the theoretical and experimental data do not agree. The same discrepancy was observed between experimental and theoretical data near Stenner Creek. For this reason no model profiles are included with this work at Crops Field C-31. Fortunately the other sites investigated in this research proved to have much better signal to noise ratios. Despite the lack of results at Crops Field C-31, the lessons learned aided in the subsequent testing at Ingley and Frontera.

5.3: Inter-Method Comparisons

Unfortunately the previous SCPT soundings were only performed to rather shallow depths. Generally when ReMi has been compared with other methods it has been shown to be adequate in its bulk approximations over large depth intervals. This study showed a reasonable fit between the ReMi method and the SCPT data, maximum depths of the CPT data were only about 11m and 18m. Profiles were initially modeled blindly by using an automatic inversion algorithm, followed by manual manipulation to obtain an optimal data fit. Additional models were also fit to the data after examining the SCPT profiles and attempting to match them within the constraints of the dispersion picks. The results shown in Figure 5.20 demonstrate the comparison of these results and indicate that, especially when fitting data to a known profile, the results can be very good.

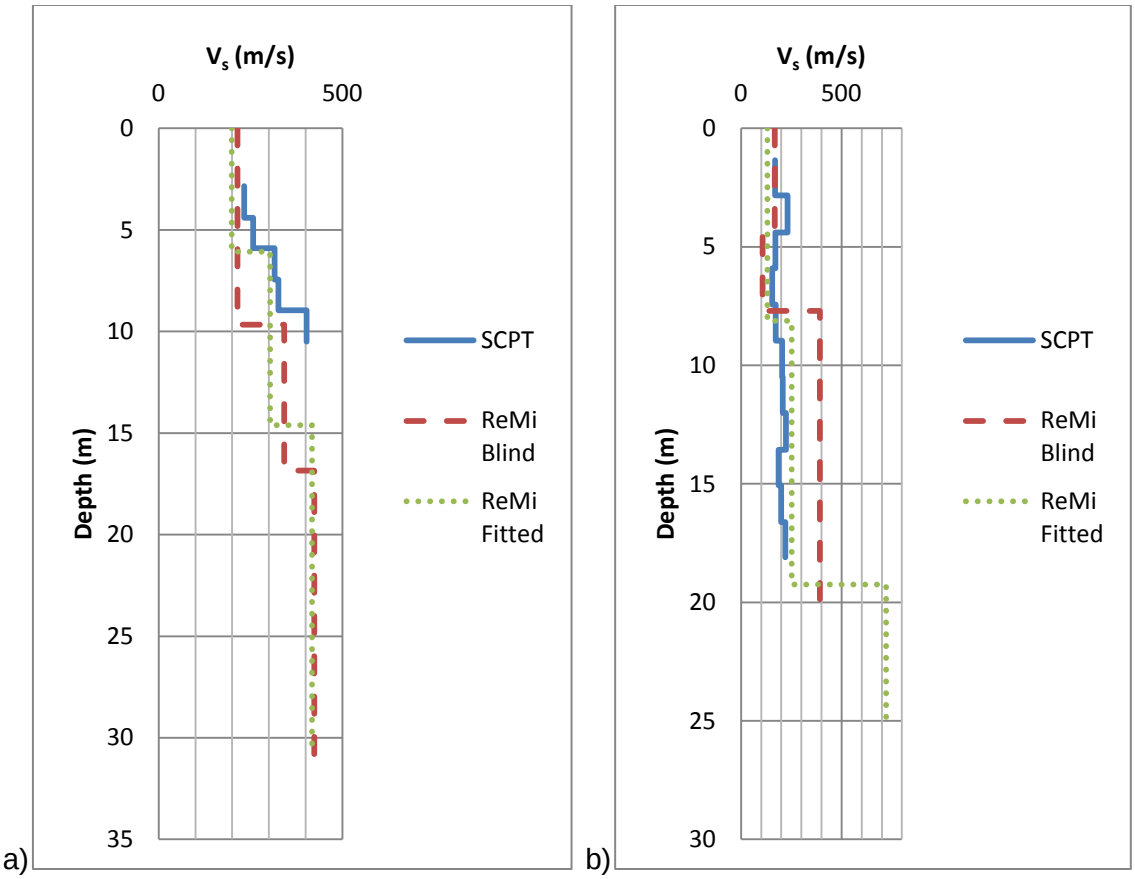

Figure 5.20: Comparisons between SCPT Data and ReMi Profiles Modeled both Blindly and in an Attempt to Match SCPT Data at (a) Highland Road and (b) Stenner Creek

5.4: Summary of Findings

The findings of this chapter explore the precision and variability within the ReMi method and suggest causes for anomalous data collection. Refraction data taken at this site helped provide insight into better field procedures that will enhance data collection. The following list highlights the primary information of interest in this chapter.

- The precision study showed a ReMi COV of 7% for V_{s30}, as much as 16% for the V_s in a given layer, and a maximum of 14% for interface depths. These values diminish with an increase in depth and/or material stiffness.

- The parametric study indicated that off-line energy sources can cause a marked increase in the apparent velocity of the dispersion trend due to the incongruence with the wave field assumptions in the method.
- The ambient records at this site showed very poor definition of the dispersion curve, likely caused by the presence of irregular subsurface structure, incoherent noise produced by utility lines, or physical clipping of the wave field by close proximity slopes.
- Blindly modeled profiles often disagree with those generated through other methods, but when using previous knowledge as a guide very close matches can be obtained.
- Refraction data at this site indicated that, in close proximity to an ambient signal source such as Highland Road, a much larger source is necessary to clearly define first break points.
- Stacking records, while effective in many situations, does not always act as an adequate substitute for a larger energy source in seismic refraction testing.
- Incoherent noise from utility lines or other sources can hamper seismic refraction data collection.
- Theoretical refraction data is very difficult to match to experimental data when the lateral variation in the substrata beneath the array is largely unknown.

Chapter 6: Ingley Site Data Analysis

The goal of the work at the Ingley site was to make geophysical measurements that corroborate the trench data and inferred local geology provided in Lettis and Hall (1994). Although bedrock was never exposed in trench T-2 (Figure 4.4), the primary fault expression was located. This Information suggests that some bedrock offset should be present at depth along the trace. The trench also indicated that the hanging wall consists of older alluvium thrust upon younger alluvium. The location of the trace can thus be deduced by either locating an immediate and drastic shift in bedrock layer depth, or by imaging significant lateral variation in bulk shear wave velocity.

This site allowed space around the scarp expression for laying out linear arrays, both parallel and perpendicular to the feature. All array locations are displayed in Figure 6.1 and the testing schedule is located in Table 4.2. This site proved ideal for generating 2D ReMi profiles by interpolation between 1D sections.

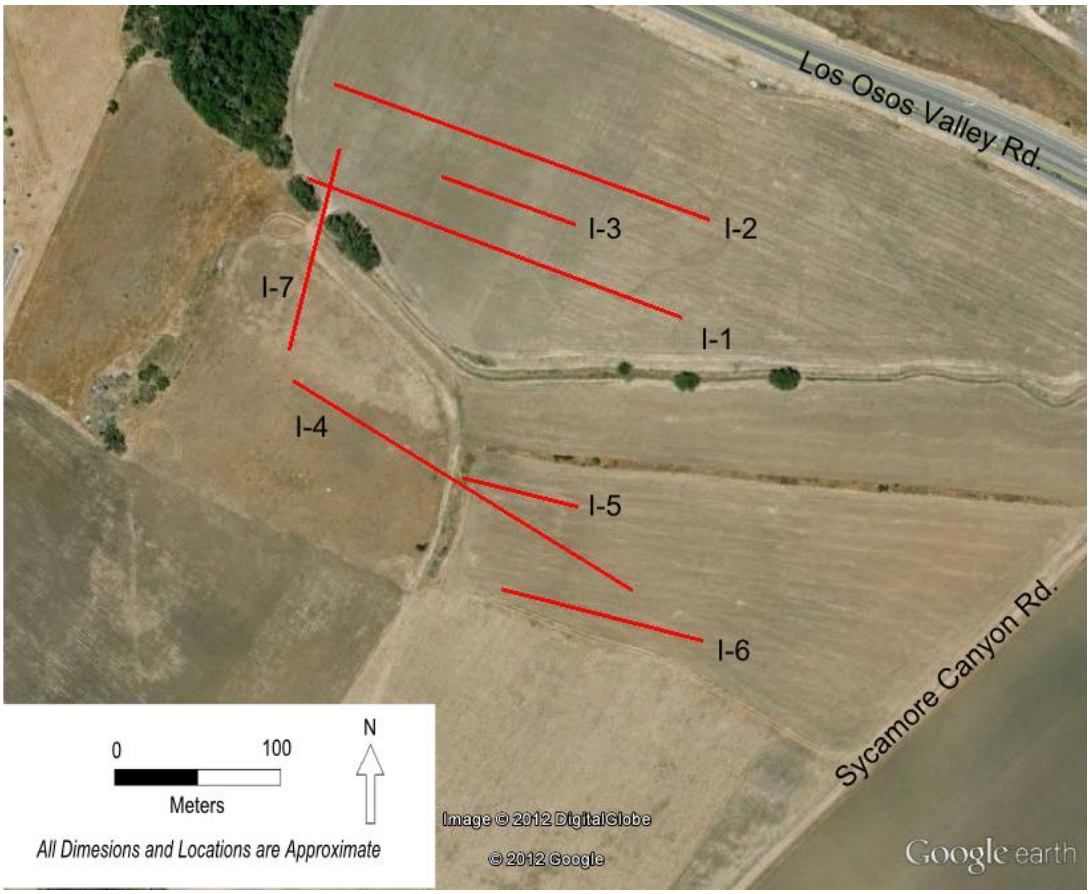

Figure 6.1: Plan of the Ingley Site Showing Sensor Array Placement in proximity to the 6m Scarp and Trench T-2 Discussed in Lettis and Hall (1994)

6.1: Refraction Microtremor

The ReMi data collected at this site consist of results from six arrays parallel to the scarp expression and perpendicular to trench T-2 of Lettis and Hall (1994). Three of these arrays are located NE of the scarp on the inferred footwall. The remaining arrays were placed on the inferred hanging wall. Space SW of the scarp on the hanging wall was limited by agricultural activities. This Section concentrates on interpretation of the p-f spectral ratio plots, 1D forward modeling and 2D assembled cross-sections.

Both this chapter and chapter 7 discuss the effects of vibrations caused unintentionally by the field team and refer to this as a pseudo-active signal source.

Because the general location and type of source are known it is not appropriate to refer to this energy as a passive signal (C. Wood, personal communication, October 5, 2012). At the same time, these vibrations are not consistent with what is typically referred to as an active signal because they were not intentionally generated at a measured location with known frequency content.

6.1.1: Lower Arrays NE of Ingley Trench T-2

These arrays sit below the scarp expression on what appears to be a floodplain. The elevation is approximately the same as that of the nearby wetlands just across Los Osos Valley Road. Agricultural soil tilling has also made the topsoil in this location very loose. The nearby road should act as a good signal source for testing at this entire site.

6.1.1.1: Individual p-f Spectral Ratio Plots and Picks

The three arrays produced similar p-f plots, but the definition quality of the lower bound varies greatly between arrays. In general, well defined or not, the three arrays agree well in the visible dispersion trend. Note that the slowness scale varies between p-f plots in this chapter in order to obtain the best possible definition of the lower bound spectral ratio trend.

Ambient recordings at the Ingley site contained the same frequency range deficiencies that were observed in Chapter 5. Figure 6.2 displays the stacked ambient recordings taken at I-1 demonstrating the lack of response above approximately 10Hz. By contrast, even a small amount of pseudo-active energy produced the results shown in Figure 6.3. Initially designated as an entirely passive recording, closer inspection of the seismographs in Figure 6.4 revealed some unintentionally produced vibrations originating at the array midpoint. This was the location of the data acquisition system,

which indicates that it was likely produced by incidental footfalls of the research team. Rayleigh waves produced at the array midpoint in this manner would travel along the array azimuth helping to strengthen the spectral ratios at the true phase velocity boundary. It is difficult to say how the SeisOpt software handles this type of data given the abnormalities in the coherence of the wave signal. Normally, a signal is tracked from geophone to geophone through the array to determine its coherence, but this situation would indicate two different coherent waves traveling in opposite directions and originating spontaneously. One of the assumptions of the ReMi method is that the wave signals are produced far enough away to arrive approximately as a plane wave, approaching each receiver on the same azimuth.

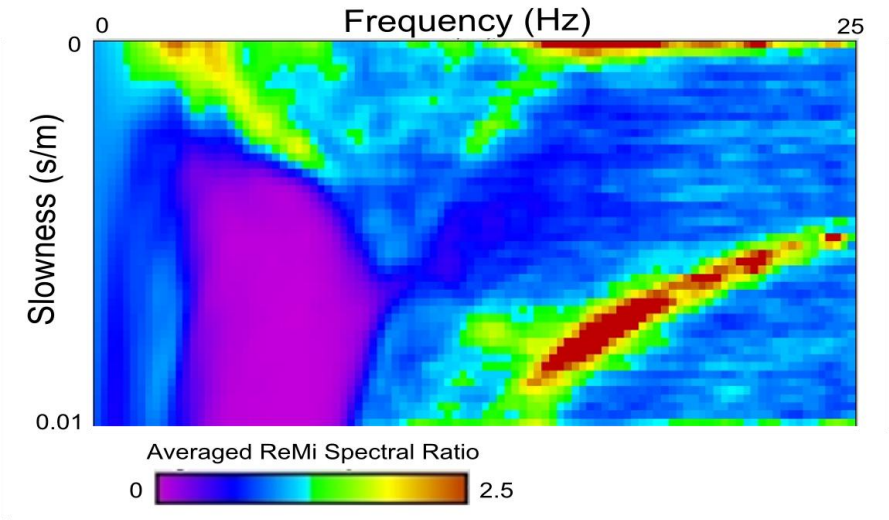

Figure 6.2: p-f Spectral Ratio Plot of Ambient Signal Record for I-1

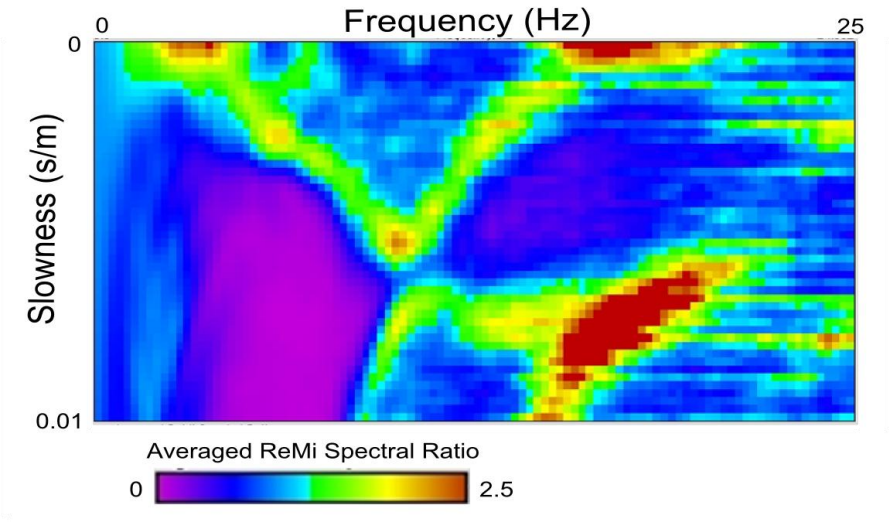

Figure 6.3: p-f Spectral Ratio Plot of Unintentional Mid-Array Vibrations Record for I-1

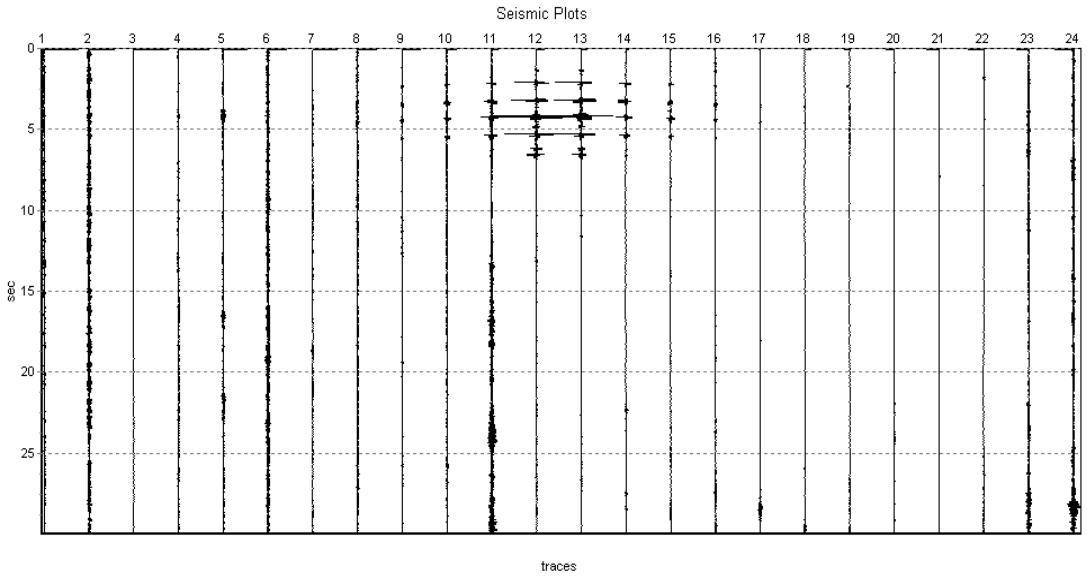

Figure 6.4: Seismographs of Unintentional Mid-Array Vibrations Record for I-1

Despite the uncertainty involved in allowing the power spectrum to be dominated by an abnormal wave field, the resulting p-f plot does not indicate any gross anomalies. In fact, the added energy seems to perfectly fill the frequency gap in Figure 6.2 along the apparent lower bound that was previously poorly defined. The data presented in Figure 6.5 also agrees with this lower bound phase velocity trend. This p-f plot was produced

by combining records taken while signal was actively induced by intentionally walking up and down the array. The dispersion curve response is strongest in this plot, but to develop a more robust p-f plot (one that is representative of more records) the better defined passive records were stacked in with those shown in Figure 6.5. Figure 6.7 displays the p-f plot and picks obtained from this stacking.

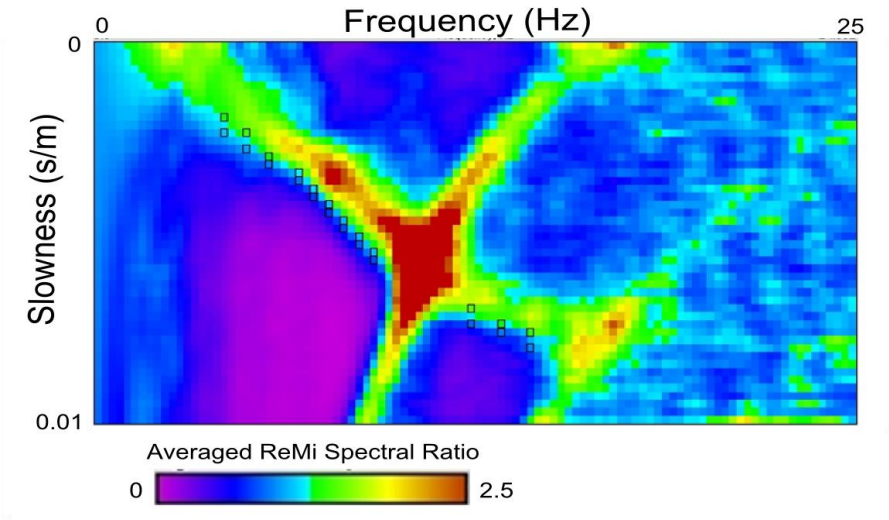

Figure 6.5: p-f Spectral Ratio Plot with Picks for Walking Record of I-1

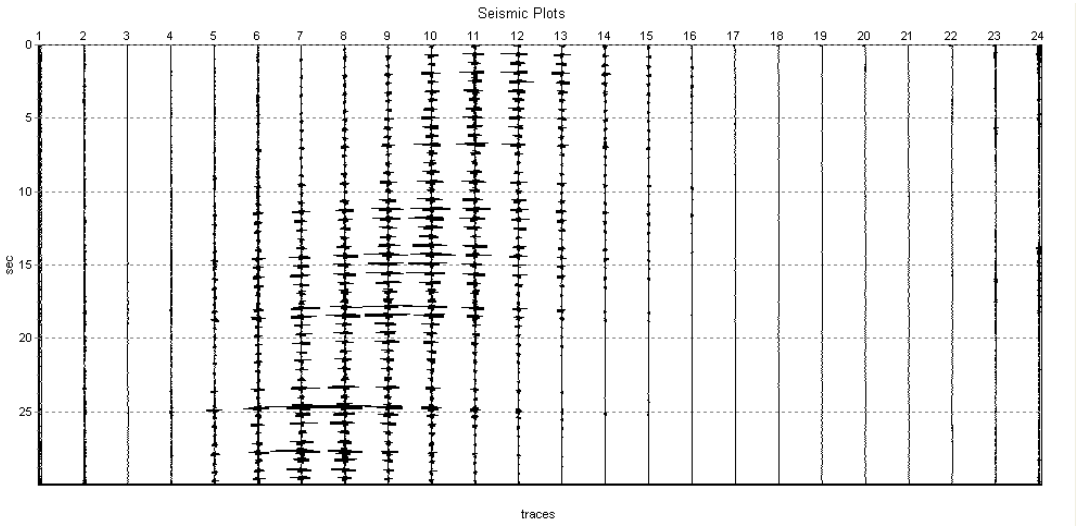

Figure 6.6: Seismographs of a Walking Record for I-1

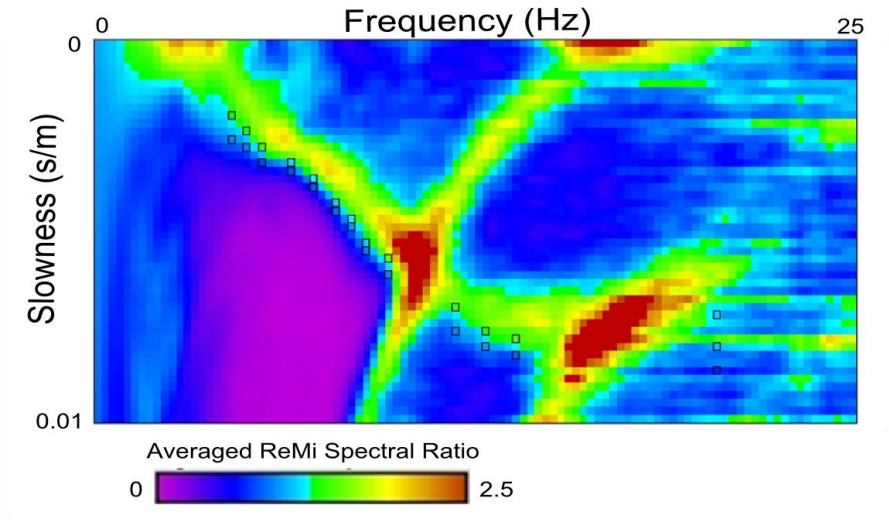

Figure 6.7: p-f Spectral Ratio Plot with Picks for Combined Active and Passive Records of I-1

The plots in Figures 6.5 and 6.7 are very similar, but with minor variation around 13Hz and slightly better high frequency definition in the combined plot. When all picks are plotted simultaneously, as demonstrated in Figure 6.8, the results are revealed to be very consistent with one another.

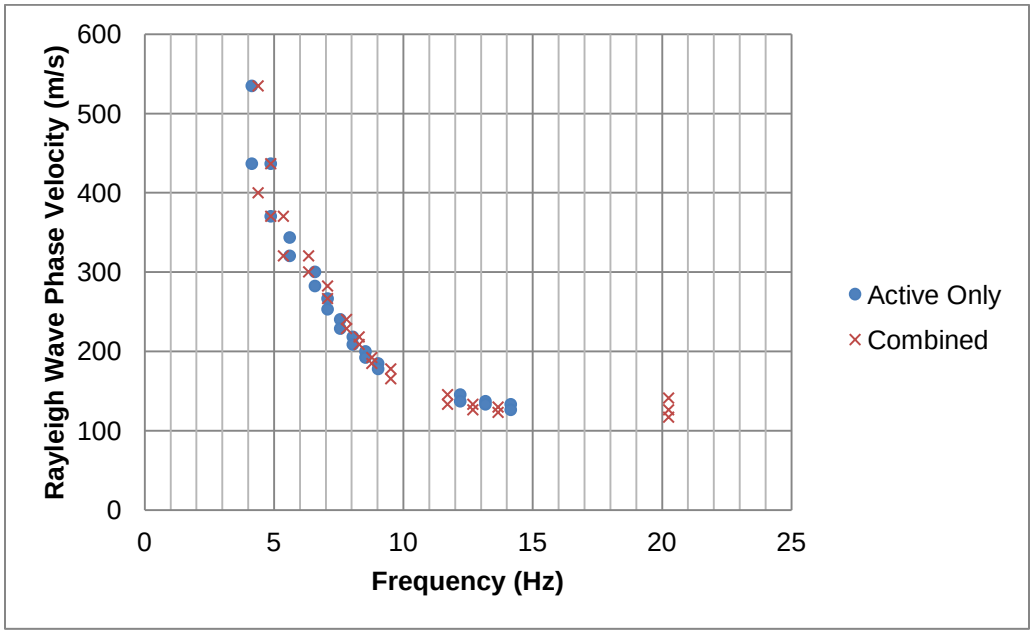

Figure 6.8: Scatter of Picks from the Active and Combined Active/Passive p-f Plots

Arrays I-2 and I-3 required the same stacking of active and passive records to adequately define the dispersion curve lower bound. Unfortunately the data collected at I-2 and plotted in Figure 6.9 contains numerous gaps in the trend. The data collected at I-3 (Figure 6.10) exhibited a better defined dispersion, but this was only achieved by reducing receiver spacing from 8m to 6m. The smaller spacing and shorter array may have helped enhance the data by reducing lateral variation effects. A 24 receiver array at 8m spacing spans 184m. This offset is easily large enough to introduce significant lateral variation beneath the array that could cause disagreement over the Rayleigh wave dispersion trend. If one end of the array indicates a different dispersion trend than the opposite end, it may manifest itself in the p-f plots as a more widely smeared region of spectral ratio peaks. This in turn could increase the average spectral power that the plot is normalized by, and thus cause both dispersion trends to be poorly defined.

Another possible cause of the poor data at arrays I-2 and I-3 may be the proximity of the road. The data collected at these three arrays looked significantly better at each offset away from the road. I-2 showed the worst results and was the nearest to the road. Again, given the number of uncontrolled variables, it is impossible to attribute the symptoms to a specific cause with any certainty. The most likely and obvious cause in this case is that the body waves (refracted P and S-waves) produced by the road may be interfering with the Rayleigh wave analysis. At further offsets away from the road these body waves would attenuate rapidly, hence the improvement in data quality with distance from the road. This effect may not be noticeable at a site with other significant signal sources that lie far enough away as to avoid body wave interference, but at a site such as Ingley this is not the case. If the other ambient vibrations are significantly lower in amplitude than the close proximity road vibrations, they will simply be “washed out” of the spectral ratio plot.

Based on the results found here, placing an array in close proximity to a large signal source with no other major energy sources in the area can produce poor results. This could be easily investigated by testing more arrays at varying offsets in proximity to a road with no other significant signal sources.

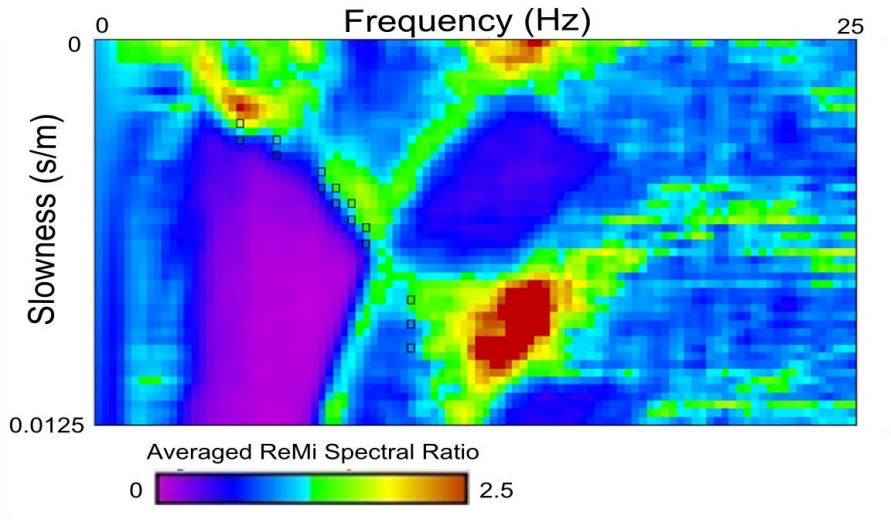

Figure 6.9: p-f Spectral Ratio Plot with Picks for I-2

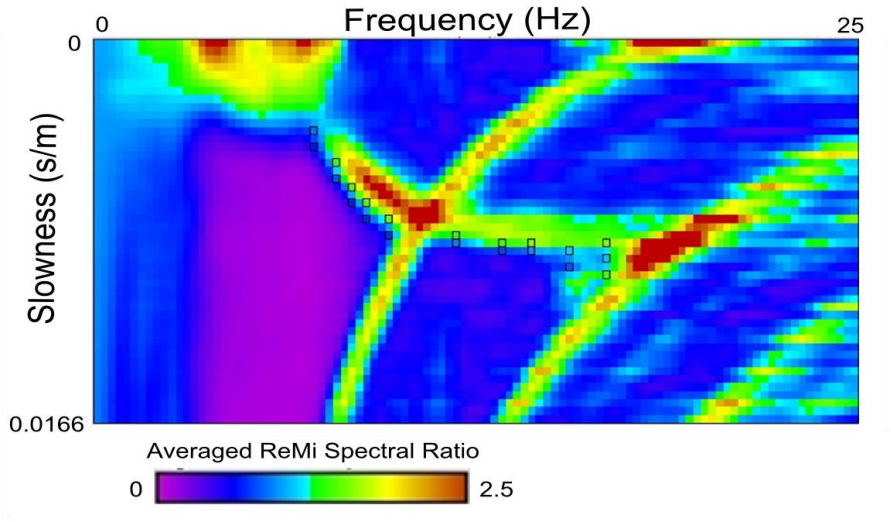

Figure 6.10: p-f Spectral Ratio Plot with Picks for I-3

6.1.1.2: Forward Modeling and Combined 2D Profiles

As previously emphasized, the forward modeling process is highly subjective and relies heavily upon user experience and knowledge. Because of this, the trends shown in assembled 2D profiles are highly uncertain. The three 1D profiles were modeled first by setting the V_s of the bottom layer to 600m/s. This is a reasonable estimate for weathered bedrock and provided a good fit to the experimental data. The upper layer velocities and boundaries are then more constrained. The 2D profile in Figure 6.11 results from assembling the three profiles modeled in this manner.

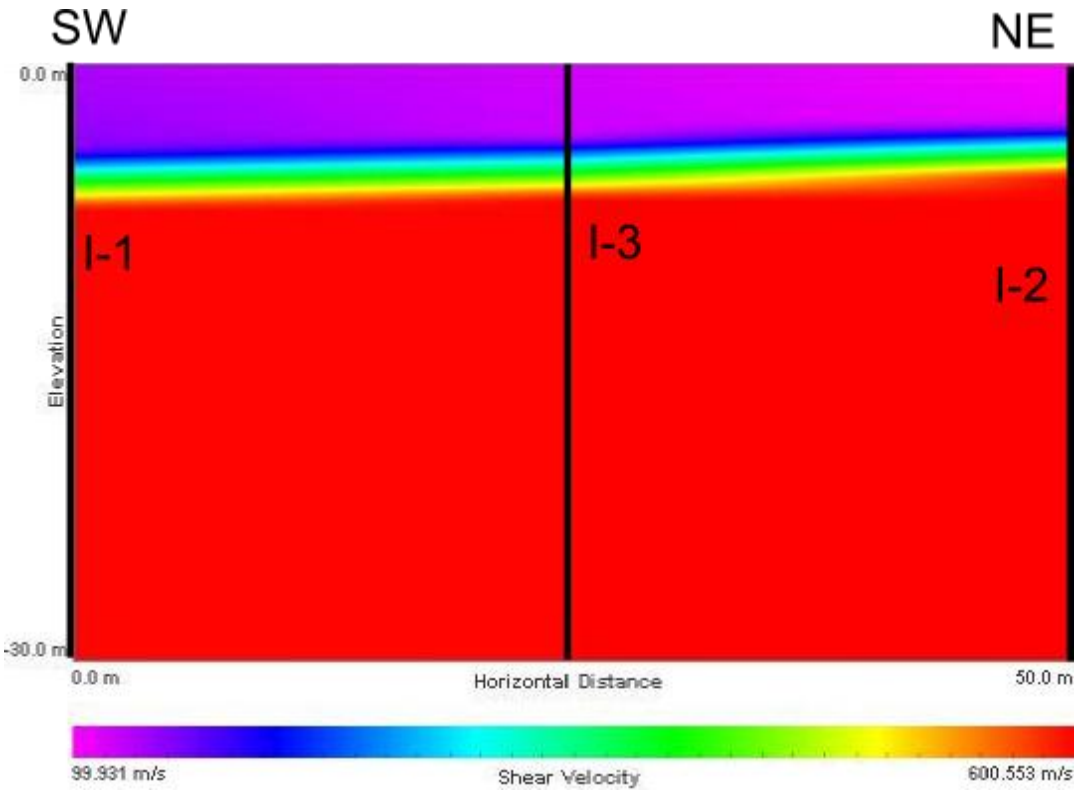

Figure 6.11: Assembled 2D Profile with Bottom Layer V_s = 600m/s

The layer dip direction indicated by the 2D profile in Figure 6.11 is opposite from what is shown in trench T-2 (Figure 4.4), and seems unlikely to be accurate based upon the observed geomorphology. Despite the skepticism, it is not impossible that the beds

do dip downwards toward the fault trace as a result of some subsidence of the footwall under the hanging wall. To illustrate the degree of uncertainty involved in the ReMi modeling process, the 2D profile in Figure 6.12 provided an equally good fit to the dispersion pick data. This profile was created by setting the bottom layer depth to 700m/s, and by attempting to keep upper layer velocities close to equal in all three models. After only allowing layer boundaries to move, a model such as the one shown in Figure 6.13 fit well to each pick set. This is the model that is used in later comparisons through this chapter because the dip direction of the deeper layer in this trial seems more in agreement with trench T-2 (Figure 4.4).

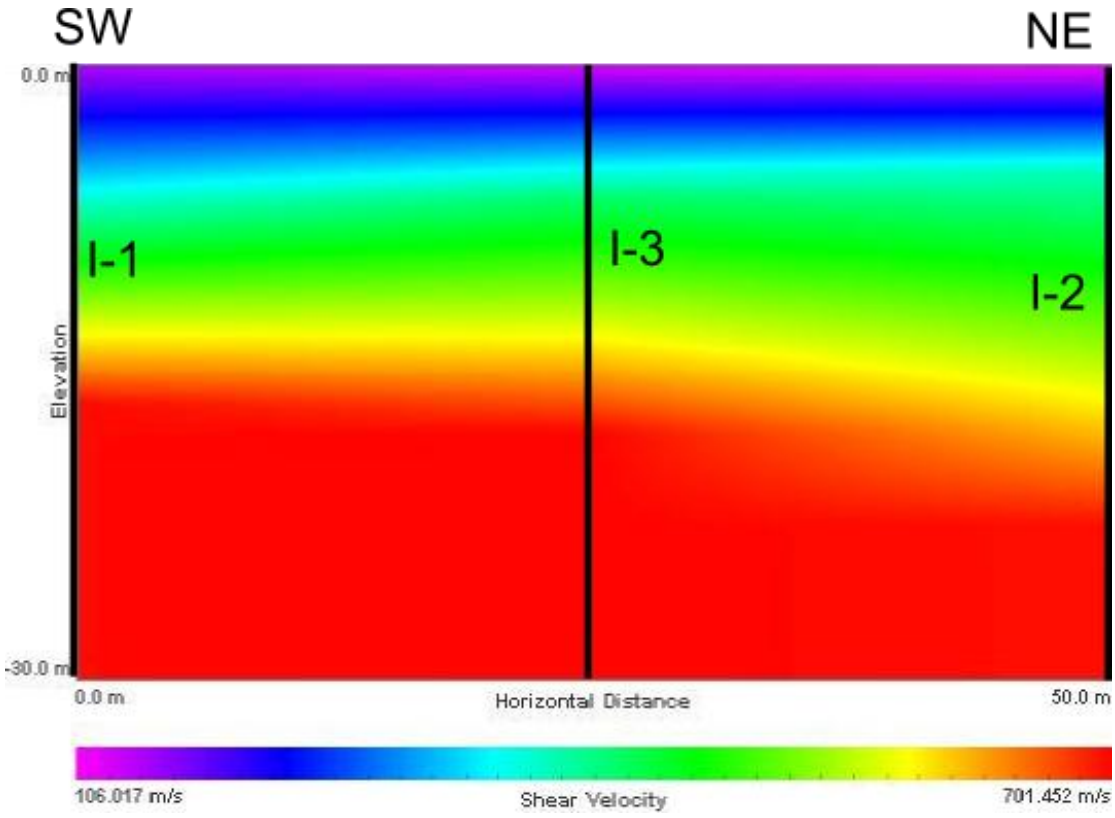

Figure 6.12: Assembled 2D Profile with Bottom Layer V_s = 700m/s and Fit to Inferred Geology in Lettis and Hall (1994)

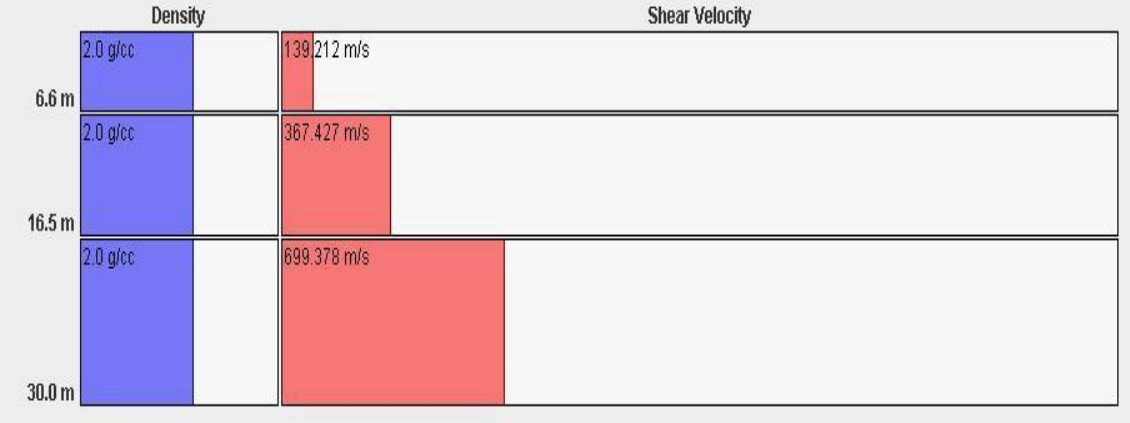

Figure 6.13: Model Profile for I-1 Fit with Bottom Layer V_s = 700m/s

6.1.2: Upper Arrays on Scarp Expression near Ingley Trench T-2

The upper Ingley arrays are located directly on the scarp expression or hanging wall and just at the top of slope. Elevation changes along array I-4 prompted an investigation into its effect on the p-f plots. This section also attempts to explain why arrays I-5 and I-6 both showed dual dispersion-like trends in their p-f spectral ratio plots. Finally, the 1D model profiles are assembled into a 2D profile.

6.1.2.1: Array I-4 Slope Sensitivity Study

Array I-4 was situated across an erosion channel in the scarp expression. Because of this, the midpoint of the array was located more than 5m below the highest elevation receiver. Figure 6.14 provides a diagram of the array setup and the locations of all receivers in vertical relation to one another. From the left end of the profile to the low point there is a 5.9m elevation change over 88m. This equates to a 6.7% elevation change, but there are locations where the grade is even steeper. Optim's Refraction Microtremor Field Tutorial (2006) indicates that up to 5% deviation from linear should not affect the method's proclaimed 15% accuracy window. This guideline is unspecific as to

other geometric possibilities, such as the lower midpoint in array I-4. Although not outside the 5% threshold for the entire array length, portions of the array change at a steeper grade, indicating that a geometry correction may be necessary in the analysis process.

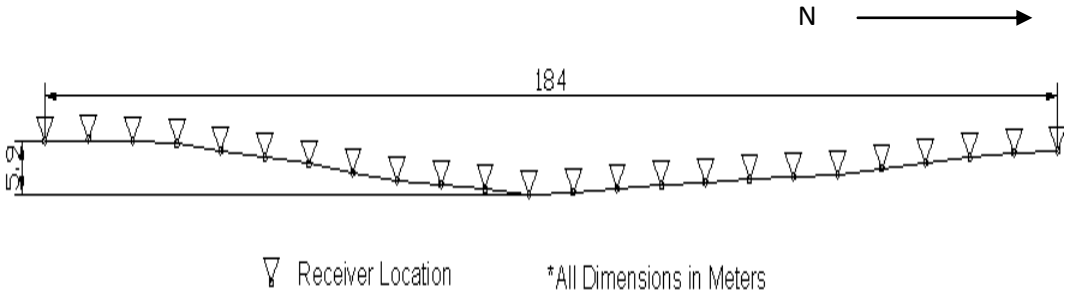

Figure 6.14: Array Elevation Profile for I-4 (no horizontal exaggeration)

Despite lacking any active source records for array I-4, the stacked ambient p-f plots produced the dispersion trend displayed in Figure 6.15. Both the elevation corrected and uncorrected plots are shown and appear to be very close to identical.

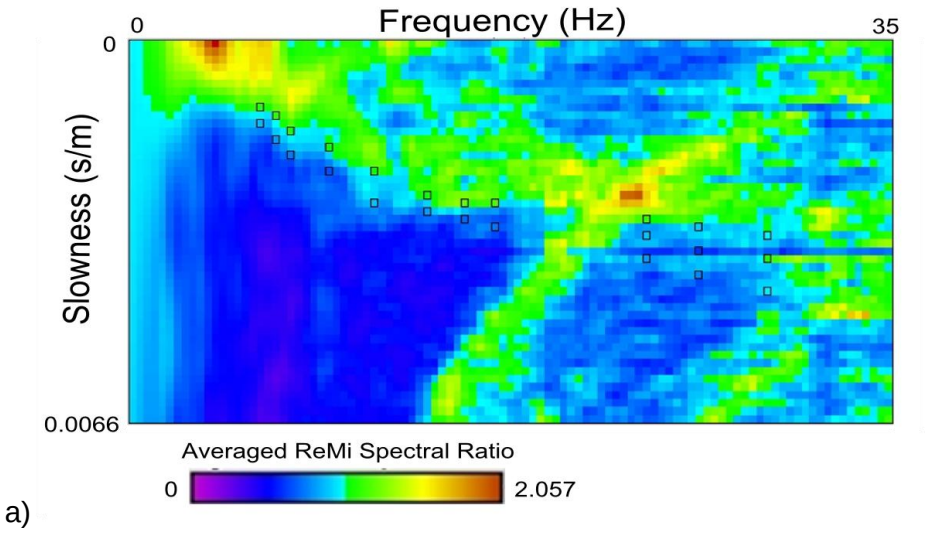

a)

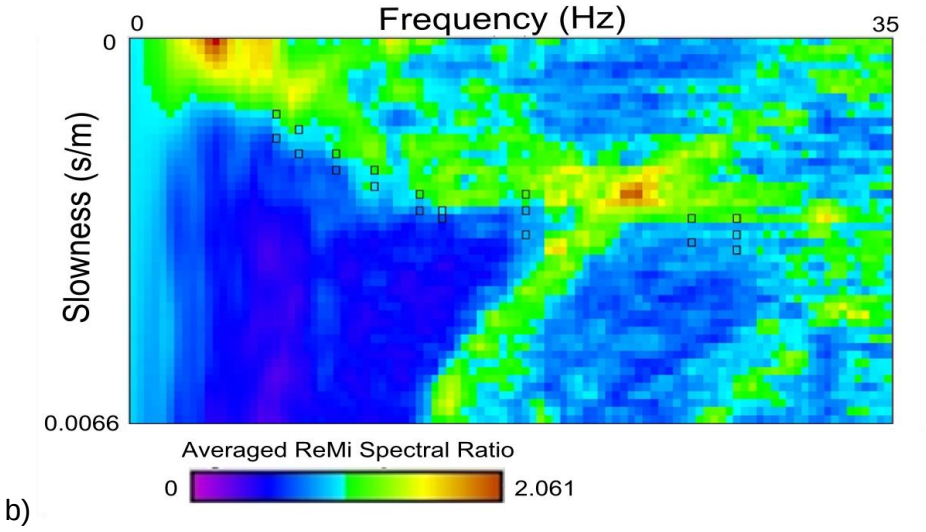

b)

Figure 6.15: Spectral Ratio p-f Plot of I-4 Data a) with Corrected Receiver Coordinates and b) without Corrected Receiver Coordinates

To directly compare them, a set of picks was chosen for each case, and then simultaneously graphed in the scatter plot shown in Figure 6.16. The picks vary to some degree, but this is more a result of decisions made during the picking process than a significant difference in the p-f plots. In this case, the subjectivity involved in the picking process is a greater source of uncertainty than the effects of the elevation change.

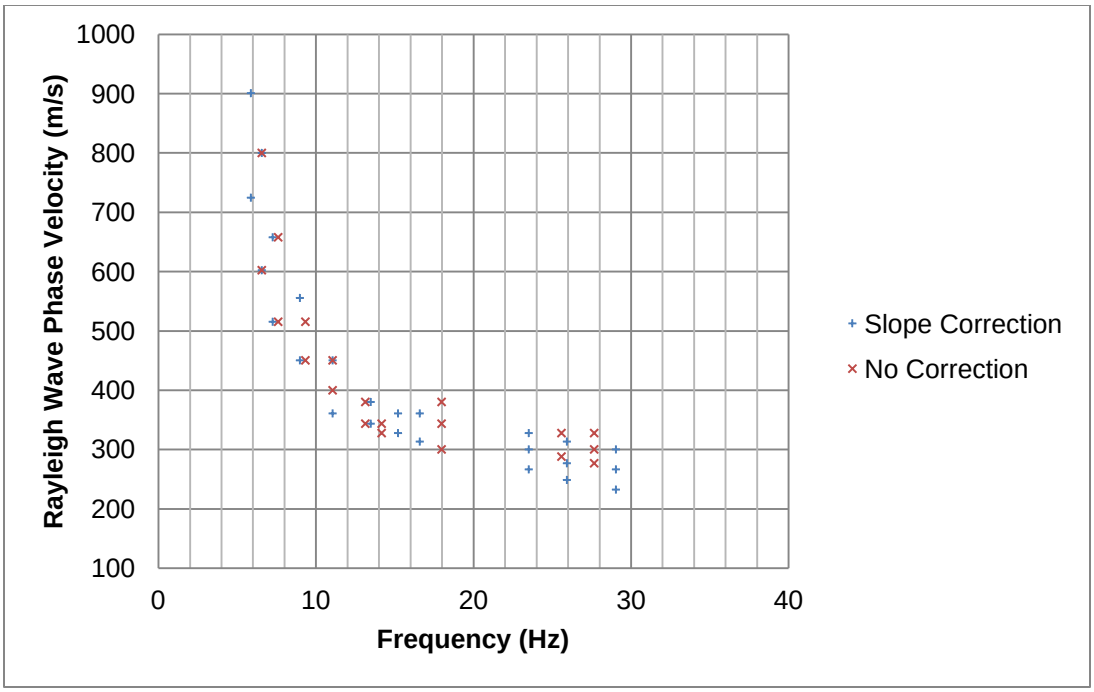

Figure 6.16: Scatter Plot of Picks from Slope Corrected and Non-Corrected p-f Plots

6.1.2.2: Multiple Trend Effects in Arrays I-5 and I-6

Arrays I-5 and I-6 displayed multiple trends that fit the slope one would expect from a Rayleigh wave dispersion curve. Comparison between the p-f plots of the passive data records in Figure 6.17 and the active record in Figure 6.18 indicates that the apparent trend of the passive data may be grossly inaccurate. The active data also shows a separate spectral ratio peak trend above the lower bound that agrees with the passive data. In addition, the passive records vaguely display the same lower bound that is clearly defined in the active plot. The lower trend of the passive data appears to have been "washed out" by the energy in the upper trend, but the boundary is still visible where the spectral ratios go from dark blue to purple. Figure 6.17 illustrates the upper and lower trend picks for the passive data. These picks and those made from the active records are also plotted in Figure 6.19 in order to determine how closely the active trend and lower passive trend agree.

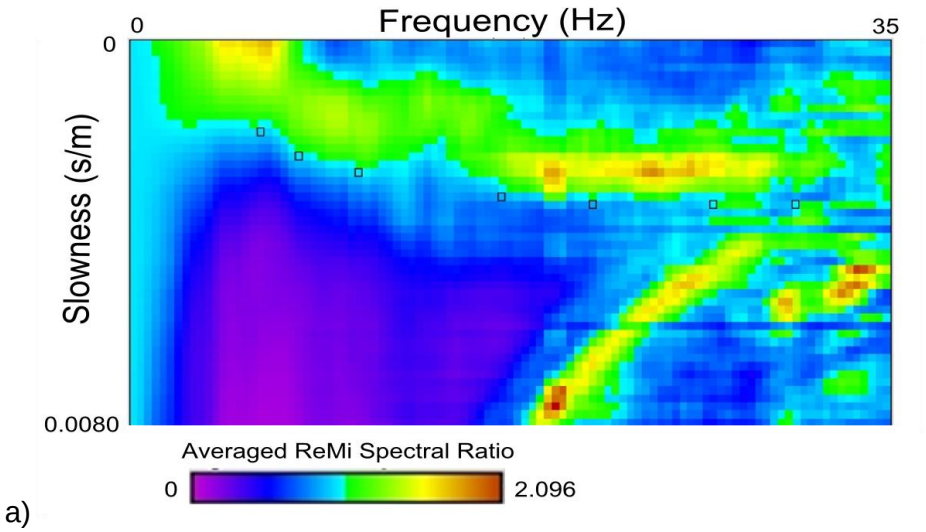

a)

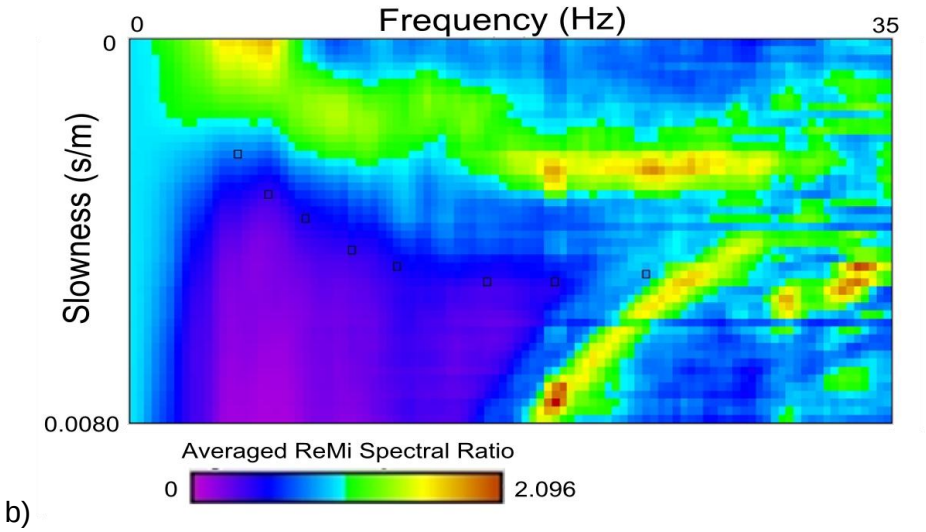

b)

Figure 6.17: Spectral Ratio p-f Plot of (a) Upper Trend and (b) Lower Trend Picks on Passive Records for Array I-5

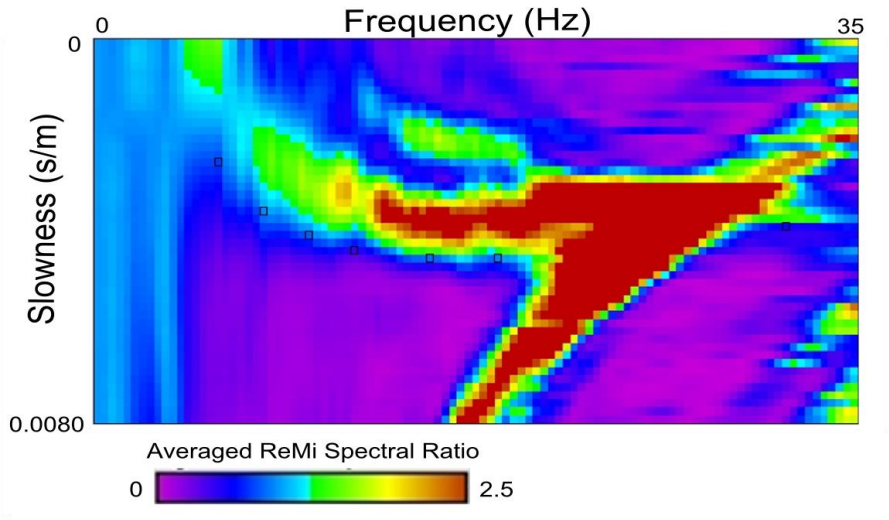

Figure 6.18: Spectral Ratio p-f Plot for Active Record with Picks for Hammer and Plate Blows at Array I-5

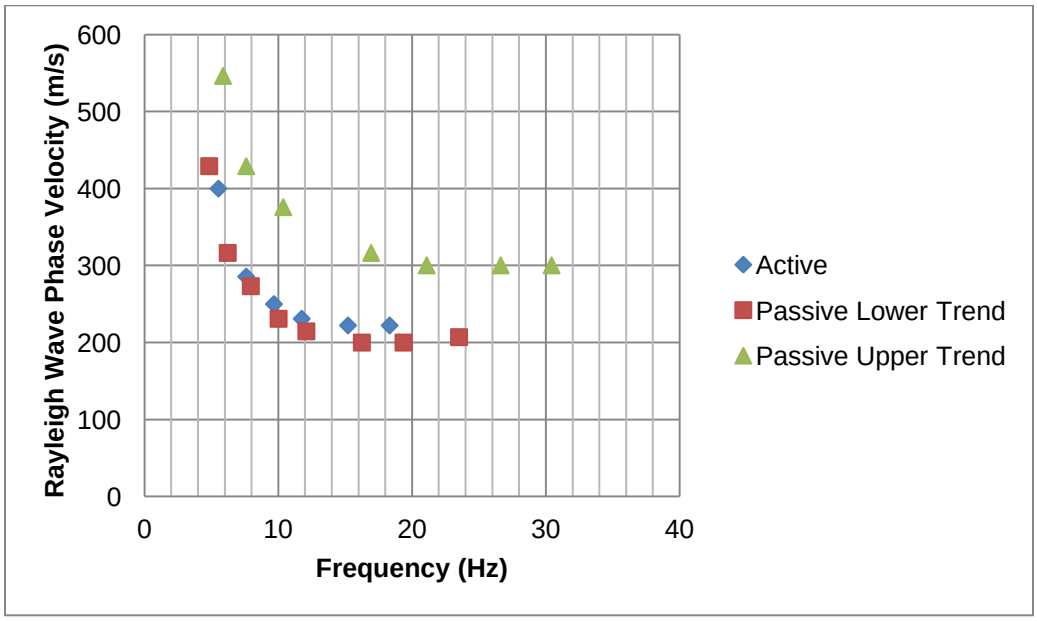

Figure 6.19: Scatter Plot Comparing Upper and Lower Trend Dispersion Picks to Active Picks

In this case, the upper trend of the passive records was likely caused by one of three possibilities. It may simply be a strong higher mode response, although why a higher mode would contain more energy than the fundamental is unclear. Other

possibilities include the presence of an air wave response or sudden and significant lateral variation in the soil strata beneath the array. The slowness range of the upper trend is approximately consistent with the speed of sound, but there remains the question as to where such a wave could have originated. There are no obvious passive sources for an air wave in the vicinity. Sudden and distinct lateral variation in the soil strata may also cause multiple dispersion curves by indicating a strong response along one trend at one end of the array, and another strong response along the other trend on the opposite end of the survey. It is possible that both are represented here. This was the reason for aligning the array parallel to the feature of interest, but it is possible that the geometry of the fault at depth is such that these efforts were unsuccessful. It is impossible to say which of these possibilities, if any, is the culprit, but should the same issue appear repeatedly with near-fault arrays, the lateral variability explanation seems the most viable.

Array I-6 yielded a similar double dispersion trend as shown in Figures 6.20 and 6.21. In this case, stacking the passive records did yield a p-f plot with a clear lower bound trend similar to that obtained by the hammer and plate active data displayed in Figure 6.22. Although the lower trends do seem to agree, the scatter plot in Figure 6.23 of the picks from each case suggests that at lower frequencies the passive records indicate a lower phase velocity, and at middle and upper frequencies the active case shows a lower phase velocity. This is likely because the upper frequency data coming from the sledge hammer has “washed out” a gap in the active record’s low frequencies. In the middle and upper ranges the hammer signal dominates and the lower bound is very tightly defined as opposed to the way it is smeared over a wider slowness range in the passive case.

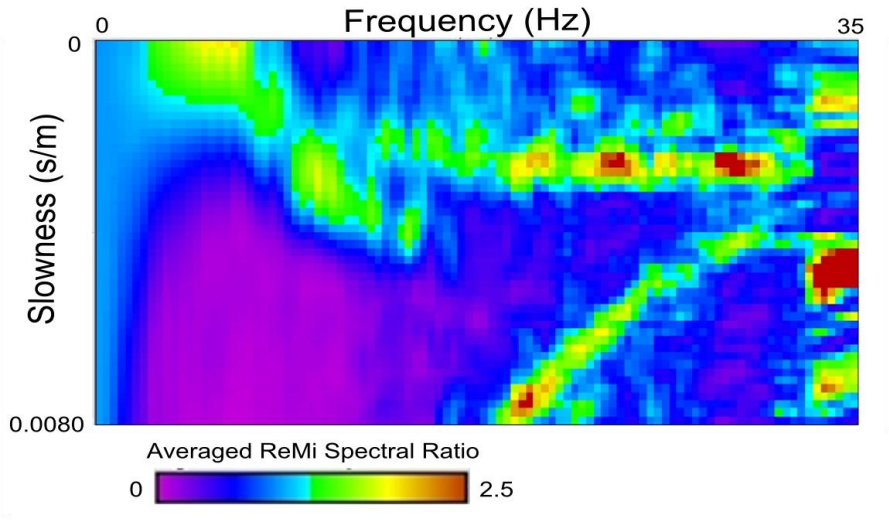

Figure 6.20: Spectral Ratio p-f Plot Showing a Typical Passive Recording at I-6

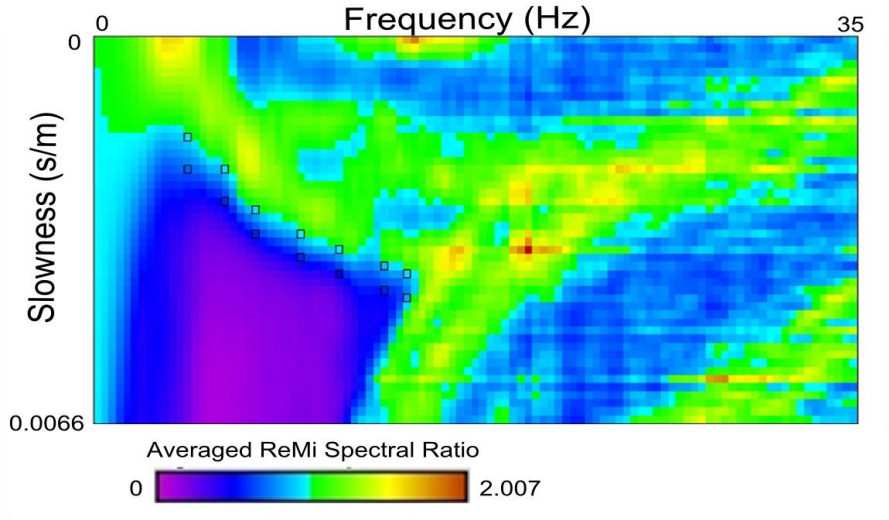

Figure 6.21: Spectral Ratio p-f Plot Showing Stacked Passive Recordings and Picks at I-6

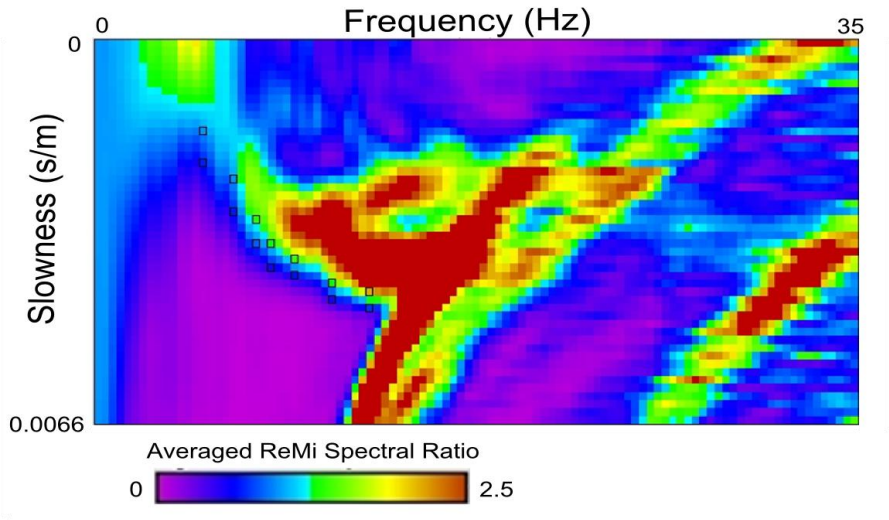

Figure 6.22: Spectral Ratio p-f Plot Showing Stacked Active Records and Picks at I-6

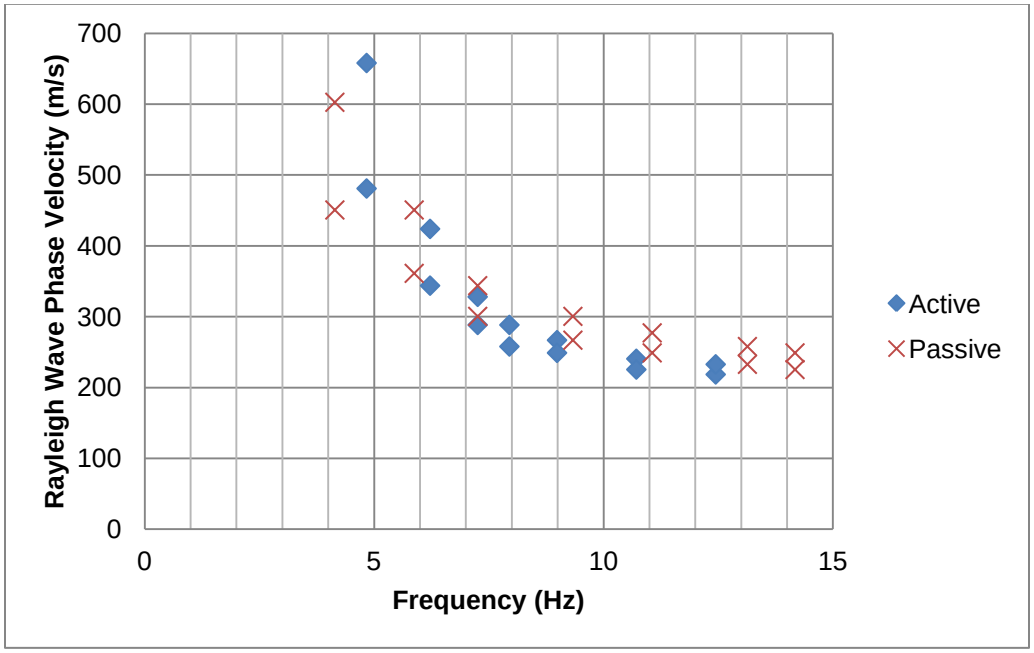

Figure 6.23: Scatter Plot of Active and Passive Record Picks for Array I-6

In terms of a cause for the double dispersion trend, the same possibilities that were discussed with array I-5 remain plausible. Further data at the Frontera site may help to isolate which cause is the most likely.

6.1.2.3: Forward Modeling and Combined 2D Profile

Because of the elevation changes in I-4, it is difficult to compare its layer depths to those of I-5 and I-6. Considering all the uncertainty already involved in the modeling process I-4 was omitted from the 2D profile assembly. The experimental dispersion picks at I-5 and I-6 were fit by setting the bottom layer velocity first, then adjusting the upper layers until a close curve fit resulted. The layer velocities between the two 1D model profiles were also adjusted to be consistent with one another, which further constrained layer depths.

As discussed in section 6.1.1.2, the fit models are highly non-unique and could change significantly when modeled with applying different criteria. The 2D assembly in Figure 6.24 seems to be a reasonable model given the geomorphology of the scarp. It indicates beds dipping down with the dip of the scarp. This could be accurate if the older layers eroded away near the offset after uplift and then received newer deposits on top. Figure 6.25 provides the layer depth and velocity details for the 1D model profile generated from array I-6 data. The bottom layer velocity in this model is significantly higher than those found in the arrays NE of the fault trace. Low frequency dispersion picks, which sample deeper material, showed much higher phase velocities on the hanging wall.

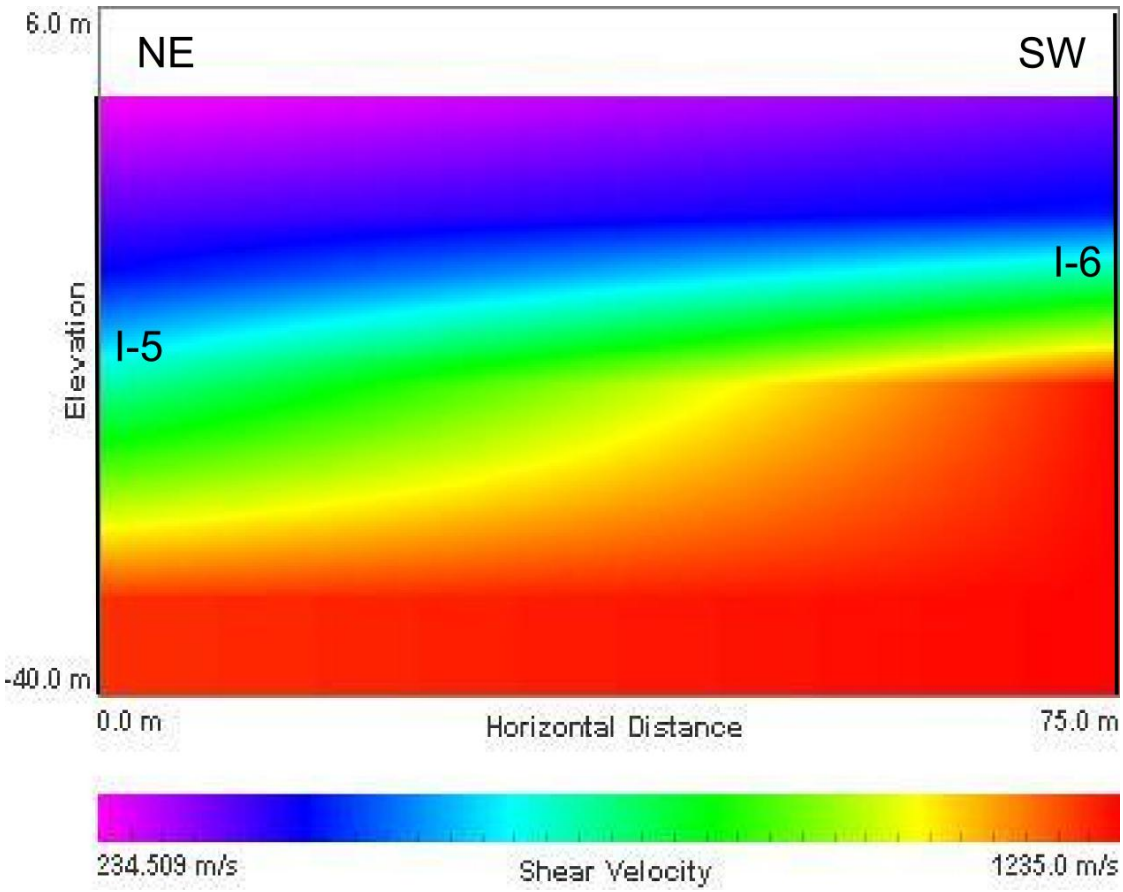

Figure 6.24: Assembled 2D Model Profile for Upper Ingley Arrays

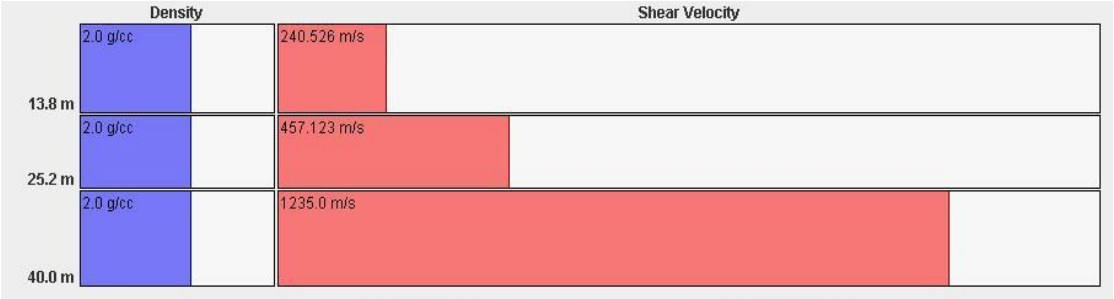

Figure 6.25: I-6 Model V_s Profile

6.1.3: Comparison of Hanging and Footwall Profiles

The uncertainty in the forward modeling process makes identifying an offset in bedrock very difficult. As has been demonstrated throughout this chapter, model profile

layer depths can be tweaked significantly by also changing layer velocities. Without knowing the true velocities of each layer, it is impossible to know for certain which model, if any, is correct. Despite this setback, the overall 2D assembly in Figure 6.26 indicates a significant increase in shear wave velocities throughout all layers on the hanging wall. While layer depths are difficult to determine, this bulk shift in shear wave velocities indicates a significant change in geologic structure somewhere between arrays I-1 and I-5. Collecting more data at arrays in the unknown shaded area would help to further isolate the location where this shift or surface fault trace exists.

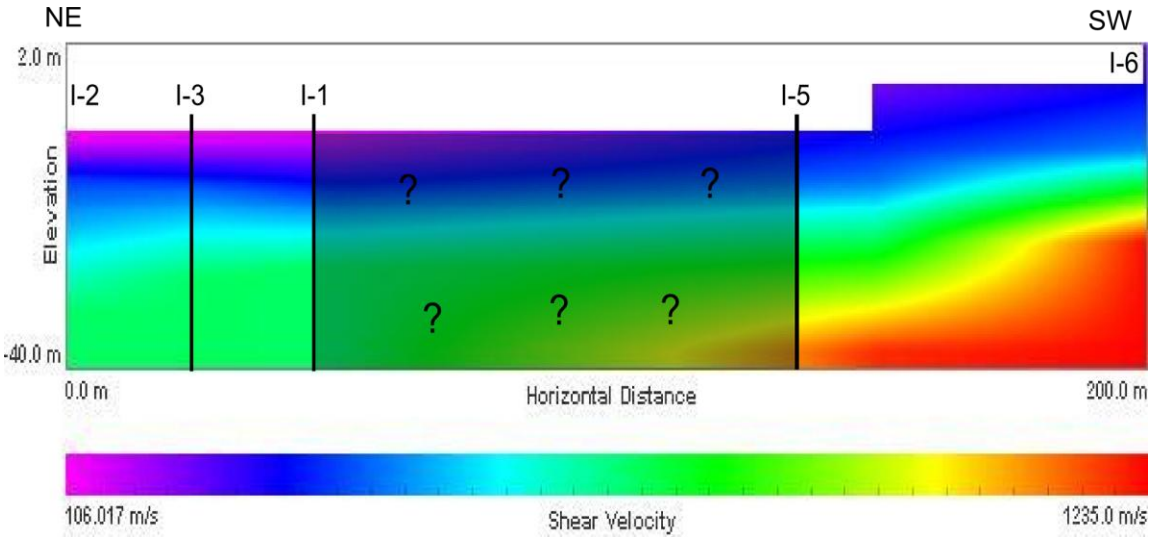

Figure 6.26: Overall Assembled 2D Model Profile of Ingley ReMi Arrays with a Zone of Uncertainty between Hanging and Footwalls

6.2: Seismic Refraction

6.2.1: Array Setup and Data Collection

The seismic refraction array at the Ingley site was situated such that it extended both well up the face of the scarp, and down into the floodplain below. In order to do this all 24 receivers were employed at a spacing of 4m as diagramed in Figure 6.27. The

intent was to cross the fault in a single array, but with only a sledge hammer for an energy source the arrivals became very difficult to interpret at large source-receiver offsets. This spacing also allows for only about a 2m resolution. A better approach would include two or three separate and overlapping arrays with smaller geophone spacing to improve the resolution and signal to noise ratio.

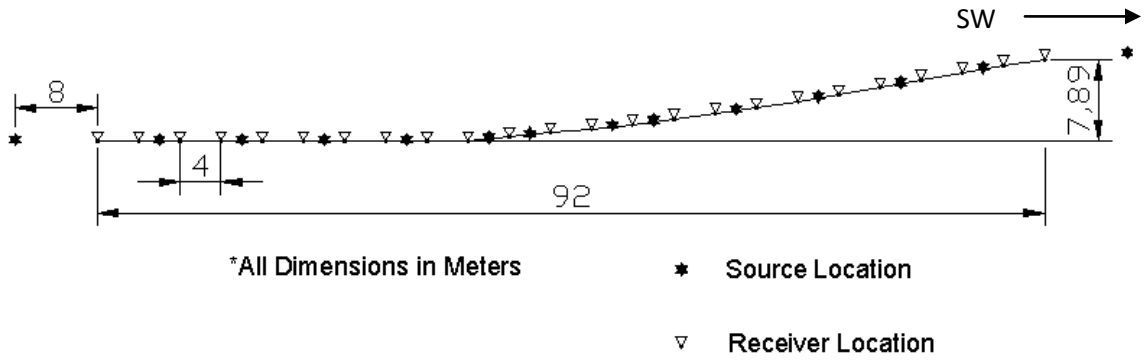

Figure 6.27: Diagram of Array I-7

6.2.2: First Break Point Picking

Despite the large source to receiver offsets, the data collected at the Ingley site was far less noise contaminated than at Crops Field C-31. Although the signal does weaken significantly, the first break arrival curve is fairly well defined. Figure 6.28 exhibits the worst case data with an off-end shot point travelling down to the far receiver. The other shot gathers provided better defined break points. To improve upon this data, the array receiver spacing could be reduced, a larger energy source could strengthen the signal, and a smaller data collection time step could allow for more precise definition of the first break points. In general the collected data proved sufficient to develop approximate 2D tomography and layer models for comparison to the ReMi method. The level of accuracy expected from ReMi modeling makes the uncertainty in the first break picking process nearly irrelevant.

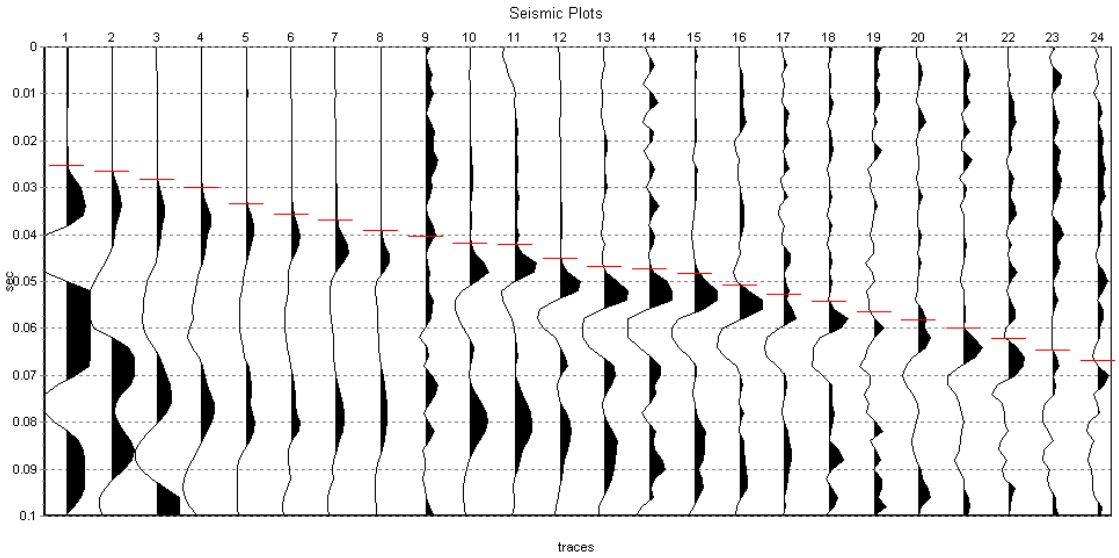

Figure 6.28: Off-End Shot Gather with First Break Point Picks at Array I-7

6.2.3: Model Profiles

When determining which 2D model resolution is the most appropriate, a good way to start is by looking at the "hitfiles" showing the amount of times a given pixel has been sampled. Many models can be quickly ruled out due to large gaps in the sampling space. The program will often create artifacts or provide inaccurate velocities in these poorly sampled regions. Figure 6.29 provides an example of a poor "hitfiles" plot, whereas a slightly different resolution in Figure 6.30 shows excellent ray coverage. All output plots from SeisOpt@2D in this work are in length units of meters and P-wave velocity units of meters per second.

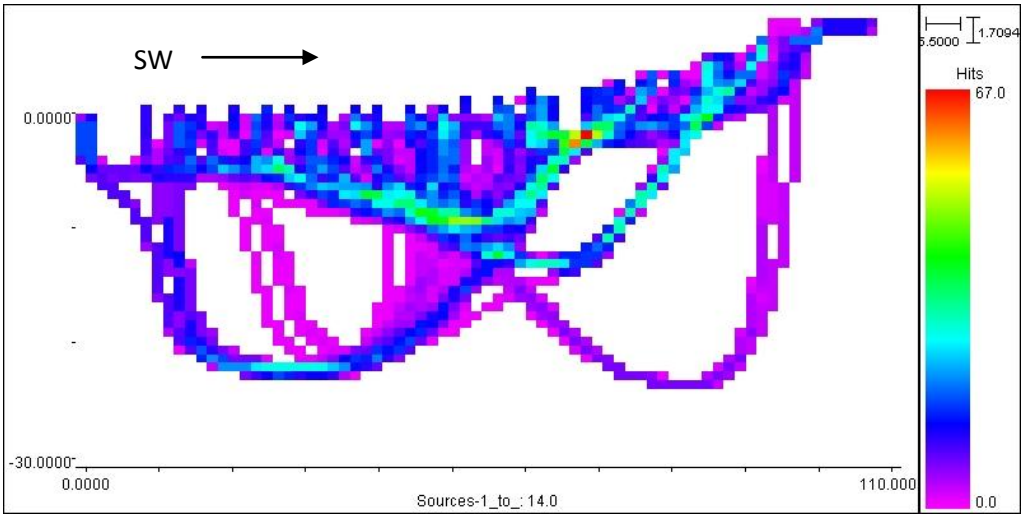

Figure 6.29: SeisOpt “hitfiles” with Large Gaps in the Sampling Space

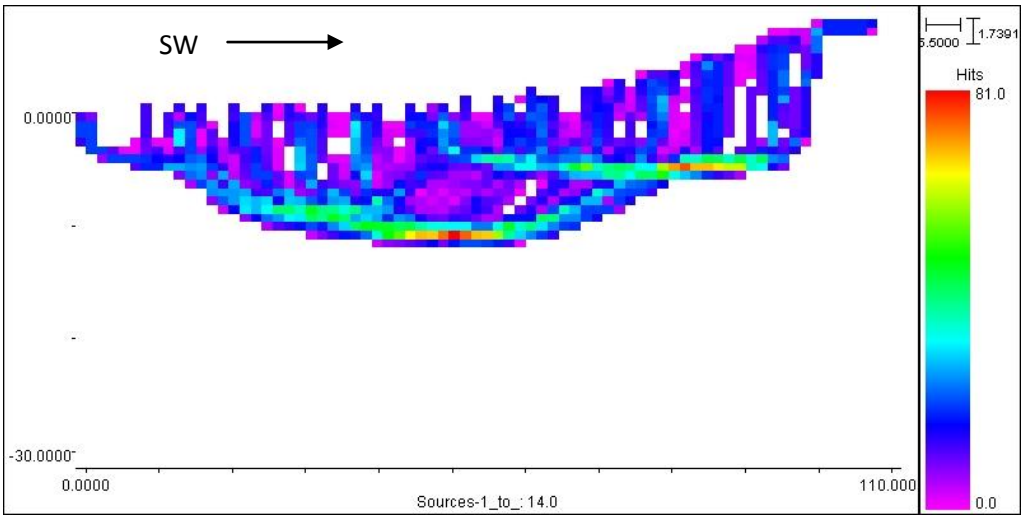

Figure 6.30: SeisOpt “hitfiles” of a Model with Good Ray Coverage

Further models can be ruled out if they show clearly anomalous results or their root-mean-square (RMS) error is significantly worse than the errors calculated for the other models. This will generally reduce the number of considered models significantly, and the remaining outputs can later be compared with results from other programs to determine which is the most robust.

The most reasonable model produced by analysis of I-7 data is displayed in Figure 6.31 with both smooth tomography, and the same results partitioned into only 5 colors. It seems to indicate extremely soft surface material, as is expected in the floodplain where the topsoil has been tilled, and also at the midpoint of the array where the soil is wet and soft in the creek bed. The edges of 2D tomography models are the most uncertain due to a reduced number of rays sampled through those points. For this reason the far left and right ends of the model should be interpreted with caution.

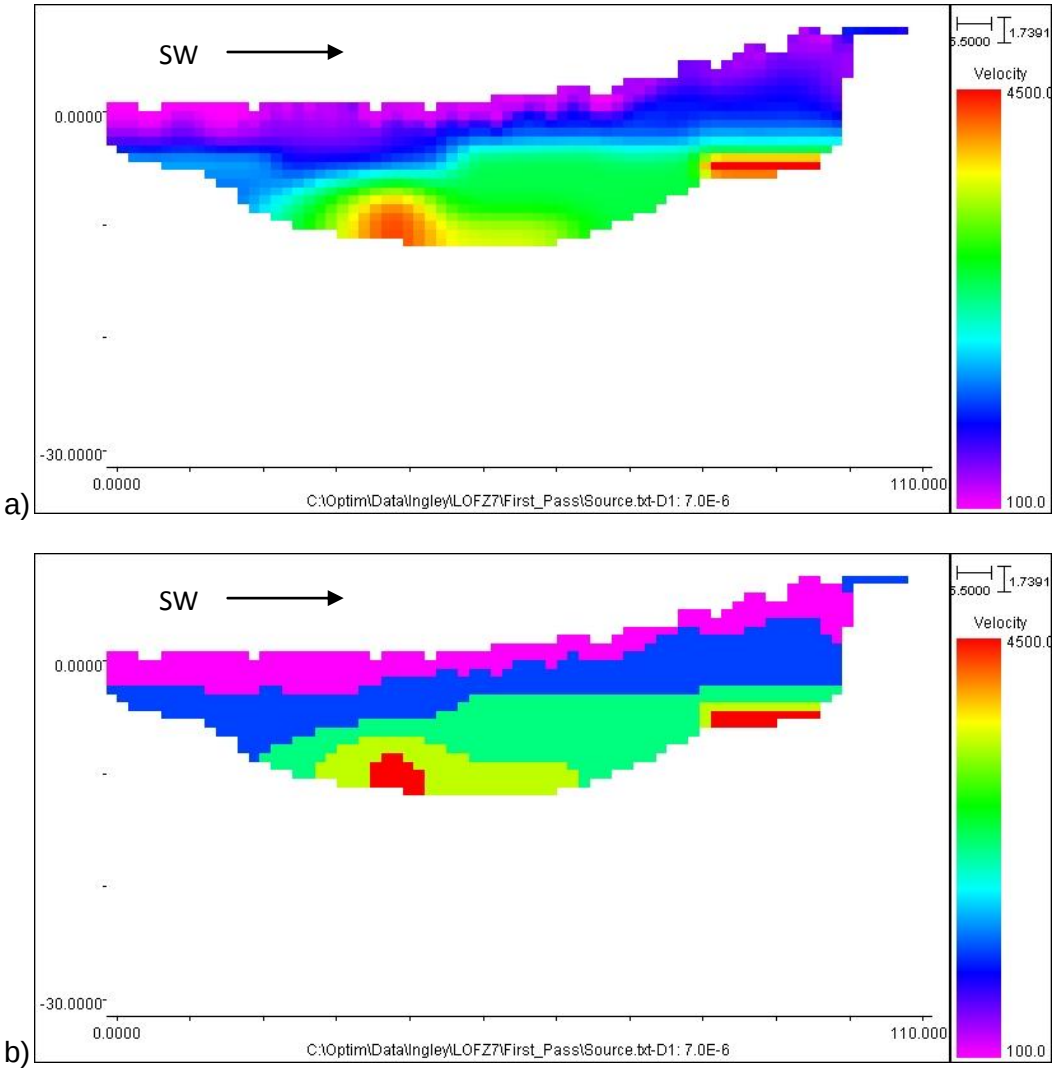

Figure 6.31: SeisOpt@2D Tomography Model for Array I-7 in (a) maximum color display and (b) 5 color display

In order to isolate the best possible 2D tomography model, the data was also analyzed using the generalized reciprocal method (GRM) in a program called IXRefraX (Palmer, 1980). This software enables layer modeling and allows for horizontal variation within the layer. It is the layer model shown in Figure 6.32 that helped to determine that the 2D tomography model in Figures 6.30 and 6.31 provided the best result. This profile has a much shallower bottom depth, but the first/second layer interface seems very similar to what appears in the tomography model, especially at approximately 20-25m from the left end.

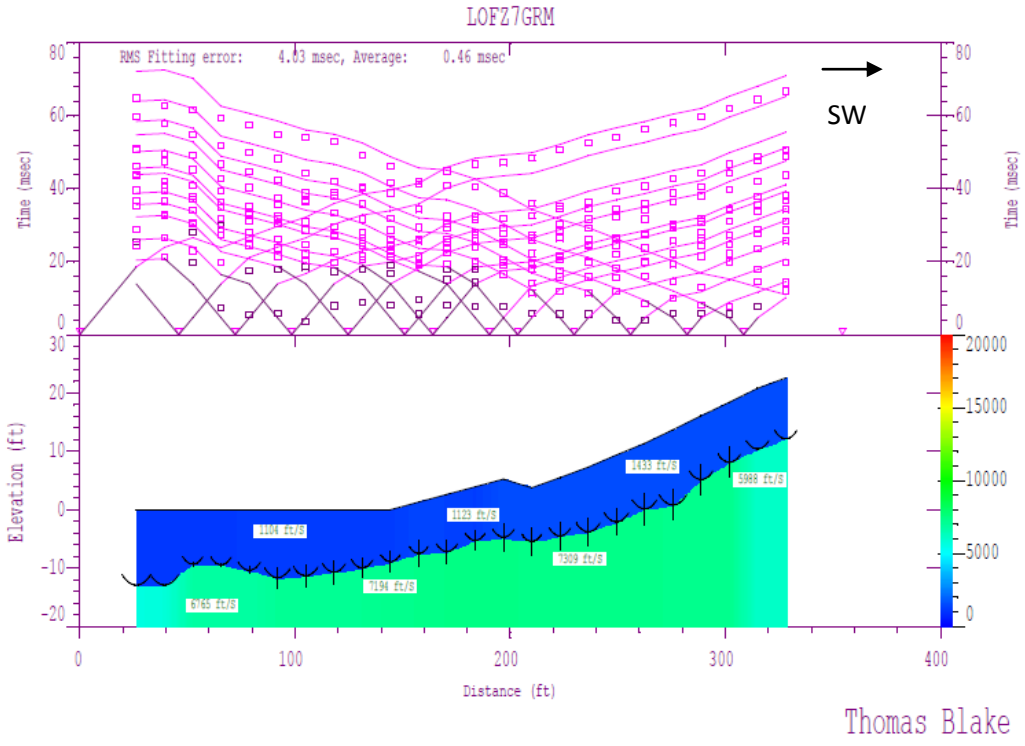

Figure 6.32: Two-Layer Model Profile of I-7 from IXRefraX

(T. Blake, personal communication, September 11, 2012)

6.3: Comparison of Results

The models generated from a p-wave refraction survey are not directly comparable to the V_s profile of a ReMi 2D assembly because of the difference between P and S-wave velocities; however, they can be compared in very general and qualitative terms for major structure or “ball-park” velocities. In both refraction models the wave velocities fall significantly on the down-slope end of the array. This agrees with the assembled ReMi profile, which indicates that somewhere between I-5 and I-1 there is a significant decrease in the V_s profile through all layers. Unfortunately the trench data is only logged to about 3m below the ground surface, and this lies entirely within the surface layer in the geophysical models. The ReMi data seems to agree well with the confirmed and inferred structure in Figure 4.5. Lettis and Hall (1994) show the depth of alluvium to be much greater on the NE side of the fault trace, and this is indeed what is indicated by the markedly lower stiffness in the 2D ReMi profile. They were also able to confine the bedrock depth on the hanging wall to 20-30m in depth (also shown in Figure 4.5) using well log data. This is also approximately the depth that the ReMi model shows the 1200m/s layer transition on the hanging wall.

6.4: Summary of Findings

This chapter has attained its goal of successfully measuring a significant lateral variation in the soil stiffness profile across a fault trace. The seismic refraction data seems extremely ambiguous, but corroborated the ReMi 2D profile. In fact, the ReMi method seems to have shown the lateral change in stiffness more clearly than the seismic refraction method did. Based upon the degree of uncertainty involved in each method, it would be unwise to base conclusions on only one. Furthermore, without the inferences made and trench data logged by experienced geologists Lettis and Hall (1994) it would be very difficult to come to any definite conclusions about the geophysics

data. One must remember that the ReMi data was fit with prior knowledge from this earlier work. Since the forward modeling process can produce such a variety of equally well fit dispersion curves, it is a leap to say that the same can be done with no prior knowledge. Figure 6.33 presents a summary of the results from the methods employed in this work, as well as the trench data from Lettis and Hall (1994).

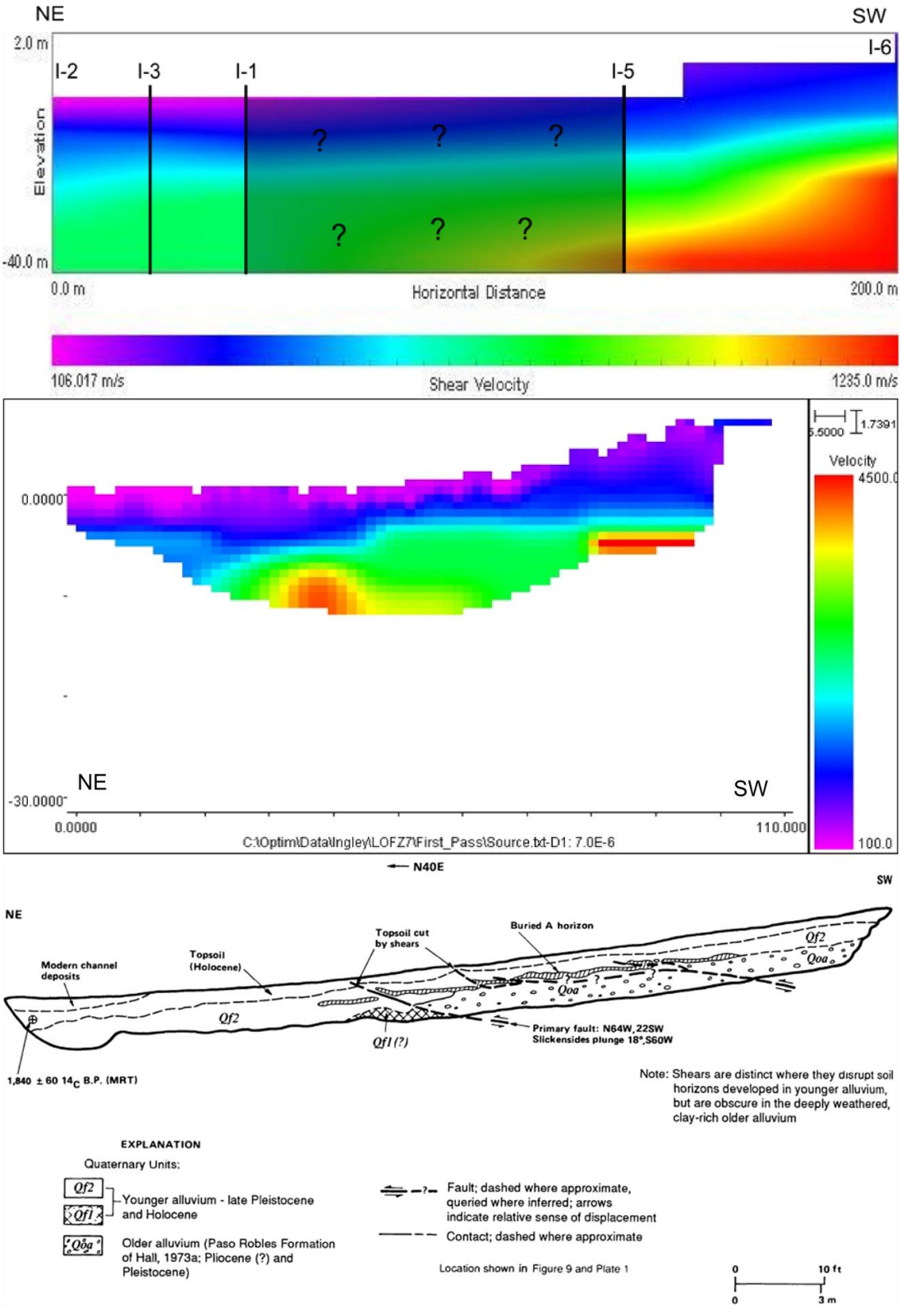

Figure 6.33: Summary of Model Figures and Past Trenching for Ingley Site

(trench data from Lettis and Hall (1994))

In the process of reaching the original goal of this chapter, a number of interesting observations arose. These are summarized here:

- Placing a ReMi array in close proximity to a strong signal source at a site that does not receive any other similar amplitude Rayleigh waves may result in interference (body wave or other) to the point that the p-f plots will be uninterpretable.
- The ReMi analysis is minimally affected by elevation change to the degree present in array I-4. This array experienced grade reversal of the slope, and in both segments the grade surpassed the 5% deviation allowance from the SeisOpt ReMi Field Tutorial (2006)).
- The spectral ratio peaks can sometimes appear much higher than the lower bound and true phase velocities. At this site this was caused by spectral ratio "wash out" due to a strong response along a higher phase velocity trend.
- Active records can experience low frequency "wash out", while passive records show a much wider spread of energy along the lower bound in the mid and upper frequency ranges. The wider spread of the spectral ratio trend causes more uncertainty in the picking process.
- At a quiet site a hammer and plate source can produce good seismic refraction break points even in longer arrays by stacking records.
- While difficult to compare the different types of data directly, watching for general qualitative trends can help the methods to corroborate one another.

Chapter 7: Frontera Site Data Analysis

The Frontera Site provided an ideal location to attempt the ReMi and seismic refraction methods in a situation where very little is known about the subsurface geology and structure. The work consisted of eight arrays providing ReMi data at each location and seismic refraction data at arrays M-5, M-6 and M-7. Only seven arrays are shown in Figure 7.1, but array M-2 was also extended off the southern end of the depicted line in order to compare results from 4 and 8m spacings.

The seismic refraction arrays lie in close proximity to the inferred fault scarp identified during preliminary site walks. Although only array M-6 crosses this observed feature, arrays M-5 and M-7 can provide data for comparison between ReMi and seismic refraction results obtained through the same array set-up. Although these arrays do not appear to cross the inferred feature, they may still indicate other structural abnormalities in the subsurface that could indicate nearby faulting.

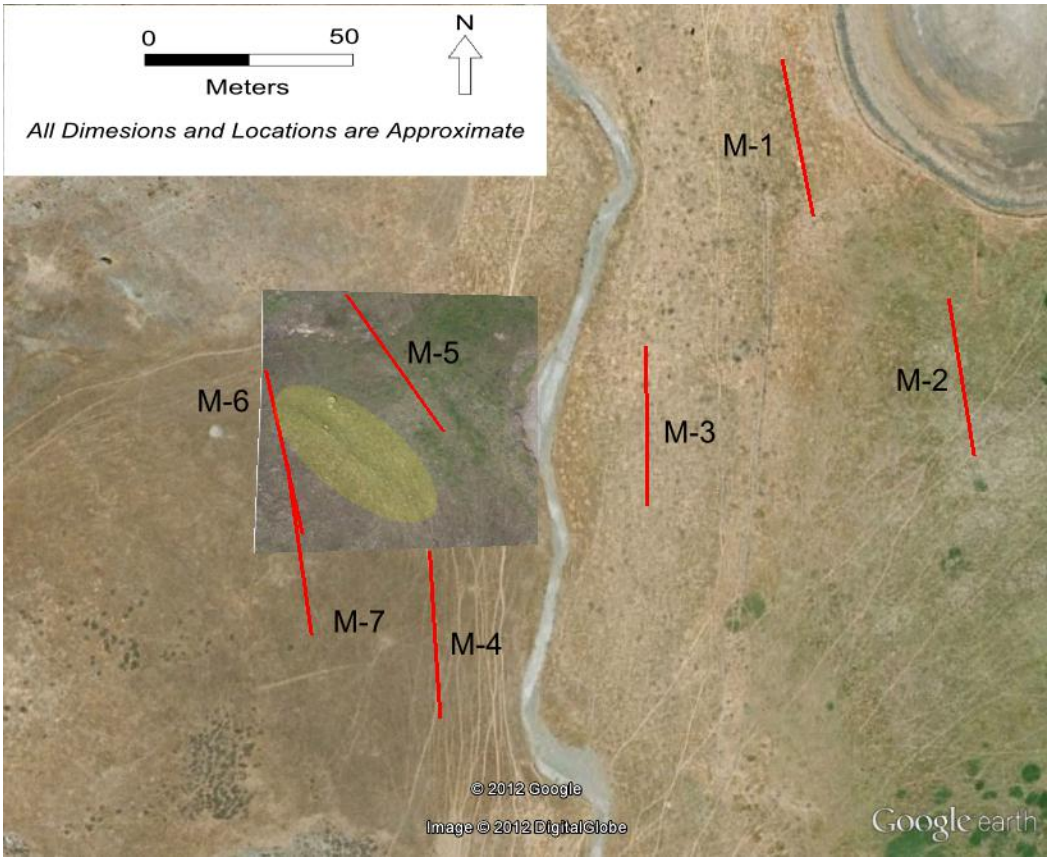

Figure 7.1: Plan of the Frontera Site Arrays with a Recent Satellite Overlay Depicting the Geomorphic Expression Identified in the Field in the Shaded Area

7.1: Refraction Microtremor

In addition to the goal of imaging a fault trace with geophysical techniques, the ReMi data at the Frontera site prompts discussion on a variety of topics that seem to affect the p-f plot spectral ratio distributions. Throughout the site, the data showed some strange results in nearly all ambient signal recordings. The seismographs of these records show a considerable amount of drift during the duration of the recordings. Possible causes for this are discussed in sections 7.1.1 and 7.1.2. The commentary on the spectral ratio plots in this chapter includes comparisons between data collected using different receiver spacings as well as varied source types and azimuths.

7.1.1: Ambient Recording Artifacts

The p-f spectral ratio plot in Figure 7.2 illustrates the common trend observed in ambient measurements recorded throughout the site. The only clear trend in spectral ratio peaks exists along the very top of the plot. This energy distribution indicates that extremely rapid phase velocities are relatively constant across all frequencies. A number of arguments lead to the belief that this is only an artifact. Velocities indicated by these spectral ratio peaks would only be present in very stiff bedrock. The fact that these velocities show up across the entire frequency band implies that the profile is made up of a single layer with very high velocity. If only due to overburden confinement, the stiffness should still increase somewhat with depth if the material in the profile is constant. The velocities actually appear to reduce at depth based upon this plot. While little is known about the geology of the subsurface at this site, figures obtained from Lettis Consultants, Inc. (unpublished and not shown) conflict with this result. The figures constrain sediment thickness and bedrock depths in the region using historical borehole data. They clearly indicate significant alluvial deposits above bedrock, especially to the east of the creek bed.

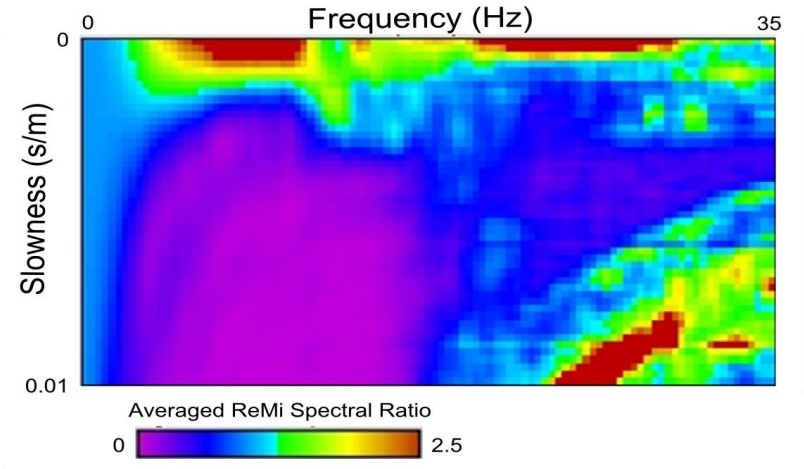

Figure 7.2: Example p-f Plot of Ambient Recordings Taken at Frontera Site Array M-3

After determining this trend to be invalid, the question yet remains as to the cause. Interestingly, this energy distribution is much less prevalent on recordings with actively or pseudo-actively applied sources. This suggests that, although these spectral ratios are very high in the ambient signal plots, they are easily "washed out" whenever a signal with significantly bigger amplitude is introduced. Additionally, in many of the ambient plots a viable dispersion trend does exist, but along the boundary of dark blue and purple spectral ratio regions, similar to what was shown at the Ingley site. This implies that the energy causing this high velocity trend is strong enough to "wash out" the dispersion trend in the ambient signal condition, but weak enough to be "washed out" by the active or pseudo-active energy.

It is unclear what could cause this result, but four hypotheses are presented here. Because the receivers were installed on the ground surface rather than imbedded, it is possible that the tall grass covering the Frontera site may have been rustling against the receivers in the wind. This should be mitigated when the wave signals are analyzed for signal coherence during processing, but it is possible that the data was not adequately filtered at this stage. Determining if this is truly the case would require a higher knowledge of the algorithms built into the Optim software.

The second possibility is the noise inherent to the measurement process. When the signal is extremely weak the noise caused by small fluctuations in the data acquisition power source or the geophones themselves is much more significant. Because the ReMi analysis process involves spectral ratios, at a site where the measurement noise is close in amplitude to that of the signal it can have a significant impact on the p-f plot.

The third potential cause involves the array placement. The arrays at this site were set up nearly parallel to a large nearby road. This means that the plane wave arrivals approaching the array will arrive approximately perpendicular to the line. If the arrivals reach all receivers at nearly the same time, this would indicate extremely high phase velocity regardless of frequency. This explanation would be more plausible if the road was clearly the most energetic signal source in the area, but a highway to the south and the nearby shopping center to the north lie almost as close. Wave front arrivals from these sources should contain approximately the same amount of energy. Furthermore, these arrivals would come from azimuths close to parallel with the arrays. Although this explanation is unlikely, it cannot be completely ruled out.

The final hypothesis addressed in this work is the possibility that the high velocity trend is an artifact of the signal drift observed in the seismograph records. This is addressed in section 7.1.2.

7.1.2: Comparison of Filtered and Non-Filtered Drift

During data collection in the field the ambient records showed significant signal drift during the duration of the measurements. The seismographs in Figure 7.3a exhibit this behavior. This was not witnessed at the other sites in this research, and is likely due to the extremely low amplitudes measured here. The Frontera site is the “quietest” of the three sites since it is offset furthest from any road or other major signal source. Because the amplitude scale is set automatically in VibraScope by the absolute maximum value in the measurements, when significant signals are recorded the drift is not noticeable. This raised the question as to how the drift may affect the data, whether noticeable or not.

It seemed unlikely that this drift would affect the results because it would be analyzed as a very low frequency wave. This frequency is far below the resonant frequency of the geophones (4.5Hz) and would fall outside of the data range where picks are made. In order to ensure that unforeseen effects were not being caused in the usable data range, a low-cut filter applied at 1Hz produced the seismographs in Figure 7.3b. This filtered data was then exported and analyzed without the drift.

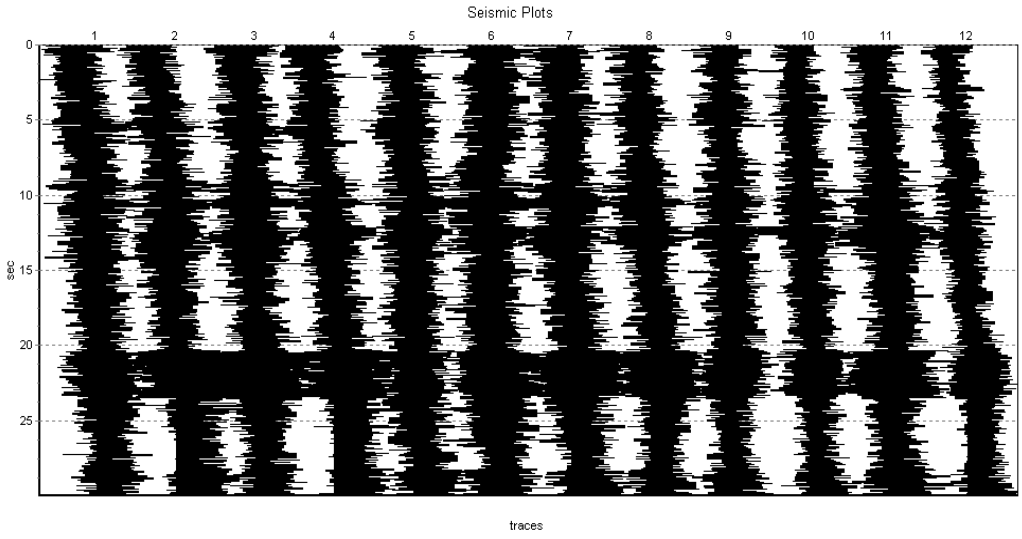

a)

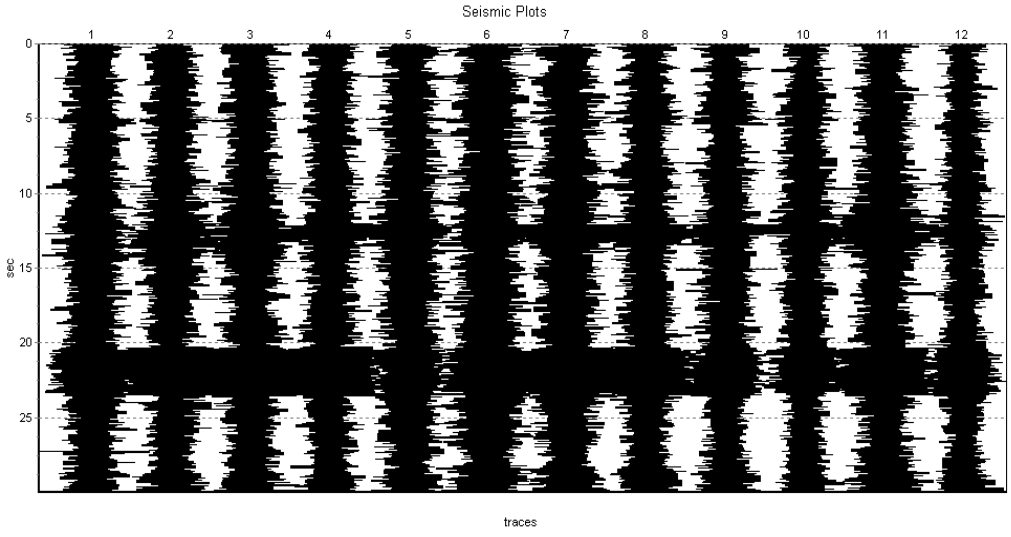

b)

Figure 7.3: Seismographs of Ambient Signal Recorded at Array M-3 (a) with Signal Drift and (b) Corrected for Signal Drift with the Application of a Low Cut Filter at 1Hz

Figure 7.4 compares the spectral ratio plots of the same data both corrected and not corrected for drift. The only apparent difference lies in the very low frequencies (approximately 0-3Hz) where the filtered data shows higher spectral ratios at low slowness. This should not affect the analysis process because picks are not made at these frequencies. Based upon this experiment, it appears that the signal drift is not responsible for the high frequency trend at the tops of the ambient p-f plots.

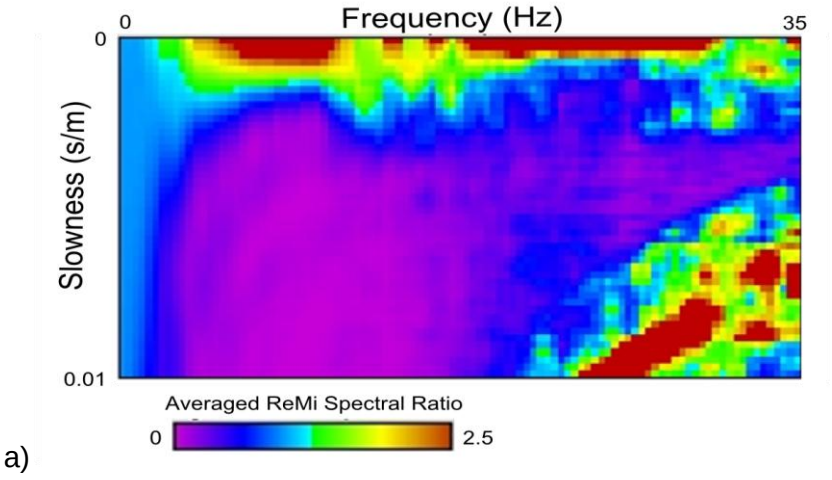

a)

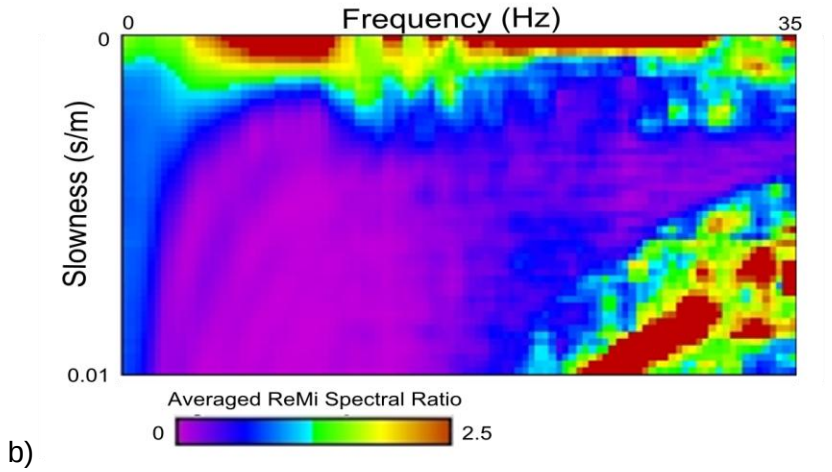

b)

Figure 7.4: p-f Spectra Ratio Plot of Data Processed (a) without Drift Correction and (b) with Drift Correction

7.1.3: Comparison of M-2a and M-2b

At array M-2 the p-f plots from the 8m receiver spacing (M-2a) contain gaps where the spectral ratios do not fully define the lower bound dispersion trend. For this reason, and to compare results between differing receiver spacings, the array was adjusted to 4m spacing. In this adjustment the northern end of the array remained in the same location (array M-2b) and the same azimuth was maintained.

Reducing the receiver spacing should allow longer period waves to be sampled by more receivers within a single wavelength, and thus characterize it more accurately. Indeed, the 8m spaced array is poorly defined above approximately 8Hz. Based upon the phase velocity picks at this frequency, the wavelength calculates as approximately 19m and therefore could be sampled by three receivers at any given moment. When the wavelength becomes smaller than 16m, an array spaced at 8m cannot sample a single wavelength more than twice along its length. However, a 4m spaced array could sample wavelengths down to 8m accurately. The p-f plot of the 4m spaced array in Figure 7.5b is well defined down to approximately a 5m wavelength. Conversely, a wavelength longer than the entire survey line is clipped spatially. This form of aliasing may degrade characterization of the waveform. A 12 receiver array spaced at 4m surveys 44m in length, and this approximately matches the wavelengths at the gap in figure 7.5b around 6Hz.

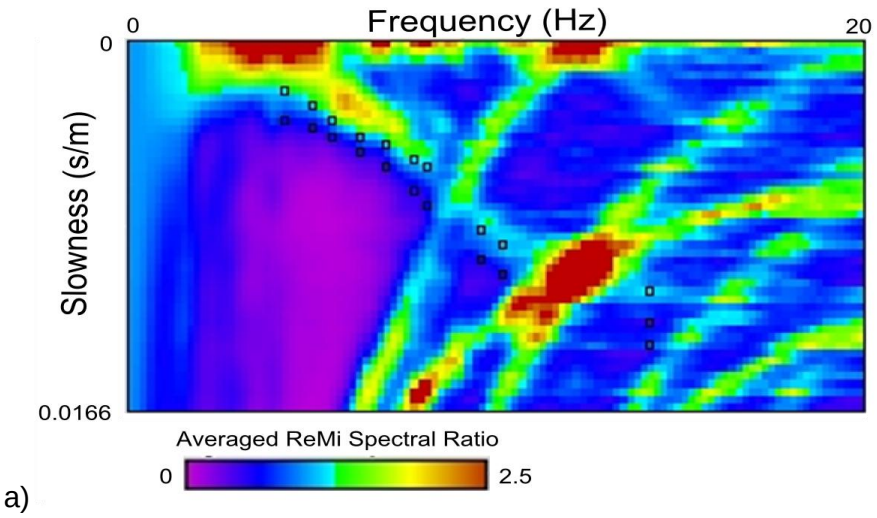

a)

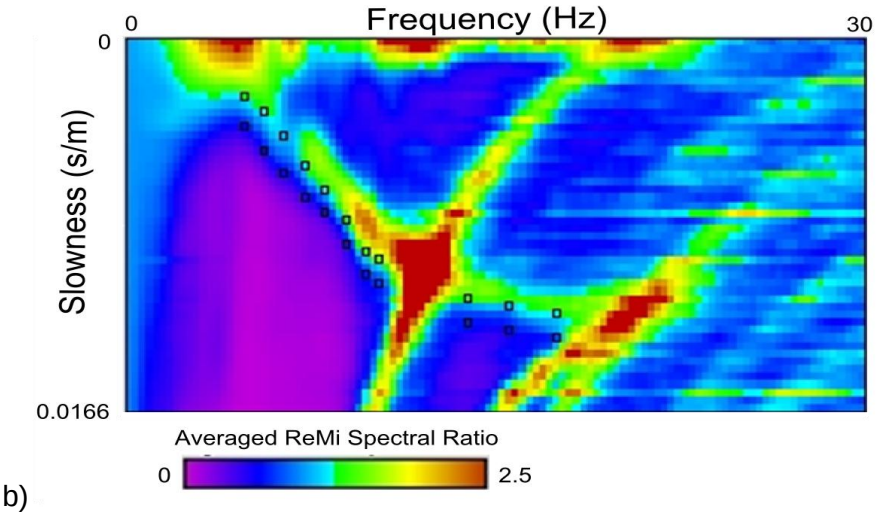

b)

Figure 7.5: p-f Spectral Ratio Plots for (a) 8m Spacing and (b) 4m Spacing at Array M-2

The picks from the 8 and 4m spaced arrays are plotted simultaneously in Figure 7.6 and show that the trends agree quite well. There is some amount of divergence between 6 and 10Hz, but this could be attributed to lateral variation in the soil strata since the 8m array is twice as long as the 4m array. Solid curves define the upper and lower bounds of the picks from both arrays, and the dashed line represents a fourth order polynomial fit to all picks from both arrays.

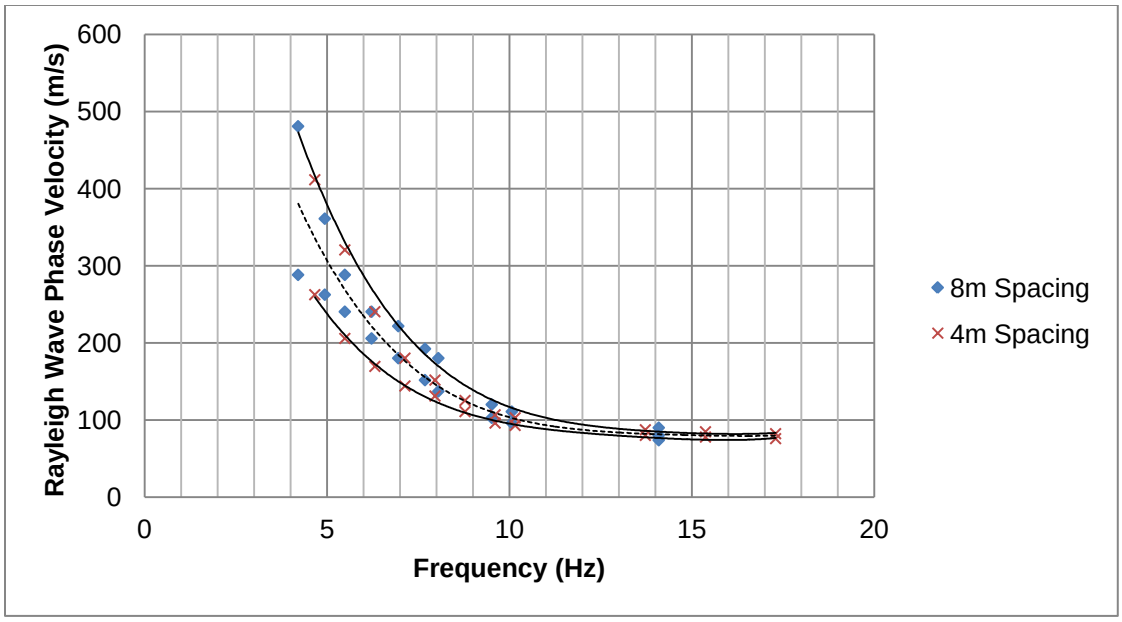

Figure 7.6: Dispersion Picks from 8 and 4m Spaced Arrays at M-2 Showing Fourth Order Polynomial Fits to the Full Data Set and Upper and Lower Bounds

7.1.4: Comparison of Arrays M-1 and M-2

As stated in section 7.1.3, the differences between the 8 and 4m spaced arrays could be attributable to lateral variation in the soil strata. Fortunately, Array M-1 lies at approximately the same offset from the inferred fault trace and along nearly the same bedrock depth contour in the figure provided by Lettis Consultants, Inc. (unpublished and not shown). In Figure 7.7 the dispersion picks made for array M-1 appear on the corresponding p-f plot. These picks were then plotted in comparison with the fourth order polynomial curve fit from array M-2. The results are displayed in Figure 7.8 and seem to imply some difference in sediment thickness and/or layer velocities. At very high and very low frequencies the dispersion picks approximately agree, but in the range of about 6-18Hz array M-1 returns significantly higher phase velocities. This could either be attributed to a shallower depth to the stiff layer interface, or a stiffening of the material laterally within layers.

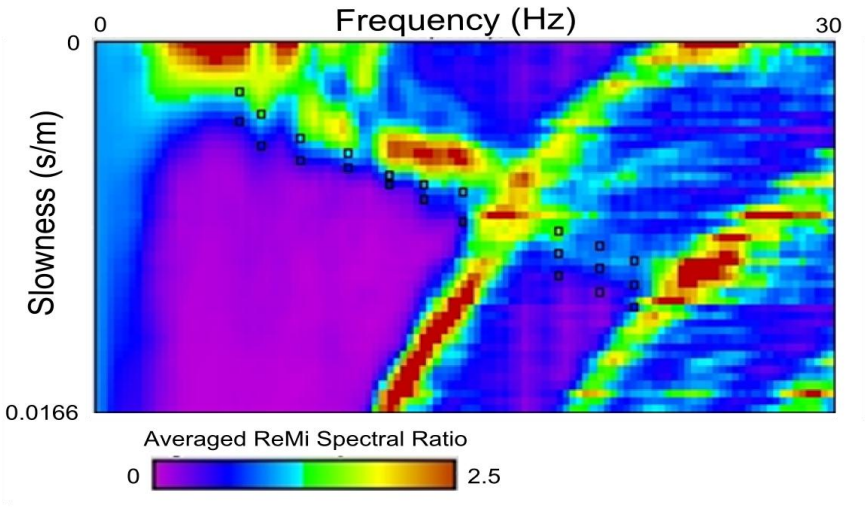

Figure 7.7: p-f Spectral Ratio Plot Including Dispersion Picks for Array M-1

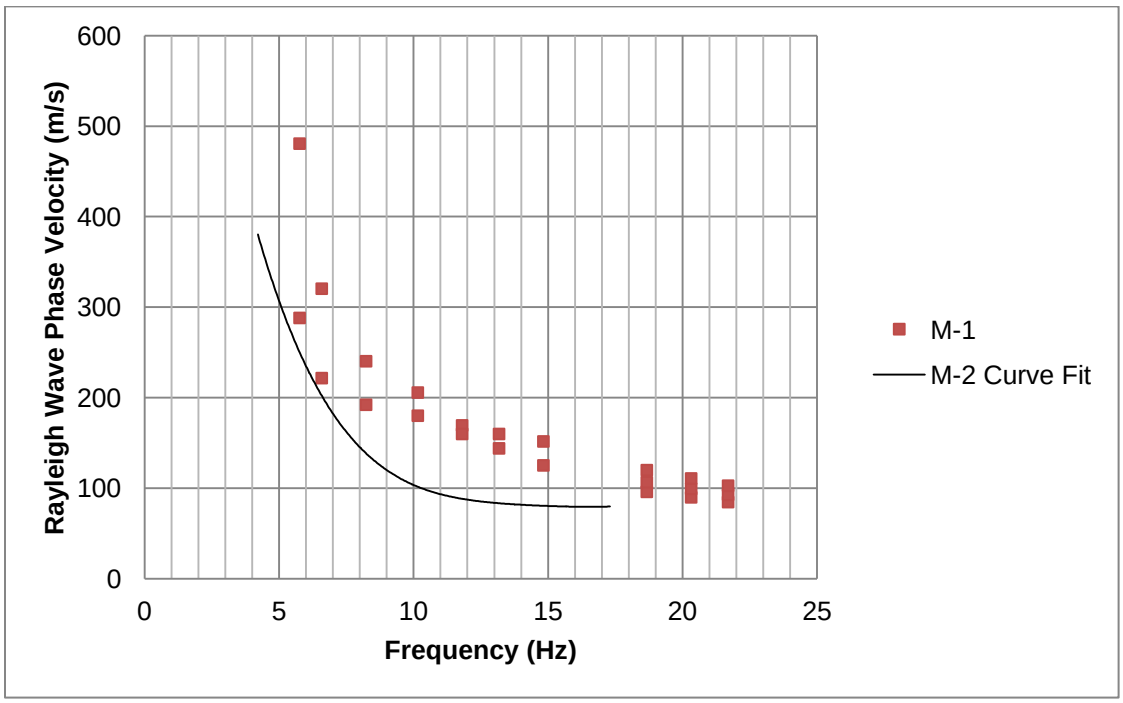

Figure 7.8: Comparison between Array M-1 Dispersion Picks and the Curve Fit to Both Sets of Dispersion Picks at Array M-2

7.1.5: Signal Source Comparison

This section focuses on comparing spectral ratio p-f plots obtained through measurement of various signal types at different azimuths. Arrays M-3 through M-7 provided some interesting data that indicated multiple response trends characteristic of Rayleigh wave dispersion. Active records at arrays M-6 and M-7 also show some very irregular response distributions that warrant discussion.

7.1.5.1: Active Source Comparison

Array M-3 produced two very different energy response trends shown in the p-f plots of Figures 7.9 and 7.10. The two signal conditions presented are actively generated by walking vibrations and hammer blows respectively. At first glance the trend exhibited in Figure 7.9a seems to be the clear dispersion trend for array M-3. However, when the walking signal data is compared to the off-end hammer data of Figure 7.10 the true dispersion trend is unclear. The dataset collected with the hammer energy presents a lower phase velocity trend in addition to that found in the walking signal records. If the walking records are interpreted with knowledge of this lower trend's existence, similar picks can be made along the blue-to-purple boundary. Picks for both trends are displayed for the walking and hammer signal records in Figures 7.9 and 7.10.

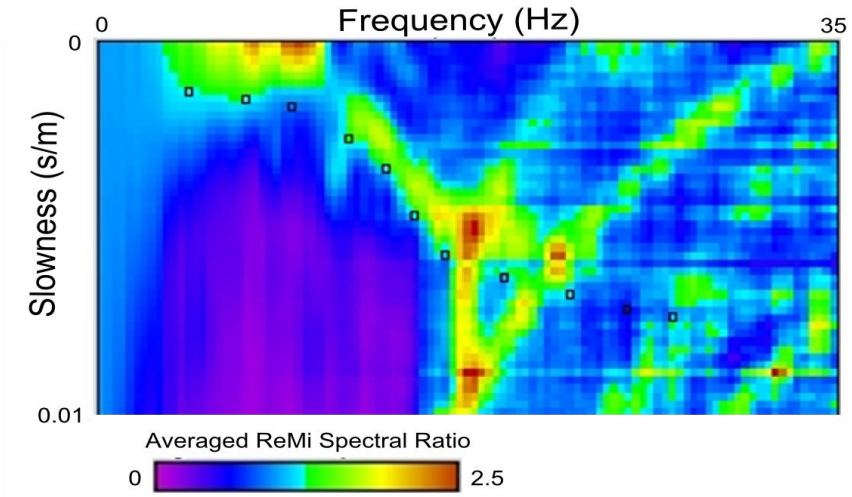

a)

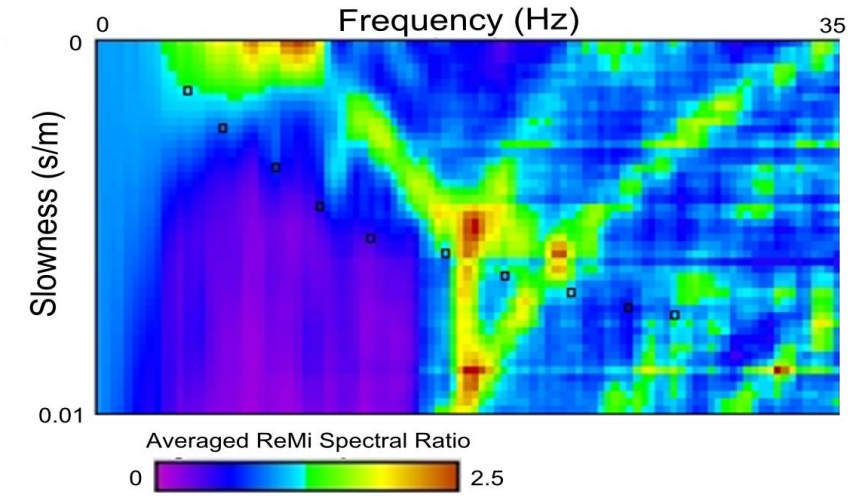

b)

Figure 7.9: p-f Spectral Ratio Plots of Walking Induced Signal at Array M-3 with Dispersion Picks along the (a) Upper Trend and (b) Lower Trend

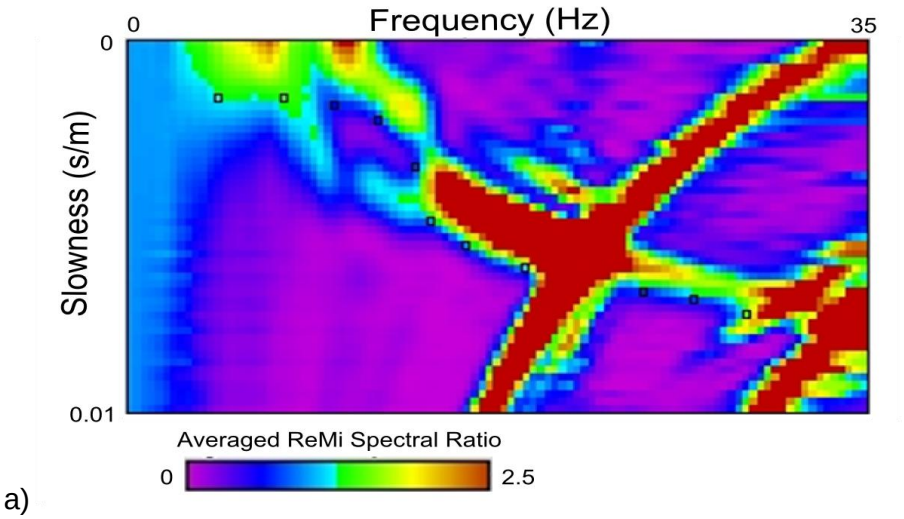

a)

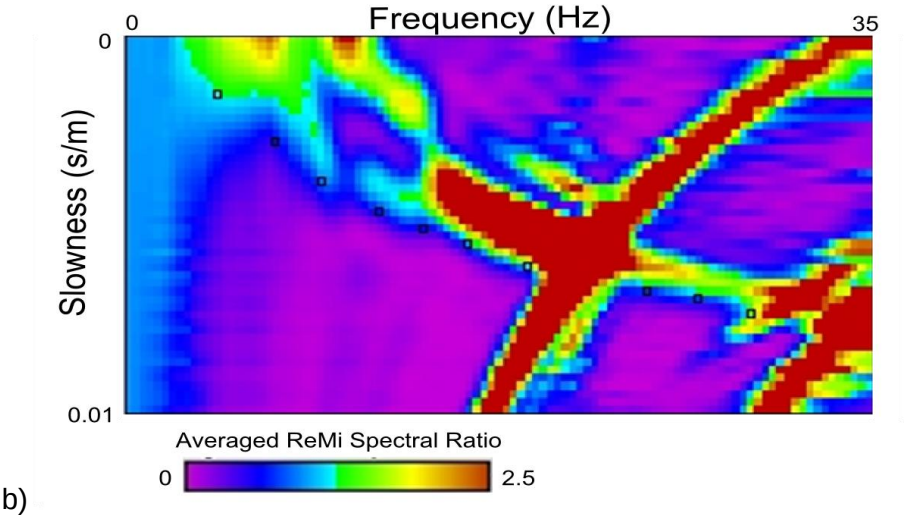

b)

Figure 7.10: p-f Spectral Ratio Plots of Off-End Hammer Blow Energy at Array M-3 with Dispersion Picks along the (a) Upper Trend and (b) Lower Trend

Because the lower trend is barely visible in the walking records and poorly defined in the hammer blow records, there is a high degree of uncertainty in making picks for this dispersion curve. To assess the commonality within trends and between walking and hammer blow records, all four pick sets are plotted simultaneously in figure 7.11. This plot shows a surprisingly close agreement between the walking and hammer blow picks for both trends. The agreement here bolsters confidence in the picks.

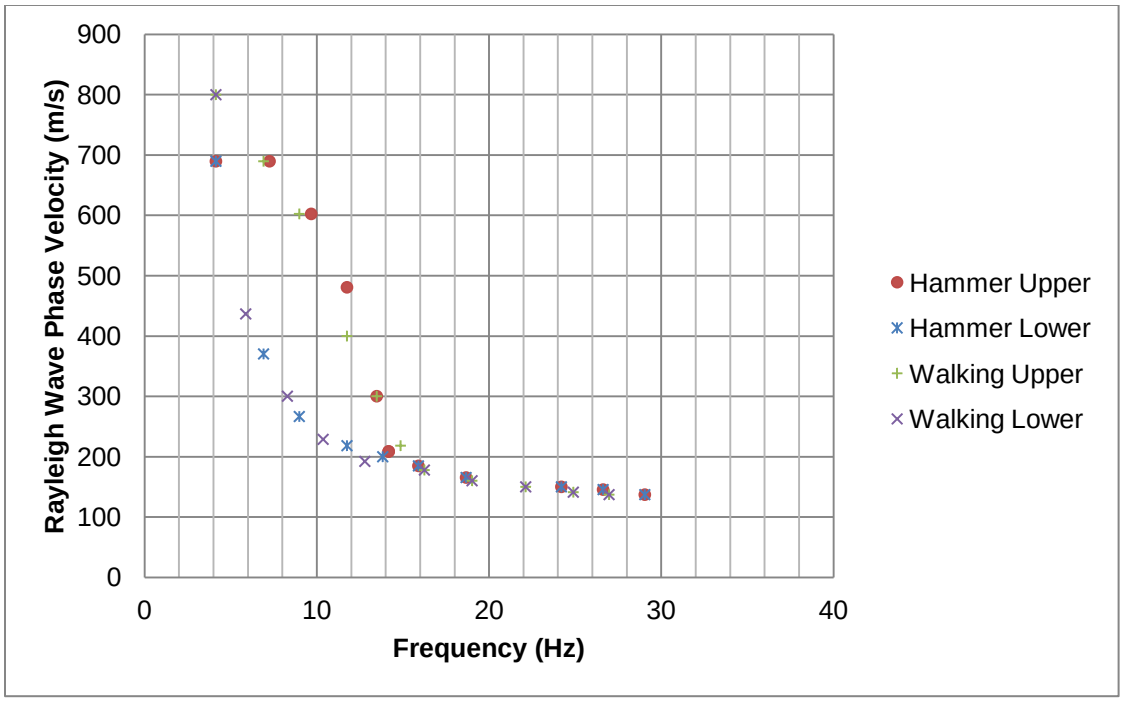

Figure 7.11: Scatter Plot of Dispersion Picks for Upper and Lower Trends with Hammer and Walking Energy at Array M-3

The comparison between the upper and lower trends in Figure 7.11 appears nearly identical to the comparison between active and passive recording methods made by Cox and Beekman (2011) in Figure 2.25. This commonality suggests that the interpreter could easily be led to pick different dispersion trends solely because of a difference in signal amplitudes. It is possible that other factors are at the root of this phenomenon, but to isolate the cause more testing will be necessary.

7.1.5.2: Off-Line Actively Induced Signal Measurements

In continuance of the parametric study in chapter 5, measurements were taken at arrays M-3 and M-4 with hammer blow energy induced at a location perpendicularly offset from the array midpoints. The p-f plots associated with this data are found in Figure 7.12. This signal condition here shows the same shift that was discovered in the

Crops Field C-31 analysis. The spectral ratio peaks appear higher on the p-f plot, indicating higher phase velocities. Again, this is likely due to the fact that the arrivals from a source off-line from the array midpoint will reach all receivers in more rapid succession than if traveling along the length of the array (see Figure 5.11).

This data also provides a new insight that was not so clearly observable in the Crops Field C-31 data. In examination of the p-f plots in Figure 7.12, there appear to be a number of trends indicating higher spectral ratios moving from the bottom left of the plot up and towards the top-right corner. These irregular trends pass through the Rayleigh wave dispersion zone of the plot and cause significant interference with the dispersion curve where they meet. This makes the lower bound very difficult to identify. The cause for these elevated spectral ratio curves is unclear, but the subject is moot because the dispersion trend is unreliable in this signal condition. The information presented here should only be used to help an interpreter recognize the effects and avoid using records exhibiting this behavior.

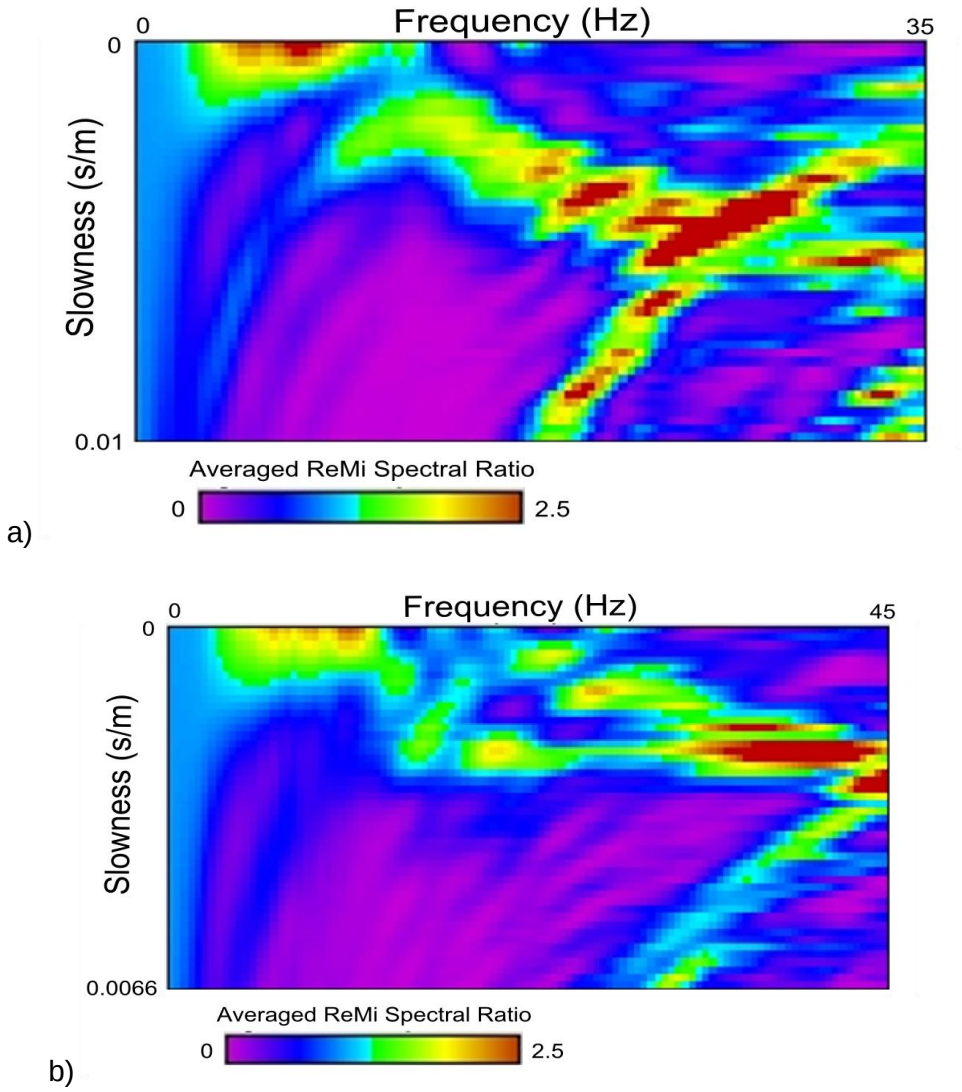

Figure 7.12: p-f Spectral Ratio Plot of Hammer Energy Originating at a Location Perpendicularly Offset from the Midpoint of Array (a) M-3 and (b) M-4

7.1.5.3: Differences Observed between In-Line Active Energy Produced Off of Opposite Array Ends

At array M-5 the dispersion trend in the p-f plots shows very good definition throughout records containing actively or pseudo-actively induced energy. Although well defined, the trends seem to diverge from one another in the frequency range above approximately 30Hz. Recordings of hammer blows off the NW end of the array differ from those of hammer blows off the SE end. Figure 7.13 displays the plots and picks for these two conditions. The difference between these plots is likely due to lateral variation in the soils strata. When hammer blows are recorded off-end of the array, the respective end of the line receives a much stronger signal and may therefore more clearly reflect the profile under those receivers. If this is the case, the signal seems to attenuate rapidly enough that the dispersion at the other end of the array is “washed out”. This effect could be mitigated by increasing the source-array offset so that the ratio of the amplitudes observed at opposite ends is smaller.

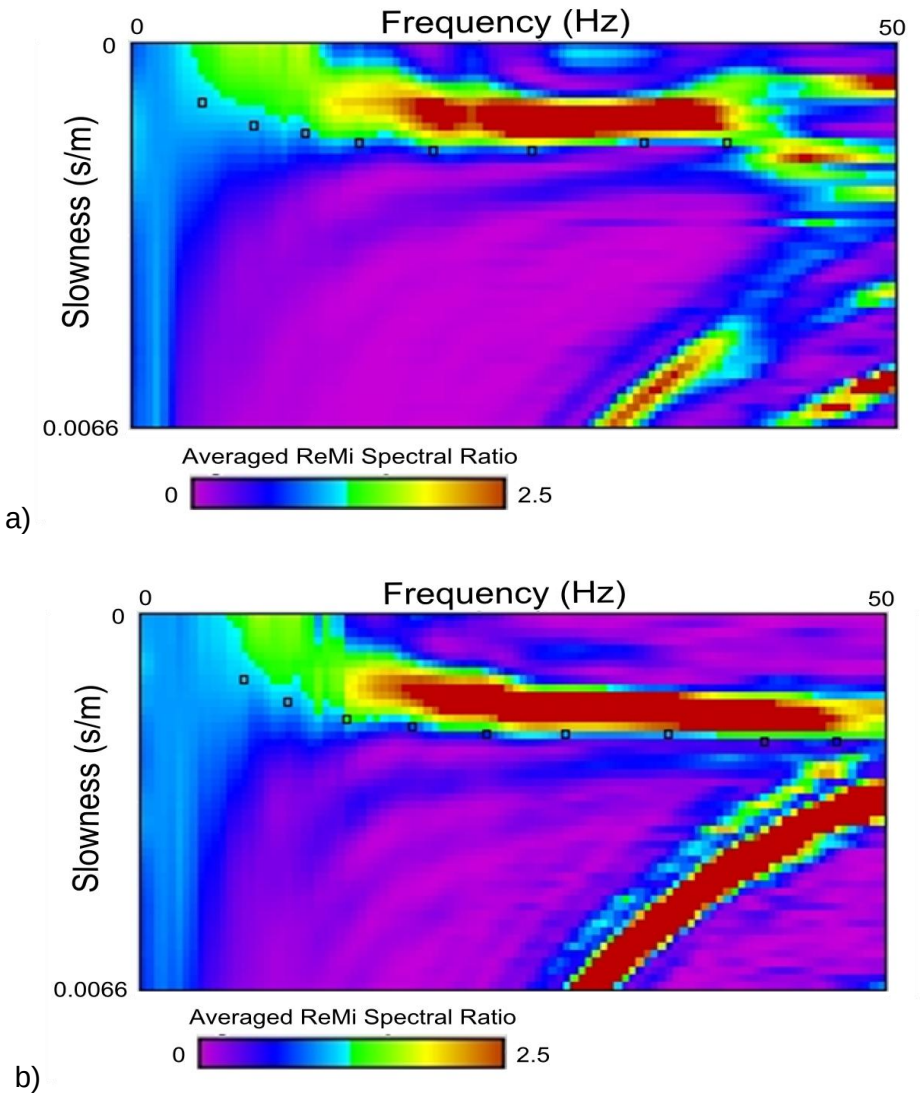

Figure 7.13: p-f Spectral Ratio Plots for Array M-5 Containing Off-End Hammer Energy from (a) the SE and (b) the NW

7.1.5.4: Irregular Spectral Power Distributions

The p-f plots for Arrays M-6 and M-7 contain scattered zones with elevated spectral ratios. This strange behavior may be a result of the proximity to the inferred fault trace. Array M-6 actually crosses the inferred fault scarp and M-7 rests just atop the inferred hanging wall. Each of the wave field cases described in this section returned considerably different dispersion trends, or at times, no clear trend whatsoever.

Because the trends vary so drastically, no picks were made for array M-6. In this case dispersion picks would be meaningless because the array crosses the inferred fault trace. Modeling an array crossing a fault offset would not help to characterize the fault since it would just smear the results across the array.

The data containing hammer blows off-end of array M-6 is presented in Figure 7.14 and indicates a high level of variance across the array. The two ends of the array do not appear to agree with one another, even in an approximate sense. Despite the disagreement, a commonality does exist. Many small zones with elevated spectral ratios appear in both plots above approximately 25Hz. These zones are uncharacteristic of typical p-f plots even above the frequencies where the dispersion trend is clearly defined. Figure 7.15 displays very similar data recorded at array M-7. This could potentially be caused by some complicated subsurface structural geometry that is resulting in ray scatter through diffraction, refraction, and reflection. If this is the case, this abnormal distribution of spectral ratio peaks could potentially indicate that the fault trace exists beneath the array and is responsible for the anomalous data.

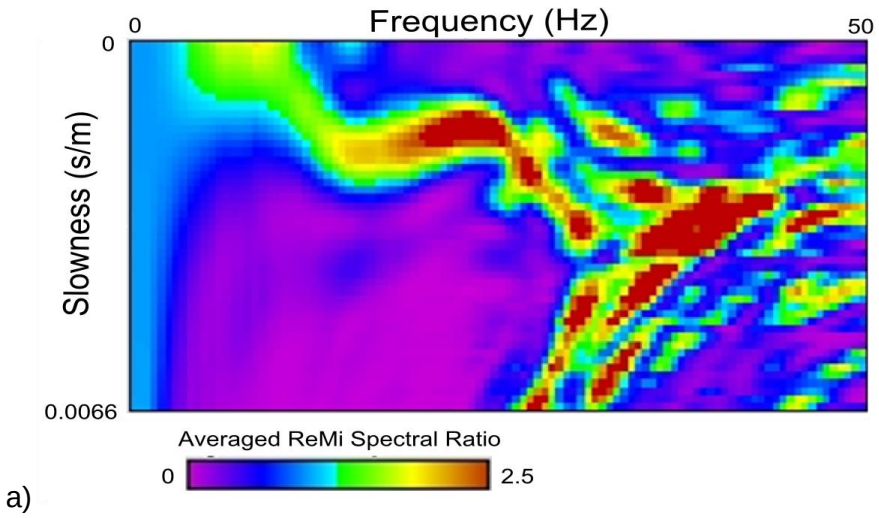

a)

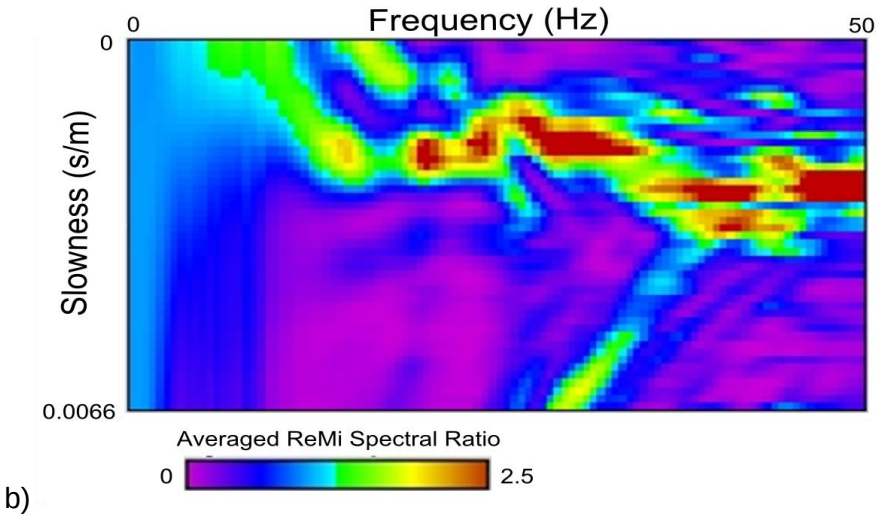

b)

Figure 7.14: p-f Spectra Ratio Plots with Hammer Blows Off-End of the (a) North and (b) South side of Array M-6

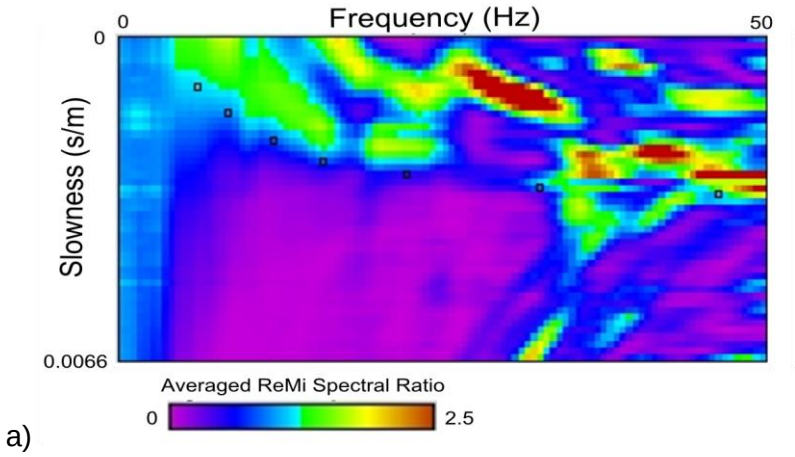

a)

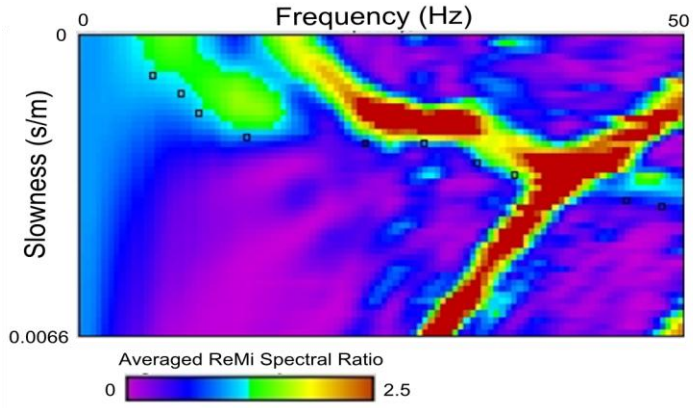

b)

Figure 7.15: p-f Spectra Ratio Plots with Hammer Blows Off-End of the (a) South and (b) North sides of Array M-6

7.1.6: Forward Modeling and 2D Profile Assemblies

The analysis of the data collected at the Ingley site revealed that ambiguity in the modeling process introduces far more uncertainty than decisions made during the dispersion picking process. Because this is the case, rather than making bracketed picks for each p-f plot, at each array all the picks made for the varied cases were combined to guide the forward modeling process. Figures showing theoretical dispersion curve fits to the experimental picks can be found in the appendix of this work. For brevity's sake only the final models are included here in the body of the report.

The figures provided by Lettis Consultants, Inc. (unpublished and not shown) provided some valuable aid during the forward modeling process. Using the sediment thickness and bedrock depth information, possible model fits for the picks at array M-2 were fairly well constrained. The top layer velocity is the most easily determined since it does not rely upon the lower layers or layer interfaces. Therefore, with the top layer velocity and bedrock depth determined, the model in Figure 7.16 provides the best fit. The first layer interface and lower layer velocities could be adjusted slightly, but as determined in the Ingley analysis, the ReMi modeling process can only be relied upon for bulk approximations. The uncertainty has been constrained as much as possible here.

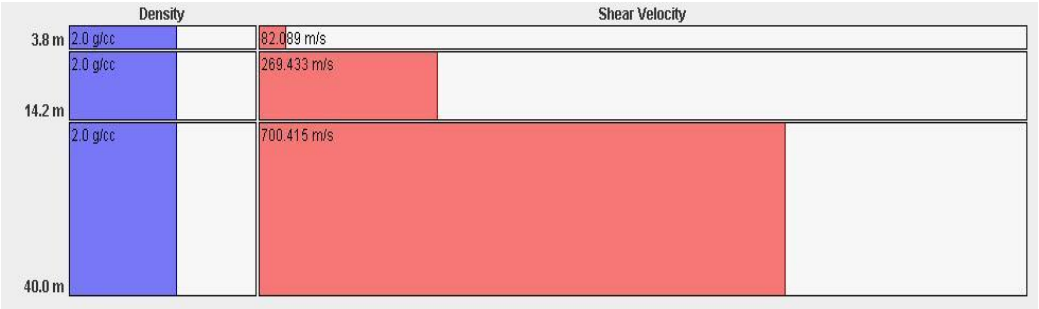

Figure 7.16: 1D Model Profile for Array M-2

Where possible, the other arrays were modeled by setting layer velocities to approximately the same values as determined at array M-2. This constrained interface depths and produced the models in Figures 7.17 and 7.18. The top layer velocities were forced to increase somewhat by the experimental data as the arrays stepped closer to the fault trace, but based upon field observations this increase in stiffness seems appropriate. Arrays M-1 and M-2 were situated on very soft and moist topsoil, while the arrays closer to the fault were placed on clearly dryer and stiffer material.

Figure 7.17: 1D Model Profile for Array M-3

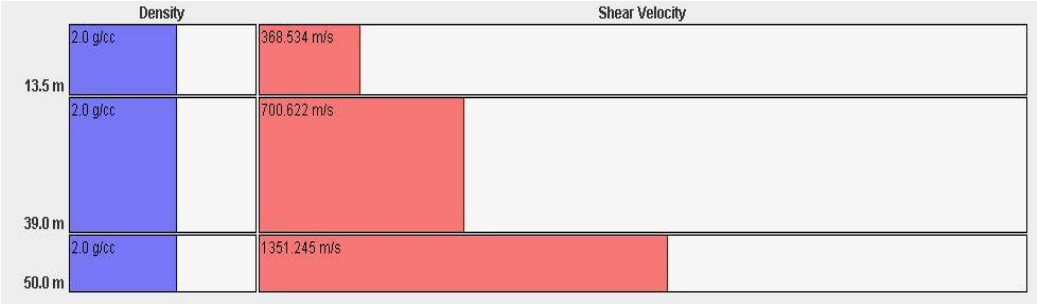

Figure 7.18: 1D Model Profile for Array M-4

Fitting array M-7 to the same layer velocities as the other models proved to be impossible. The entire profile showed a marked increase in stiffness similar to the hanging wall at the Ingley site. This increase in stiffness is the anticipated shift that indicates the possibility of a fault offset.

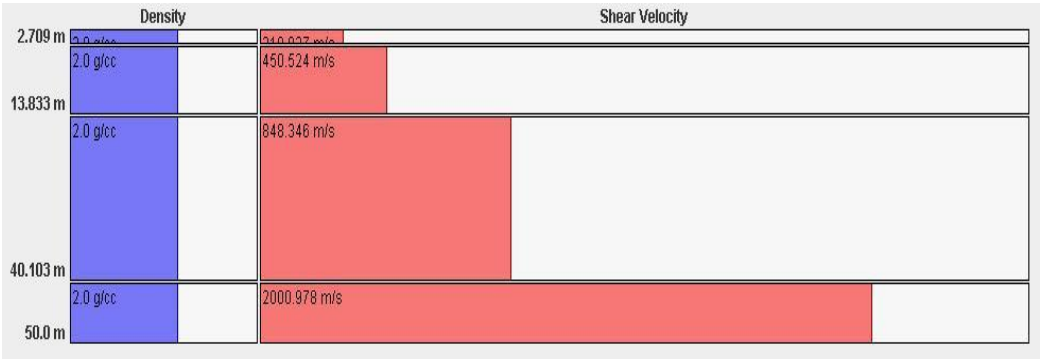

Figure 7.19: 1D Model Profile for Array M-7

In order to better illustrate the degree that the overall profile stiffness changes across the Frontera site, Figure 7.20 displays the complete 2D profile assembly. It is

important to remember that SeisOpt ReMi v4.0 interpolates between profiles, so the velocities between the annotated sections are highly uncertain.

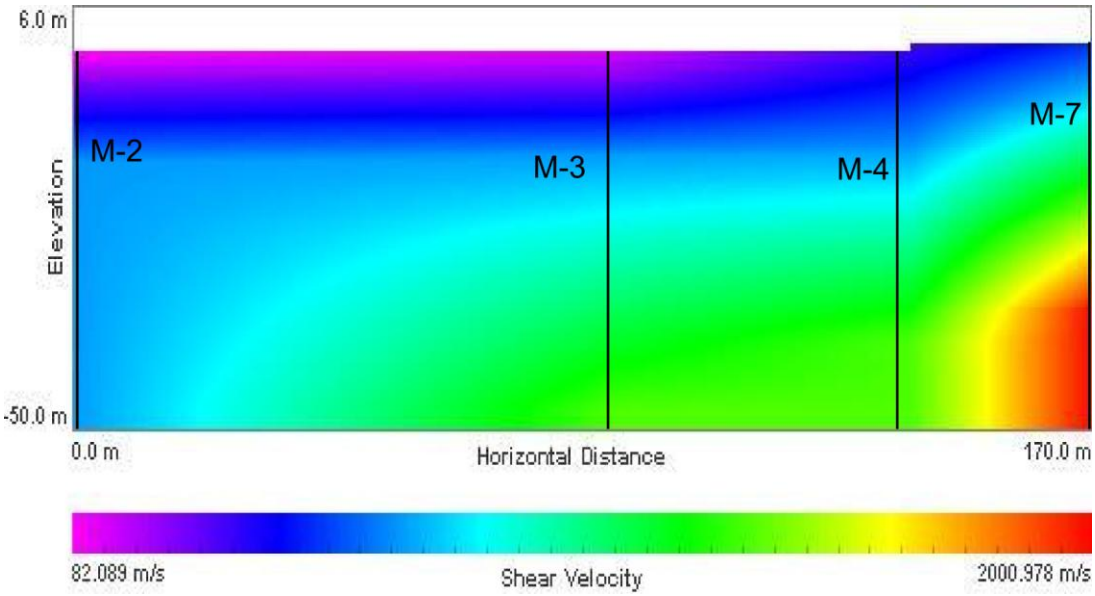

Figure 7.20: Assembled 2D ReMi Profile for the Frontera Site

7.2: Seismic Refraction

To aid in characterizing the stiffness profile in close proximity to the inferred fault trace, three arrays were deployed for seismic refraction data collection. While only one of these arrays directly crosses the inferred fault trace, the others provide valuable information that can be used to confirm weathered layer velocities and directly compare ReMi and seismic refraction results obtained by the same array.

7.2.1: Array Setup and Data Collection

The same array setup and source locations were used at each of the three testing locations at the Frontera site. The diagram in Figure 7.21 illustrates this configuration, ignoring elevation change along the array. None of the arrays were placed completely perpendicular to the inferred fault trace because of the extreme

elevation change that would have to be traversed. The slope is dramatic enough that it would be necessary to survey horizontal receiver offsets as well as elevation change to obtain reliable results. This would prove problematic without a survey grade GPS unit or total station. Instead, array M-6 was situated such that the survey obliquely crosses the inferred fault trace with minimal elevation change. Although the vertical deviation was reduced by taking this approach, the receiver elevations were still approximated using a surveying tape and hand held sight level.

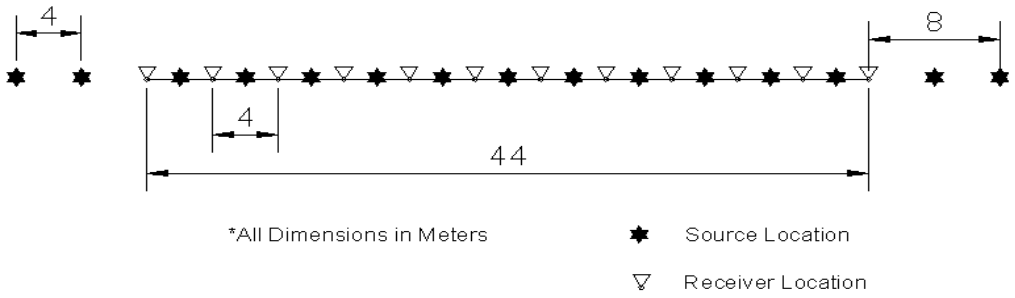

Figure 7.21: Diagram of Frontera Seismic Refraction Arrays

7.2.2: First Break Picking

The seismographs for all three arrays at the Frontera site suggest a significant amount of ray scatter in the records. Due to a combination of refracted, reflected and diffracted wave arrivals, the recordings show some very convoluted signals after the initial arrivals. This is especially visible in Figure 7.22 where the records become highly erratic. While filtering can help to remove some of the incoherent noise, it also tends to cause slight shifts in the first break point arrivals. Therefore, it is more accurate to make picks without filtering when possible. Rather than filtering all channels, approximate picks were made on traces with bad signal to noise ratios. Picks made from filtered data would likely be equally uncertain.

The picking process for array M-5 proved problematic due to some confusion in the first arrivals. This could be in part due to the ray scatter effect that was discussed in the previous paragraph. One end of the array lies near the creek bed where deposited cobbles and boulders could cause rays to take complicated paths. At approximately the array midpoint lies an erosion channel that appears to have similar deposits. Fortunately, the off-end shots provided clearer arrivals. An example of the seismographs and associated first break point picks of an off-end source record is shown in Figure 7.23. This array was modeled using only off-end data.

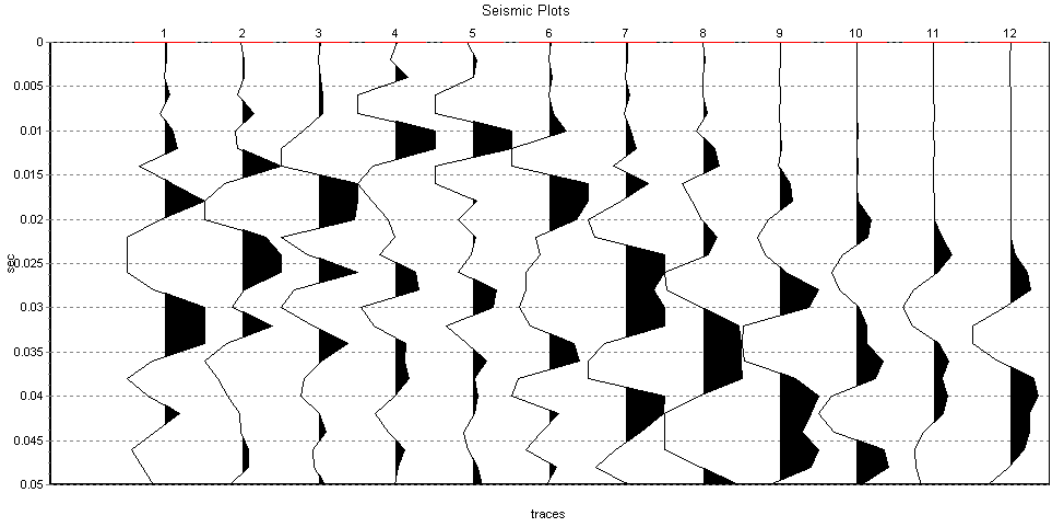

Figure 7.22: Seismic Refraction Record for Array M-5 with Source Located between Receivers 4 and 5

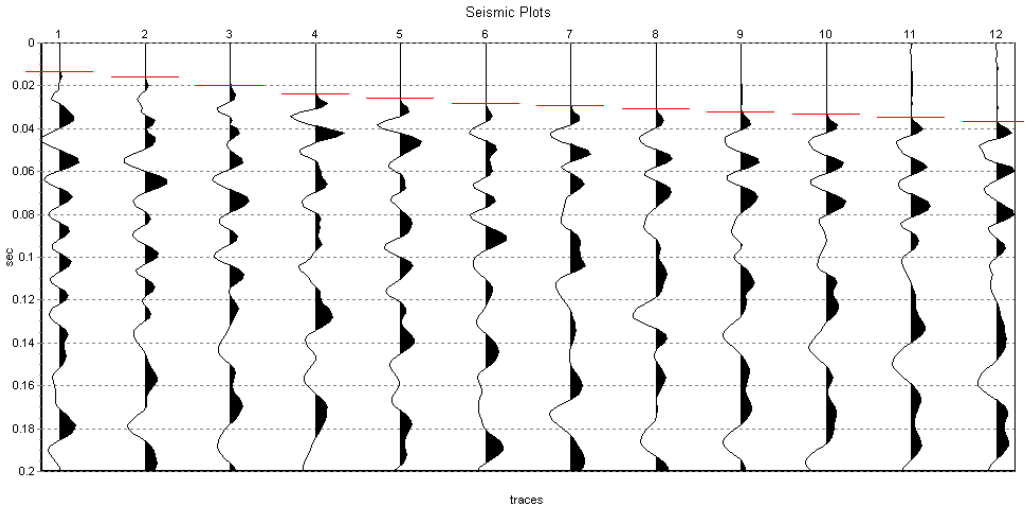

Figure 7.23: Seismic Refraction Record for Array M-5 with Source Located 8m Off-End of Receiver 1

Fortunately, Arrays M-6 and M-7 showed better first break point arrivals for all source locations. They too exhibit some erratic behavior later in the recordings, but the first break points are well defined. Examples of the stacked records and associated picks appear in Figures 7.24 and 7.25.

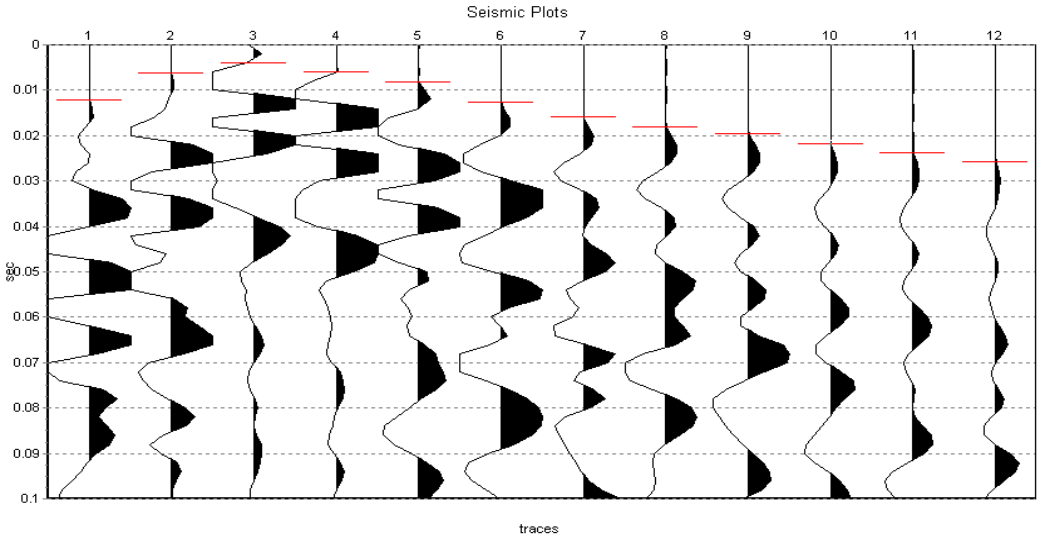

Figure 7.24: Seismic Refraction Record for Array M-6 with Source Located between Receivers 3 and 4

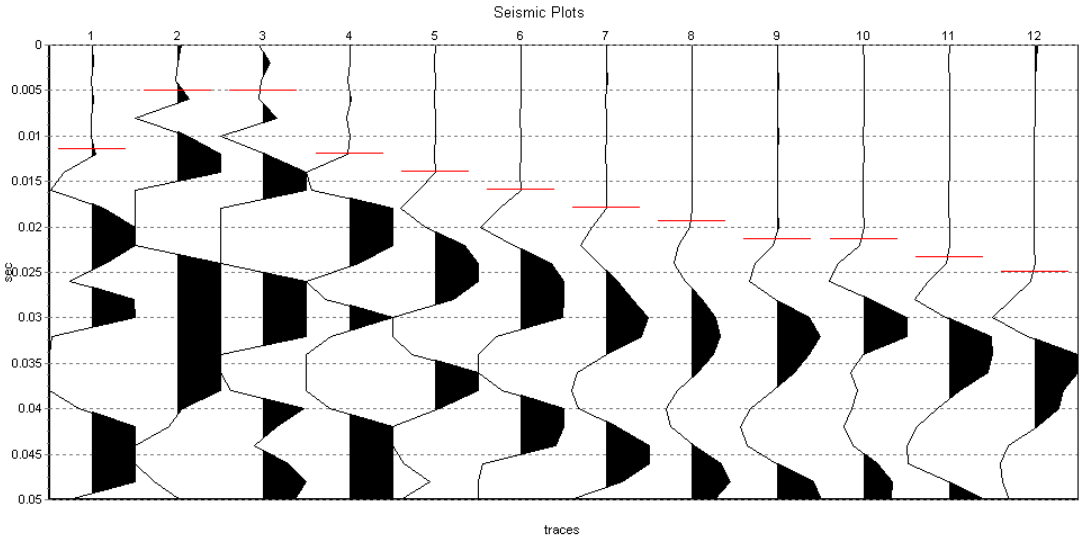

Figure 7.25: Seismic Refraction Record for Array M-7 with Source Located between Receivers 2 and 3

7.2.3: Model Profiles

This section discusses the 2D tomography and layer models generated from the seismic refraction data in SeisOpt@2Dv5.0 and IXRefraX. Again, all Optim plots in this work are in distance units of meters and P-wave velocity units of meters per second. The seismic refraction models are also compared with results obtained through the ReMi method, and array M-7 provides a number of possible model fits from SeisOpt that demonstrate the uncertainty involved in the forward modeling process.

The 2D tomography models presented here have been chosen based upon RMS error from the fit of theoretical travel time curves to the experimental data, “hitfiles” ray coverage plots like the one in section 6.2.3, inferred knowledge about the local geology, and agreement with the layer models output from IXRefraX.

7.2.3.1: M-5 Models

The plots in Figure 7.26 provide the 2D tomography model determined the most appropriate for array M-5. The depth to the first layer interface approximated by the green/pink boundary in Figure 7.26b agrees closely with the layer interface of the IXRefraX layer model depicted in Figure 7.27. The P-wave velocities also appear to agree, increasing confidence in the model.

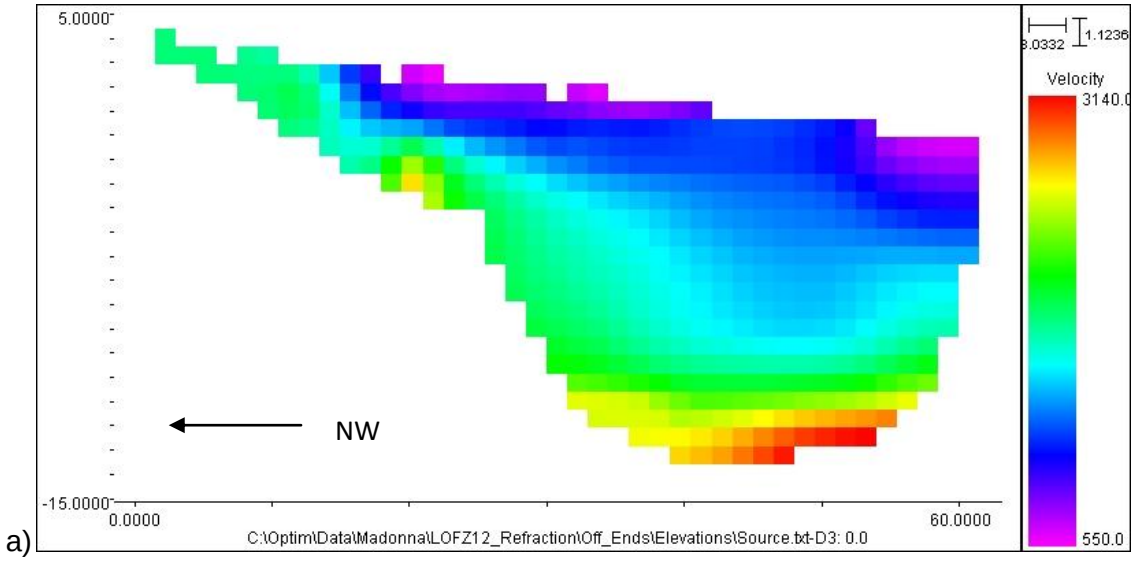

a)

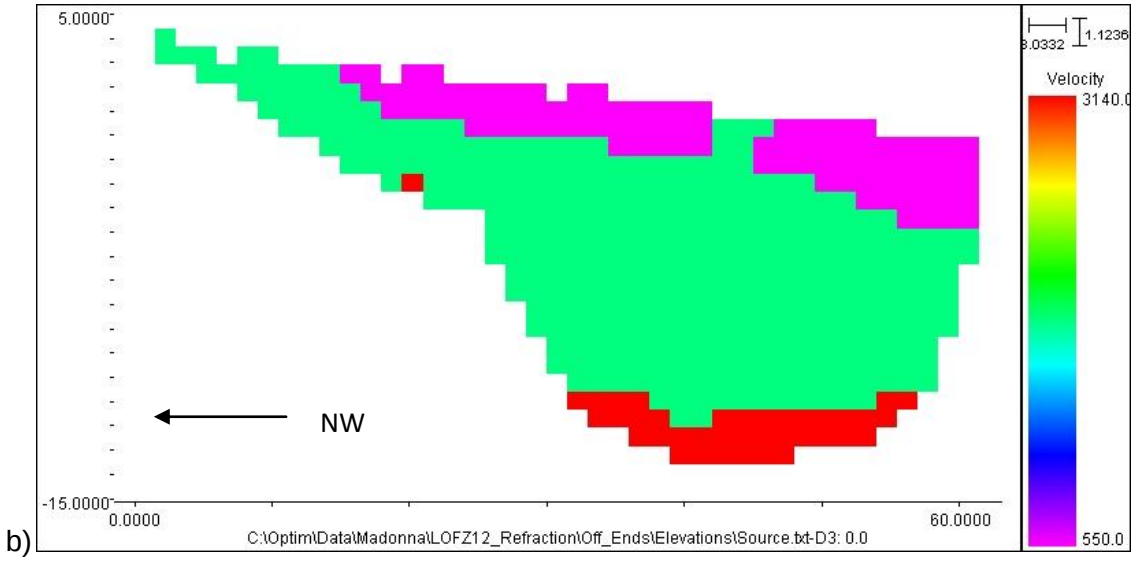

b)

Figure 7.26: 2D Tomography of Array M-5 Data with (a) 257 Colors and (b) 3 Colors

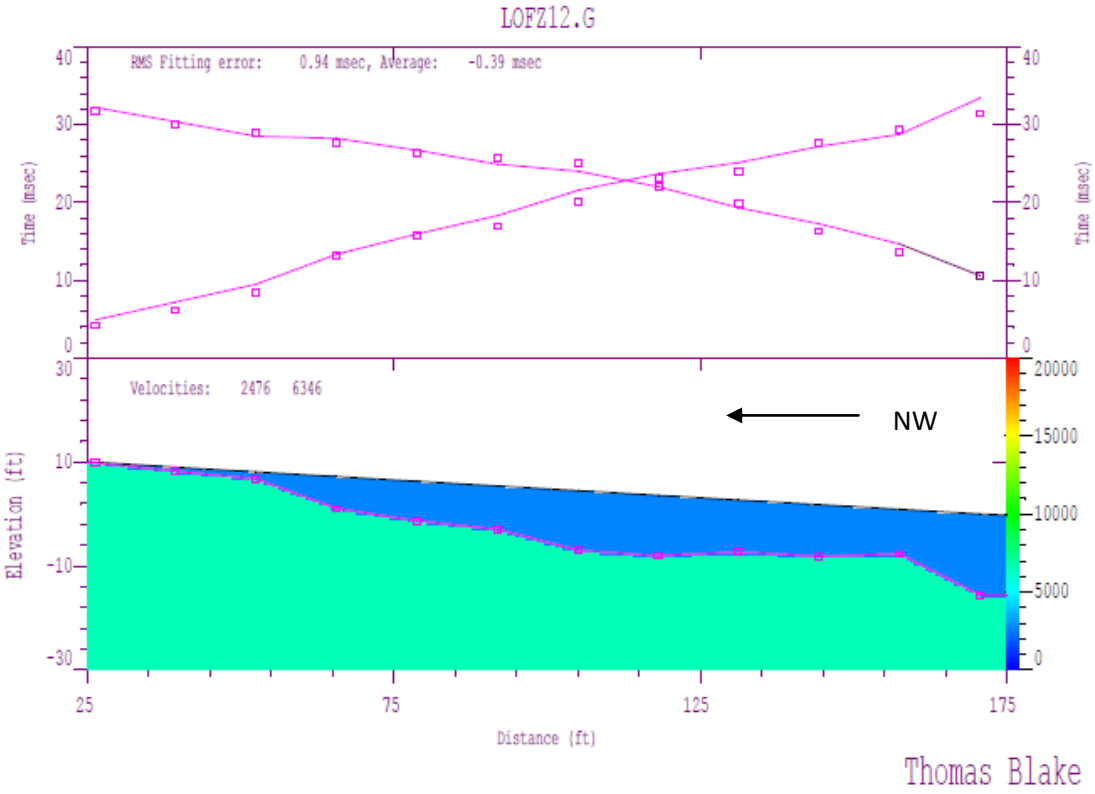

Figure 7.27: Layer Model of Array M-5 Data Output from IXRefraX

(T. Blake, personal communication, September 11, 2012)

The 1D ReMi model for this array shown in Figure 7.38 does not agree well with the seismic refraction data. The velocities in the surface layer seem to be consistent if the S-wave velocity is approximated as 2/3 the P-wave velocity, but the layer depth at the first interface is far deeper in the ReMi model. The deeper layer velocities are also much higher in the seismic refraction models. This could be explained by the fact that the lower portion of the 2D tomography is very unreliable due to limited ray coverage. Based upon the frequency and phase velocity of the picks that define the top layer in the ReMi model, the wavelengths being measured sample a minimum depth of about 5m. This is already below the layer interface suggested by the seismic refraction models. The data indicates that, for very near surface measurements, the ReMi method needs data at higher frequencies than are easily generated in the field.

The bottom layer of the ReMi model agrees with the velocity of the bottom layer in the seismic refraction layer model, as well as the 2D tomography model, but the depth to that layer is in disagreement by as much as 30m. It is unclear why there is such a gross difference between methods here. More testing is necessary to determine what is causing the discrepancy.

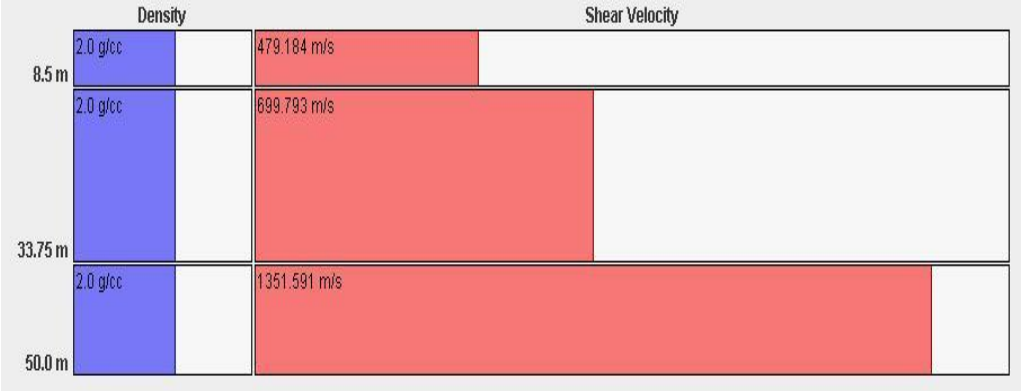

Figure 7.28: 1D Model Profile for Array M-5

7.2.3.2: M-6 Models

The models generated by SeisOpt and IXRefraX are included here in Figures 7.29 and 7.30. The IXRefraX models clip the ends of the survey where ray coverage is limited, and the 2D tomography model only provides approximate inferences. Along the middle of the survey the models seem to agree insofar as the depth to the first layer interface and the general geometry of that interface. For instance, both models indicate a bulge in the layer interface at approximately 15m from the north end of the plot. The velocities in the top layer also seem to be in general agreement with one another. There is no ReMi model to compare with these results due to the uncertainty in the generated p-f plots and the fact that the array crosses the inferred fault trace.

a)

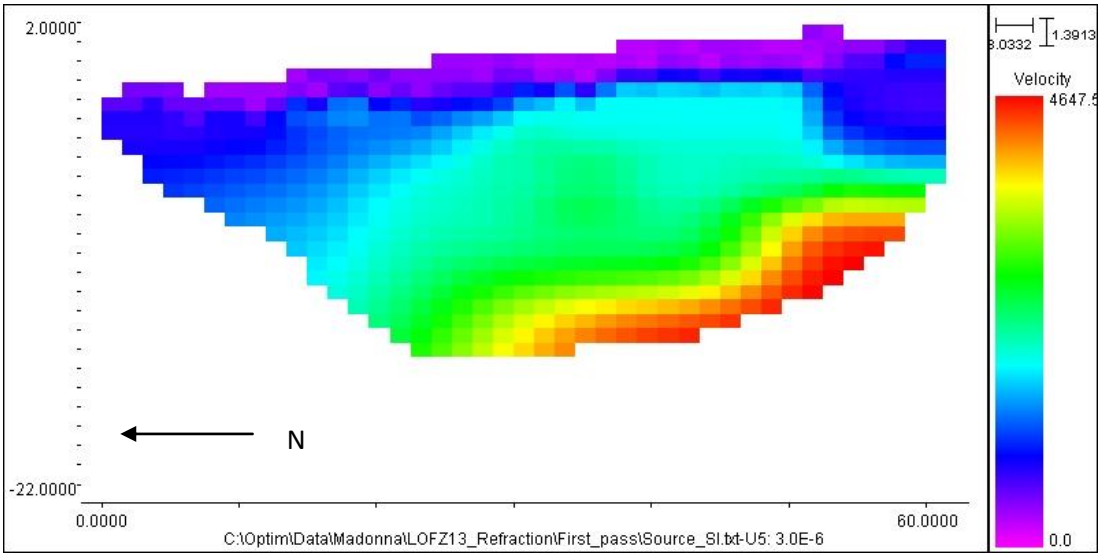

b)

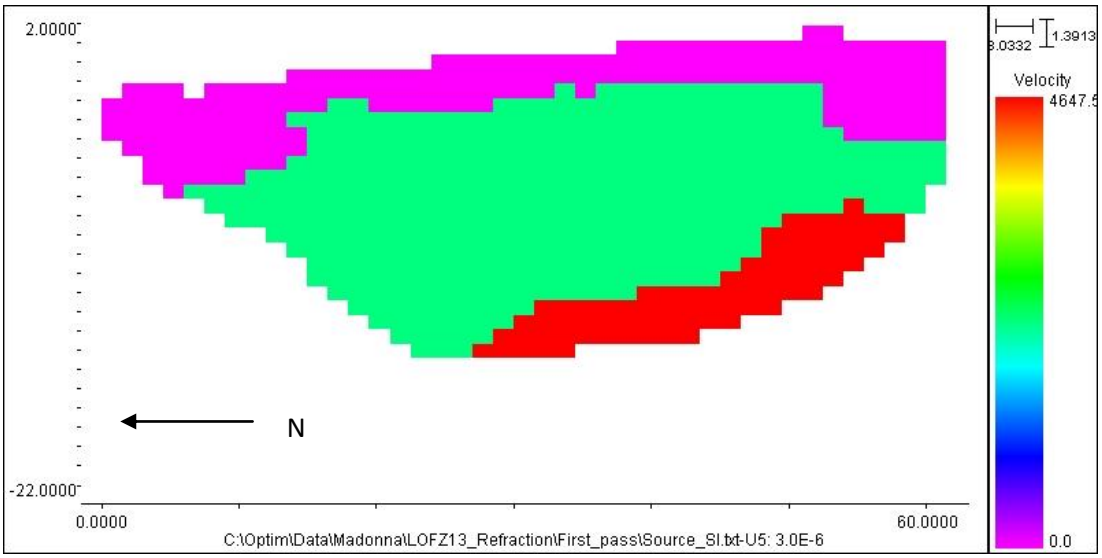

Figure 7.29: 2D Tomography of Array M-6 Data with (a) 257 Colors and (b) 3 Colors

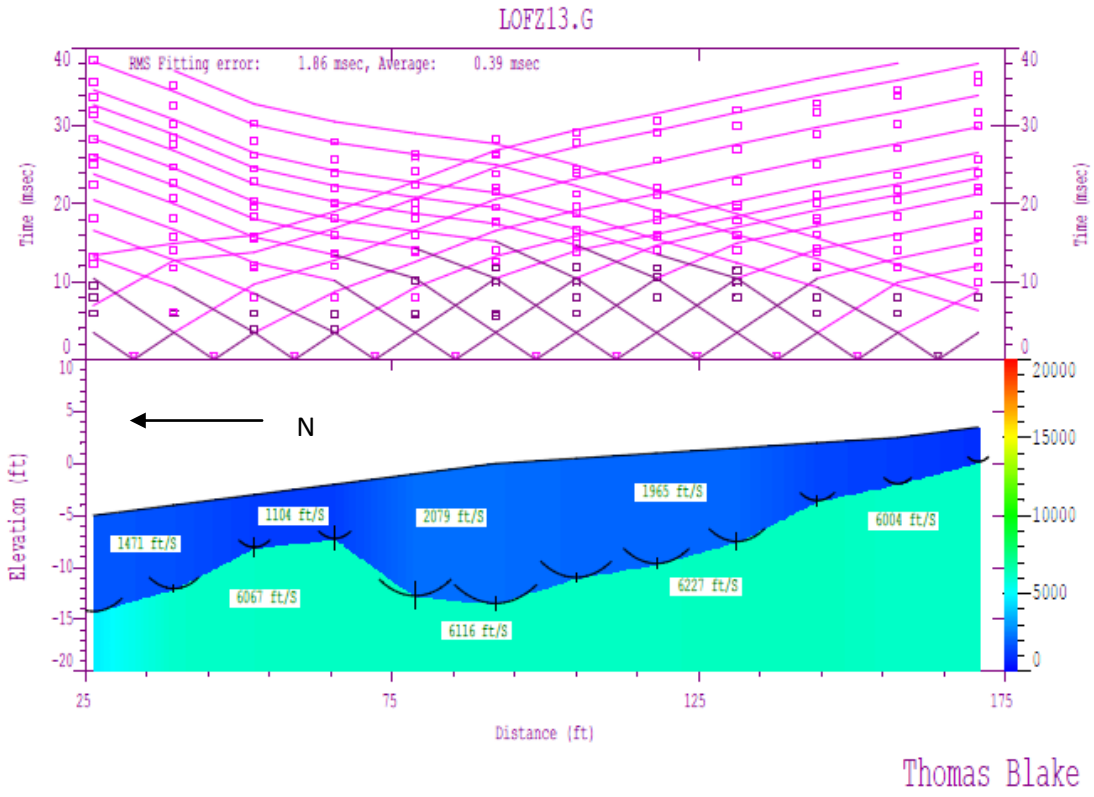

Figure 7.30: Layer Model of Array M-6 Data Output from IXRefraX

(T. Blake, personal communication, September 11, 2012)

7.2.3.3: M-7 Models and Demonstration of Modeling Uncertainty

Occasionally, after eliminating the obviously erroneous 2D tomography models there are still a number that seem to be equally valid. This is where using another modeling program such as IXRefraX can help further isolate the best profile. If other software is not available, or the results do not adequately support any given model, it can be very difficult to decide which is more accurate. To demonstrate this modeling uncertainty, a few of the SeisOpt outputs with varying resolution are included on the following pages. All were generated using the same data set and agree fairly well with the IXRefraX layer model.

a)

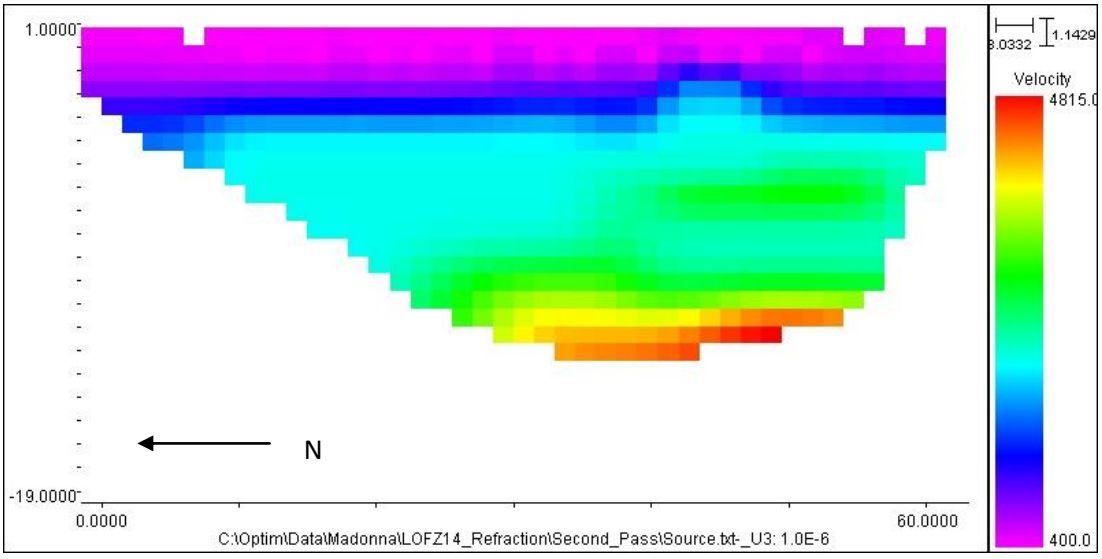

b)

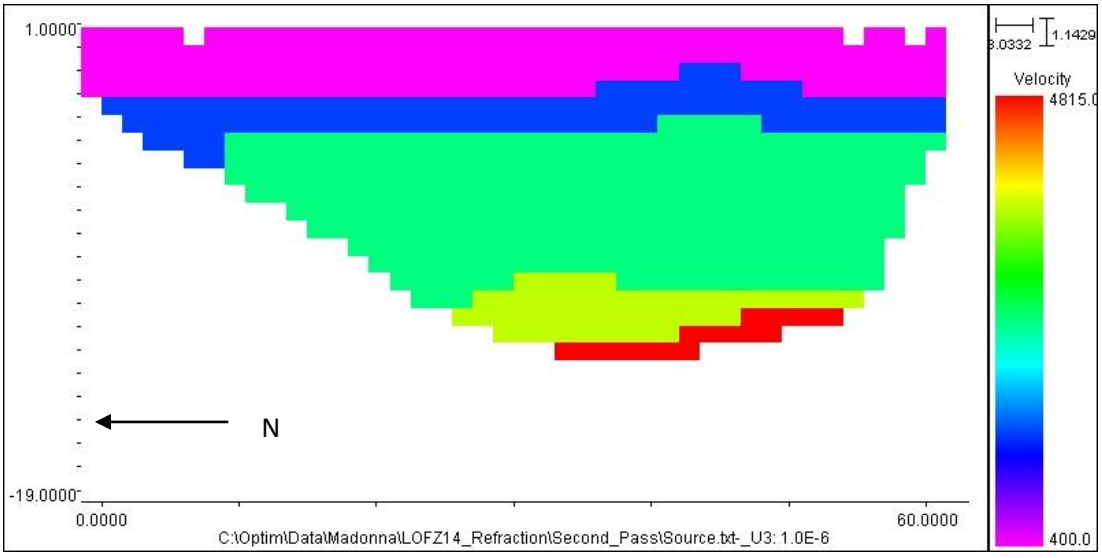

Figure 7.31: 2D Tomography Model Output from SeisOpt for Array M-7 with

(a) 257 Colors and (b) 5 Colors

a)

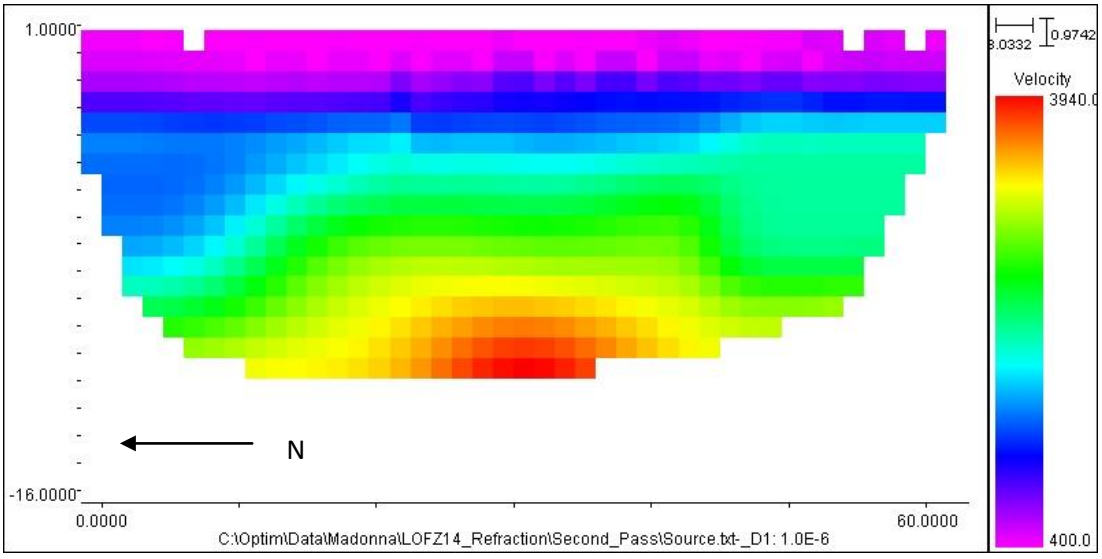

b)

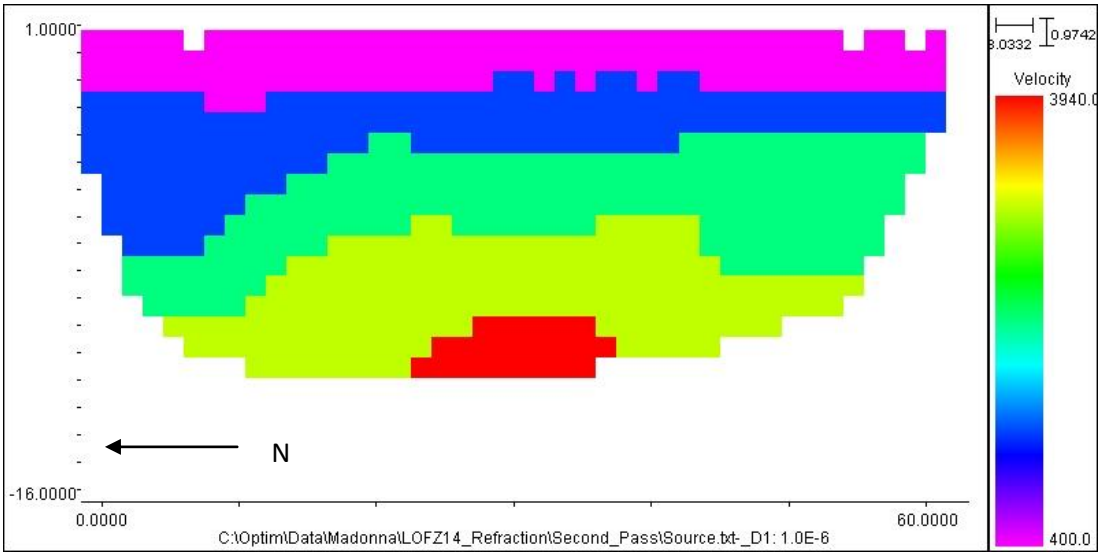

Figure 7.32: 2D Tomography Model Output from SeisOpt for Array M-7 with

(a) 257 Colors and (b) 5 Colors

a)

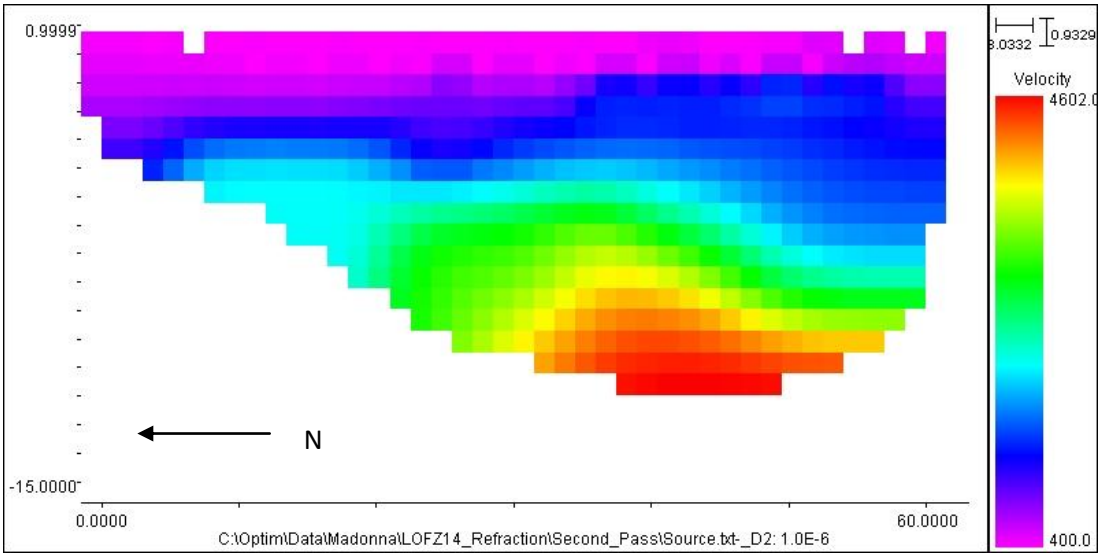

b)

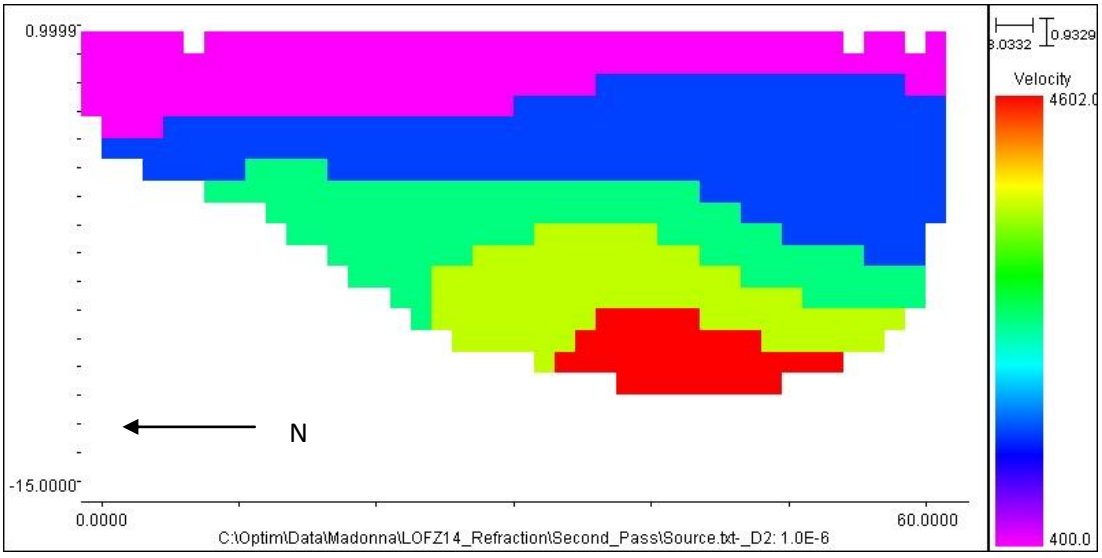

Figure 7.33: 2D Tomography Model Output from SeisOpt for Array M-7 with

(a) 257 Colors and (b) 5 Colors

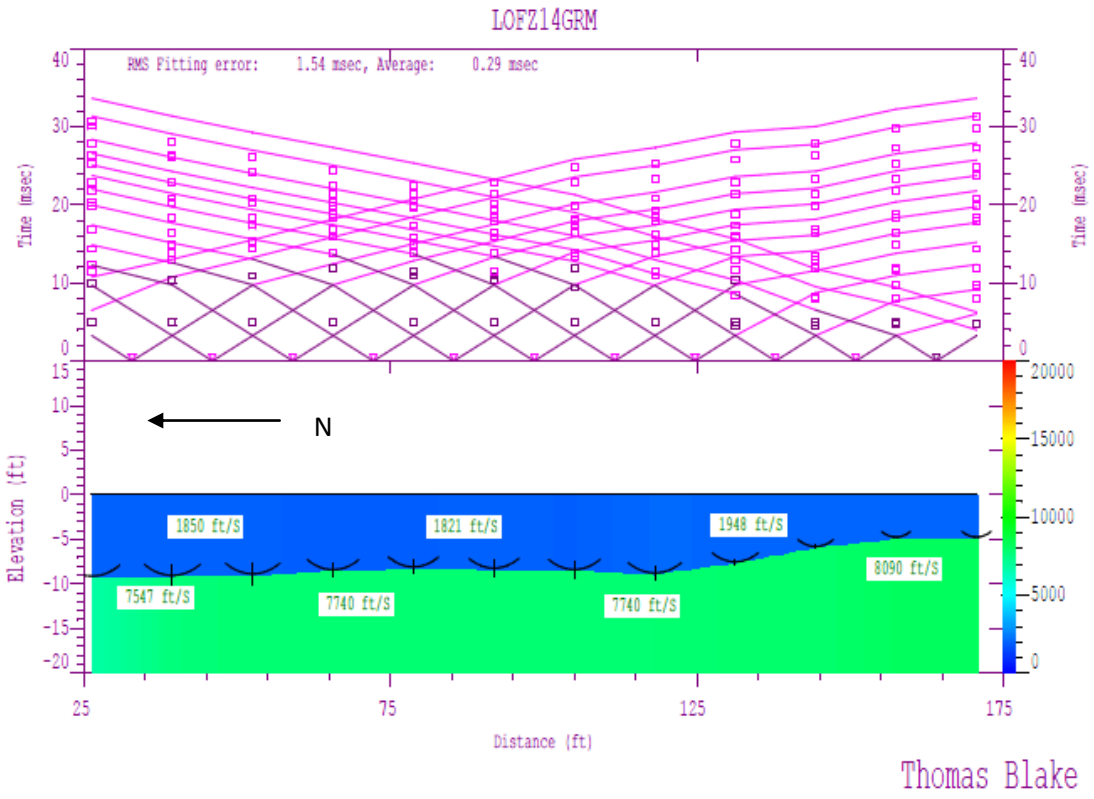

Figure 7.34: Layer Model of Array M-7 Data Output from IXRefraX

(T. Blake, Personal Communication, September 11, 2012)

It's possible that different 2D tomography software such as Rayfract may provide a better comparison with SeisOpt better help to determine which model is most accurate. Unfortunately, this study was confined to the modeling software presented herein. The layer models output by IXRefraX do not include information to nearly as great of depths as the output from SeisOpt. Given that ray coverage is worse near the bottoms of the SeisOpt models and there is no other software to compare with at these depths, any interpretations here should be made with extreme caution.

In comparison with the ReMi 1D model, the methods again show extreme disagreement. The refraction models seem more appropriate given the visible geomorphology at the site. There appear to be bedrock outcrops very near to array M-7,

yet the ReMi method shows softer (about 450m/s) deposits all the way down to approximately 14m. While this interface depth is uncertain, the method should be able to locate the interface to better than 11m accuracy (the difference between stiff layer interfaces of the two methods). Ultimately, it is impossible to know for certain which test is more accurate without further investigation.

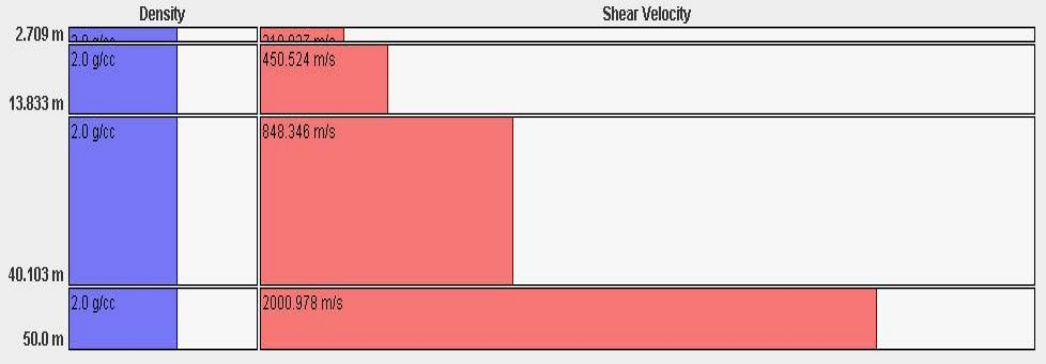

Figure 7.35: 1D Model Profile for Array M-7

7.3: Summary of Findings

This chapter partially met its goal to locate a blind fault trace using the seismic refraction and ReMi methods with little supporting information. The ReMi data throughout the site indicates a marked increase in stiffness laterally as the inferred fault trace is approached and traversed. This finding gives some hope that further research may develop the ReMi method into a useful tool to aid in fault mapping. Unfortunately, the seismic refraction models did not provide much added insight into the fault location or geometry.

During the analysis of the data in this chapter a number of important observations came to light that provide topics for further research and may aid future work.

- ReMi data collected at quiet locations such as the Frontera site can indicate false dispersion trends due to “wash out” of the true Rayleigh wave dispersion. This might be caused by vegetation contacting the receivers, noise inherent to the measurement equipment, or the presence of a dominant signal source coming from an azimuth out of line with the receivers.
- Signal drift through the course of a ReMi recording can be ignored because it is processed as a low enough frequency that it does not affect the range of data where dispersion picks are made.
- The data collected at this site seems to suggest that by adjusting the receiver spacing and array length such that it can sample a given wavelength at three locations simultaneously may improve the data.
- Close proximity energy sources offset perpendicularly from the midpoint of the array can produce a high density of elevated spectral ratio curves moving from bottom left to top right of the p-f plots.
- Close proximity energy sources arriving in line with the array from one end can produce significantly different results than when approaching from the opposite end. This may be due to lateral variation in the soil strata beneath the array in conjunction with “wash out” of the data caused by significantly higher energy arrivals at the near end.
- Abnormal distributions of spectral ratio peak zones in the p-f plots such as those generated from arrays M-6 and M-7 may indicate abnormal subsurface structural geometry. This could potentially indicate the presence of a fault and can easily be tested further to determine if this is a consistent result in the presence of such a feature.

- Erratic seismic refraction recordings may indicate a high degree of ray scatter from diffraction, reflection and refraction. This could again indicate abnormal subsurface structural geometries and potentially a fault.
- The ReMi and seismic refraction methods showed extreme disagreement in this chapter. A more controlled comparison between methods is warranted before the two should be further used together for fault mapping.

Chapter 8: Conclusions and Recommendations

8.1: Summary

Locating blind fault traces can be a time consuming and costly process using typical borehole or trenching investigation techniques. At the same time, it is a crucial part of the design process and is often times a determining factor in whether or not a project is feasible in a given location. In the cases of large infrastructure such as highways or rail lines it is impossible to avoid crossing active fault traces at some point, but knowledge of the location where displacements may occur can help engineers mitigate the risk as much as possible. This body of work investigated the potential of the non-invasive seismic refraction and ReMi methods as tools to aid in locating these elusive fault traces.

In the process of achieving the primary goal of this thesis a number of parametric and precision studies were carried out in order to better understand the ReMi method. In addition, this work contains novice observations made while learning to use both the ReMi and seismic refraction methods. Although experienced geophysicists may find some of this information obvious, it is the hope of the author that this body of work can serve as a guide to students or other newcomers who wish to be able to contribute to the topic.

After developing a workable understanding of the theory and practice involved with the ReMi and seismic refraction methods, the techniques are applied to the goal of successfully imaging lateral variation in the soil strata. A dramatic change in the soil stiffness profile over a short horizontal distance could indicate the presence of a reverse or normal fault. This research first attempts the methods at a location where the fault

trace has been thoroughly investigated through trenching and drilling, then proceeds to a site with very little available subsurface information

The ReMi and seismic refraction methods require relatively minimal time and cost, and can be employed entirely at the ground surface. This research showed promise that these techniques may through further development and testing provide a means to rapidly isolate the location where a blind fault trace likely exists. However, based upon the levels of uncertainty here observed within these methods, it is unlikely that they will ever be reliable enough to completely replace traditional trenching or borehole investigations.

The subsequent sections of this chapter present the primary findings of this project, suggest improvements to the testing procedures, and offer opportunities for future research.

8.2: Research Findings

This project produced a number of important findings that are summarized in this section. In addition to the larger goal of applying the ReMi and seismic refraction methods to fault mapping, the parametric, sensitivity and precision studies carried out in this work provided some valuable insight into the intricacies of the ReMi method. A number of key observations made along the way are also presented.

The precision study carried out at Crops Field C-31 helped to characterize the uncertainty that can be expected within the ReMi method when all controllable variables are held constant. Results indicate a 7% COV in V_{s30}, and as high as 14 and 16% in layer interfaces and velocities respectively. This dataset also suggests that at larger

depths and/or higher phase velocities the method becomes more stable. At the bottom layer of the models in this study only an 8% COV was found in V_s.

Parametric studies on the ReMi method at both Crops Field C-31 and the Frontera site indicated that, when a dominant off-line source is introduced to the wave field, the dispersion trend in the p-f plots will shift to higher phase velocities due to the obliquity of the wave front arrivals with respect to the array. The response at the true phase velocities is “washed out” here due to the strength of active signal used for this study.

A sensitivity study at the Ingley site helped to evaluate the effect that relative elevation change between receivers can have on the ReMi method. Slope corrected and non-corrected results appear nearly identical at array I-4. This array traversed grades sometimes steeper than 6.7% without adversely affecting the measurements.

Throughout this work the passive ReMi measurements exhibited weakly lit dispersion trends or uninterpretable data. The list of potential causes for this is provided below, but not all of these hypotheses apply to every array.

1. Significant lateral variation in the subsurface beneath the array, causing the spectral ratio peak trend to be more widely distributed and less sharply defined
2. Body wave interference generated by close proximity utility lines
3. Body wave interference from a nearby dominant signal source
4. Nearby slopes acting as a discontinuity in the soil strata thereby affecting wave propagation
5. Vegetation contact with receivers
6. Noise inherent to the measurement equipment

With respect to the primary goals of this work, these methods do show potential for future development. In particular, the 2D assemblies of 1D ReMi profiles indicated marked lateral variation in the V_s profiles at both the Ingley and Frontera sites. While this bulk shift can be trusted in a very general sense, the data is too uncertain to rely upon quantitatively. It should also be noted that the layer velocities do not agree quantitatively between methods.

The final ReMi models from the Ingley site arrays also showed general agreement with the work by Lettis and Hall (1994). These models were not constructed through a blind analysis, but fitting them to the available subsurface data was not difficult. The theoretical dispersion curves that characterize the modeled profiles fit the data as closely as if no attempt were made to match the available information.

At the Frontera site the 2D assembled ReMi model qualitatively matches the observed geomorphology. While the method does not definitively prove that the inferred scarp feature is a fault, it does vindicate the suspicion that was previously based solely upon the site topography. Despite the uncertainty in the ReMi method, this could potentially become a litmus test as to whether or not further investigation is warranted at a given location.

The seismic refraction results did not as clearly indicate any evidence of faulting. At the Ingley site the layer and tomography models helped to corroborate general interface depths and velocities found in the ReMi testing, but at the Frontera site the methods showed complete disagreement. To further employ the seismic refraction method in conjunction with the ReMi method for fault mapping, the two should be first successfully matched in a more controlled situation.

The final and possibly most important finding of this work is in the irregularity of data collected in close proximity to the known and inferred fault traces. Both the ReMi and seismic refraction data displayed odd behavior in the p-f plots and seismographs respectively. When plotted in p-f space, the ReMi data exhibited abnormally distributed energy. Many spectral ratio peak zones appeared above the general dispersion trend. While the exact cause for this phenomenon is unclear, the consistency of this occurrence among records taken in close proximity to the fault should not be ignored. Similarly, the seismographs for the seismic refraction data became very erratic in the arrays near the inferred fault trace at the Frontera site. The anomalous behavior of both methods may possibly be attributed to abnormalities in the subsurface structure caused by faulting.

8.3: Improvements on Testing Methods

To aid future researchers in better planning their geophysical surveys, this section provides a number of suggestions that may help enhance data collection and lead to better results.

For the ReMi method:

1. Arrays should be spaced such that the wavelengths of interest are most effectively measured. If a given wavelength can be measured simultaneously at three or more points spread out along the full length, it will be more accurately characterized.

2. If a wide variety of wavelengths are of interest multiple array spacings can be deployed with the same survey midpoint. Picks that are made independently from each array can be combined manually for forward modeling.
3. Underground utility lines and nearby dominant signal sources should be avoided to minimize record contamination by body waves.
4. If a majority of the ambient signal is coming from a known direction it is helpful to orient the array such that the arrivals will be traveling parallel to the array azimuth.

For the seismic refraction method:

1. Overlapping multiple arrays with smaller receiver spacing is preferable to using a single array if time warrants. This can greatly improve imaging resolution and signal strength.
2. If available, a more energetic source is helpful.
3. A smaller data acquisition time step (0.125ms) makes first break picking easier.
4. If available, survey equipment can help to greatly reduce the uncertainty caused by receiver location input error.

8.4: Opportunities for Further Investigation

A number of opportunities for future research were uncovered during this project. While not within the scope of work for this dissertation, the following list provides future researchers with some potential avenues for investigation.

- The precision study within this body of work could be built upon with much larger datasets. Three suites of testing are not an adequate dataset to make reliable

statistical conclusions. It would be easy to take a large quantity of data for this purpose in a single day.

- As mentioned in section 8.2, the ReMi and seismic refraction methods generally did not quantitatively agree in this research. If the two are ever to be used in conjunction with one another, the analysis techniques need to first be calibrated so that the methods agree in a controlled situation. Only then can they be trusted in their agreement in more complex scenarios.
- Further testing at the sites investigated in this work could help to isolate the cause(s) of the poor results obtained through passive measurements. The list of hypotheses summarized in section 8.2 provides a good starting point for this endeavor.
- A method for determining measurement noise levels and thus the required signal amplitude to collect good passive data would aid future researchers in determining when a site is too quiet for the ReMi method.
- Further data collection from either method in close proximity to reverse or normal fault traces may help to either corroborate or disprove the hypothesis that the irregular data collected in this work resulted from fault-related subsurface structure.

References

Aki, K. (1957). “Space and time spectra of stationary stochastic waves, with special reference to microtremors.” *Bull. of the Earthquake Res. Inst., University of Tokyo,* 12(5), 415-456.

American Society for Testing and Materials (ASTM). (2006), "Standard guide for using the seismic refraction method for subsurface investigation." D 5777, West Conshohocken, PA.

American Society for Testing and Materials (ASTM). (2007), " Standard test methods for crosshole seismic testing." D 4428, West Conshohocken, PA.

American Society for Testing and Materials (ASTM). (2008), " Standard test methods for downhole seismic testing." D 7400, West Conshohocken, PA.

Cox, B.R. and Beekman, A.N. (2011). “Intramethod variability in ReMi dispersion measurements and V_s estimates at shallow bedrock sites.” *J. Geotech. and Geoenv. Eng.,* 137(4), 354-362.

Jones, R.B. (1958). “In-situ measurement of dynamic properties of soil by vibration methods.” *Geotechnique*, 8(1), 1-21.

Kitsunezaki, C. (1975). “Shear wave logging by suspension type geophone, I.” *Butsuri-tanko,* 28, 13-21.

Lay, T. and Wallace, T. C. (1995). “Modern Global Seismology.” *Academic Press,* San Diego, CA.

Lettis, W. and Hall, T. (1994). "Los Osos fault zone, San Luis Obispo county, California." *Special Paper – Geol. Soc. of Amer.*, 292, 73-102.

Louie, J. N. (2001). “Faster, better: shear wave velocity to 100 meters depth from refraction microtremor arrays.” *Bull. Seismol. Soc. Am.*, 91(2), 347-364.

McMechan, G. and Yedlin, M. (1981). "Analysis of dispersive waves by field transformation." *Geophysics*, 46(6), 869-874.

Moss, R. E. S. (2008). *"*Quantifying measurement uncertainty of thirty-meter shear-wave velocity." *Bull. Seismol. Soc. Am.,* 98(3), 1399-1411.

Nazarian, S. and Stokoe, K . H. (1984). "In situ shear wave velocities from spectral analysis of surface waves." *Proc., Eighth World Conf. on Earthquake Eng.,* Prentice-Hall, Inc., Englewood Cliffs, Nj., 3, 1-38.

Ohya, S., Ogura, K., and Imai, T. (1980). "The suspension PS velocity logging system." *Proc., Offshore Technology Conference*, Offshore Technology Conference, Houston, Tx., 1, 291-298.

Palmer, D. (1980). "The Generalized Reciprocal Method of Seismic Refraction Interpretation." *Soc. of Exploration Geophysicists.,* Tulsa, OK.

Parasnis, D. S. (1986). "Principles of Applied Geophysics". *Chapman and Hall*, Boundary Row, London, UK.

Park, C. B., Miller, R. D., and Xia, J. B. (1998). "Imaging dispersion curves of surface waves on multi-channel record." *Proc. SEG Annual Meeting,* Soc. of Exploration Geophysicists, New Orleans, LA.

Park, C. B., Miller, R. D., and Xia, J. B. (1999). "Multichannel analysis of surface waves." *Geophysics*, 64(3), 800-808.

Park, C. B., Miller, R. D., Ivanov, J., Xia, J. B., and Ryden, N. (2005). "Combined use of active and passive surface waves." *J. Env. and Eng. Geophys.*, 10(3), 323-334.

Pérez-Santisteban, I., García-Mayordomo, J., Martín, A. M., and Carbó, A. (2011). "Comparison among SASW, ReMI and PS-logging techniques: Application to a railway embankment." *J. Applied Geophys.*, 73(1), 59-64.

Redpath, B. B. (1973). "Seismic refraction exploration for engineering site investigations." *Army Engineer Waterways Experiment Station*, Livermore, CA.

Thorson, J. R. and Claerbout, J. F. (1985). "Velocity-stack and slant-stack stochastic inversion." *Geophysics*, 50(12), 2727-2741.

Tokimatsu, K., Shinzawa, K., and Kuwayama, S. (1992). “Use of short-period microtremors for V_s profiling.” *J. of Geotech. Eng.*, 118(10), 1544-1558.

Yuan, J. (2011). “Field studies comparing SASW, Beamforming and MASW test methods and characterization of geotechnical materials based on V_s.” Doctoral dissertation, University of Texas, Austin, TX.